High-Performance, Multi-Functional, and Miniaturized Integrated Antennas

by

Nader Behdad

A dissertation submitted in partial fulfillment
of the requirements for the degree of
Doctor of Philosophy
(Electrical Engineering)
in The University of Michigan
2006

Doctoral Committee:
Professor Kamal Sarabandi, Chair
Professor Eric Michielssen
Professor Christopher Ruf
Associate Professor Michael P. Flynn
Associate Professor Mahta Moghaddam

To my mother Mehri and my father Mohsen

To my wife Fariba and my lovely daughter Elena

ACKNOWLEDGEMENTS

First and foremost I would like to thank my parents. If it was not for their love, support, sacrifices, and the great interest that they took in my education, I would not be able to accomplish what I did. It is for all of this that I dedicate this dissertation to them.

There are many people who contributed to my academic success throughout the past two decades of formal education that I received. I remember the names of many of them and I have forgotten the names of others but I am grateful to all of them from my first grade teacher to my Ph.D. adviser. Among the people who contributed to my academic success at the University of Michigan, my greatest appreciation surely belongs to Professor Kamal Sarabandi. I appreciate the opportunity that he gave me to come to the University of Michigan to continue my post graduate studies and to work with him in the research field that I truly love. I certainly could not have asked for a better adviser or a greater opportunity. He has been an outstanding teacher and mentor and I have learned a lot from him. I also would like to thank the members of my dissertation committee Professors Michael Flynn, Mahta Moghaddam, Eric Michielssen, and Christopher Ruf for their guidance and support in every step of the way, particularly during the past two years.

This list will not be complete without acknowledging my wife Fariba for her support during the past nine years. Presence of my lovely daughter Elena, who was born in March of 2004 and brought a great deal of joy into my life, was also a great motivation for me. During the past four and a half years at the University of Michigan,

I have enjoyed the friendship of many great people. I would like to thank all of my good friends at the University of Michigan, especially those at the Radiation Laboratory. I especially would like to thank Mr. Alireza Tabatabaeenejad, who has always been a very good friend and willing to help me in many ways. A phone conversation with him in Fall of 2001 was my main motivation to try to come to the University of Michigan and he was a great help in that process.

I have been extremely fortunate to get a chance to work on a project associated with the Center for Wireless Integrated MicroSystems (WIMS) at the University of Michigan. Working at this interdisciplinary center was certainly an excellent experience. I would like to acknowledge the financial support that I received from the WIMS center, which facilitated my research and my graduate life in the first three years of my studies. I am also thankful to the Rackham School of Graduate Studies for awarding me the Rackham Predoctoral Fellowship that generously funded the final year of my Doctoral research during the 2005-2006 academic year.

Nader Behdad

Ann Arbor, Michigan

June 14, 2006

TABLE OF CONTENTS

LIST OF TABLES

LIST OF FIGURES

CHAPTER 1

Introduction

1.1 Motivation

The exponential advancement of the human race is perhaps best visible in the twentieth century. Never before had mankind seen such rapid advancements in science and technology. In the course of one century we have moved from traveling on horses and carriages to traveling faster than the speed of sound into space. It is interesting to imagine where we will be at the end of the twenty-first century. The twentieth century was full of brilliant innovations that have touched our lives in many levels. Wireless communications is undoubtedly one of these innovations that has affected our lives at a personal level. The pioneers of wireless technology who invented and perfected radio in the beginning of the twentieth century could not have imagined the impact of their invention a century later. Current advancements in telecommunication, electronics, and computer industries have fundamentally altered the way we communicate.

The telecommunication revolution that began with the invention of telephone by Bell continued with the invention of radio by Marconi then it was elevated to a whole new level by the introduction of other new technologies such as satellite communication, mobile communication, and later on the convergence of the two in ambitious projects such as IRIDIUM and Global STAR. This revolution continues today with the widespread use of the Internet for data transfer and electronic correspondence as well as voice and video transmission. Recent technological advancements in science and engineering have blurred the traditional boundaries between previously different services such as the long distance telephone, radio and television broadcasting, and data transmission through the Internet. The number of Internet radio and television stations has increased significantly and continues to increase at a fast pace. Voice over IP technology is successfully being exploited by small corporations to provide a cheaper alternative to traditional long distance phone services offered by established providers. Nowadays consumers rapidly utilize new technologies and the time between the introduction of such technologies and their marketing has significantly decreased to a level that today's researchers must work hard to keep up with consumer's demands. These recent technological advancements and the growth in consumer demands has tremendously increased the need for more reliable, power efficient, cheaper, and above all, smaller wireless devices. Novel wireless devices that are not limited to one standard, one network, or one particular task will be in great demand in the near future. Small portable devices that have the capability of transferring voice, data, and video at blazing speeds over a wireless network are the vision of tomorrow. Tomorrow's wireless consumers demand 100% network coverage, 100% of the time, and this is becoming a reality with the development of seamless mobile services. The principle behind such services is that the user will connect seamlessly to the optimum available network at any given time, from one handset. For example, to the Wireless Local Area Network (WLAN) hotspot at the airport, the 3G network within city limits, and the GSM network elsewhere.

As more people begin to appreciate the true benefits of Wireless LANs, which are turning cafes, hotels, airports, and rail stations into wireless hotspots, the wireless sector is gearing up for the hardest-fought standards-setting battle yet. The next generation of WLAN standards, IEEE 802.11n, promises data rates of at least 100Mbit/s, whereas the current fastest speed achievable, from 802.11g, is theoretically 54Mbit/s and in practice is actually about half of that. It is expected that the 802.11n will be based on multiple input multiple output (MIMO) antenna technology.

Future wireless devices will be compatible with different standards and need to be able to operate at multiple frequency bands. Furthermore, as the size of these devices become smaller and smaller, the need for compact and miniaturized antennas with desirable radiation characteristics is on the rise. Antennas are devices that transform electric signals flowing in wires to electromagnetic waves propagating in space and are vital components in any wireless system. The antenna dimensions are mainly determined by its frequency of operation and are inversely proportional to this frequency. Since most wireless systems work at relatively low frequencies (a few GHz at most), antennas are usually the largest components of any such system. In future wireless devices, where many different sub-systems exist and the overall area of the entire system should be as small as possible, having a small antenna becomes extremely important. Miniaturized antennas are also sought for other applications such as RF telemetry interfaces for communicating with implantable medical devices or environmental sensor networks. Therefore, antenna miniaturization is a necessary task in achieving optimal designs for future wireless systems. Such antennas need to be efficient and able to operate over the frequency band(s) specified by each application. Since reducing the size of the antenna reduces its bandwidth and efficiency [1], new techniques must be developed to design highly efficient miniaturized antennas with sufficient bandwidth. Furthermore, the existence of numerous standards and technologies, currently in use, requires miniaturized and compact antennas with different capabilities. Applications such as cellular phones, Wireless Local Loop (WLL) systems, Ultra Wideband (UWB) communication systems, or WLANs require antennas with drastically different characteristics. For example, many of the existing WLAN devices use two different unlicensed frequency bands in the 2.4 GHz and 5 GHz bands.

Thus, the antennas used in these systems must be able to operate at these two frequency bands whereas a UWB radio requires UWB antennas with bandwidths on the order of 3:1.

1.2 Literature Review

1.2.1 Design of Electrically Small Antennas

The bandwidth, radiation characteristics, and polarization of an antenna is a function of its geometrical parameters. The dimensions of an antenna are mainly determined by its frequency of operation and the environment in which it operates. These dimensions are inversely proportional to the frequency of operation. Antenna miniaturization is not a new topic and has been extensively investigated by numerous researchers. In 1947, Wheeler investigated the fundamental limitations on small antennas [2], and a year later Chu published his famous paper "Physical Limitations on Omni-directional Antennas", deriving a theoretical relationship between the dimensions of an antenna and its minimum quality factor [1]. Since then, the famous Chu limit has been used as a means of comparison for performances of small antennas. As brilliant as Chu's derivation was, it is only applicable to a certain class of antennas and provides a rather loose limit. Other researchers have also extensively studied these fundamental limitations [3]. In 1996, McLean re-examined the derivation of the Chu limit and obtained a more accurate limit based on Chu's derivation [4]. In all of these studies, the lower bound for the antenna Q is derived using different methods. A number of different techniques exist for calculating the Q factor of an antenna. In [5], Collin proposes a method for calculating the antenna Q in which the Q of an antenna is defined similar to the definitions used in conventional network theory. In [6], the Foster reactance theorem is used to define the radiation Q of an antenna, which is then related to its measured input impedance. Time domain evaluation of Q of antennas is studied in [7] and another method to evaluate the Q of small antennas is given in [8]. Because of the importance of electrically small antennas, the studies in determining the lower bound of Q of small antennas have continued well into the new century [9, 10, 11], and this area is still an active area of research [12, 13].

These studies have mainly focused on the theoretical limitations of small antennas and evaluation of the Q of antennas. However, antenna miniaturization, in spite of its adverse affects, is still a challenging problem and needs to be addressed. Techniques for reducing the dimensions of an antenna can be categorized into two general categories: 1) Antenna miniaturization using optimal antenna topology and 2) Antenna miniaturization using magneto-dielectric materials. In the first category, the electrical dimensions of the antenna are reduced by modifying its topology. For example, a linear wire antenna may be bent in different directions to reduce the maximum linear dimension of the antenna and thereby reduce its overall occupied space. Wheeler studies several such miniaturization methods in [14]. Other researchers have also extensively used this method for reducing the antenna dimensions [15, 16, 17]. In [18], electrically small self resonant wire antennas are designed using a genetic algorithm optimization method. Use of fractal geometries in reducing the antenna size and the characteristics of such antennas are examined in [19] and [20].

In the second category, miniaturization is achieved by loading the antenna with high permittivity and/or high permeability materials. High-permittivity materials have long been used to reduce the dimensions of printed antennas. Examples of such antennas are given in [21]. More recently, this technique is used in [22] to design an electrically small antenna on a package. In [23], a dielectric resonator loaded slot antenna is used to achieve a wideband compact antenna. Use of high permeability materials, however, were traditionally limited to low frequency applications where magnetic materials such as ferrites have considerable relative permeabilities (μ_r). As frequency increases beyond a few hundred Mega Hertz, however, μ_r becomes lossy and such materials cannot be used for antennas with high efficiency requirements. In [24], the combination of magnetic and dielectric materials is used to circumvent this problem to some extent and achieve a compact wideband antenna. Another solution to this problem is to make use of artificial magnetic materials. These materials usually consist of some sort of resonant circuits embedded in a dielectric substrate, which behaves as a magnetic material over a limited frequency band. These and other types of artificial substrates have been used to design miniaturized antennas [25]. For example, a reactive impedance surface is used in [26] to obtain an electrically small antenna with reasonable bandwidth. In [27], a volumetric metamaterial substrate that acts as a perfect magnetic conductor (PMC) is used as the substrate of an antenna.

1.2.2 Bandwidth Enhancement of Narrow-band Antennas

As mentioned in the previous sub-section, wide bandwidth, small size, ease of fabrication, low cost, and compatibility to the rest of the RF front end are desirable features of an antenna. Because of their low profile, simple design, ease of fabrication, and low cost, planar antennas have found a special place in today's wireless communication devices. Microstrip patch antennas, printed monopoles and dipoles, and slot antennas fall within this category. However, these antennas are usually narrow-band by nature and miniaturizing them further reduces their useful bandwidth. This has motivated many researchers to work on enhancing the bandwidth of such antennas. Most of the techniques that have been used to improve the bandwidth of narrow-band resonant antennas fall within one of the following two general categories:

1. Using multiple radiating elements including parasitic elements
2. Increasing the number of resonances of a narrow-band antenna

Using multiple radiating elements with different resonant frequencies seems a natural way of enhancing antenna bandwidths. This technique has widely been used in designing wideband microstrip antennas [28]. Examples of this includ patch antennas with parasitic patch elements on the same substrate (Chapter 4 of reference [28]), patch elements with parasitic patch antennas on a different layer (Chapter 5 of [28]), and a combination of these two [29, 30, 31, 32, 33, 34, 35]. This technique does help increase the bandwidth and, in some cases, the gain of such antennas. However, it also increases the occupied area and/or volume of the antenna, which is very undesirable.

The second category of techniques, which either does not increase the occupied area of the antennas or increases it minimally, makes use of increasing the number of resonances of a narrow-band antenna. If these resonances are designed to be close enough in frequency, they can be merged to achieve a wideband antenna. Microstrip patch antennas with embedded slots are examples of this category. In [36], bandwidth of a patch antenna is enhanced by embedding a U-shaped slot etched on the patch. Similarly, E-shaped patch antennas with two $\lambda/4$ notch slots are shown to have a wide bandwidth [37]. In this case, a double-resonant antenna is obtained where one resonance comes from the patch and the other from the two $\lambda/4$ notch slots. Similar methods are also used widely and are described in [21, 28, 38, 39].

1.2.3 Dual-Band and/or Reconfigurable Antenna Design

Dual-band antennas are of interest in many wireless applications that use two different frequency bands. These could be two different bands that are used for transmit and receive operations in order to minimize interference or two frequency bands that are used for a certain application such as Wireless LAN. In the latter case, two unlicensed frequency bands in the 2.4 GHz and 5 GHz ISM bands are usually used. Different WLAN devices are compatible with one or more of the available standards that use frequencies in one or both of the two bands. Current advancements in printed antenna technology have resulted in a variety of different techniques for designing low profile, cost effective, and highly efficient dual-band antennas [21]. Some of the techniques that are used to design wideband antennas can also be used to design dual-band antennas. For example, using multiple radiating elements with different resonant frequencies is an obvious choice. This is done in [40] to achieve a WLAN antenna. However, because of space limitations, it is desirable to design single-element multi-band antennas that occupy the same area as a single-band antenna. Most of the available methods that allow for design of such single-element dual-/multi-band antennas use a variety of techniques to manipulate the current distribution of one of the higher order resonant modes of the structure. Higher resonant modes of an antenna do not have current distributions similar to the current distribution of its fundamental mode. This translates to having different radiation patterns at both bands of a dual-band antenna, which is not desirable. Therefore, this manipulation should be done in a fashion that allows for controlling both the resonant frequency and the current distribution of the higher order mode.

In [41], a patch antenna is loaded with a reactance along the center of the patch and a dual-band operation is achieved. In [42], one and/or two open circuited stubs, which are equivalent to reactive impedances, are used to load a circular patch antenna along its edge and obtain a dual-band antenna. In [43], a fractal geometry with two parasitic elements is used to obtain a dual-band antenna with enhanced impedance bandwidth. In [44], a dual-band rectangular patch antenna is obtained by loading the patch with a slot at a particular location along the patch. This way, the slot affects one of the resonant modes of the patch more than the other in order to obtain a dual-band operation with desired characteristics. However, the range of achievable frequency ratio (f_2/f_1) for this antenna is limited to 1.6-2. This idea was later applied to circular and triangular patch antennas where frequency ratios of 1.3-1.4 and 1.35-1.5 were respectively achieved [45, 46]. Variations of these techniques with differently shaped slots and patches have also been investigated and discussed in detail in Chapter 4 of [21]. Similar methods are used in [47] to achieve dual-band operation for suspended plate radiators.

The configuration and radiation characteristics of slot antennas appear to be more amenable to reconfigurability than their patch antenna counterparts. In a recent study, the design of a reconfigurable slot antenna was demonstrated with an octave band tunability using five PIN diode switches [48]. The drawback of this design is that the PIN diodes are forward biased to change the resonant length of the antenna and a significant amount of electric current flows through each diode. Given the ohmic resistance associated with each diode, this results in loss of RF power and, hence, reduces the radiation efficiency of the antenna. In [49], a single-element, dual-band, CPW-fed slot antenna with similar radiation patterns at both bands is studied. However, this antenna shows high levels of cross polarized radiation in its second band of operation. In [50], a compact, dual-band, CPW-fed slot antenna, with a size reduction of about 60% compared to a conventional slot antenna, is studied. However, this antenna is designed for two particular frequency bands, and little attention has been paid to investigating its frequency tuning capabilities. Furthermore, it suffers from high levels of cross polarized radiation, which at some angles are equal to or even larger than the co-polarized component. Other topologies have also been used to achieve dual-/multi-band operations. Examples of these include structures that make use of parasitic elements and multiple radiating elements [51, 52]. As mentioned previously, a relatively wide rectangular slot shows a dual-band behavior and frequency ratios from 1.1 to 1.7 can easily be obtained by choosing the appropriate location for the feed. However, once the antenna is fabricated, the frequency ratio and the location of the two bands cannot be changed.

1.2.4 Ultra Wideband Antenna Design

A few decades after the early investigations on ultra-wideband wireless systems, UWB devices have found a large range of applications including ground penetrating radars, high-data-rate short-range wireless local area networks, communication systems for military, and UWB short pulse radars for automotive and robotics applications to name a few [53]. UWB radio is a fast emerging technology with attractive features for applications such as the fourth generation (4G) personal wireless communication systems (PCS) [54, 55]. Such systems require antennas that are able to operate across a very large bandwidth with consistent polarization and radiation pattern parameters over the entire band. A number of techniques have been developed in past to design antennas with wideband impedance matched characteristics. Among these, traveling wave antennas, spiral antennas, self-complementary antennas, and multi-element antennas (e.g, log-periodic antennas) have been used extensively.

In general all antennas whose current and voltage distributions can be represented by one or more traveling waves, usually in the same direction, are referred to as traveling or non-resonant antennas. Since these antennas are non-resonant, they are inherently broadband [56, 57]. The famous tapered slot antenna, which is also a planar antenna, is an example of this class of antennas. This antenna was investigated in [58] in 1985. This study was further pursued by a number of other studies to achieve optimum geometrical parameters of this antenna, and its application in end-fire arrays is described in [59, 60, 61]. However, traveling wave antennas must usually be at least a few wavelengths long to be efficient radiators. In a potential UWB PCS device, having such a long antenna is not practical due to limited device dimensions.

Another class of UWB antennas is antennas that have rotation invariant geometries, which are shown to have inherently wideband characteristics [56, 62]. Printed spiral antennas are examples of this class of UWB antennas and have been used in a variety of different applications [62]. Because of their usefulness, research on spiral antennas has continued to this date. In [63], a broadband (2-18 GHz) spiral antenna is proposed. Other forms of spiral antennas such as the non-planar conical spiral have also been used as broadband antennas [64].

Self complementary concept [65] is used to design antennas that show a constant input impedance, irrespective of frequency, provided that the size of the ground plane for the slot segment of the antenna is large and an appropriate self-complementary feed can also be designed. Theoretically, the input impedance of self-complementary antennas is 186 Ω and cannot be directly matched to standard transmission lines. Another drawback of self-complementary structures is that they cannot be printed on dielectric substrates, since the dielectric constant of the substrate perturbs the self-complementary condition. Another technique for designing wideband antennas is to use multi-resonant radiating structures. Log-periodic antennas, microstrip patches with parasitic elements, and slotted microstrip antennas for broadband and dual-band applications are examples of this category [28, 56, 66]. In [67], UWB operation is achieved by combining a dielectric resonator antenna with a $\lambda/4$ monopole. In [68] a planar stepped impedance dipole antenna consisting of multiple sections with different widths is proposed and shown to have very large impedance bandwidth. A general introduction on the history and design of UWB antennas as well as the general requirements of such antennas in wireless systems are studied in [69], [70], and [71] respectively.

The electric dipole and monopole above a ground plane are perhaps the most basic types of antennas available. Variations of these antennas that demonstrate considerably larger bandwidths than those of traditional designs have recently been introduced [72, 73]. Impedance bandwidth characteristics of circular and elliptical monopole plate antennas are examined in [72]. Wideband characteristics of rectangular and square monopole antennas are studied in [74], and a dielectric loaded wideband monopole is investigated in [73]. The advantage of this class of antennas is that UWB operation is achieved by using a single element that occupies a relatively compact area. The biggest disadvantage of these types of antennas is that antenna polarization as a function of frequency changes.

1.3 Dissertation Overview

The goal of the center for Wireless Integrated MicroSystems (WIMS) at the University of Michigan is to develop functional microsystems that could be in the form of either a totaly implantable neural prostheses or an integrated environmental monitoring sensor network. In the environmental monitoring test-bed, the goal is to design miniaturized microsystems that include a micro-sensor, appropriate analog and digital circuitry for processing the acquired data, and a wireless interface that uses an integrated antenna to transmit and receive RF signals. The main objective of this dissertation is to develop multi-functional antennas for such wireless integrated microsystems. In order to accomplish this, new methods for reducing the size of planar antennas must be developed. Such methods should result in antennas that have moderate to high efficiency values. Furthermore, it should be possible to match the input impedance of such antennas to a wide range of source impedances, easily. This has been done in part in [75] and in Chapter 1 of this thesis. One major drawback of these and other miniaturization methods is the reduction in the antenna bandwidth that occurs as a result of miniaturization. Therefore, it becomes necessary to develop methods to address this major problem. Several methods for bandwidth enhancement of compact printed antennas have been developed, which are covered in the remainder of this dissertation. The outline of this dissertation is presented in the following sub-sections.

1.3.1 Chapter 2: Antenna Miniaturization

Recently, a new class of miniaturized slot antennas was proposed by the Radiation Laboratory of the University of Michigan [76]. The proposed antenna occupies an area of $0.15\lambda \times 0.15\lambda$ and has a bandwidth of about 1%. In Chapter 2 of this dissertation, new methods and topologies for miniaturizing slot antennas and enhancing the bandwidth of this class of slot antennas are proposed. In particular, techniques such as parasitic coupling and inductive loading to achieve higher bandwidth and further size reduction for this class of miniaturized slot antennas are examined. A new double-resonant miniaturized antenna based on the topology proposed in [76] is developed. The overall bandwidth of a proposed double resonant antenna is shown to be increased by more than 94% compared with a single resonant antenna occupying the same area. The behavior of miniaturized slot antennas, loaded with series inductive elements along the radiating section, is also examined. The inductive loads are constructed by two balanced short circuited slot lines placed on opposite sides of the radiating slot. These inductive loads can considerably reduce the antenna size at its resonance. Prototypes of a double resonant antenna at 850 MHz and inductively loaded miniaturized antennas at around 1 GHz are designed and tested. Finally the application of both methods in a dual-band miniaturized antenna is presented. In all cases measured and simulated results show excellent agreement.

1.3.2 Chapter 3: Wideband/Dual-Band Slot Antennas

As mentioned in 1.2.2, design of wideband antennas that occupy small areas on a printed circuit board (PCB) is much desired. A simple method of addressing this problem is to enhance the bandwidth of ordinary narrow-band antennas such as planar microstrip or slot antennas. In Chapter 3 of this dissertation this problem is addressed. A wideband slot antenna element is developed as a building block for designing single- or multi-element wideband or dual-band slot antennas. It is shown that a properly designed, off-centered, microstrip-fed, moderately wide slot antenna shows a dual-resonant behavior with similar radiation characteristics at both resonant frequencies. Therefore, it can be used as a wideband or dual-band element. This element shows bandwidth values up to 50%, if used in the wideband mode. When used in the dual-band mode, frequency ratios up to 1.6 with bandwidths larger than

10% at both frequency bands can be achieved without putting any constraints on the impedance matching, cross polarization levels, or radiation patterns of the antenna .

This technique is further modified, and the single-element moderately wide slot antenna is fed at two locations along the slot with a two-prong microstrip feed. This way, the aperture's electric field distribution is manipulated to create two fictitious short circuits along the slot. This creates two additional resonances besides the main one. The frequencies of these fictitious resonances can be chosen such that the overall bandwidth of the antenna is drastically increased. By using this technique, a slot antenna with a 1.8:1 bandwidth ratio is designed and fabricated. The measurement results of this antenna show similar radiation patterns at different frequencies in its band of operation. Furthermore, the antenna has a relatively constant gain and more importantly, it has an excellent polarization purity over the entire bandwidth. The proposed wideband slot element, with a single microstrip feed, can also be incorporated in a multi-element antenna topology resulting, in a very wideband antenna with a minimum number of elements. It is also shown that, by using only two of these elements in a parallel feed topology, an antenna with good radiation parameters over a 2.5:1 bandwidth ratio can be obtained. In order to achieve such a large bandwidth using ordinary slot radiators in a multi-element antenna topology, one should use additional radiating elements. For example, a planar log-periodic slot antenna is recently proposed in [77], which has five radiating elements with less than 50% impedance bandwidth.

1.3.3 Chapters 4 & 5: Dual-Band Reconfigurable Slot Antennas

As mentioned in Section 1.2.3, a growing number of different applications use more than one frequency band, and a number of different topologies have been proposed for designing dual-band antennas. However, most of these topologies suffer from limited tunability range. In other words, the ranges of frequency ratios, f_2/f_1, that can be achieved from most designs are relatively limited. Furthermore, only a couple of the available techniques can be used to design dual-band reconfigurable antennas. In Chapters 4 and 5, I propose a new technique for designing dual-band and/or reconfigurable narrow slot antennas that can easily be modified to obtain a single-band tunable antenna. Furthermore, the frequency ratio of the antenna will be determined by the applied DC bias voltage or by choosing the right value for the lumped elements and not by changing the geometrical parameters of the antenna. The proposed technique is based on loading a slot antenna with a fixed or variable capacitor at a certain location along the slot. One of the advantages of this technique is that the current that flows through a capacitor, or a reverse biased varactor, is small compared to a PIN diode or a MEMS switch, and hence, the finite Q of the device does not deteriorate the antenna efficiency. As will be shown, such an antenna exhibits a dual-resonant behavior. In addition, placing a capacitor in parallel with the slot results in reduction of its resonant frequency. This occurs for both the first and second resonant modes. However, the decrease is not uniform and depends on the location of the capacitor along the slot. It is shown that the location of the capacitor can be chosen to minimize the variations of one mode, hence obtaining a dual-band antenna with adequate control over its frequency ratio.

1.3.4 Chapter 6: Improved Wire and Loop Slot Antennas

In this chapter, a new technique for enhancing the bandwidth of annular wire or slot antennas is proposed. Using this technique, the geometry of a simple wire or slot ring antenna is modified to obtain a new type of ring antenna, henceforth referred to as the bi-semicircular ring antenna. While occupying the same area, the modified antennas have much wider bandwidth than the ordinary printed annular slot or strip antennas. The bandwidth enhancement factor for such antennas is maximized by optimizing their geometrical parameters. Prototypes of the wideband bi-semicircular strip and slot antennas are designed, fabricated, and tested. Measurement results confirm that the modified antennas provide bandwidth values much larger than the original annular slot and strip antennas. Furthermore, the antennas demonstrate consistent radiation patterns, low cross-polarized radiation levels, and high efficiency values across their entire bands of operation

1.3.5 Chapter 7: Compact Ultra-Wideband Antennas for Time- and Frequency-Domain Applications

In Chapter 7, a new type of single-element, wideband antenna is proposed that can provide wider bandwidth and consistent polarization over the frequency range that the antenna is impedance matched. The basis for achieving such an ultra-wideband operation is through proper magnetic coupling of two adjacent sectorial loop antennas in a symmetrical arrangement. The antenna is composed of two parallel coupled sectorial loop antennas (CSLA) that are connected along an axis of symmetry. The geometrical parameters of this antenna are optimized, and it is shown that the antenna can easily provide a wideband impedance match over an 8.5:1 frequency range. The gain and radiation patterns across the frequency range of operation remain almost constant particularly over the first two octaves of its return-loss bandwidth. The antenna geometry is then modified in order to reduce its size and weight without compromising its bandwidth. This helps fabrication and installation of the antenna operating for lower frequency applications such as ground penetrating radars or broadcast television where the physical size of the antenna is large. It is expected that after properly modifying the topology of the antenna to reduce its overall dimensions, an antenna with maximum dimension of $0.35\lambda_0 \times 0.1\lambda_0$ at the lowest frequency of operation will be designed.

1.3.6 Appendix: A Measurement System for Ultra-Wideband Communication Channel Characterization

In this appendix a novel wideband propagation channel measurement system with high dynamic range and sensitivity is introduced. The system enables the user to characterize signal propagation through a medium over a very wide frequency band with fine spectral resolution (as low as 3 Hz) by measuring the attenuation and phase characteristics of the medium. This system also allows for the study of temporal, spectral, and spatial de-correlation. The high fidelity data gathered with this system can also be utilized to develop empirical models or used as a validation tool for physics based propagation models, which simulate the behavior of radio waves in different environments such as forests, urban areas, or indoor environments. The mobility and flexibility of the system allows for site specific measurements in various propagation scenarios.

CHAPTER 2

Bandwidth Enhancement and Further Size Reduction of a Class of Miniaturized Slot Antennas

Current advancements in communication technology and significant growth in the wireless communication market and consumer demands demonstrate the need for smaller, more reliable and power efficient, integrated wireless systems. Integrating entire transceivers on a single chip is the vision for future wireless systems. This has the benefit of cost reduction and improving system reliability. Antennas are considered to be the largest components of integrated wireless systems; therefore, antenna miniaturization is a necessary task in achieving an optimal design for integrated wireless systems. The subject of antenna miniaturization is not new and has been extensively studied by various authors [1, 2, 3, 4]. Early studies have shown that for a resonant antenna, as size decreases, bandwidth (BW) and efficiency will also decrease [1]. This is a fundamental limitation which, in general, holds true independent of antenna architecture. However, research on the design of antenna topologies and architectures must be carried out to achieve maximum possible bandwidth and efficiency for a given antenna size. Impedance matching for small antennas is also challenging and often requires external matching networks; therefore, antenna topologies and structures that inherently allow for impedance matching are highly desirable. The fundamental limitation introduced by Chu [1] and later re-examined by McLean [4] relates the radiation Q of a single resonant antenna with its bandwidth. However, whether such limitation can be directly extended to multi-resonant antenna structures or not is unclear. In fact, through a comparison with filter theory, designing a relatively wide-band antenna may be possible using multi-pole (multi-resonant) high Q structures. In this chapter we examine the applicability of multi-resonant antenna structures to enhance the bandwidth of miniaturized slot antennas.

Different techniques have been used for antenna miniaturization such as: miniaturization using optimal antenna topologies [76, 78, 79] and miniaturization using magneto-dielectric materials [80, 81]. In pursuit of antenna miniaturization while maintaining ease of impedance matching and attaining relatively high efficiency, a novel miniaturized slot antenna was recently presented [76]. Afterwards, a similar architecture in the form of a folded antenna topology was presented in order to increase the bandwidth of the previously mentioned miniaturized slot antenna [79]. Here we re-examine this topology [76] and propose modifications that can result in further size reduction or bandwidth enhancement of this structure without imposing any significant constraint on impedance matching or cross polarization level. In Section 2.1 a dual-resonant antenna topology is examined for bandwidth enhancement. This miniaturized antenna shows a bandwidth which is 94% larger than that of a single-resonant miniaturized antenna with the same size.

Using series inductive elements distributed along the antenna aperture results in the increase of inductance per unit length of the line. Therefore, the guided wavelength of the resonant slot line is shortened. Thus, the overall length of the antenna is decreased. In Section 2.2 this technique is first demonstrated using a standard resonant slot antenna and then incorporated in the miniaturized antenna topology of [76] to further reduce the resonant frequency without increasing the area occupied by the antenna.

The aforementioned techniques for bandwidth enhancement and further size reduction can be used individually or in conjunction with one another. The combined application of the techniques of Sections 2.1 and 2.2 is presented in Section 2.3 by demonstrating the design of a dual-band miniaturized slot antenna.

2.1 Miniaturized Slot Antenna with Enhanced Bandwidth

2.1.1 Design Procedure

In this section, the design of coupled miniaturized slot antennas for bandwidth enhancement is studied. The configuration of the proposed coupled slot antenna is shown in Figure 2.1(b), where two miniaturized slot antennas are arranged so that they are parasitically coupled. Each antenna occupies an area of about $0.15\lambda_0 \times 0.13\lambda_0$ (Figure 2.1(a)) and achieves miniaturization by the virtue of a special topology described in detail in [76]. However, this antenna demonstrates a small bandwidth (less than 1%). A close examination of the antenna topology reveals that the slot-line trace of the antenna only covers about half of the rectangular printed-circuit board (PCB) area. Therefore, another antenna, with the same geometry, can be placed in the remaining area without significantly increasing the overall PCB size. Placing two antennas in close proximity of each other creates strong coupling between the antennas, which, if properly controlled, can be employed to increase the total antenna bandwidth.

As seen in Figure 2.1(b), only one of the two antennas is fed by a microstrip line. The other antenna is parasitically fed through capacitive coupling mostly at the elbow section. The coupling is a mixture of electric and magnetic couplings that

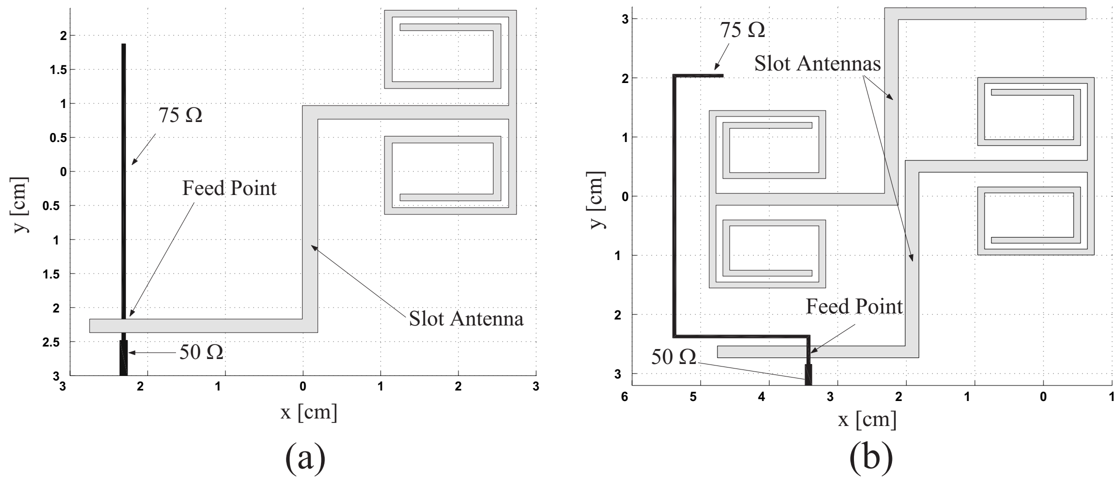

Figure 2.1: The geometry of single- and double- element miniaturized slot antennas. (a) Single-element miniaturized slot antenna. (b) Double-element miniaturized slot antenna.

counteract each other. At the elbow section, where the electric field is large, the slots are very close to each other. Therefore, it is expected that the electric field coupling is the dominant coupling mechanism and the electric fields (magnetic currents) in both antennas will be in phase, thus enhancing the radiated far field.

The two coupled antennas are designed to resonate at the same frequency, $f_{r1} = f_{r2} = f_0$, where f_0 is the center frequency and f_{r1} and f_{r2} are the resonant frequencies of the two antennas. In this case, the S_{11} spectral response of the coupled antenna shows two nulls, the separation of which is a function of the separation between the two antennas, s, and their overlap distance, d. In order to quantify this null separation a coupling coefficient is defined as:

$$k_t = \frac{f_u^2 - f_l^2}{f_u^2 + f_l^2} \tag{2.1}$$

where f_u and f_l are the frequencies of the upper and lower nulls in S_{11}. Therefore, k_t can easily be adjusted by varying d and s (Figure 2.1(b)), and decreases as s is increased and d is decreased. A full-wave electromagnetic simulation tool can be used to extract k_t as a function of d and s in the design process. Bandwidth maximization

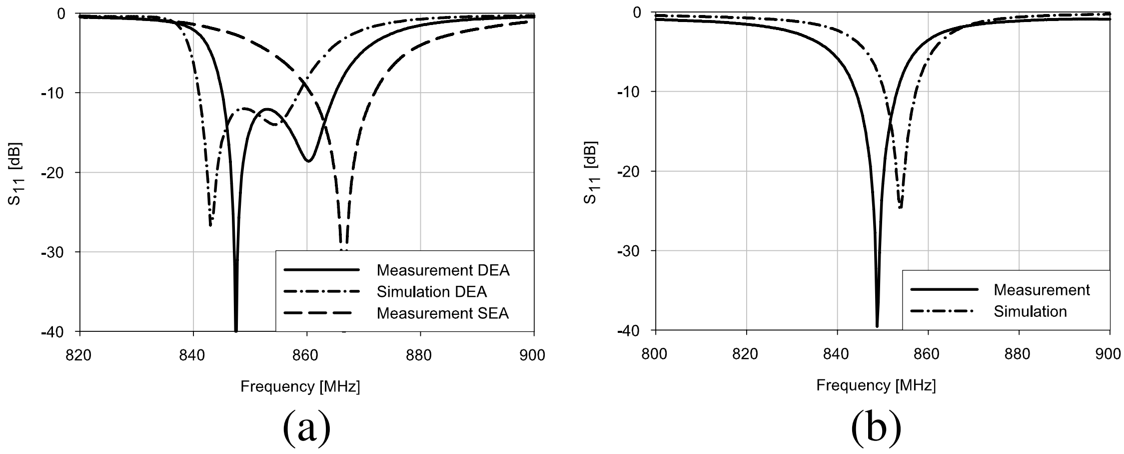

Figure 2.2: S_{11} of double-element antenna and single-element antennas. DEA: Double-Element Antenna, SEA 2: Single-Element Antenna with the same size as DEA. (a) S_{11} of the double-element antenna and single-element antenna of the same size (SEA 2). (b) S_{11} of the single-element antenna that constitutes the double-element antenna (SEA 1)

is accomplished by choosing a coupling coefficient (by choosing d and s) such that S_{11} remains below -10 dB over the entire frequency band. Here the resonant frequencies of both antennas are fixed at $f_{r1} = f_{r2}$ =850 MHz and k_t is used as the tuning parameter. However, it is also possible to change f_{r1} and f_{r2} slightly, in order to achieve a higher degree of control for tuning the response.

The input impedance of a microstrip-fed slot antenna, for a given slot width, depends on the location of the microstrip feed relative to one end of the slot and varies from zero at the short circuited end to a high resistance at the center. Therefore, an off-center microstrip feed can be used to easily match a slot antenna to a wide range of desired input impedances. The optimum location of the feed line can be determined from the full-wave simulation. In the double antenna example, the feed line consists of a 50 Ω transmission line connected to an open-circuited 75 Ω line crossing the slot (Figure 2.1(b)). The 75 Ω line is extended by $0.33\lambda_m$ beyond the strip-slot crossing to couple the maximum energy to the slot and also to compensate for the imaginary part of the input impedance. Using this 75 Ω line as the feed allows for compact and localized feeding of the antenna and tuning the location of the transition from 50 Ω

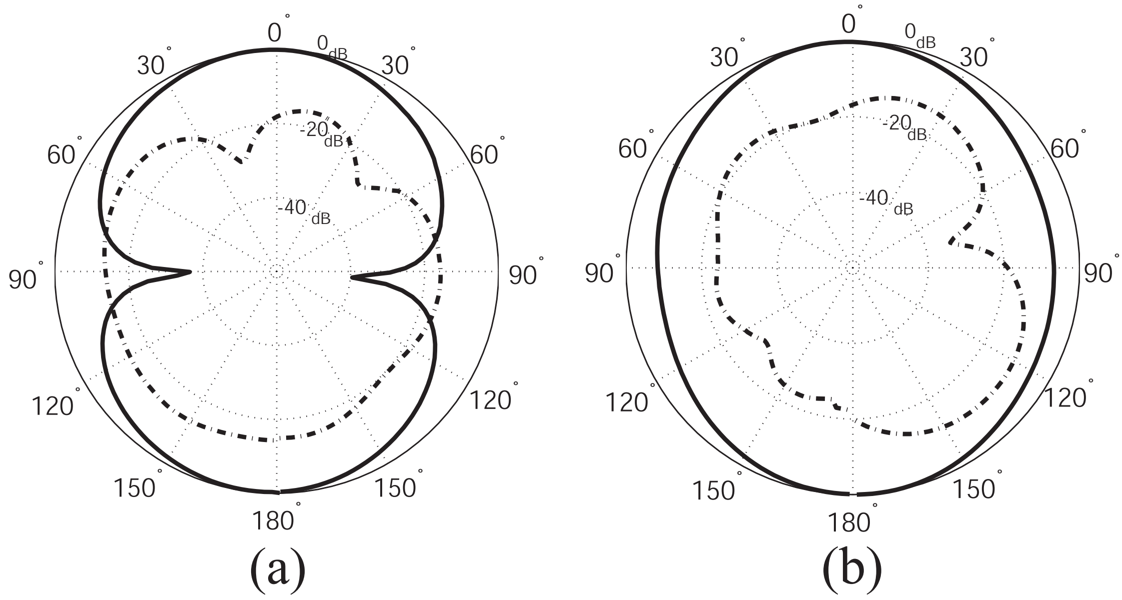

Figure 2.3: Far field radiation patterns of the double-element miniaturized slot antenna at 852 MHz. (a) E-Plane. (b) H-Plane.

to 75 Ω provides another tuning parameter for obtaining a good match.

2.1.2 Fabrication and Measurement

A double-element antenna (DEA) and two different single-element antennas (SEA 1 and SEA 2) were designed, fabricated, and measured. SEA 1 is the constitutive element of DEA and SEA 2 is a single element antenna with the same topology as SEA 1 (see Figure 2.1(a)) but with the same area as the DEA. SEA 2 is used to compare the bandwidth of the double resonant miniaturized antenna with that of the single-resonant miniaturized antenna with the same size. All antennas were simulated using IE3D [82], which is a full wave simulation software based on Method of Moments (MoM), and fabricated on a Rogers RO4350B substrate with thickness of 500 μm, a dielectric constant of $\epsilon_r = 3.5$, and a loss tangent of $\tan(\delta) = 0.003$ with a copper ground plane of 33.5×23 cm^2. The input reflection coefficient, S_{11}, of the single-element antennas (SEAs) as well as the double-element antenna are presented in Figure 2.2. SEA 1 shows a bandwidth of 8 MHz or nearly 0.9% and SEA 2 shows

Type	-10 dB BW	Gain			
		f(MHz)	848	852	860
Double Slot	2.4%	G(dBi)	1.5	1.7	1.7
Single Slot 1	0.9%	0.8dBi			

Table 2.1: Comparison between the radiation parameters of the double-element antenna and its constitutive single element antennas of Figure 2.1.

a bandwidth of 11.7 MHz or 1.31% whereas the bandwidth of the double-element antenna is 21.6 MHz (2.54%), which indicates a factor of 1.94 increase over a single-element antenna with the same area. Choosing a different substrate, with different thickness and dielectric constant, can increase the overall bandwidth of both antennas. However, it is also expected that the bandwidth ratio of the double-element antenna to the single-element antenna remains the same. The overall size of the DEA is $0.165\lambda_0 \times 0.157\lambda_0$, which shows a 25% increase in area when compared to the size of the SEA 1 ($0.133\lambda_0 \times 0.154\lambda_0$). The Q of each antenna has also been calculated using the method presented in [6] and compared with the fundamental limit on the Q of small antennas [4] in Table 2.2. Demonstrably the quality factors of both single-element antennas are well above the minimum theoretical limit. Since Q is only defined for single resonant structures, no value for Q is reported for the double-element antenna in Table 2.2. In calculating the minimum Q for the slot antennas using the Chu limit, it is necessary to find the radius of the smallest sphere that encloses the antenna. At first, it may not be clear whether this sphere should only cover the aperture or, in addition to that, some portion of the ground plane too (because of the electric currents that exist in the ground plane). This becomes clear by applying the equivalence theorem to this problem, which shows that the magnetic currents responsible for radiation exist only on the aperture; therefore, according to the derivation of the Chu limit, the smallest sphere that encloses these radiating magnetic currents should be used.

The gain of the double resonant antenna was measured at three different frequen-

Type	Size	Measured Q*	Min Q**
Single Element 1	$0.133\lambda_0 \times 0.154\ \lambda_0$	70.0	5.34
Single Element 2	$0.165\lambda_0 \times 0.157\lambda_0$	66.4	3.9
Double Element	$0.165\lambda_0 \times 0.157\lambda_0$	N/A	3.9

Table 2.2: Comparison between the measured Q of the slot antennas of Section 2.1 and the minimum attainable Q specified by the Chu limit.

cies and is presented in Table 2.1. Radiation patterns of the antenna were measured at $f = 848, 852$, and 860 MHz and found to be similar to each other. Figure 2.3 shows the co- and cross-polarized E- and H-Plane radiation patterns at f =852 MHz. The E- and H-Plane radiation patterns of this antenna are expected to be dual of those of a short electric dipole. Figure 2.3(b) shows the H-Plane radiation pattern, which is similar to the E-Plane radiation pattern of an electric dipole. Figure 2.3(a), however, does not show a uniform radiation pattern like the H-Plane radiation of a short electric dipole. This can be attributed to the finiteness of the ground plane where some radiation comes from the electric currents on the antenna ground plane at the edges of the substrate. Since there is a phase difference between the electric currents around the slot edge and those at the substrate edge, radiated fields from these currents interfere destructively, causing the deeps in the E-Plane around $\theta = \pm 90°$. The H-Plane pattern is expected to have deep nulls at these angles; therefore, this effect is not significant for the H-Plane pattern. Table 2.1 shows the radiation characteristics of the double- and single-element antennas. It is seen that the gain-bandwidth product of the proposed double-antenna is significantly higher than that of the single antenna.

2.2 Improved Antenna Miniaturization Using Distributed Inductive Loading

2.2.1 Design Procedure

A microstrip-fed slot antenna has the length of $\lambda_g/2$, where λ_g is the wavelength in the slot, at its first resonance. The electric current distribution can be modeled by the voltage distribution over a $\lambda/2$ transmission line short-circuited at both ends. The resonant length of a transmission line (λ_g) can be made smaller if the inductance per unit length of the line is increased. This can be accomplished by inserting a number of series inductors in the transmission line. For slot-lines, insertion of series lumped elements is not possible. Besides, series lumped elements usually have low Qs which adversely affect the antenna efficiency (gain). To realize a slot line with higher inductance per unit length, an array of distributed, short circuited, narrow slot-lines can be placed along the radiating segment of the slot antenna as shown in Figure 2.4(b). The impedance of a short circuited slot line is obtained by:

$$Z_S = jZ_{0s}\ tan(\beta_g l) \tag{2.2}$$

where β_g is the propagation constant, Z_{0s} is the characteristic impedance, and l is the length of the short circuited slot-line. The characteristic impedance of a slot-line is inversely proportional to its width [83]; therefore, by using wider series slots, more inductance can be obtained for a fixed length of short circuited transmission line. The best location to put series inductors in a slot is near its end where the amplitude of magnetic current is small. Putting them at the center of the slot where the magnetic current is at its maximum, strongly degrades radiation efficiency. It can easily be seen that by increasing the number and value of inductors, the length of transmission line necessary to satisfy the boundary conditions at both ends of the slot decreases.

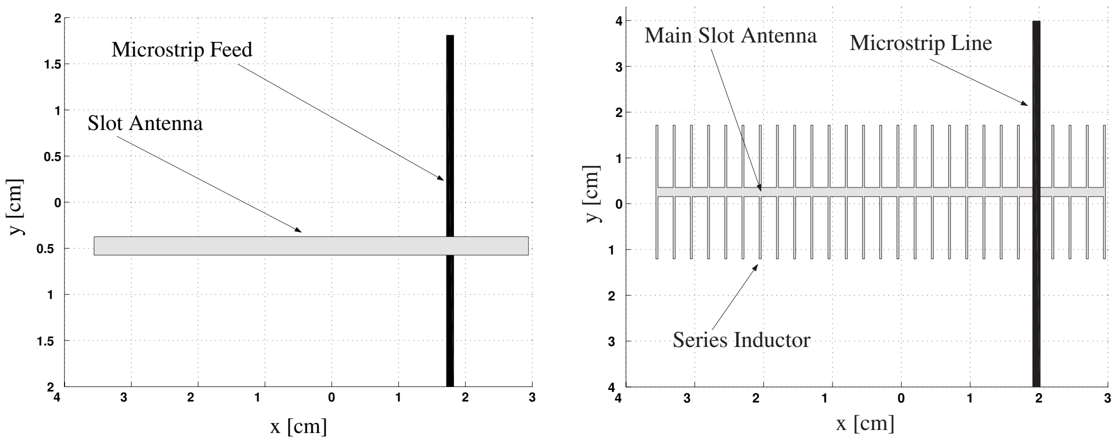

(a) (b)

Figure 2.4: Topologies of the loaded and unloaded straight slot antennas. (a) An ordinary microstrip-fed slot antenna. (b) A microstrip-fed straight slot antenna loaded with an array of series inductive elements.

The size reduction may also be explained by considering the electric current distribution in the conductor around the slot. There are two components of electric current in the ground plane of the slot, one that circulates around the slot and one that is perpendicular to it. The latter is described by the continuity of the electric current and displacement current at the slot discontinuity. Putting a discontinuity (a slit) normal to the circulating current path forces the current to circle around the discontinuity. Hence the electric current traverses a longer path length than the radiating slot length, which in turn lowers the resonant frequency. Figure 2.4(b) shows a slot antenna loaded with a number of narrow slits that act as an array of series inductors. These slits are designed to have a length smaller than $\lambda_g/4$ and carry a magnetic current with a direction normal to that of the main radiator. Placing them only on one side of the radiating slot results in asymmetry in phase and amplitude of the current along the slot, which could create problems in matching and worsen cross polarization. In order to circumvent this problem, two series slits are placed on the opposite sides of the main slot. These slits carry magnetic currents with equal amplitudes and opposite directions. Since the lengths of these narrow slits are small

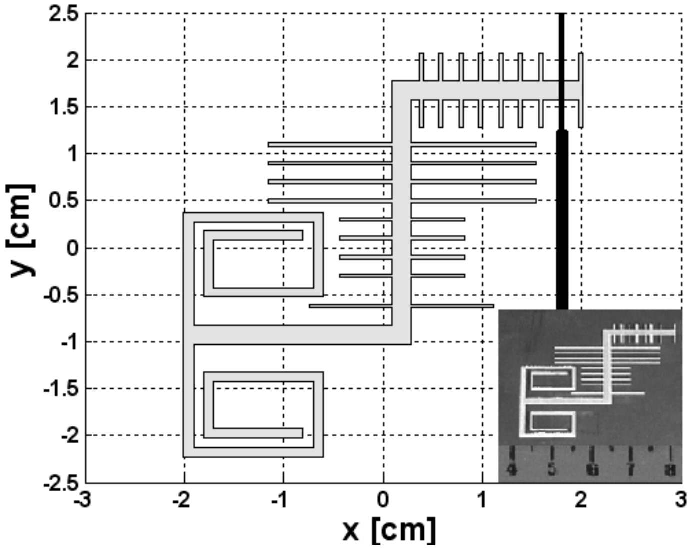

Figure 2.5: Topology of a miniaturized slot antenna loaded with series distributed inductors (slits).

compared to the wavelength and because of their close proximity, the radiated fields from the opposite slits cancel each other and they do not contribute to the radiated far field. Matching is performed by using an off-centered, open-circuited microstrip feed. The optimum location and length of the microstrip line are found by trial and error, using full wave simulations. For both straight slots (with and without series inductors), the lengths of the extended microstrip lines are found to be $\lambda_m/4$, where λ_m is the wavelength in the microstrip lines at their respective resonance frequencies. Figure 2.5 shows a miniaturized slot antenna (similar to the topology in [76]) loaded with series inductive slits to further reduce its resonance frequency. The antenna, without the series inductors, is already small and adding series inductive elements further reduces the resonant frequency or equivalently the electrical dimensions of the antenna. Instead of using identical inductive elements along the radiating slot, differently sized inductive slits are used to cover most of the available area on the PCB in order to maintain the area occupied by the antenna. The antenna is matched to a microstrip transmission line in a manner similar to the straight slots described

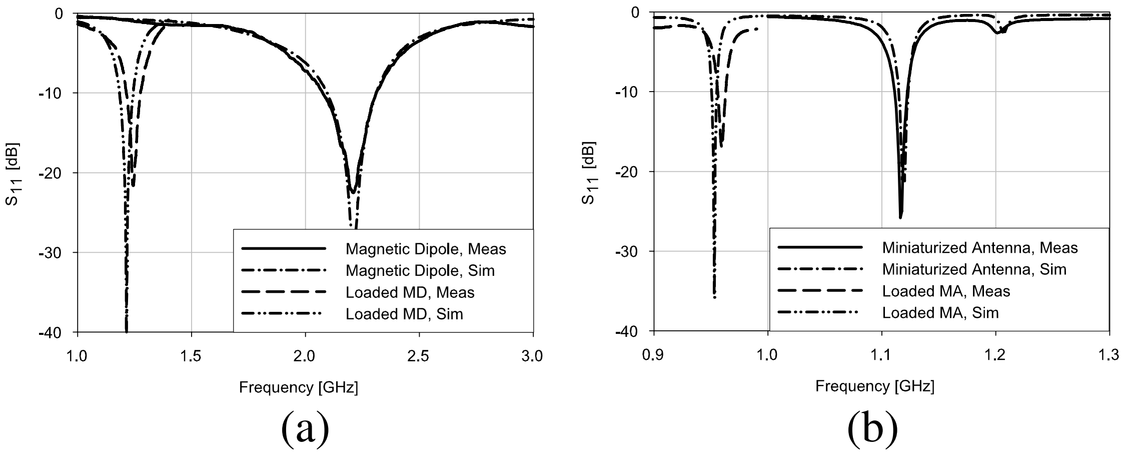

Figure 2.6: Simulated and measured S_{11} of the straight slot antennas and miniaturized slot antennas with and without inductive loading. (see Figures 2.4 and 2.5). (a) S_{11} of straight loaded and unloaded slot antennas. (b) S_{11} of ordinary and loaded miniaturized slot antennas.

earlier. The feed line is composed of a 75 Ω open-circuited microstrip line connected to a 50 Ω feed line. In this case, the open-circuited microstrip line is extended beyond the slot strip crossing by $0.3\lambda_m$ and $0.26\lambda_m$ respectively for the miniaturized antenna and the loaded miniaturized antenna.

2.2.2 Fabrication and Measurement

The straight slots with and without series inductors were simulated using IE3D and fabricated on a 500 μm thick Rogers RO4350B substrate. Figure 2.6(a) shows the simulated and measured S_{11} for the slot antennas with and without inductive loading. This figure shows the resonant frequency and -10 dB bandwidth of 2.2 GHz and 235 MHz (10.7%) for the straight slot. The loaded slot with the same length as that of the unloaded slot has a resonant frequency of 1.24 GHz and a bandwidth of 63 MHz (5%). This result indicates a 44% reduction in the resonant frequency and a similar reduction in the bandwidth, as expected. The overall size can still be reduced by using longer short circuited slits, if they could be designed in a compact fashion. The radiation patterns of the small slot antenna were measured in the anechoic chamber

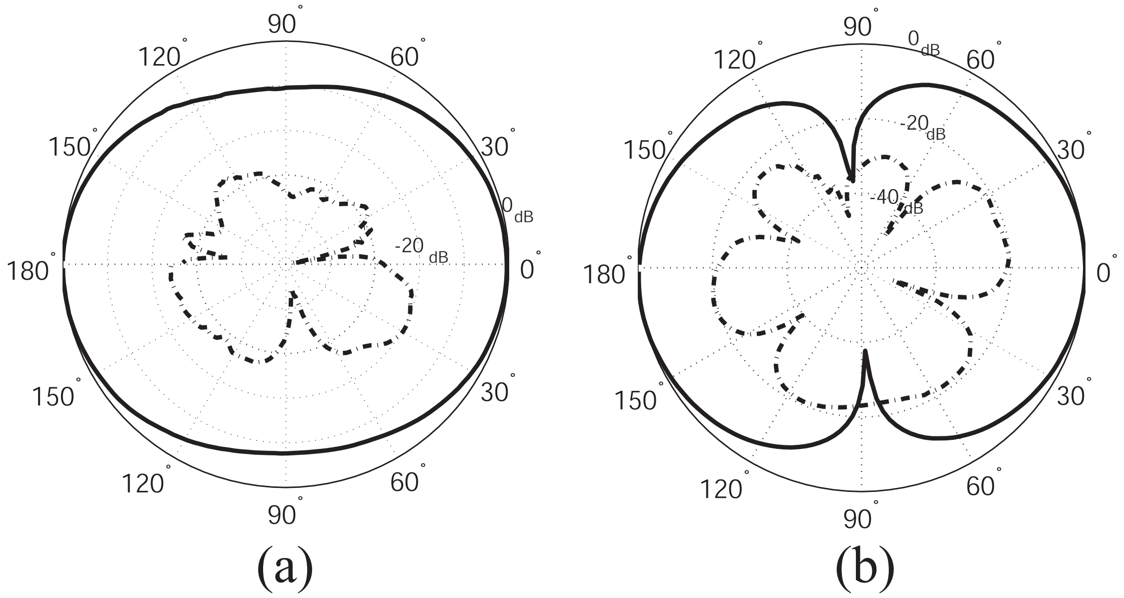

Figure 2.7: Far field radiation patterns of loaded straight slot antenna shown in Figure 2.4(b). (a) E-Plane. (b) H-Plane.

of the University of Michigan and are presented in Figure 2.7. It is seen that the cross polarization components in the far field region in both E- and H-planes are negligible, thereby confirming the fact that the radiation from the magnetic currents in the inductive loadings with opposite directions cancel each other in the far field region. The miniaturized loaded and unloaded slot antennas were also fabricated using RO4350B substrate. Figure 2.6(b) shows the simulated and measured input reflection coefficients of the loaded and unloaded miniaturized antennas. It is shown that, by inserting the series inductors, the resonance frequency of the antenna shifts down from 1116 MHz to 959 MHz (14% reduction). In this design, the overall PCB size is unchanged. Figure 2.8 shows the E- and H-Plane co- and cross-polarized radiation patterns of the loaded miniaturized antenna. It is seen that the cross polarization level is negligible at broadside. The gains of the loaded and unloaded miniaturized slot antennas (antenna in Figure 2.5) were also measured in the anechoic chamber using a standard log-periodic reference antenna and were found to be 0.8 dBi and 0.7 dBi respectively. Table 2.3 shows a comparison between Q of the miniaturized

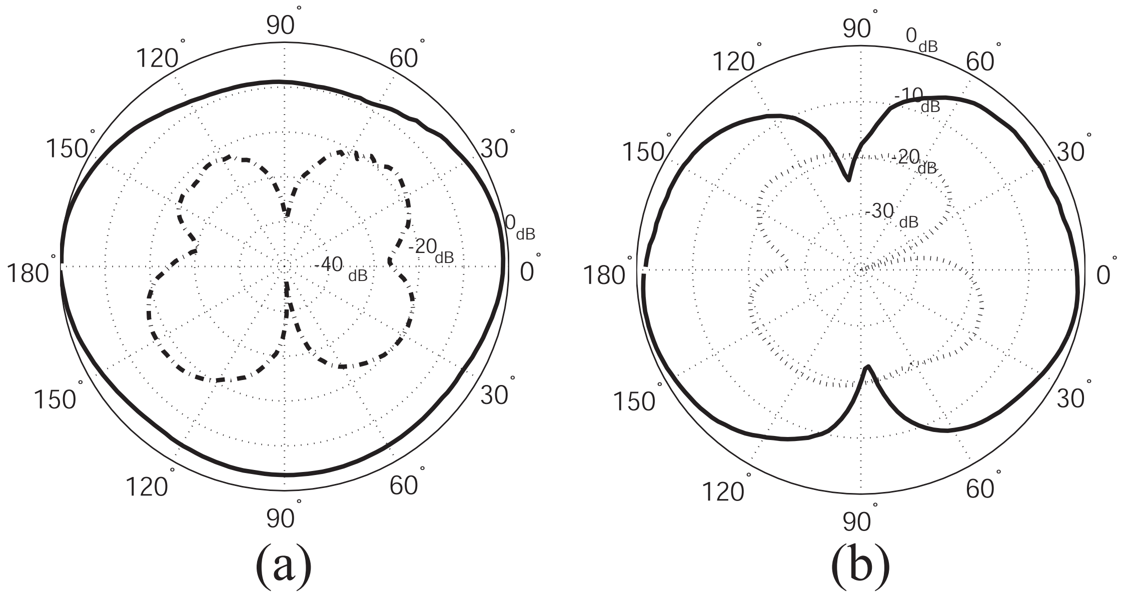

Figure 2.8: Far field radiation patterns of loaded miniaturized slot antenna shown in Figure 2.5. (a) E-Plane. (b) H-Plane.

Antenna Type	Size	-10 dB BW	Measured Q	Min Q
Min. Straight Slot	$0.260\lambda_0 \times 0.120\lambda_0$	5%	17.5	2.43
Min. S-shaped Slot	$0.15\lambda_0 \times 0.15\lambda_0$	0.98%	67.50	4.97
Loaded Min. S-Shaped Slot	$0.128\lambda_0 \times 0.128\lambda_0$	0.73%	98.4	7.21

Table 2.3: Comparison between BW, measured Q and the minimum attainable Q of the miniaturized antennas in Section 2.2.

antennas presented in this section and the fundamental limit on Q of small antennas with the same size[1, 4]. It is observed that the Q of these antennas are well above the Chu limit.

2.3 Dual-Band Miniaturized Slot Antenna

In this section, the techniques introduced in the previous sections are used in the design of a dual-band miniaturized slot antenna. The geometry of this antenna is shown in Figure 2.9. The resonant frequencies of the slot antennas (f_{r1} and f_{r2}) and the value of the coupling coefficient (k_t) are used as design parameters to achieve the desired response. Increasing the vertical displacement, d, and decreasing the horizontal separation, s, cause k_t to increase or equivalently result in a larger separation between the two frequency bands. Small changes in the resonant lengths of the slots result in slight changes in f_{r1} and f_{r2}, which can be used as a means of fine-tuning the response. Note, however, that resonant frequencies f_{r1} and f_{r2} should be close to each other so that coupling can take place. The separation between the two bands is limited by practical values of k_t. Large k_t values cannot be obtained easily, since both electric and magnetic couplings are present and add destructively. In addition to this problem, matching the antenna at the two bands becomes increasingly difficult as the separation increases. A parameter δf is defined as a measure of separation between the two frequency bands:

$$\delta f = \frac{\Delta f}{f_0} = \frac{f_u - f_l}{f_0} \tag{2.3}$$

where f_0 is the center frequency. In practice by changing k_t, f_{r1}, and f_{r2}, values of δf up to 10% can easily be obtained. This architecture is particularly useful for wireless applications that use two separate frequency bands (different bands for transmit and receive for example) that are close to each other but still cannot be covered with the available bandwidth of these types of miniaturized antennas.

In order to achieve a higher miniaturization level for the given size, series inductive elements are also placed along slots to reduce the resonant frequencies of each element. Figure 2.10 shows the simulated and measured S_{11} of this dual-band antenna. The discrepancies between the simulated and measured results are due to the finiteness of the ground plane as described in [76]. The measured results indicate an f_l = 761.5 MHz and f_u = 817.5 MHz or equivalently a $\delta f = 7.1\%$. A good match at both bands is obtained by using an off center open-circuited microstrip feed where the microstrip line is extended by 7 cm over the slot-strip transition. Table 2.4 shows a comparison between the antenna size, -10 dB bandwidth, measured Q, and minimum attainable Q for the two bands. It is seen that the Q of both bands are well above

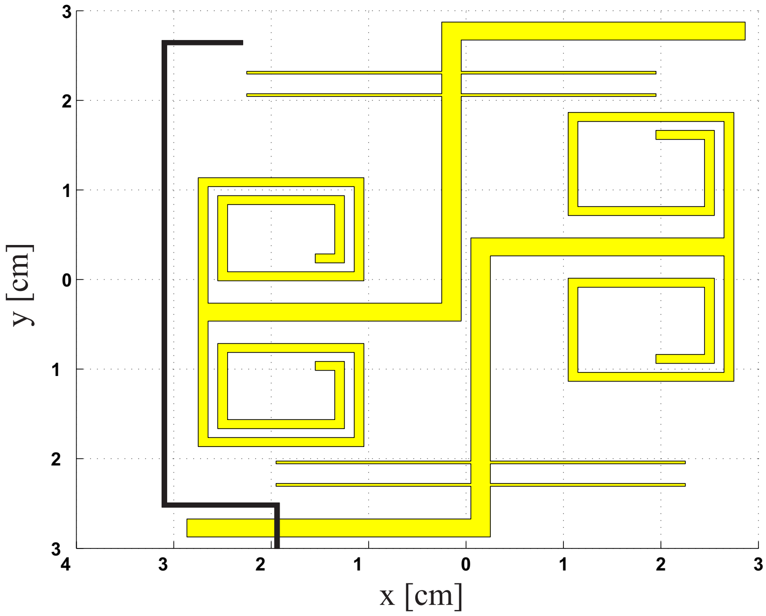

Figure 2.9: Topology of the dual-band inductively loaded miniaturized slot antenna of Section 2.3.

Resonance Frequency	Size	-10 dB BW	Measured Q	Min Q
771.5 MHz	$0.14\lambda_0 \times 0.15\lambda_0$	0.4%	200	5.25
827.5 MHz	$0.15\lambda_0 \times 0.16\lambda_0$	1.2%	104	4.44

Table 2.4: Comparison between BW, Measured Q and the Minimum attainable Q of the dual-band miniaturized antenna.

the Chu limit. The overall size of the structure is 5.73 cm $\times$ 5.94 cm or equivalently $0.145\lambda_0 \times 0.15\lambda_0$ at the lowest frequency of operation. Radiation patterns of the antenna at the two bands are measured and found to be similar to those of the single element antenna topology as shown in Figure 2.8.

2.4 Conclusions

Two approaches are introduced for increasing the bandwidth and reducing the size of miniaturized slot antennas. Placing two similar slot antennas in close proximity of each other creates a double resonant structure, the response of which is a function of the relative spacing between the two antennas. The coupled miniaturized antenna

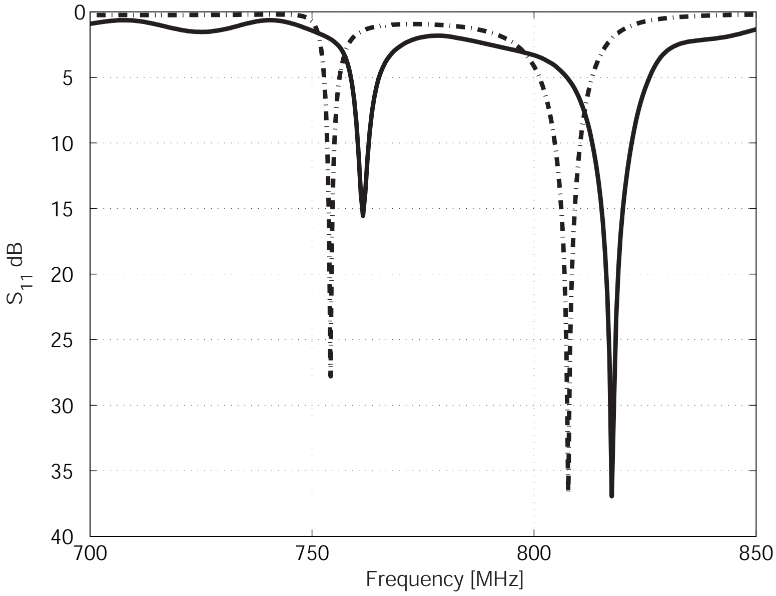

Figure 2.10: Measured and simulated S_{11} of the miniaturized dual-band slot antenna of Section 2.3.

can be designed to have a bandwidth that is larger by 94% than the bandwidth of a single resonant antenna with the same area or to behave as a dual-band antenna.

For a fixed resonance frequency, adding series inductive elements to a slot antenna reduces its size. The size reduction is a function of number and values of the inserted inductive elements. Using series inductive elements does not adversely affect impedance matching and the cross polarization level. This technique is also used in combination with other miniaturization techniques to further decrease the size of the radiating structure. The technique is applied to a straight as well as a miniaturized slot antenna and for a given antenna size, significant reduction in resonance frequencies are observed.

Finally, both techniques are applied to the design of a miniaturized dual-band antenna. Series inductors are used to reduce the resonant frequencies of each resonator. A large coupling coefficient is used to achieve a large separation between the two nulls in the S_{11} response of the parasitically coupled antenna. The values of k_t, f_{r1}, and f_{r2} are used as design parameters in order to obtain a miniaturized dual-band slot antenna with relatively good simultaneous matching.

CHAPTER 3

A Wideband Slot Antenna Employing a Fictitious Short Circuits Concept

Wide bandwidth, small size, ease of fabrication, low cost, and compatibility to the rest of the RF front end are desirable factors of an antenna. The literature concerning the design of frequency independent or very wideband antennas is enormous and extends beyond the scope of this chapter. The vast majority of techniques developed for achieving frequency independent behavior make use of topologies that result in relatively large antennas, hence eliminating their use for mobile wireless applications. Therefore, it is desirable to develop other techniques to increase the bandwidth of, otherwise narrow-band, small-sized antennas, without significantly increasing their sizes. This can be accomplished by increasing the number of resonances of single resonant antennas such as a half-wavelength slot. For example, by feeding a $\lambda/2$ slot near an edge by a microstrip line, the magnetic current distribution (electric field along the slot) can be manipulated to create a null near the feed point producing a second resonance with a frequency slightly larger than that of the first one. When appropriately fed, these two resonances can merge and result in an antenna with a much larger bandwidth or two separate bands of operation with similar radiation characteristics. Microstrip-fed, wide slot antennas have been theoretically studied in [84]. Also experimental investigations on very wide slot antennas are reported by various authors [85, 86, 87, 88]. The drawback of these antennas are two fold: 1) they require a large area for the slot and a much larger area for the conductor plane around the slot, 2) the cross polarization level changes versus frequency and is high at certain frequencies in the band [49, 85, 86, 87]. This is mainly because of the fact that these antennas can support two orthogonal modes with close resonant frequencies. The advantages of the proposed dual-resonant slots to these antennas are their simple feeding scheme, low cross polarization levels, and amenability of the elements' architecture to the design of series-fed multi-element broadband antennas. That is, the proposed wideband element can be used as a building block in design of multi-element antennas that can produce larger overall bandwidths with fewer radiating elements and much smaller size than existing multi-element antennas such as log-periodic arrays. In this chapter, first the design and measurement results of the double-resonant slot antenna in the wideband mode is presented. Then the application of this technique in the design of dual-band slot antennas is examined and finally, the use of this element in a parallel fed double-element antenna topology is investigated. The latter antenna shows very good radiation characteristics over a 2.5:1 bandwidth ratio by using only two radiating elements.

3.1 Off-Centered Microstrip-Fed Slot Antenna As A Broadband Element

3.1.1 Antenna Design

A resonant narrow slot antenna is equivalent to a magnetic dipole and, at its first resonance, it has an equivalent length of $\lambda_g/2$ (λ_g is the guided wavelength in the slot). If the slot antenna is fed near an edge by a microstrip line and the slot width is properly chosen, at a frequency above that of the first slot resonance, a fictitious short circuit near the microstrip feed may be created. Basically, the tangential component of the electric field created by the microstrip line at a particular distance cancels out the electric field of the slot excited by the return current on the ground plane of the microstrip line. A full wave simulation shows the field distribution for this situation in Figure 3.1(b) whereas Figure 3.1(a) shows the electric field distribution in the slot at its normal first resonance. The field distribution is shown to have a null along the slot between the two ends at a frequency slightly above that of the first resonance. The width of the microstrip feed, the slot width, and the distance between the center of the microstrip feed and the edge of the slot antenna, L_s, are the parameters that affect the existence and location of this fictitious short circuit. As L_s increases, the second resonant frequency also increases; therefore, by choosing L_s properly, the second resonant frequency can be chosen such that the total antenna bandwidth is increased or a dual-band operation is achieved. Meanwhile, the frequency of the first resonance, which is determined by the overall effective length of the antenna, does not change significantly. Matching is achieved by tuning the length of the open-circuited microstrip line, L_m. As can be observed from Figure 3.1, the electric field distribution at this second resonant frequency is similar to that of the first one. Therefore, it is expected that the radiation patterns of the antenna at the two frequencies are similar.

In order to test this concept, two wideband double-resonant slot antennas with different L_s values are designed and fabricated. The antennas (Figure 3.1(c)) are similar rectangular slots with lengths and widths of $L = 37$ mm and $W = 6$ mm and L_s of 3.6 mm and 4.6 mm for Antenna 1 and Antenna 2, respectively. The antennas are fed with a 110 Ω open circuited microstrip line connected to a 50 Ω main line that is connected to a 50 Ω SMA connector. The structures were simulated using IE3D [82] and fabricated on a 500 μ m, RO4350B substrate with a dielectric constant of 3.4, loss tangent of 0.003, and ground plane size of $L_g \times W_g = 15$ cm $\times$ 12 cm. Figure 3.2

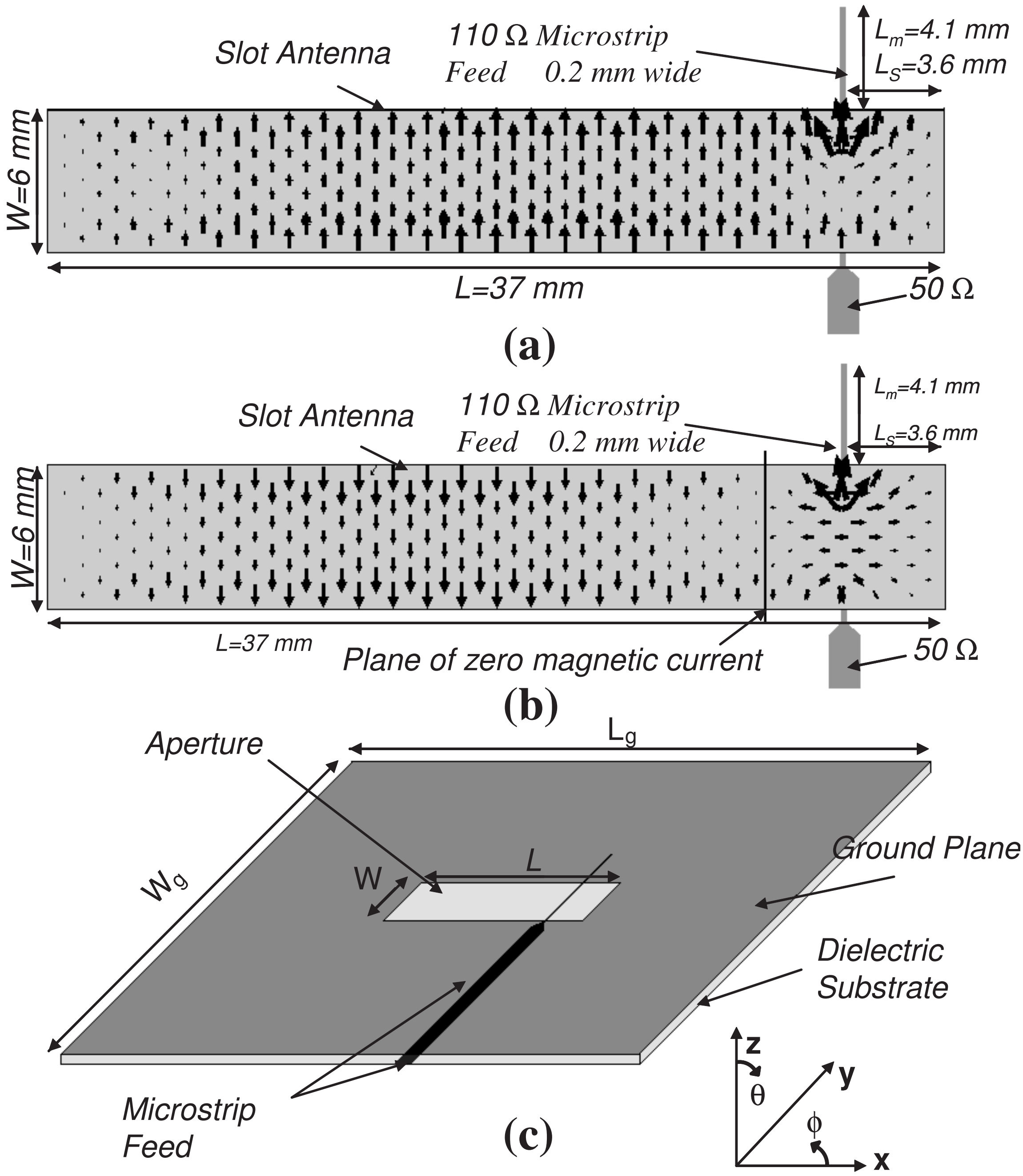

Figure 3.1: The electric field distributions and three-dimensional geometry of a 0.08λ wide microstrip-fed slot antenna. (a) Normal field distribution. (b) Field distribution at a slightly higher frequency showing a fictitious short circuit along the slot causing the second resonance. (c) Three-dimensional geometry.

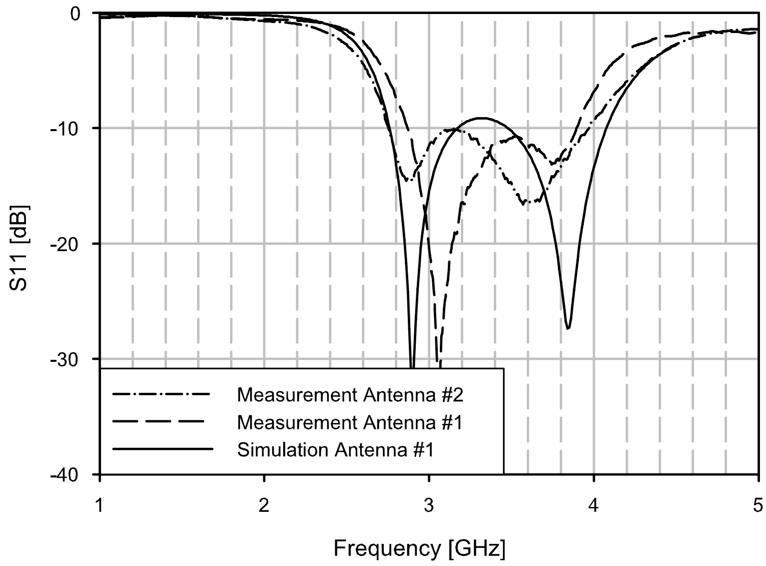

Figure 3.2: Measured and simulated input reflection coefficients of the proposed broadband slot antenna. The two measured responses correspond to two values of $L_S = 3.6$ mm and $L_S = 4.6$ mm.

shows the simulated and measured input reflection coefficients of both antennas and Table 3.1 shows a summary of the radiation parameters and physical dimensions of the two antennas. The -10 dB S_{11} bandwidth of Antenna 1 is 1022 MHz (30.3%), whereas Antenna 2 shows a bandwidth of 1220 MHz (37%). The slight discrepancy between the simulation and measurement results can be attributed to the finiteness of the ground plane, which causes a shift in the resonant frequency, and to the fact that the response of the antenna is sensitive to the exact location of the microstrip feed, which is subject to alignment errors in the fabrication process.

The radiation patterns of Antenna 1 were measured in the anechoic chamber of the University of Michigan at the two resonant frequencies. Figures 3.3(a) and 3.3(b) show the E- and H-Plane co- and cross-polarized patterns of this antenna at 3.077 GHz and 3.790 GHz, respectively. It is observed that the patterns at both resonant frequencies are similar, confirming the fact that electric field distributions along the slot are similar at both frequencies. As can be observed from this figure, the E-Plane patterns of the antenna are not the dual of those of an electric dipole. From

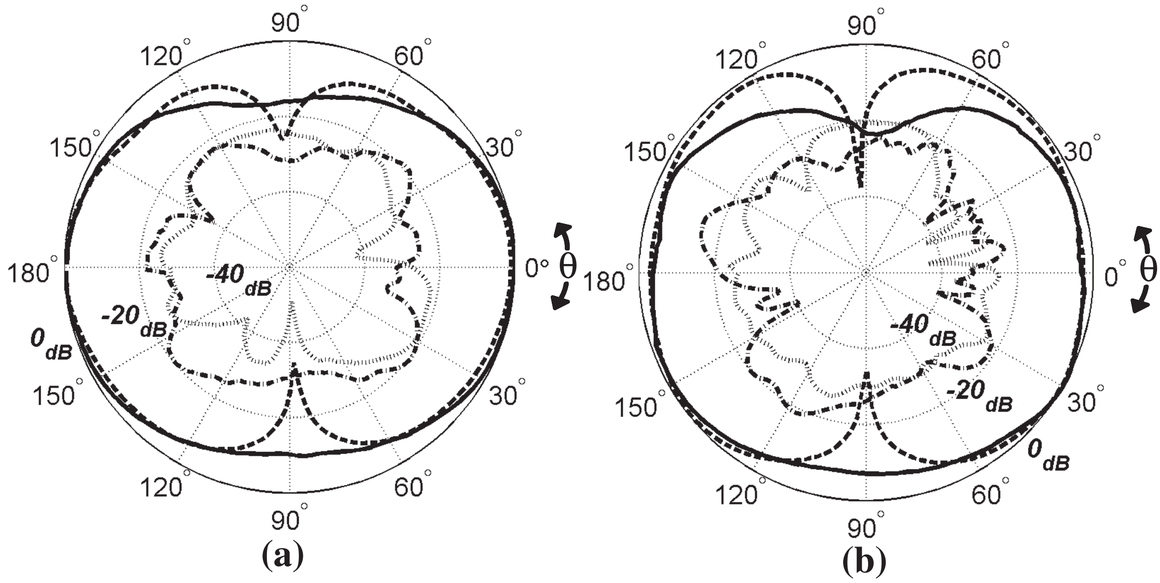

Figure 3.3: E- and H-Plane co- and cross-polarized radiation patterns of the broadband slot antenna. '-': H-Plane Co-Pol, '- -': E-Plane Co-Pol, '-.': H-Plane X-Pol, and '...': E-Plane X-Pol.

duality theorem, it is expected that the E-Plane patterns are similar to the H-Plane pattern of an electric dipole, which is a circle. However, in Figure 3.3 the E-Plane patterns have two minima at $\theta = \pm 90°$. This is caused by two different mechanisms. The first mechanism is the cancelation that occurs at grazing angle as a result of the phase difference between E-fields on the top and bottom of the ground plane. The second reason for having these minima is that the slot antenna is covered with a dielectric substrate at one side. This forces the normal component of the electric field at grazing angle to go to zero as described in [56]. It is also observed that the normalized cross polarization level at broadside is less than -25 dB and small for other observation angles as well. The gains of the antennas were measured in the anechoic chamber using a standard double ridged horn antenna at the two different resonant frequencies and are reported in Table 3.1. The antenna gains at both frequencies are very similar, which assures the similarity of the radiation mechanisms and the field distributions at both frequency bands.

3.1.2 Parametric Study

Now that the broadband behavior of the microstrip-fed slot antenna has been shown, the effect of the three parameters that affect its double-resonant behavior must also be examined. These parameters are the impedance of that section of microstrip line that feeds the slot antenna, the aspect ratio of the antenna (W/L), and the distance between the edge of the slot antenna and the center of the microstrip feed, L_s. Using full-wave simulations in IE3D, a number of slot antennas with different W/L, L_s, and feed impedance values are designed and matched to 50 Ω by changing the length of the open-circuited microstrip line (L_m in Figure 3.1). Then their impedance bandwidths ($|S_{11}| < -10$ dB) are calculated and reported in Figure 3.4. The antennas have aspect ratios (W/L) ranging from 0.0003 to 0.25. In this chapter, the antennas that have aspect ratios in the range of $0.05 < W/L < 0.25$ are referred to as "moderately-wide" and those with $W/L < 0.05$ and $W/L > 0.25$ are referred to as "narrow" and "wide" slot antennas, respectively. Figure 3.4(a) shows the fractional bandwidth versus aspect ratios of the antennas when they are fed with 50 Ω microstrip lines. It can be observed that, for fixed L_s, as W/L increases, the antenna bandwidth increases as well. However, the increase in bandwidth for $0.2 < W/L < 0.25$ is not significant. This saturation behavior is explained by defining a quality factor for the antenna and relating it to the Fourier transform of the electric field distribution over the aperture. It can be shown that, for a single-resonant slot antenna, bandwidth increases as W increases and a similar saturation behavior is observed [89]. This can then be extended to each of the resonances of this double-resonant antenna. The double-resonant behavior for the 50 Ω line impedance is only observed for $W/L > 0.07$. For $L_s/L = 5.5\%$, the antenna is hard to match for small W/L values and hence, its impedance bandwidth goes to zero faster than other cases. It is also observed that, for a fixed $W/L \geq 0.07$, the antenna bandwidth increases as L_s increases. This increase continues until $L_s/L = 10\%$. Beyond this

Type	L, W [mm]	L_s, L_m [mm]	BW	Gain @ f_l, f_u	L_g, W_g [cm]
Antenna 1	37, 6	3.6, 4.1	30.3%	2.5 dBi, 2.6 dBi	15, 12
Antenna 2	37, 6	4.6, 3.9	37%	2.5 dBi, 2.5 dBi	15, 12

Table 3.1: Physical and radiation parameters of the two broadband microstrip-fed slot antennas of Section 3.1.

value, increasing L_s increases the second resonant frequency such that a wideband match cannot be obtained and the antenna enters into the dual-band mode of operation. Figure 3.4(b) shows a similar study in the same W/L range for antennas fed with 80 Ω microstrip lines. In this case, the double-resonant behavior is observed for $W/L \geq 0.05$ and the antenna bandwidth has a similar characteristics as those of the previous case. Similar to the previous case, the antenna goes to a dual-band mode for $L_s/L > 10\%$. Figure 3.4(c) shows a similar figure for a 110 Ω feed line. In this case, the antenna does not go to dual-band mode until $L_s/L > 11.5\%$. This occurs because the separation between the two resonant frequencies ($f_u - f_l$) is smaller for the same L_s value and matching the antenna, by only changing L_m, is found to be easier. Comparing Figures 3.4(a), 3.4(b), and 3.4(c) shows that, for the same W/L and L_s values, the bandwidth of the antenna slightly decreases as the feed impedance increases. This can be attributed to the presence of the discontinuity in the transition region from the main 50 Ω line to 80 Ω or 110 Ω feed lines. However, under the same condition, matching is easier and lower S_{11} values can be obtained for higher feed impedances.

3.2 Dual-Band Microstrip-Fed Slot Antenna

3.2.1 Antenna Design

In this section, we will show that the moderately-wide slot antenna presented in the previous section can also be designed to demonstrate a dual-band behavior. Re-

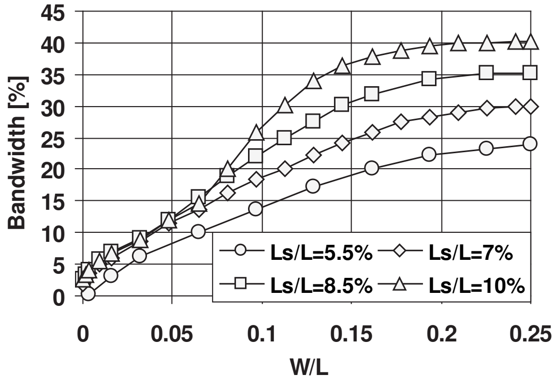

(a)

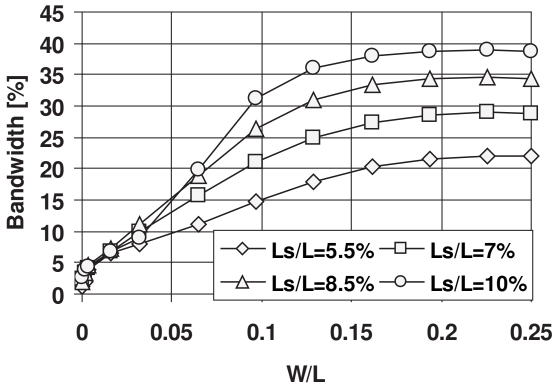

(b)

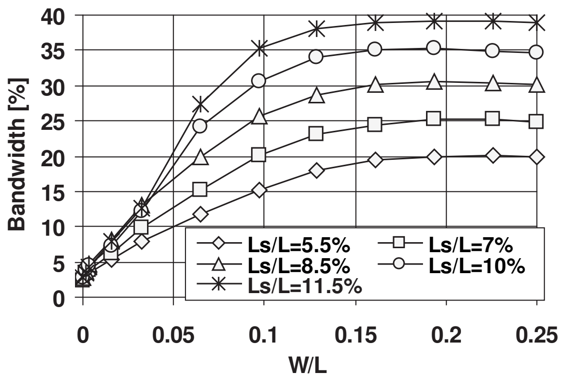

(c)

Figure 3.4: Bandwidth of moderately-wide slot antenna in the wideband mode of operation as a function of aspect ratio (W/L), feed impedance, and location of the feed. (a) 50 Ω Feed impedance, (b) 80 Ω Feed impedance, and (c) 110 Ω Feed impedance.

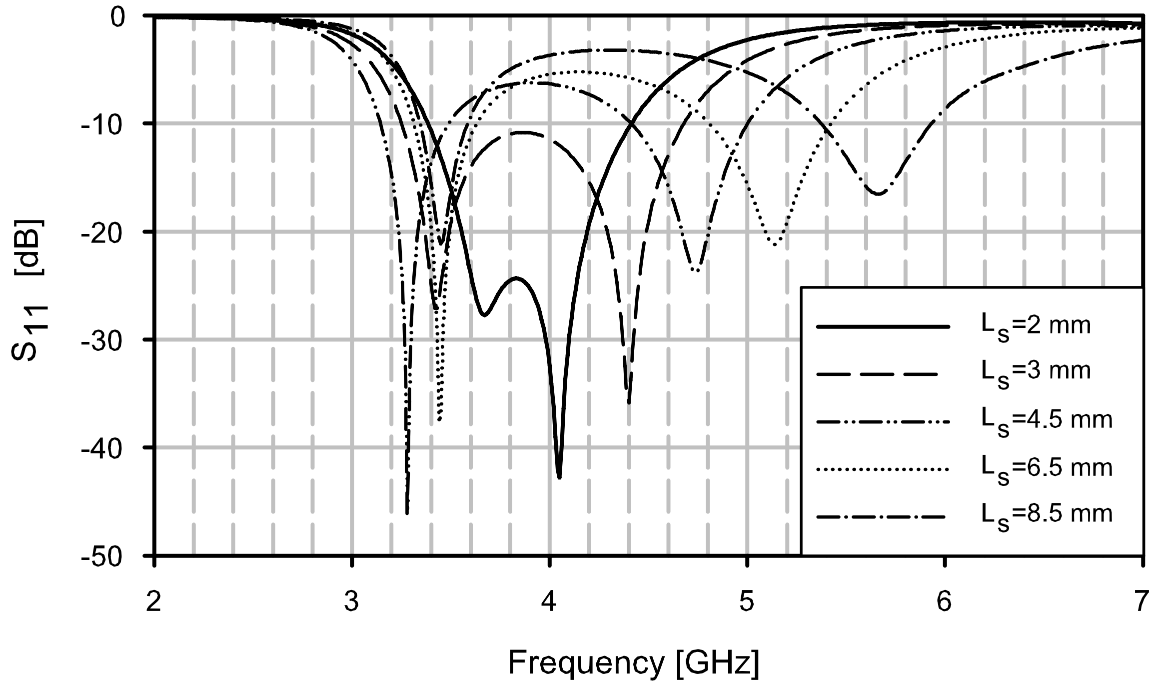

Figure 3.5: Simulated input reflection coefficients of a dual-band antenna with $W =$ 6 mm and $L = 31$ mm on a substrate with $\epsilon_r = 3.4$ for different values of L_s.

ferring to Figure 3.1(b), if the distance L_s is increased, the equivalent length of the second resonance decreases. Therefore, the second resonant frequency (f_u) increases while the frequency of the first resonance (f_l) is not expected to change considerably, as this resonance is set by the overall length of the antenna. This way, the antenna becomes a dual-band one in which the separation between the two resonant frequencies is a function of the resonant length of the second resonant frequency or, equivalently, the distance of the feed from the antenna edge, L_s. Figure 3.5 shows the full-wave S_{11} simulation results of an antenna with $W = 6$ mm and $L = 31$ mm on a substrate with dielectric constant of 3.4, for different values of L_s. By increasing L_s from 2 mm to 8.5 mm, f_l varies between 3.3 GHz and 3.7 GHz and f_u increases from 4 GHz to 5.2 GHz. This corresponds to an f_u/f_l variation from 1.1 to 1.6 while retaining an S_{11} lower than -15 dB. Based on the simulation results of Figure 3.5, a dual-band antenna with $L = 31$ mm and $W = 6$ mm was designed and fabricated on

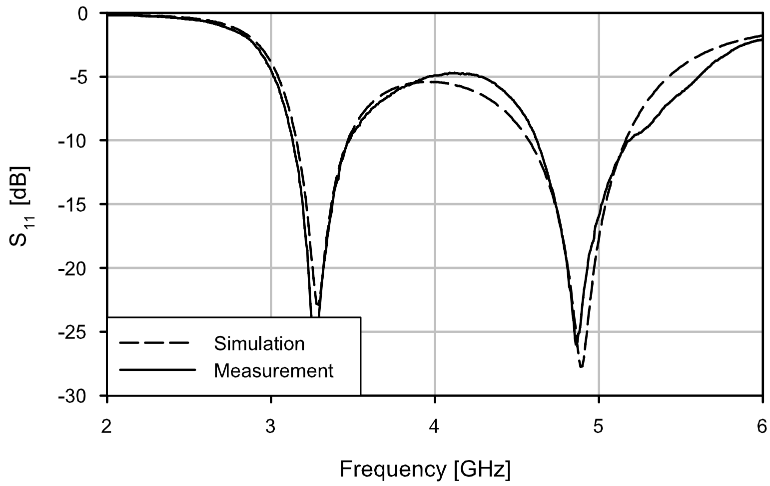

Figure 3.6: Simulated and measured input reflection coefficients of the dual-band antenna of Section 3.2.

a 500 μm thick, RO4350B substrate with a ground plane size of 15 cm $\times$ 12 cm. The simulated and measured S_{11} of this antenna are plotted in Figure 3.6, where excellent agreement between them is observed. The antenna shows a f_u/f_l of 1.47 with relative bandwidths of 10.6% and 12.1% at the lower and upper bands, respectively. As described in Section 3.1, the magnetic current distributions at both frequencies are similar, and therefore, the resulting radiation patterns are expected to be similar as well. The co- and cross-polarized E- and H-Plane radiation patterns of the antenna at both bands were measured, and the results are presented in Figures 3.7(a) and 3.7(b). It is shown that the radiation patterns at both bands are similar and the levels of cross polarized radiation are negligible. The antenna gains are measured using a standard horn antenna and are reported in Table 3.2.

3.2.2 Parametric Study

A similar parametric study as the one presented in Section 3.1.2 was performed for the antenna in the dual-band mode. In this study, the bandwidth and frequency ratio (f_u/f_l) of the antenna in the dual-band mode are studied as functions of the aspect ratio, feed impedance, and feed location. A number of different moderately-wide dual-

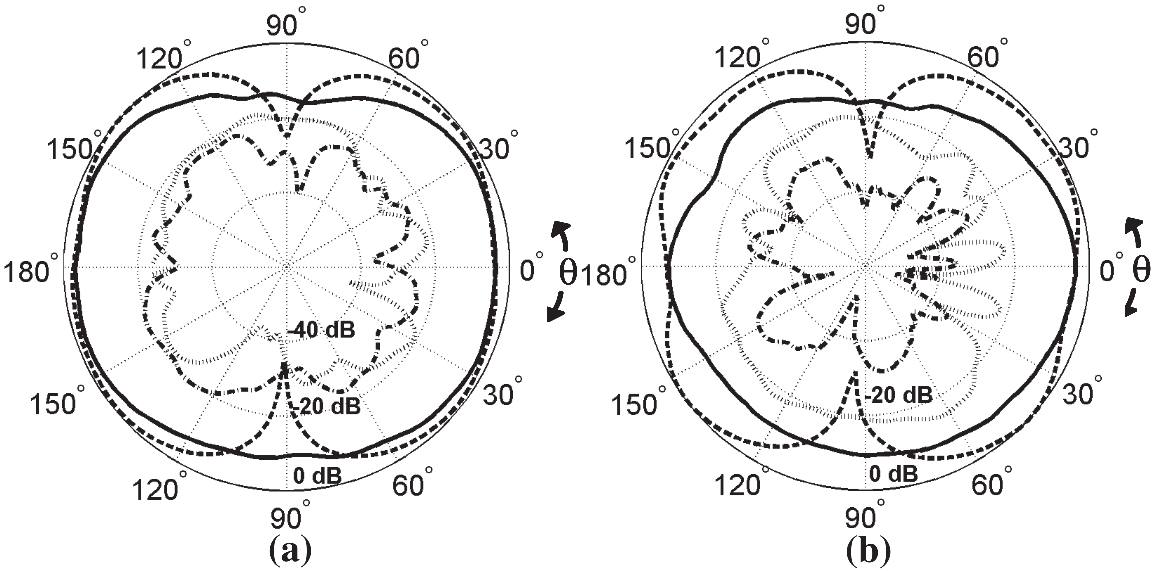

Figure 3.7: E- and H-Plane co- and cross-polarized radiation patterns of the dual-band slot antenna of Section 3.2 at (a) f=3.3 GHz and (b) f=4.85 GHz. '-': H-Plane Co-Pol, '- -': E-Plane Co-Pol, '-.': H-Plane X-Pol, and '...': E-Plane X-Pol.

band slot antennas with different W/L, L_s, and feed impedance values are designed and simulated in IE3D. Simultaneous matching at both bands to 50 Ω is obtained by changing the length of the open-circuited microstrip line (L_m in Figure 3.1). Figure 3.8 shows the fractional bandwidth of the lower and upper bands (f_l and f_u) as functions of W/L and L_s, for different values of feed impedances. For narrow microstrip feeds (high impedance lines) achieving simultaneous match at both bands was found to be easier than wider lines and lower $|S_{11}|$ values were obtained. As a result, the dual-band operation, for a fixed L_s, occurs at lower aspect ratios for narrower feeds. For example, for the 110 Ω feed, the dual-band operation starts at $W/L = 0.065$, which increases to $W/L = 0.080$ and $W/L = 0.095$ for 80 Ω and 50 Ω lines, respectively. However, one drawback of higher impedance feeds to lower ones is the slightly lower fractional bandwidths that are obtained as explained in Section 3.1. The effects of W/L, feed impedance, and L_s on the frequency ratio of the two bands of the dual-band antenna (f_u/f_l) are also studied in Figure 3.9. It is seen that increasing L_s has

L, W	L_s, L_m	f_l, f_u (GHz)
31 mm, 6 mm	5 mm, 2.3 mm	3.3, 4.85
BW @ f_l, f_u	Gain @ f_l, f_u	L_g, W_g
10.6%, 12.1%	2.5 dBi, 2.8 dBi	15 cm, 12 cm

Table 3.2: A summary of the physical and radiation parameters of the dual-band slot antenna of Section 3.2.

the largest effect on f_u/f_l. The antenna aspect ratio, W/L, also slightly affects this frequency ratio, as shown in Figure 3.9.

3.3 An Octave Bandwidth Double-Element Slot Antenna

In this section, the design and measurement results of a very wideband, double-element slot antenna is presented. As demonstrated in Section 3.1, a single-element, moderately-wide slot antenna can be designed to have a wideband response. Therefore, it is expected that a properly designed antenna that is composed of two or more such radiators can show very wideband characteristics. There are a number of different multi-element feeding topologies, in which such an element can be used. These include feeding the two elements in series, parallel, or through parasitic coupling. The wideband behavior is only observed when the antenna is fed directly with a microstrip line; therefore, parasitic coupling does not provide the best results. Series feeding of both elements, using a single microstrip line, is possible and is a good choice for end fire arrays such as printed log-periodic arrays. However, using a parallel feed configuration, such as the one shown in Figure 3.10(a), provides more flexibility in the design of the broadband feed network and allows for designing antennas with a broadside radiation pattern. In this arrangement, a broadband antenna with good impedance matching and consistent radiation patterns over the band of operation can easily be obtained.

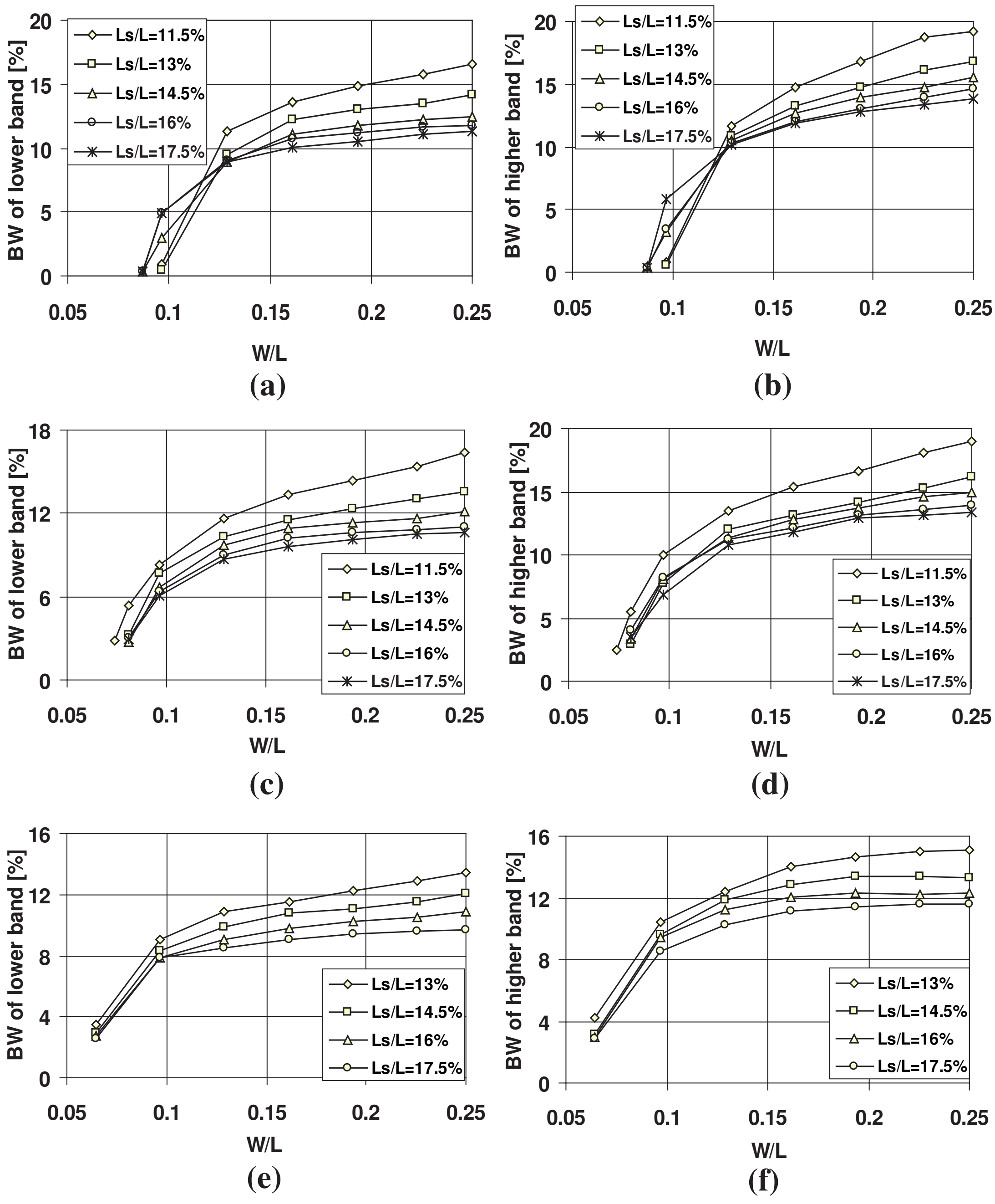

Figure 3.8: Bandwidth of moderately-wide slot antennas in the dual-band mode of operation as a function of aspect ratio (W/L), feed impedance, and location of the feed. (a) 50 Ω feed impedance, lower band. (b) 50 Ω feed impedance, higher band. (c) 80 Ω feed impedance, lower band. (d) 80 Ω feed impedance, higher band. (e) 110 Ω feed impedance, lower band. (f) 110 Ω feed impedance, higher band.

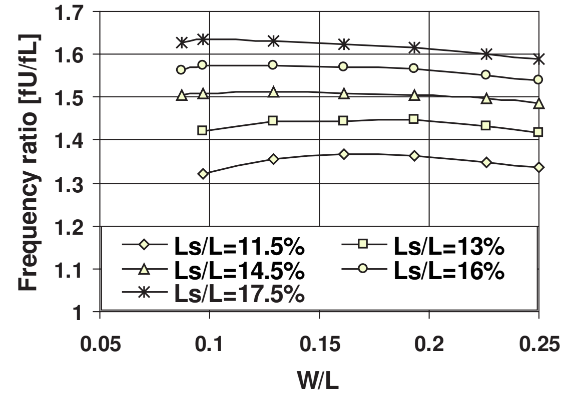

(a)

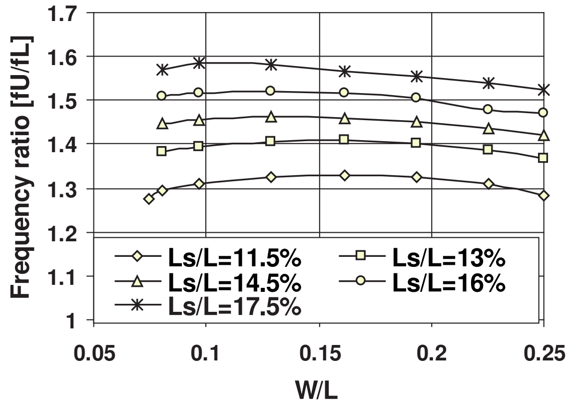

(b)

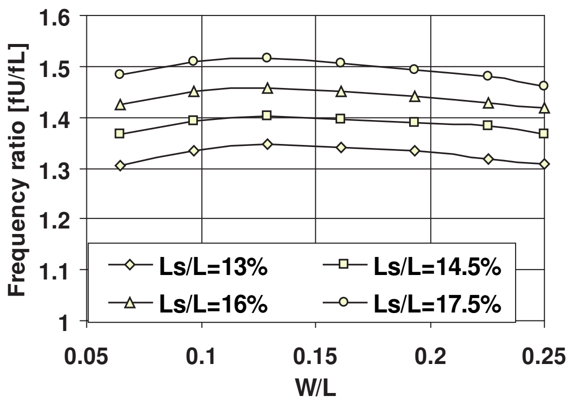

(c)

Figure 3.9: Frequency ratios of the upper band to the lower band of the moderately-wide slot antenna in the dual-band mode of operation as functions of the aspect ratio (W/L), feed impedance, and location of the feed. (a) 50 Ω microstrip feed. (b) 80 Ω microstrip feed. (c) 110 Ω microstrip feed.

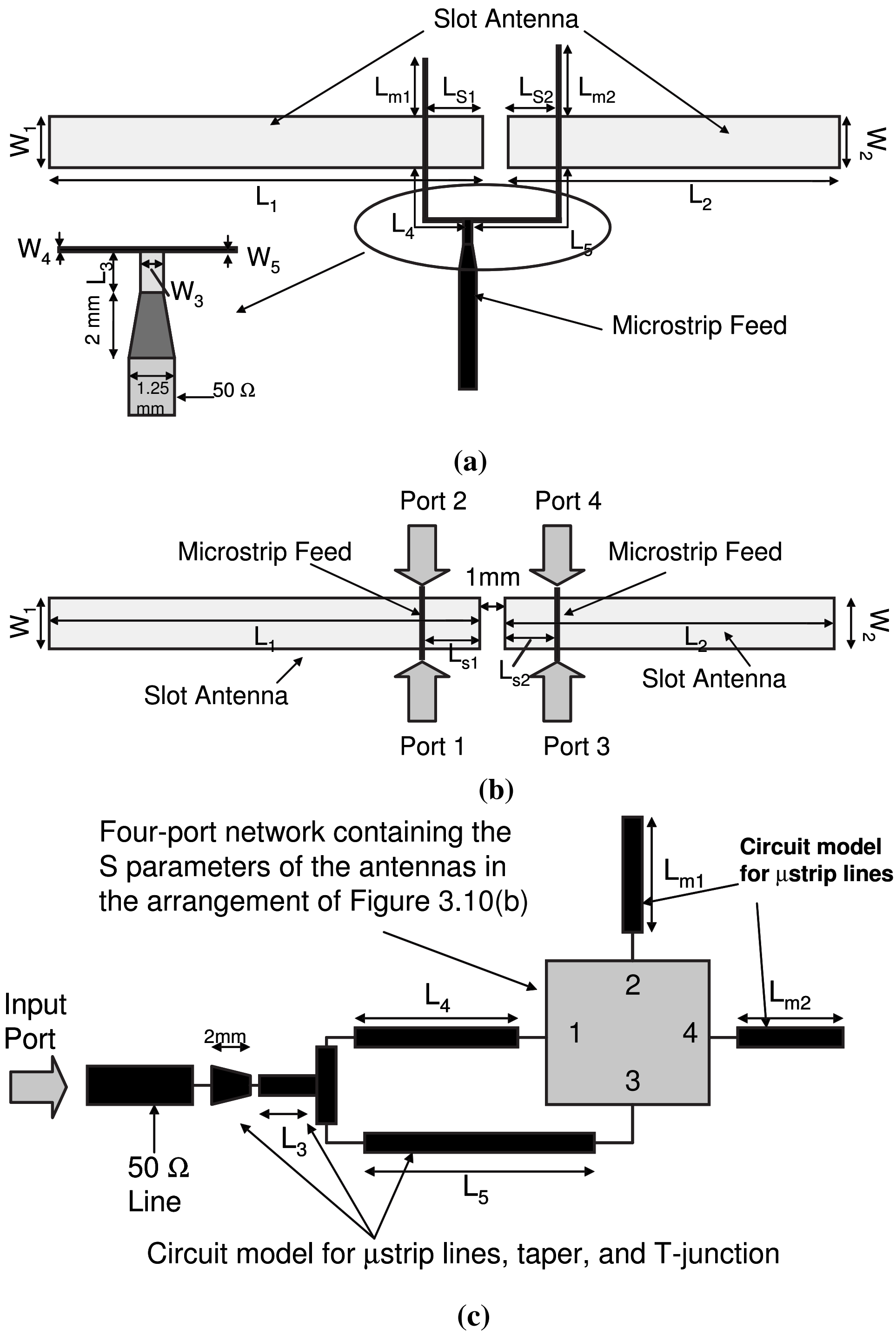

Figure 3.10: Geometry and circuit model of the double-element broadband slot antenna of Section 3.3. (a) Antenna geometry. (b) The four-port network, which models the antennas, their coupling effects, and their microstrip feeds. The S-Parameters of this network are used in the simulation of the circuit shown in Figure 3.10(c). (c) Circuit model of the antenna in Figure 3.10(a) used in optimizing the feed network parameters.

The objective is to design an antenna that covers at least an octave bandwidth. For this design, the upper and lower frequencies are chosen such that they cover both of the bands designated for Wireless LAN operation. The schematic of the proposed antenna is shown in Figure 3.10(a), where two slots with different lengths are used in a parallel feed arrangement. The larger antenna covers the lower and the smaller antenna covers the higher frequency bands. The lengths L_1 and L_2 are determined from the lowest resonant frequency of each element. W_1 and W_2 are chosen to be equal and wide enough such that the aspect ratio of both elements are in the range of $0.15 \leq W/L \leq 0.25$. From Figure 3.4(c), it is seen that in this range, the antennas have their maximum bandwidth. Choosing $W_2/L_2 = 0.25$ results in $W_2 = 7$ mm. Although it is not necessary, W_1 is chosen to be equal to 7 mm as well. This results in $W_1/L_1 = 0.175$, which is in the desired range. Then, the larger slot antenna is simulated and L_{S1} is optimized such that the antenna covers a bandwidth of 2.3 GHz to 3.6 GHz. Similarly, L_{S2} is optimized such that the second antenna covers a bandwidth of 3.7 GHz to 5.5 GHz. The feed network dimensions L_3, L_4, L_5, W_3, W_4, L_{m1}, and L_{m2} (see Figures 3.10(a)), must be optimized to achieve the desired response in the band of operation. This is accomplished by performing a full-wave simulation on the four-port structure shown in Figure 3.10(b) and obtaining the S-parameters of this network. Then, the calculated S-parameter matrix is used in ADS and a circuit simulation is performed on the circuit shown in Figure 3.10(c). In this simulation, the software replaces all of the microstrip lines, the Tee-junction, and the microstrip taper by their equivalent circuit models. The values L_3, L_4, L_5, W_3, W_4, L_{m1}, and L_{m2} are defined as optimization variables in this circuit simulation. The optimization goal is to have $|S_{11}| < -10$ dB over the frequency range of 2.4 GHz to 5.5 GHz. Two constraints are set on the variables; first, the width of microstrip lines must be larger than 0.15 mm. The reason for this is that the fabrication of very narrow microstrip lines is difficult in our facilities. The second constraint is that

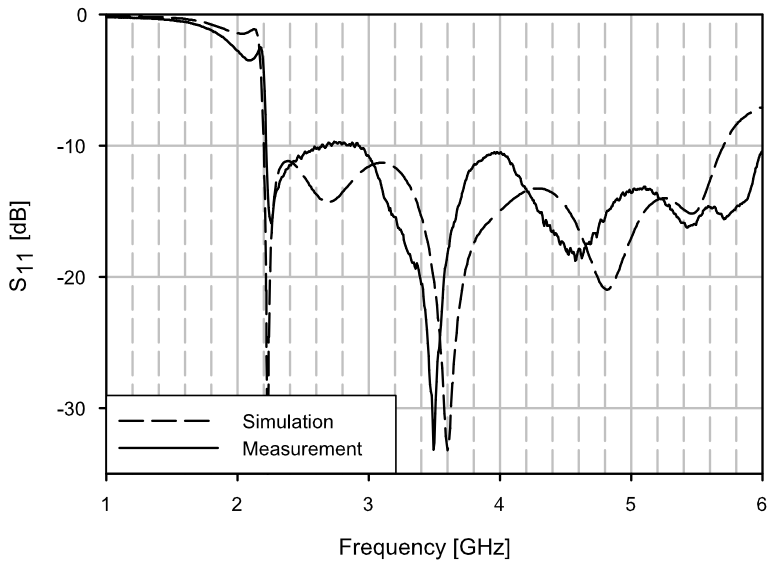

Figure 3.11: Simulated and measured input reflection coefficient (S_{11}) of the double-element broadband antenna of Section 3.3.

the difference between L_4 and L_5 (see Figure 3.10(a)) must be smaller than 6 mm. Since the electrical length of a 6 mm microstrip line at 5.5 GHz (which is the highest desired frequency) on the RO4350B substrate is about 60°, the two antennas will not be excited with a phase difference larger than 60° at any frequency in the desired band of operation. Even though each antenna covers a certain portion of the band, there is an overlap frequency band in which both of the antennas can operate. Therefore, the second constraint is necessary for having consistent radiation patterns over the entire frequency band. The circuit was then optimized using the embedded optimization engine in ADS [90] and the optimum values of the parameters were obtained. Since the circuit simulation and optimization process ignores the mutual coupling effects between the microstrip lines, a full-wave simulation was performed on the entire structure and the optimization parameters were fine tuned in the full-wave simulation. For the aforementioned frequency band, the final physical parameters of the antenna are listed in Table 3.3. The final design was fabricated on a RO4350B substrate with a ground plane size of 15 cm $\times$ 12 cm. The S_{11} of the antenna was measured using a calibrated HP-8753D vector network analyzer and is presented in Figure 3.11 along with the full-wave simulation result obtained from IE3D. The discrepancies between the two results can mostly be attributed to the finite size of the ground plane, inaccuracies in the fabrication process, uncertainties in the exact permittivity of the substrate ($\pm 3\%$ error specified by the manufacturer), and numerical errors in the simulation results. Nevertheless, the measured S_{11} shows a -10 dB impedance bandwidth from 2.3 GHz to 6 GHz. However, in order to determine the useful bandwidth of the antenna, other parameters such as radiation patterns, gain, polarization, and cross polarization levels must also be carefully examined over the entire bandwidth. In order to study the effect of ground plane size on the radiation patterns of the wideband antenna, another antenna with the same dimensions was also fabricated on a substrate with a larger ground plane (23 cm $\times$ 30 cm). The radiation patterns of both antennas were measured in the anechoic chamber at 9 different frequencies ranging from 2.5 GHz to 6 GHz. However, for brevity, only the radiation patterns at 3 GHz, 4 GHz, 5 GHz, and 5.8 GHz are reported. Figures 3.12 and 3.13 show the H- and E-Plane radiation patterns for both co- and cross-polarizations at different frequencies. In these figures SGP and LGP denote "Small Ground Plane" and "Large Ground Plane" respectively. The experimental results show that the size of the ground plane alters the radiation pattern, especially in the H-Plane cut due to the out of phase radiation from the edges of the substrate.

The measured gain and directivity of the antenna at boresight are shown in Figure 3.14. Also the directivity at the direction of maximum radiation is shown in this figure. The antenna gain and directivity at boresight are very close to each other, indicating a high radiation efficiency. This figure also shows that above 5.5 GHz the direction of maximum radiation shifts away from the boresight direction. There are two reasons for this: First, at 5.5 GHz the larger antenna has an electrical length that is about 1λ. Since it is off-centered fed, its electric field distribution is anti-symmetric with respect to the center of the antenna. Therefore, there is a null in

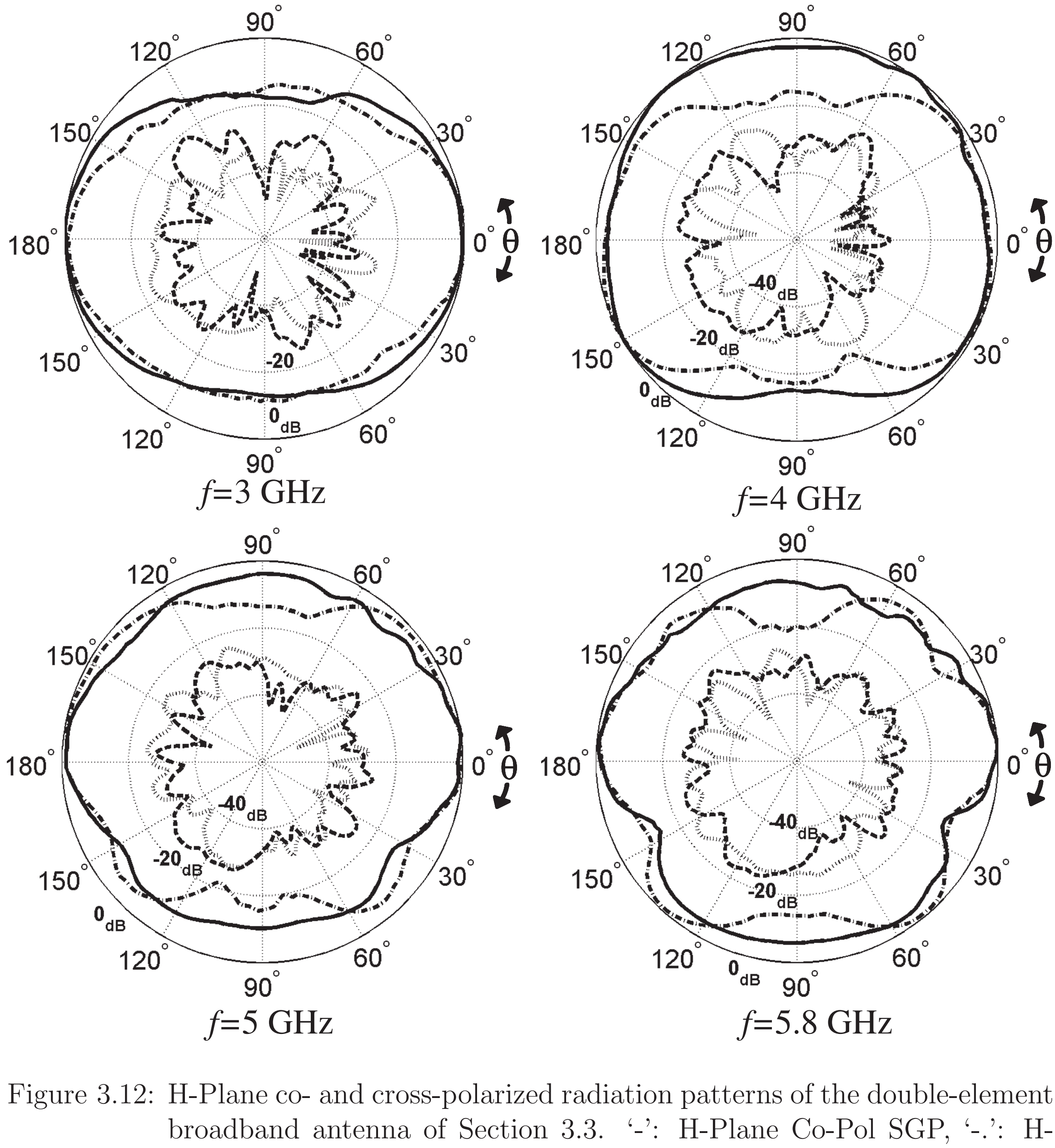

Figure 3.12: H-Plane co- and cross-polarized radiation patterns of the double-element broadband antenna of Section 3.3. '-': H-Plane Co-Pol SGP, '-.': H-Plane Co-Pol LGP, '- -': H-Plane X-Pol SGP, and '...': H-Plane X-Pol LGP.

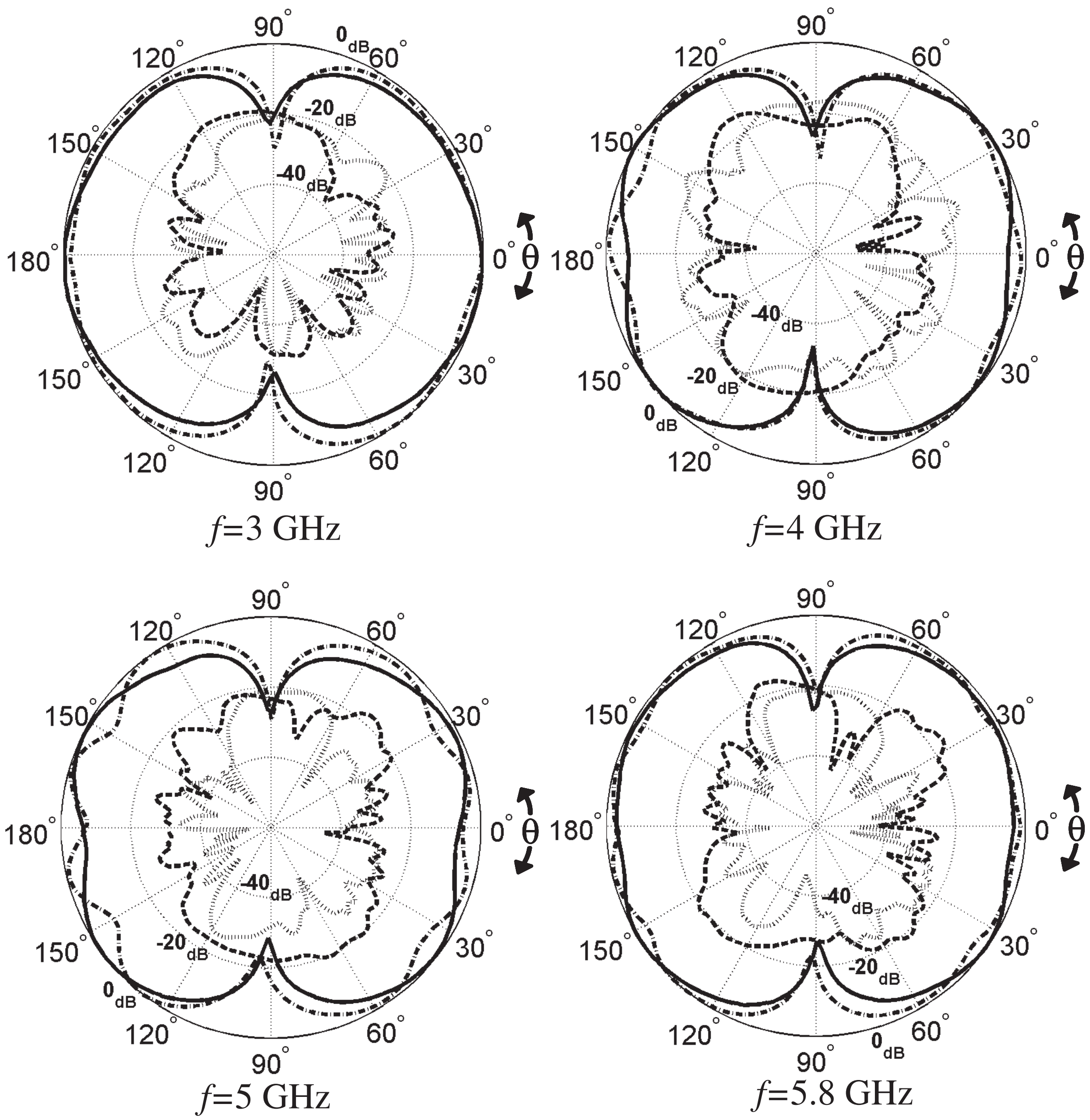

Figure 3.13: E-Plane co- and cross-polarized radiation patterns of the double-element broadband antenna of Section 3.3. '-' Solid line: E-Plane Co-Pol SGP, '-.' Dash-Dotted Line:E-Plane Co-Pol LGP, '- -' Dash-Dashed Line: E-Plane X-Pol SGP, and '...' Dotted Line: E-Plane X-Pol LGP.

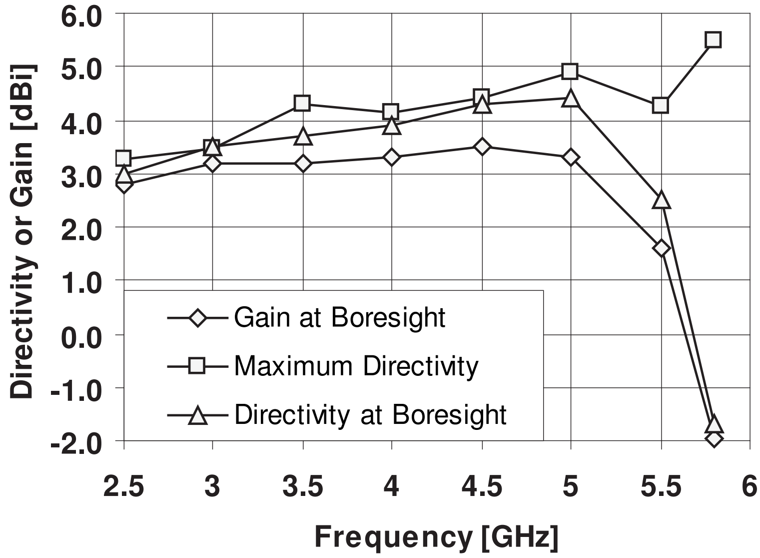

Figure 3.14: Measured values of the gain and computed values of the directivity of the double-element broadband antenna.

Parameter	L_1	L_2	L_{s1}	L_{s2}	L_{ml}	L_{m2}	L_3
Value	40	28	6.1	4.6	3.5	4.6	1.25
Parameter	L_4	L_5	W_1	W_2	W_3	W_4	W_5
Value	7.3	12.6	7	7	0.7	0.2	0.2

Table 3.3: A summary of the physical dimensions of the broadband double-element antenna of Section 3.3. All dimensions are in mm.

the radiation pattern of this element at boresight and the maximum radiation occurs at $\theta = 45°, 135°$. Since this element is resonant at around 1 λ, it can radiate rather efficiently and distort the overall radiation pattern. The second reason is that, as frequency increases, the two antennas are excited with a larger phase difference, which also shifts the direction of maximum radiation. However, this happens outside of the desired band of operation. Based on the measured S_{11}, consistency of the radiation patterns, and polarization purity over the entire frequency band, it can be concluded that the antenna has a bandwidth from 2.3 GHz to 5.8 GHz or equivalently a 2.5:1 bandwidth ratio.

3.4 Conclusions

A novel slot antenna element is proposed that allows for easy design of wideband or dual-band antennas. The single element shows bandwidths up to 37% when used in the wideband mode. When operated in a dual-band mode, the structure has the ability to cover a 1.6:1 frequency ratio easily. Furthermore, it is shown that this broadband antenna element is an excellent choice for constructing multi-element antennas with a much larger bandwidth. To demonstrate this, a two-element antenna configuration was considered and a wideband broadside radiating antenna with a bandwidth ratio of 2.5:1 was designed. This allows the designer to obtain very wideband antennas by using a smaller number of antenna elements than was previously possible. An important and unique feature of this design is that the polarization purity of the antenna and high efficiency are unchanged over the entire frequency band.

CHAPTER 4

A Varactor Tuned Dual-Band Antenna

Dual-band antennas are of interest in many wireless applications that use two different frequency bands for receiving and transmitting. Current advancements in printed antenna technology have resulted in a variety of different techniques for designing low profile, cost effective, and highly efficient dual-band antennas [21]. Most techniques make use of certain approaches to manipulate the current distribution at one of the higher order resonant modes of the structure to change its resonant frequency. For example in [44], a rectangular patch antenna is loaded with a slot at a particular location along the patch such that it affects one resonant mode more than another. This way, a dual-band operation is obtained. However, the range of achievable frequency ratios (f_2/f_1) is limited to $1.6 - 2$. This idea was later applied to circular and triangular patch antennas where frequency ratios of $1.3 - 1.4$ and $1.35 - 1.5$ were respectively achieved [45, 46]. Variations of these techniques with differently shaped slots and patches have also been investigated and discussed in detail in Chapter 4 of reference [21].

The configuration and radiation characteristics of slot antennas appear to be more amenable to reconfigurability than their patch antenna counterparts. In a recent study, the design of a reconfigurable slot antenna with an octave tunability bandwidth was demonstrated [48]. This antenna uses five PIN diode switches to achieve reconfigurability. The drawback of this design, however, is that the PIN diodes are forward biased to change the resonant length of the antenna and significant amount of electric current flows through each diode. Given the ohmic resistance associated with each diode, this results in loss of RF power and hence, reduces the antenna's radiation efficiency. In [49], a single-element, dual-band, CPW-fed slot antenna with similar radiation patterns at both bands is studied. However, this antenna shows high levels of cross polarized radiation at its second band of operation. In [50], a compact, dual-band, CPW-fed slot antenna, with a size reduction of about 60% compared to a conventional slot antenna, is studied. However, this antenna is designed for two particular frequency bands and little attention has been paid to investigating its frequency tuning capabilities. Furthermore, it suffers from high levels of cross polarized radiation, which at some angles are equal or even larger than the co-polarized component. Other topologies have also been used to achieve dual-/multi-band operations. Examples of these include structures that make use of parasitic elements and multiple radiating elements [51, 52]. Among other categories, design of a wideband or dual-band relatively wide slot antenna fed by a microstrip line can be mentioned. In Chapter 3 of this dissertation it is shown that, for a rectangular slot with width to length ratios larger than 0.15, a dual-resonant behavior can be achieved and frequency ratios from 1.1 to 1.7 can easily be obtained by choosing the appropriate location for the microstrip feed. The antenna is shown to have very small cross polarization levels and similar radiation patterns at both bands.

In this Chapter, we propose a new technique for designing dual-band narrow slot antennas that can easily be modified to obtain a tunable antenna. Furthermore, the frequency ratio of the antenna will be determined by an applied DC bias voltage or by choosing the right value for the lumped element and not by changing the geometrical parameters of the antenna. The proposed technique is based on loading a slot antenna with a fixed or variable capacitor at a certain location along the

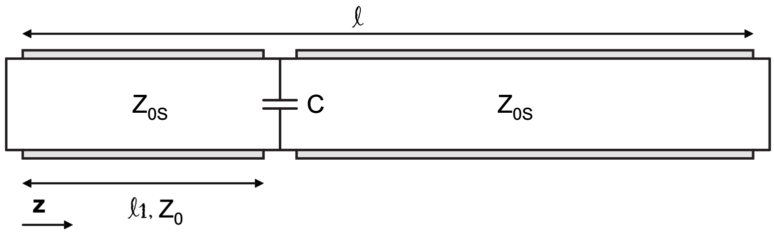

Figure 4.1: Transmission line equivalent circuit model of a slot antenna loaded with a lumped capacitor.

slot. One of the advantages of this technique is that the current that flows through a capacitor, or a reverse biased varactor, is small compared to a PIN diode or a MEMS switch. Therefore, the finite Q of the device does not deteriorate the antenna's radiation efficiency. As is shown, such an antenna exhibits a dual-resonant behavior. In addition, placing a capacitor in parallel with the slot results in reduction of its resonant frequency. This occurs for both the first and the second resonant modes. However, the decrease is not uniform and depends on the location of the capacitor along the slot. It is shown that the location of the capacitor can be chosen to minimize the frequency variations of one mode and, therefore, obtain a dual-band antenna with adequate control over its frequency ratio. In what follows, we will first develop an approximate transmission line model as a design tool for determining the resonant frequencies of the slot antenna for a given value and location of the capacitor. Exact location of the capacitor can then be obtained using full wave analysis of the antenna. Then, a tunable dual-band antenna is designed in which a varactor, with its proper biasing network, is used to tune the frequency ratio of the antenna. Finally, measured results for the radiation patterns and input reflection coefficients of the antenna are presented, compared with the simulation results, and discussed. It is shown that the simulation and measurement results agree very well and the antenna has good simultaneous match at both bands while maintaining similar radiation patterns across the entire band of operation.

4.1 Loaded Slot Antennas For Dual-Band Operation

A resonant, narrow slot antenna at its first resonance may be considered as a $\lambda/2$ transmission line, short circuited at both ends [91]. Loading such a structure with a capacitor, as shown in Figure 4.1, increases the line capacitance at one point and, therefore, reduces the frequency of its first and all higher order resonances. This reduction, however, is not uniform and depends on the location of the capacitor (ℓ_1 in Figure 4.1), its value, and the slot line impedance. Applying the transverse resonance condition to the structure shown in Figure 4.1 results in the following equation for the resonant frequencies of the structure:

$$\tan(\beta(\omega)(\ell - \ell_1)) + \tan(\beta(\omega)\ell_1) - \omega C Z_{0s} \tan(\beta(\omega)(\ell - \ell_1)) \tan(\beta(\omega)\ell_1) = 0 \quad (4.1)$$

where $\beta(\omega)$ is the frequency dependent, slot-line propagation constant, C is the capacitance of the lumped capacitor, and ω is the angular frequency. This equation can be solved numerically as a function of frequency and capacitance value, for fixed values of ℓ_1, to obtain the resonant frequencies of the loaded slot. For different ℓ_1 values, this equation is solved for a loaded slot antenna with slot length and width of $\ell = 60$ mm and $w = 2$ mm, which is printed on a 0.5 mm thick substrate with $\epsilon_r = 3.4$. The propagation constant, $\beta(\omega)$, and impedance of this line, Z_{0s}, are calculated using equations provided in [83] and the results are shown in Figure 4.2. The variations of f_1 and f_2 are seen to be dependent on ℓ_1 and C. However, this model does not take into account the effect of the antenna feed and its matching network, which affect the resonant frequencies of the antenna.

At its first resonance, the magnitude of the electric field of a slot antenna (voltage magnitude) is maximum at the center of the slot and zero at the edges. On the other

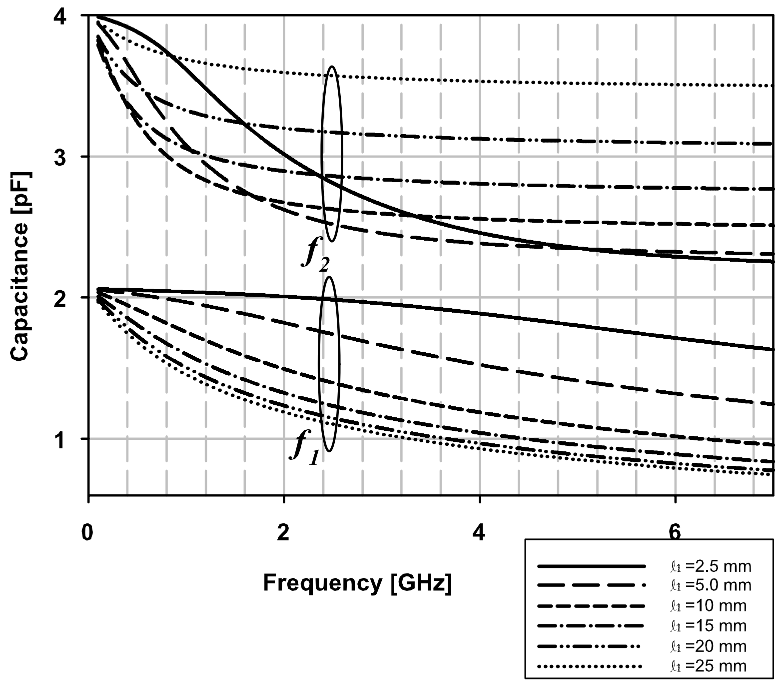

Figure 4.2: First and second resonant frequencies of a loaded slot antenna (with $\ell =$ 60 mm, $w = 2$ mm, $\epsilon_r = 3.4$, and the substrate thickness of 0.5 mm) as a function of value and location of the capacitor. The curves are obtained from solving (4.1) numerically.

hand, the magnitude of the electric current that flows around the slot is minimum at the center and maximum at the edges [91]. Therefore, if the slot antenna is fed at the center, its input impedance, as seen from the feed terminals, will be very large (ratio of a large voltage to a small current). However, if the feed terminals move away from the center of the slot antenna and approach its edge, the observed input impedance drops until it assumes a value of zero when the feed terminals are right at the edge of the slot (since it is short circuited). Thus, it is possible to match the impedance of the antenna to a wide range of line impedances by choosing the right location for the feed (from center to the edge). In this chapter, we use an open circuited, off-centered, microstrip line to feed the antenna. Therefore, in addition to choosing the feed location, the length of the open circuited microstrip line can be tuned such that it compensates the reactive part of the input impedance of the antenna to obtain a good match. This way, the antenna can easily be matched to the line impedance, by

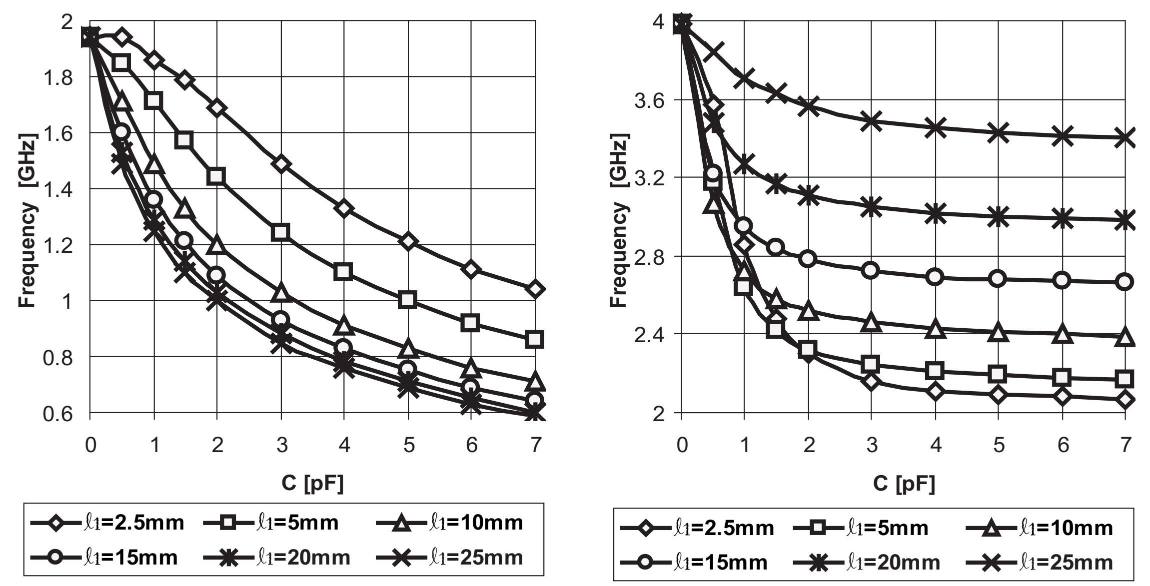

(a) (b)

Figure 4.3: Resonant frequencies of a microstrip-fed loaded slot antenna, with $\ell =$ 60 mm and $w = 2$ mm printed on a substrate with $\epsilon_r = 3.4$ and thickness of 0.5 mm, obtained from full-wave simulations in IE3D. (a) First resonant frequency and (b) Second resonant frequency.

only choosing the appropriate location and length of the open circuited microstrip line (L_s and L_m as shown in Figure 4.5). This feeding mechanism is very well known and is comprehensively studied in [91, 92, 93] and their references. Using full-wave simulations in IE3D [82], better approximations for the resonant frequencies of the first and second bands of the loaded slot antenna (for different values of ω, C, and ℓ_1) can be obtained. Figures 4.3(a) and 4.3(b) show the frequencies of the first and second resonances of a straight slot antenna with an overall length of $\ell = 60$ mm and a slot width of $w = 2$ mm, which is printed on a 0.5 mm thick substrate with $\epsilon_r = 3.4$. This antenna is fed with a 50 Ω microstrip line with $L_s = 6$ mm and $L_m = 6$ mm. As can be seen from this figure, the first and second resonances of this antenna, without a capacitor, occur at 2 GHz and 4 GHz, respectively. As C is increased, the frequencies of both of these resonances decrease. However, this decrease is a function of ℓ_1. For $\ell_1 = 2.5$ mm, and $0 \leq C \leq 2$ pF, the decrease in the frequency of the first resonance

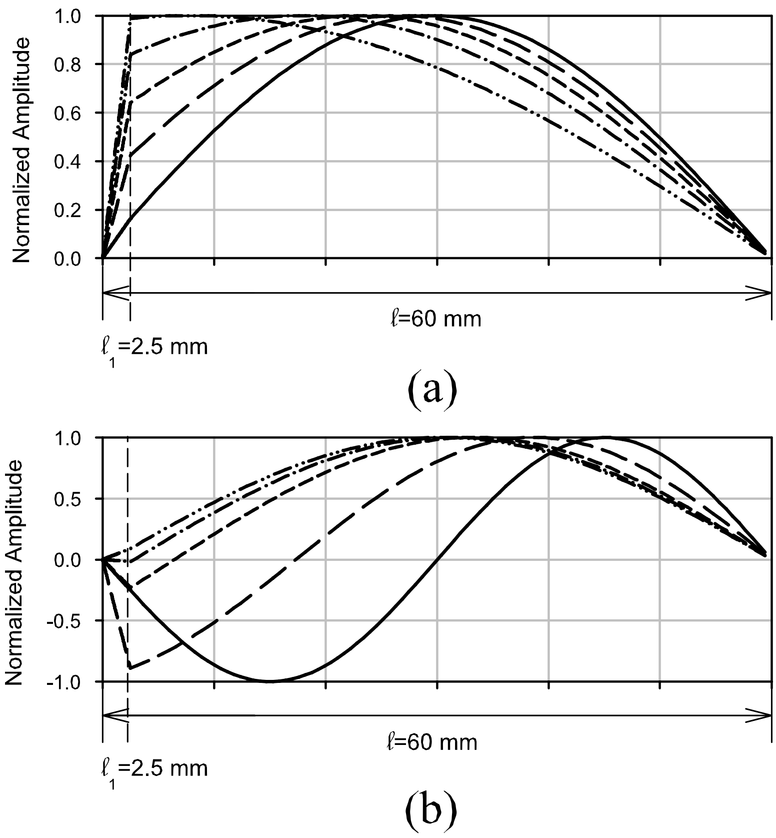

Figure 4.4: Electric field distribution of a loaded slot antenna at (a) first and (b) second resonant frequencies. The antenna has $\ell = 60$ mm, $w = 2$ mm, $\ell_1 = 2.5$ mm, $\epsilon_r = 3.4$, and substrate thickness of 0.5 mm. Solid: $C = 0$ pF, Long-dashed: $C = 1$ pF, Short-dashed: $C = 2$ pF, Dash-dot: $C = 3$ pF, and Dash-dot-dot: $C = 5$ pF.

is much smaller than that of the second one (see Figure 4.3(a) and 4.3(b)). This suggests that a dual-band antenna, with a relatively constant f_1 and variable f_2, can be designed by only changing the value of C.

The radiation patterns of the antenna at the two bands are determined by the electric field distribution across the slot at the first and second resonances. The electric field distribution in the presence of the capacitor cannot easily be obtained from full-wave simulations. However, by using the equivalent model of Figure 4.1 and solving the Maxwell's equations for the voltages and currents of the transmission line, in conjunction with the boundary conditions at $z = 0$, $z = \ell_1$, and $z = l$, the following expression for the normalized voltage (electric field) distribution across the transmission line (slot antenna) can be obtained:

$$V(z) = \begin{cases} \frac{\sin(\beta(l-\ell_1))}{\sin(\beta\ell_1)} \sin(\beta z) & z \leq \ell_1 \\ \sin(\beta(l-z)) & z > \ell_1 \end{cases}$$

In this equation the effect of the microstrip feed on the current distribution is ignored. However, examining it for different values of capacitance provides significant intuition in the operation of the antenna and its radiation patterns at both bands of operation. Figures 4.4(a) and 4.4(b) show the normalized electric field distribution across a straight slot antenna with $\ell = 60$ mm, $w = 2$ mm, and $\ell_1 = 2.5$ mm for different values of C. As can be seen in Figure 4.4(b), the electric field distribution at the second resonance, when there is no capacitance, is antisymmetric and therefore the radiation pattern of this mode will have a null at bore-sight. This is significantly different from the radiation pattern of the first mode, which has maximum directivity at its bore-sight. In order to circumvent this problem and obtain a dual-band antenna with similar radiation patterns at both bands, the slot topology of Figure 4.5 is used. In this case, the straight slot antenna is bent such that the longer (including the 7 mm bend) and shorter arms of the slot antenna are respectively $0.7\lambda_2$ and $0.3\lambda_2$ long at the second resonant frequency (λ_2 is the guided wavelength of the unloaded slot at the second resonant). The antenna shown in Figure 4.5 still has the same model given in Figure 4.1 and has the electric field distributions shown in Figures 4.4(a) and 4.4(b). By bending the slot as shown in Figure 4.5, the magnetic current at the lower section of the slot antenna is forced to flow in opposite direction relative to the current in the upper (longer) section of the slot antenna. If the length of the lower slot is at least $\lambda_2/4$ at the second resonant frequency, when the antenna is not loaded, these two oppositely directed currents have almost the same current distribution (as can be seen from Figure 4.4(b)) with a 180° phase difference caused by bending the slot. Therefore, the part of the antenna to the left of the dashed line (see Figure 4.5)

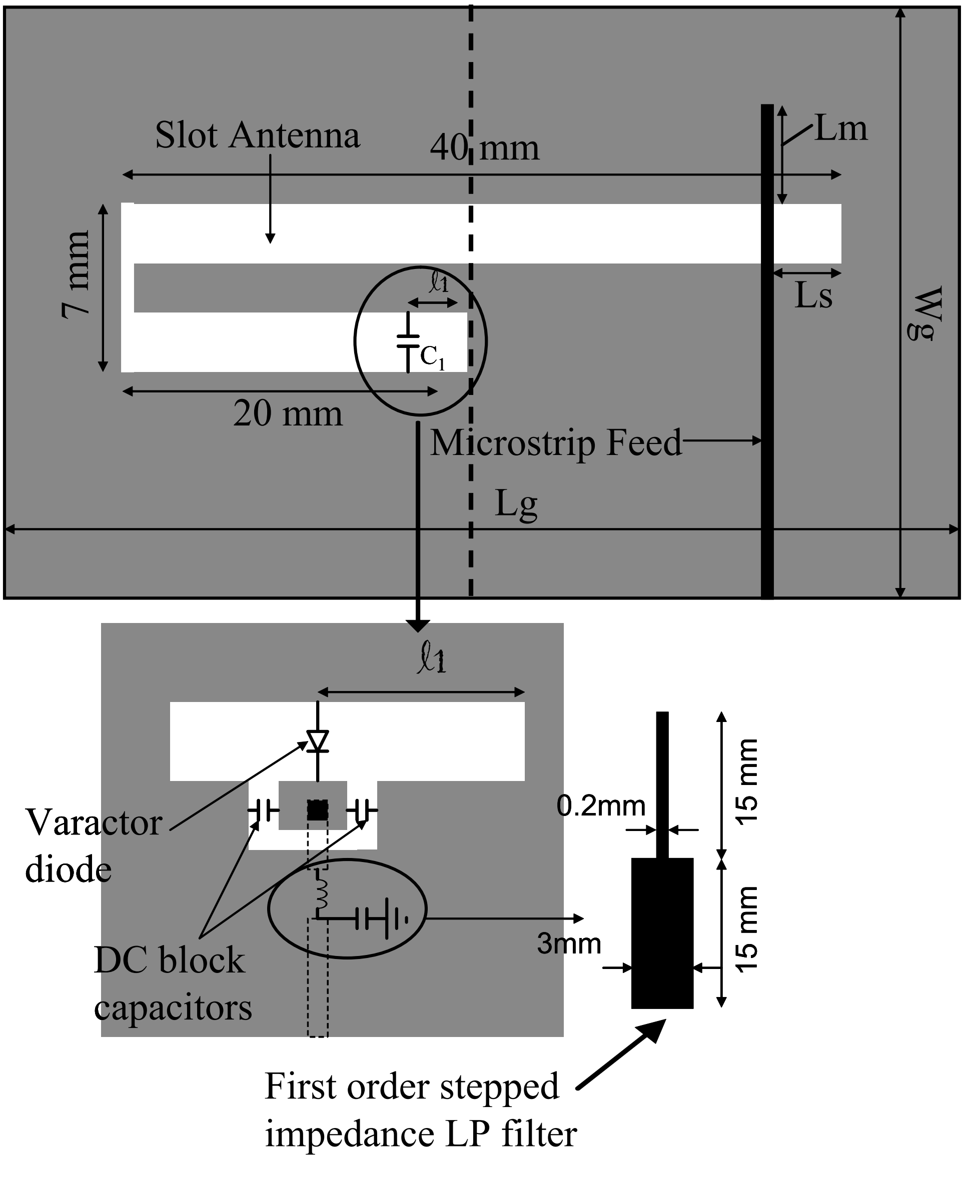

Figure 4.5: Topology of the reconfigurable dual-band slot antenna of Section 4.1.

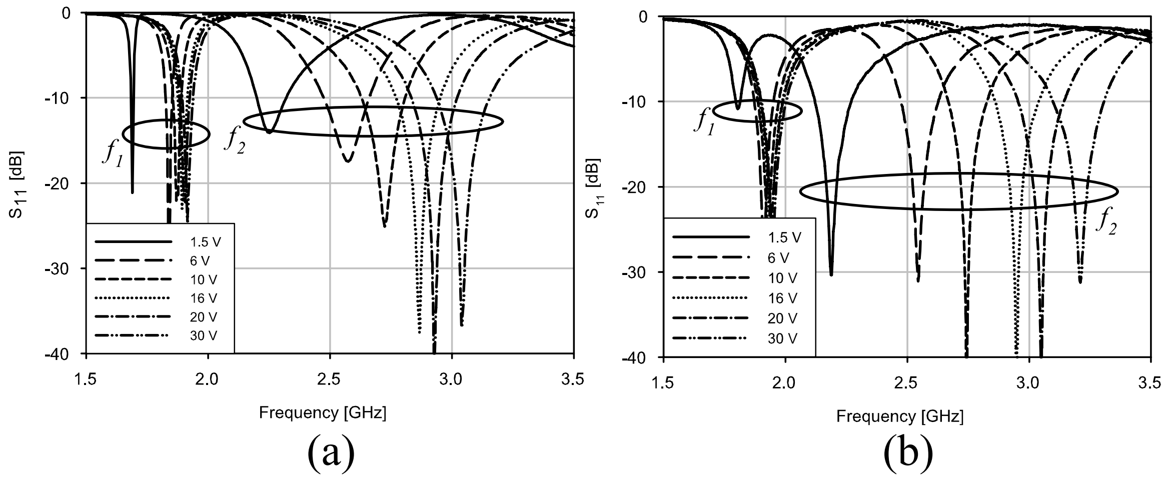

Figure 4.6: S_{11} of the dual-band reconfigurable slot antenna of Section 4.1 for different bias voltages. (a) Simulation and (b) Measurement.

does not significantly contribute to the far field radiation of the second band. In this case, the radiation comes only from that part of the slot antenna to the right of the dashed line, which has an electric field distribution similar to that of the first mode. At the first resonance, however, the magnetic currents of the lower part and upper part have different magnitudes; therefore, they do not completely cancel each other. Nevertheless, this somewhat reduces the radiation efficiency of the antenna and can be viewed as a tradeoff for having similar radiation patterns at both bands of operation. In this case, the overall effective length of the lower slot is chosen to be slightly larger than $\lambda_2/4$. This length is optimized, using full wave simulations in IE3D, to ensure that the antenna will have similar radiation patterns at both bands, when the effects of the microstrip feed and the loading capacitors are considered. In the next section, simulation and measurement results of the antenna are presented and discussed.

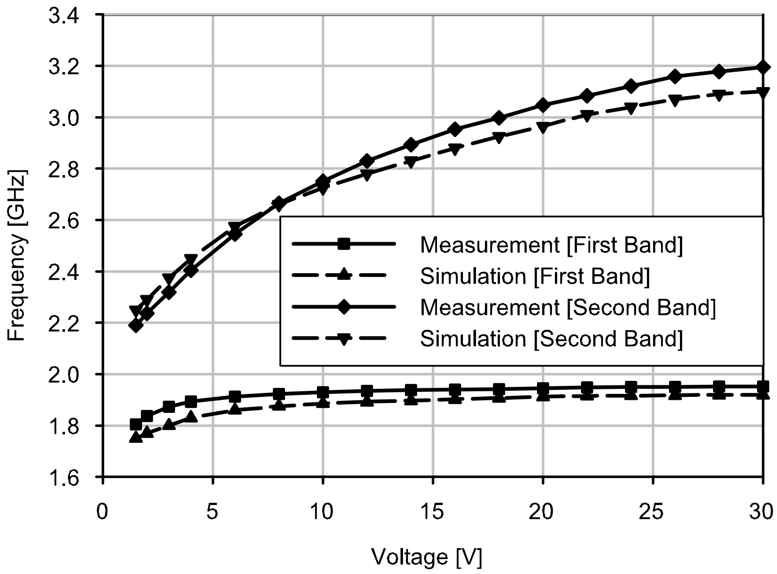

Figure 4.7: Comparison between the measured and simulated operating frequencies of the first and second bands of the dual-band reconfigurable slot antenna of Section 4.1.

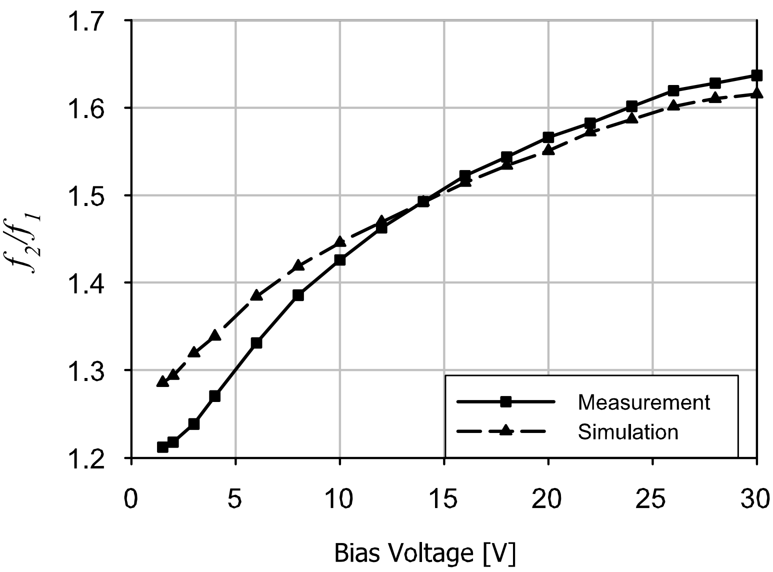

Figure 4.8: Simulated and measured frequency ratio (f_2/f_1) of the reconfigurable slot antenna of Section 4.1 as a function of applied DC bias voltage.

Parameter	L_g	W_g	L_s	L_m
Value	12.0 cm	10.0 cm	6.0 mm	6.0 mm
Parameter	f_2/f_1 range	RF/DC isolation	V_{DC}	Capacitance range
Value	$1.2 - 1.65$	Min. of 24 dB	1.5 V$-$30 V	0.5 pF$-$2.2 pF

Table 4.1: Physical and electrical parameters of the dual-band reconfigurable slot antenna.

4.2 Simulation, Fabrication, and Measurement of The Reconfigurable Dual-Band Antenna

4.2.1 Simulation and Measurement Results

The bias network of the varactor used in tuning the antenna is shown in Figure 4.5. The DC bias voltage is isolated from the RF by cutting the ground plane around the varactor cathode. The RF connectivity around the slot antenna is achieved using two large capacitors that connect the cathode path to the surrounding ground plane. The antenna is fed with an off-centered microstrip line and the length of the open circuited line, L_m, and its position, L_s, are tuned to obtain good simultaneous match at both bands. The antenna is designed to operate on a 0.5 mm thick RO4350B substrate with $\epsilon_r = 3.4$, tan $\delta = 0.003$, and ground plane size of 12 cm $\times$ 10 cm (Table 7.1). A high quality varactor manufactured by Metelics (SODT 3001) with a tuning range of 0.5 pF to 2.2 pF for 30 V $\geq V_{DC} \geq 0$ V is used. In order to improve the DC/RF isolation, a first order low pass filter is placed in the path of the DC bias line. The filter is implemented using stepped impedance microstrip lines with a rejection band covering the frequency range of 1.5 GHz to 4 GHz, which covers the entire band of operation of the antenna.

The antenna is then simulated using IE3D, which is a full-wave simulation tool based on the method of moments [82], and its input reflection coefficient and radiation patterns are studied for various different capacitance values. The antenna

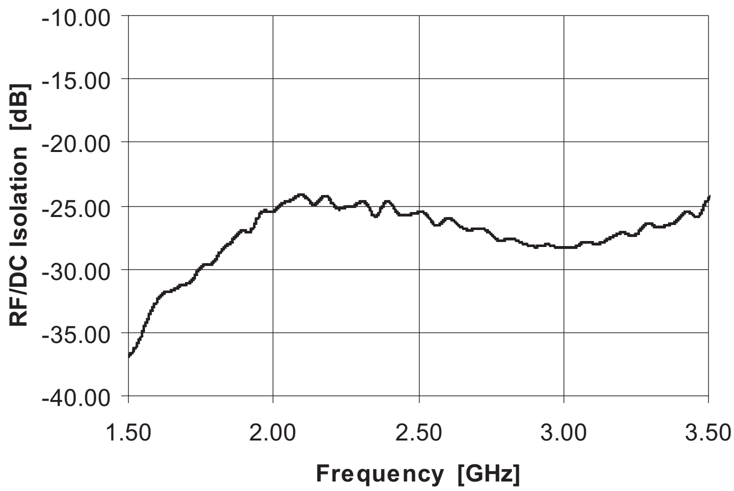

Figure 4.9: Measured RF to DC isolation of the dual-band reconfigurable slot antenna of Section 4.1.

is then fabricated on the same 12 cm $\times$ 10 cm, RO4350B substrate and its S_{11} spectral response is measured using a calibrated vector network analyzer. The simulated and measured S_{11} of this antenna, for different bias voltages, are presented in Figures 4.6(a) and 4.6(b), respectively. The simulation results indicate that good simultaneous impedance match at both bands can be obtained by just choosing the appropriate values of L_s and L_m (Figure 4.5). Figure 4.6(b) shows that by increasing the DC bias voltage from 1.5 V to 30 V, the frequency of the first resonance is increased from 1.8 GHz to 1.95 GHz. However, this change is fast for small values of bias voltage and exhibits a saturation behavior for bias voltage values beyond 6 Volts. On the other hand the resonant frequency of the second band increases from 2.15 GHz to 3.22 GHz in a rather smooth fashion. In order to compare the measurement and simulation results more easily, the simulated and measured values of the operating frequencies of the antenna are presented in Figure 4.7 as a function of the applied DC bias voltage of the varactor. The maximum error between the predicted and measured values of the operating frequencies is 3.6% and 3% for the first and second bands, respectively. The discrepancies between the two results can mostly be attributed to the inaccuracies in the fabrication process (alignment errors), uncertainties in the

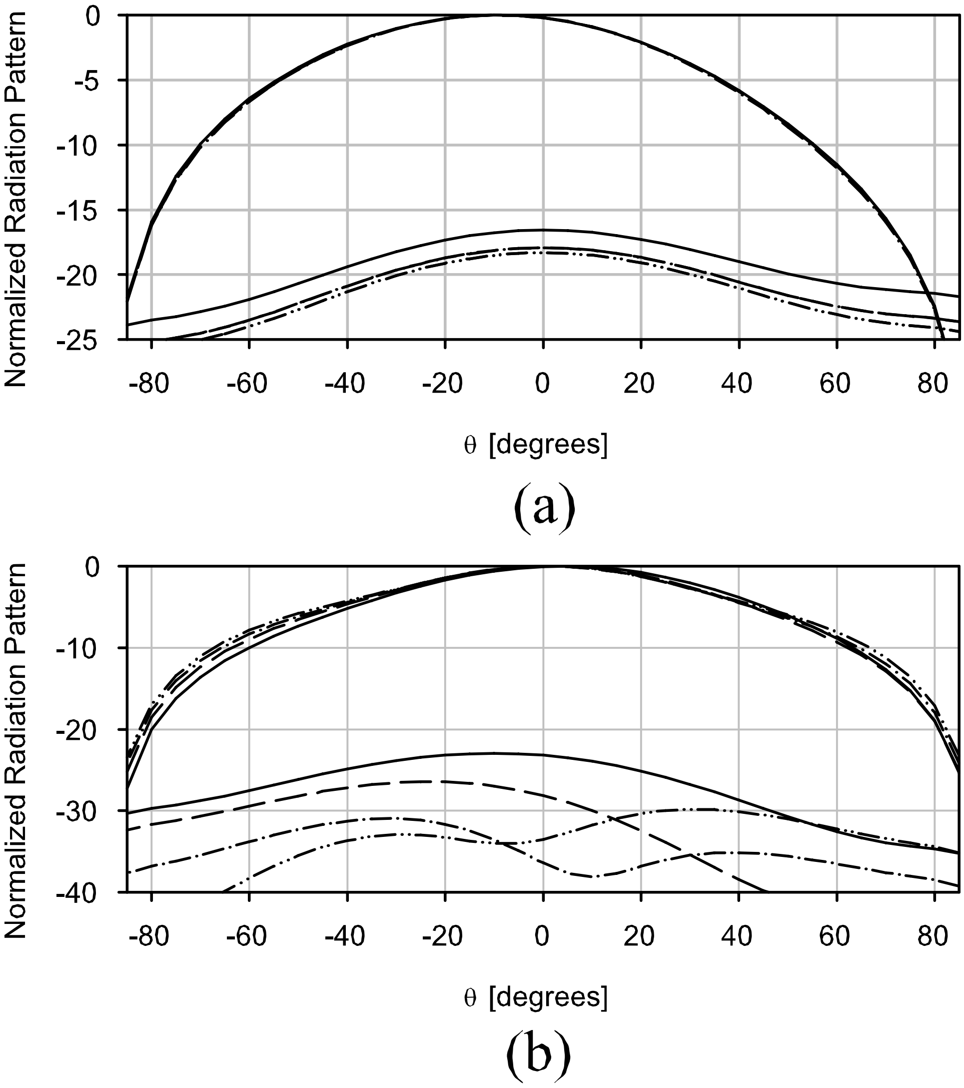

Figure 4.10: Simulation results for the E-Plane co- and cross-polarized radiation patterns of the dual-band slot antenna of Section 4.1 at (a) First band and (b) second band. Solid line: $V_{DC} = 4$ V, Dash-dash: $V_{DC} = 10$ V, Dash-dot: $V_{DC} = 20$ V, and Dash-dot-dot: $V_{DC} = 30$ V.

exact permittivity of the substrate (±3% error specified by the manufacturer), uncertainties in the capacitance values of the varactor diode, and numerical errors in the simulation results. Nevertheless, a good agreement between the simulation and measurement, with a maximum error of 3.6%, is observed.

Figure 4.8 shows the measured and simulated frequency ratios of the antenna as a function of the applied DC bias voltage to the varactor. It is observed that by changing the bias voltage from 1.5 V to 30 V the frequency ratio (f_2/f_1) can continuously be tuned from 1.2 to 1.65. For bias voltage values below 1.5 V, simultaneous matching at both bands cannot easily be obtained. However, for $V_{DC} > 1.5$ V a very good simultaneous match is obtained by only choosing the length of the open circuited microstrip line, L_m, and its location, L_s, appropriately [91, 92, 93]. The RF to DC isolation of the antenna is also measured using a VNA and is shown in Figure 4.9. The RF to DC port isolation of better than 24 dB across the entire band of operation is demonstrated.

The radiation patterns of the antenna, for bias voltages of $V_{DC} = 4$ V, 10 V, 20 V, and 30 V, are simulated in IE3D and the simulated patterns in the E- and H-Planes are presented in Figures 4.10 and 4.12, respectively. The radiation patterns of the antenna, for the same DC bias voltages, are also measured in the anechoic chamber of the University of Michigan and are presented in Figures 4.11 and 4.13. Since the antenna is bi-directional and is almost symmetric with respect to the plane containing it, the fields in the lower half-space are similar to those in the upper half-space. Therefore, only the pattern plots in the range of $0° < \theta < 90°$ are shown.

Figures 4.10(a) and 4.10(b) show the simulated co- and cross-polarized radiation patterns of the antenna in E-Plane for the first and second bands respectively. It is observed that the antenna has similar radiation patterns at both bands and the shape of the pattern in this plane does not strongly depend on the applied bias voltage. Figures 4.11(a) and 4.11(b) show the measured co- and cross-polarized radiation

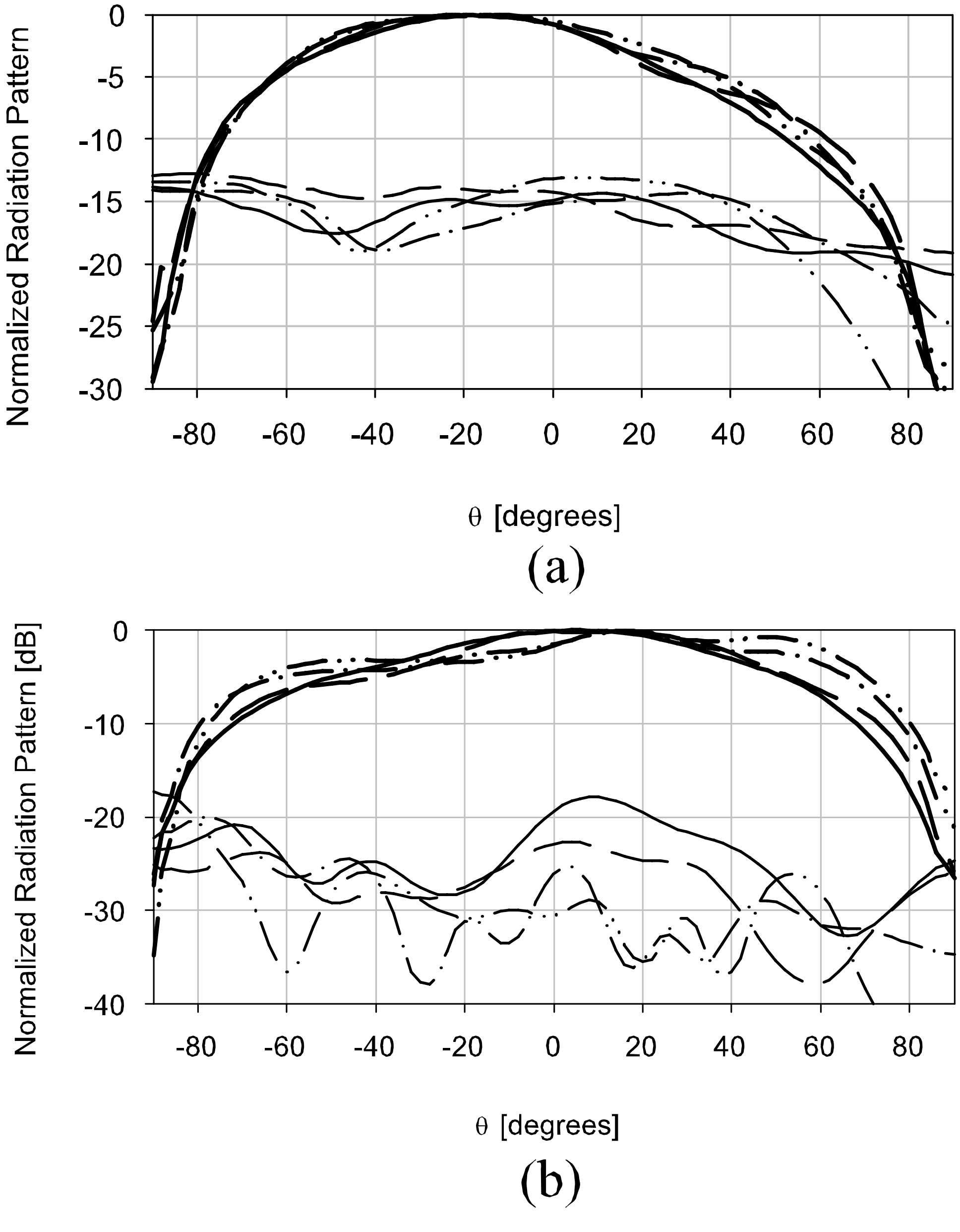

Figure 4.11: Measured E-Plane co- and cross-polarized radiation patterns of the dual-band slot antenna of Section 4.1 at (a) First band and (b) second band. Solid line: $V_{DC} = 4$ V, Dash-dash: $V_{DC} = 10$ V, Dash-dot: $V_{DC} = 20$ V, and Dash-dot-dot: $V_{DC} = 30$ V.

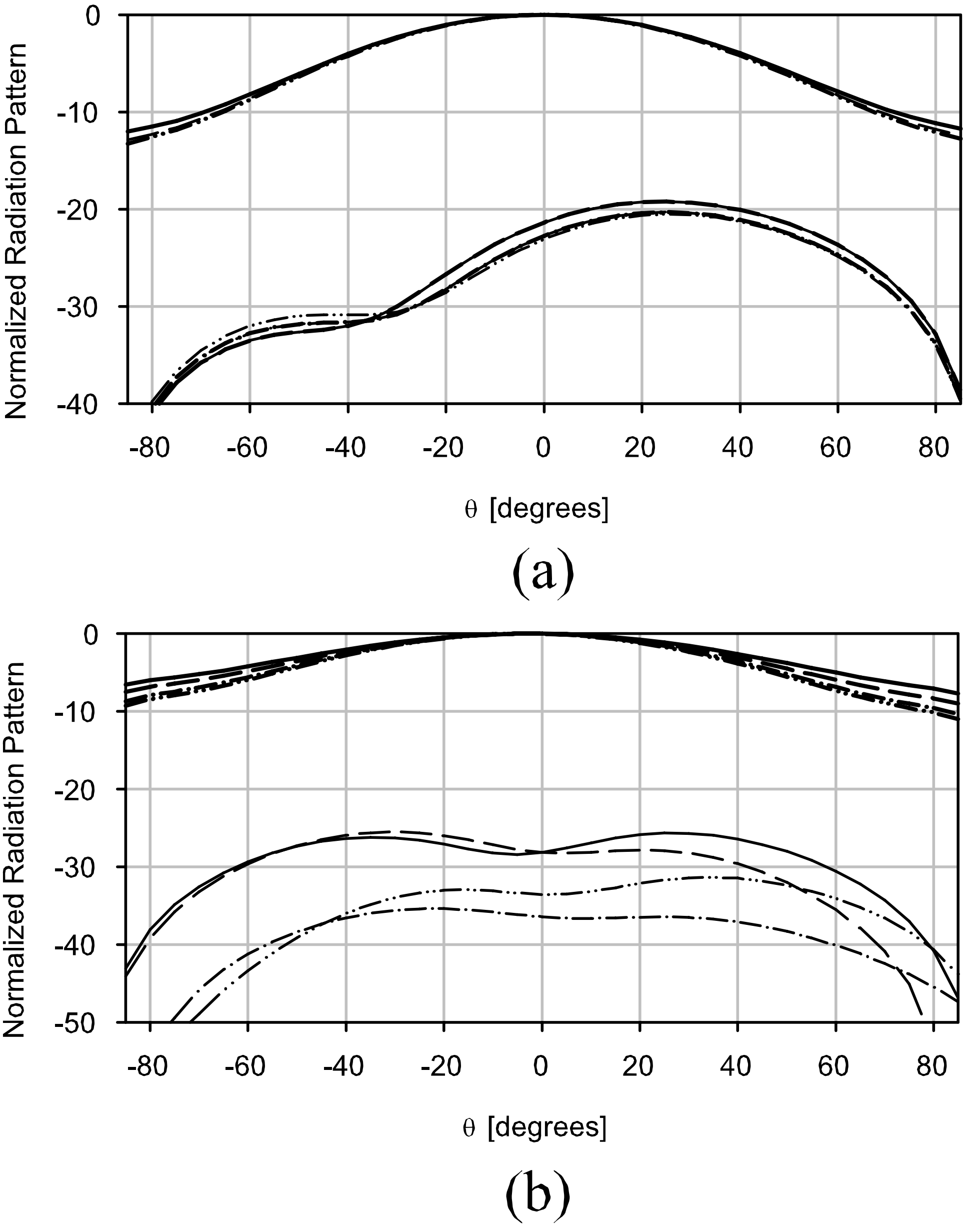

Figure 4.12: Simulated H-Plane co- and cross-polarized radiation patterns of the dual-band slot antenna of Section 4.1 at (a) First band and (b) second band. Solid line: $V_{DC} = 4$ V, Dash-dash: $V_{DC} = 10$ V, Dash-dot: $V_{DC} = 20$ V, and Dash-dot-dot: $V_{DC} = 30$ V.

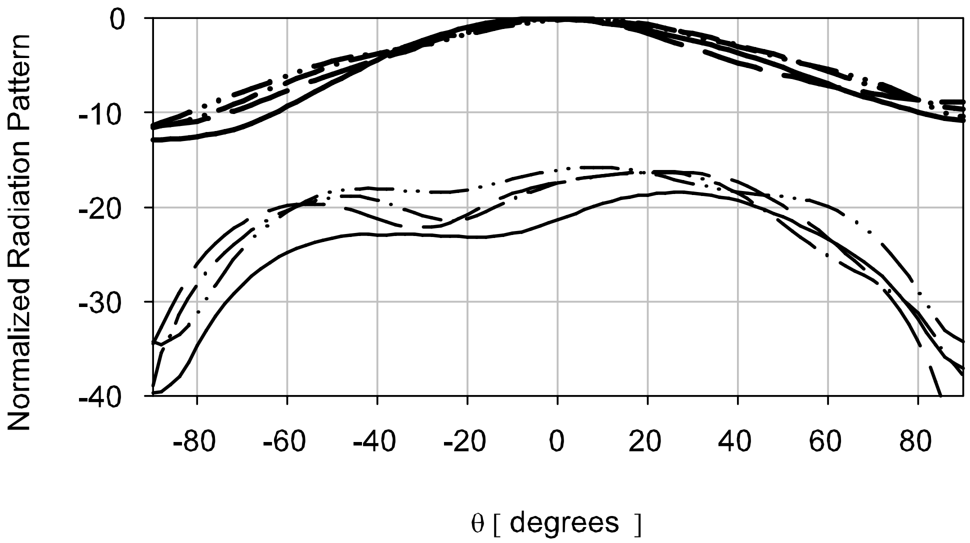

(a)

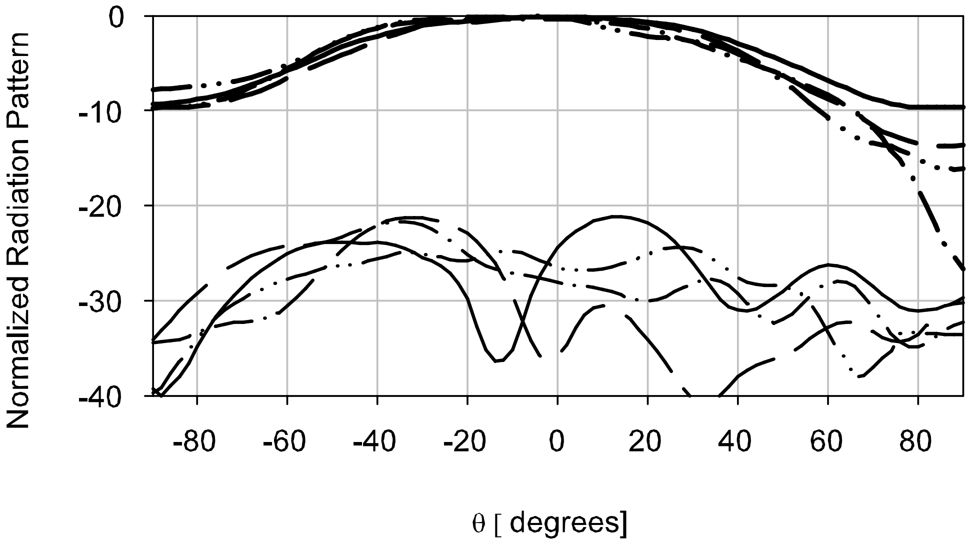

(b)

Figure 4.13: Measured H-Plane co- and cross-polarized radiation patterns of the dual-band slot antenna of Section 4.1 at (a) First band and (b) second band. Solid line: $V_{DC} = 4$ V, Dash-dash: $V_{DC} = 10$ V, Dash-dot: $V_{DC} = 20$ V, and Dash-dot-dot: $V_{DC} = 30$ V.

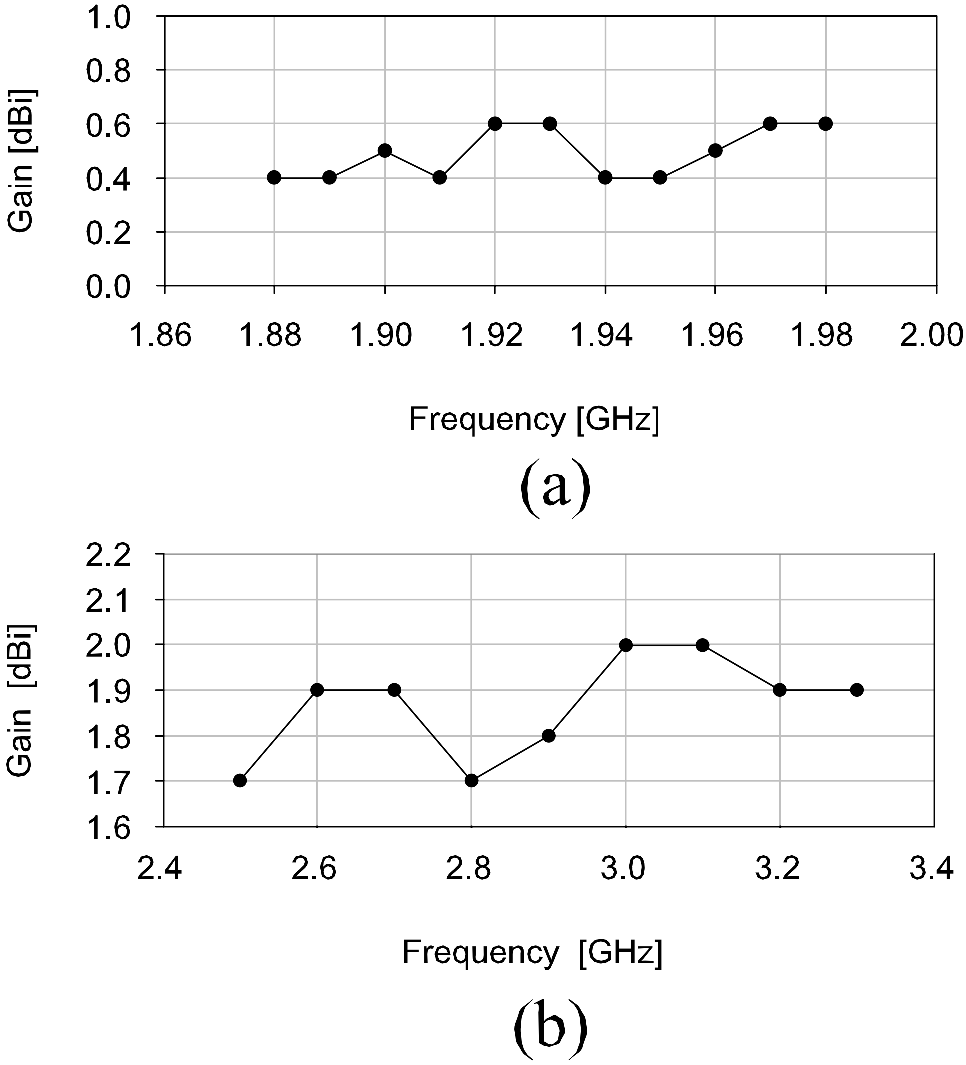

Figure 4.14: Measured gain of the dual-band reconfigurable slot antenna of Section 4.1. (a) First band and (b) Second band.

patterns of the antenna in the E-Plane for the first and second bands, respectively. The measurement results also indicate that the antenna has similar patterns at both bands. Furthermore, low levels of cross polarized radiation are observed. The cross polarization levels are, however, larger in the first band due to the larger values of the electric field magnitude at the bent section. The simulated and measured radiation patterns in the H-Plane are presented in Figures 4.12 and 4.13 respectively. Figure 4.12(a) and 4.12(b) show the simulated H-Plane pattern of the antenna at the two bands, for different DC bias voltage values. Similar radiation patterns at both bands and for different bias voltage values are observed. Figure 4.13(a) and 4.13(b) show the measured H-Plane radiation patterns of the antenna for the first and second bands. It is observed that the radiation patterns of the antenna, in the H-Plane, are also similar to each other for both frequency bands and for different bias voltages. Comparison of the simulated radiation patterns of Figures 4.10 and 4.12 with the measured radiation patterns of Figures 4.11 and 4.13 shows that the co-polarized simulated and measured radiation patterns are in a relatively good agreement with each other whereas the cross-polarized components are not. The discrepancies between the simulation and measurement radiation patterns can be attributed to the presence of the coaxial cables and connectors, which feed the antenna and bias the varactor diode, in close proximity to the antenna during the pattern measurements. The induced currents on these components radiate and distort both the co-polarized and the cross-polarized components of the radiation patterns of the antenna. Since the cross-polarized component generated by the antenna is much weaker than its co-polarized component, the distortions caused by the cables and connectors completely change the shape of the cross-pol pattern but only moderately affect the co-pol component.

The gain of the antenna is also measured across the entire band of operation using a double-ridged horn as a reference and is shown in Figure 4.14. The antenna shows an

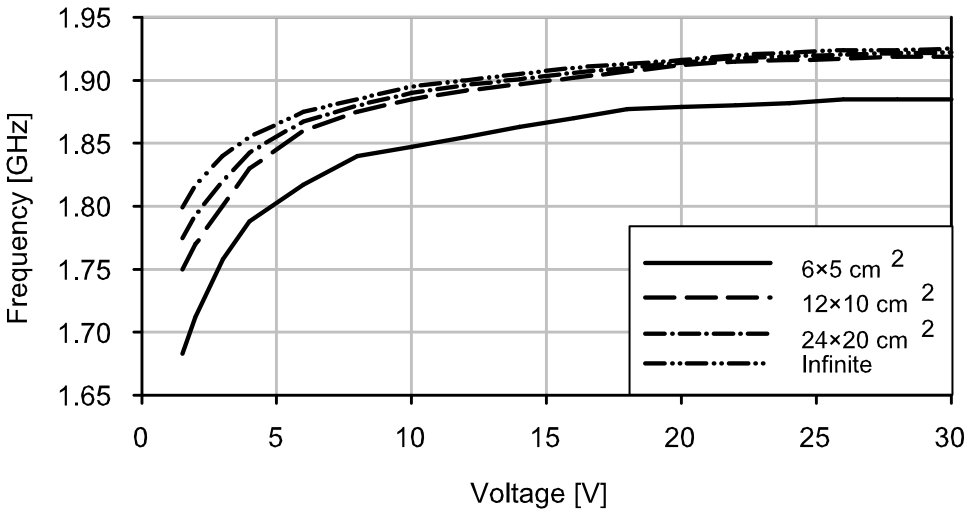

(a)

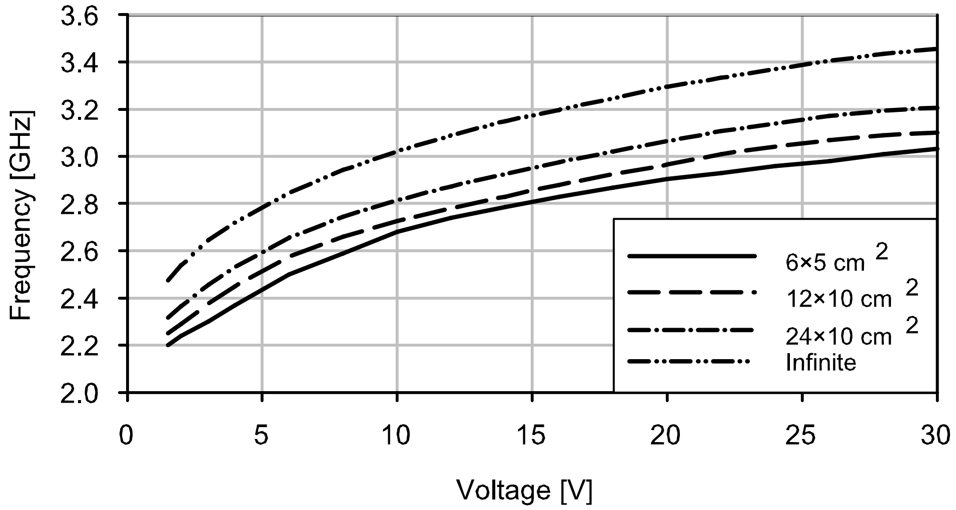

(b)

Figure 4.15: Simulated results of the operating frequencies of the dual-band reconfigurable slot antenna, shown in Figure 4.5, as a function of the varactor bias voltage for different ground plane sizes. (a) First band and (b) Second band.

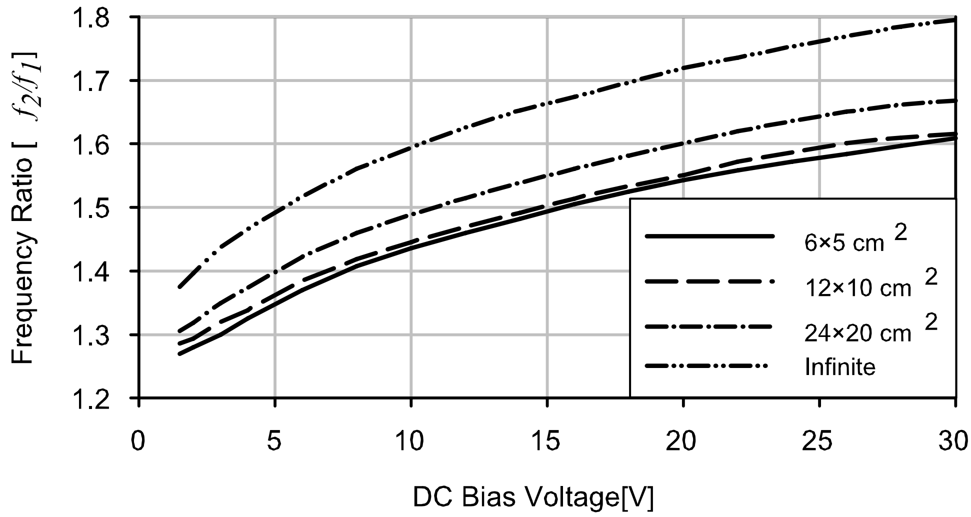

Figure 4.16: Simulated results of the frequency ratios (f_2/f_1) of the dual-band reconfigurable slot antenna, shown in Figure 4.5, as a function of the varactor bias voltage for different ground plane sizes.

average 0.5 dBi gain at the first band and 1.8 dBi gain at the second band of operation in the direction of maximum radiation. The lower gain of the first band is caused by the smaller electrical dimensions of the antenna at this band. The lower bound of the efficiency of the antenna can be calculated using the measured gain values of the loaded antenna and simulated directivity values for an unloaded antenna. Based on this calculation, the lower bound efficiency of 70% and 85% for the first and second bands are calculated. The major factor that contributes to the reduced efficiency of the antenna is its topology and the reduction of its electrical size that occurs as a result of capacitive loading [1]. Nevertheless, as these lower bound values indicate, the antenna radiates rather efficiently.

4.2.2 Finite Ground Plane Effects

The dimensions of the ground plane of a slot antenna affect its electrical and radiation parameters such as the radiation pattern, resonant frequency, and the gain of the antenna. For a single band slot antenna, these effects have extensively been studied in the literature [76, 94, 95, 96, 97, 98, 99]. The effects of the finite ground plane size on the radiation patterns of a slot antenna are examined in [94, 95]. In [94], the edge diffractions of surface waves in a slot antenna are modeled and it is shown that these diffractions cause ripples in antenna's radiation patterns. In [96], the effects of finite ground plane size on bandwidth and gain of a U-shaped slot antenna are studied. The effects of the finite ground plane on the input matching and radiation parameters of a microstrip-fed, cavity-backed slot antenna are examined in [99]. In [76], [97], and [98], the effects of the ground plane dimensions on the gain and bandwidth of electrically small slot antennas are examined. It is shown that as the ground plane dimensions are increased, the antenna gain increases and approaches the gain of the antenna with an infinitely large ground plane size.

Since the effects of finite ground plane size on the radiation patterns and the gain of slot antennas are well known, in this chapter we only examine the effects of the finite ground plane size on the resonant frequencies and frequency ratios of the dual-band reconfigurable slot antenna of Section 4.1. In order to do this, full-wave simulations have been performed on the antenna shown in Figure 4.5 for four different ground plane sizes of 6 cm $\times$ 5 cm, 12 cm $\times$ 10 cm, 24 cm $\times$ 20 cm, and ∞. Figures 4.15(a) and 4.15(b) show the effect of the ground plane size on the frequencies of the first and second bands of the dual-band antenna. As is observed from this figure, for fixed antenna and feed network dimensions, the resonant frequencies of both the first and second bands increase as the ground plane size increases and approach the resonant frequencies of the antenna with an infinitely large ground plane. Figure 4.16 shows the effect of the ground plane size on the frequency ratio of the second band to that of the first band of the tunable antenna. Similar to the previous case, for fixed antenna dimensions and bias voltage, the frequency ratio increases as the ground plane size increases. As can be observed from Figures 4.15 and 4.16, the ground plane size moderately affects the frequency response of the antenna. However, these effects can be taken into account in the simulation process and a very good agreement between the measurement and simulation results can be obtained as shown in Section 4.2.1.

4.3 Conclusions

A new technique for designing dual-band reconfigurable slot antennas is proposed. The technique is successfully applied to design a dual-band slot antenna with similar radiation patterns at both bands. Measurement results of the antenna indicate that it has a frequency ratio (f_2/f_1) that continuously increases from 1.2 to 1.65 by increasing its DC bias voltage from 1.5 V to 30 V. Furthermore, good simultaneous impedance match is observed at both bands of operation for the entire range of applied DC bias voltages, low levels of cross-polarized radiation is observed, and the radiation patterns of each band remain practically unchanged as the DC bias voltage is changed.

CHAPTER 5

Dual-Band Reconfigurable Antenna With A Very Wide Tunability Range

Availability of different unlicensed frequency bands in the congested spectrum of electromagnetic (EM) waves, compatibility of wireless devices with different standards (i.e, GSM and CDMA), or interference reduction in a two-way radio system are typical reasons why many existing wireless systems make use of two different simultaneous frequency bands. Whatever the reason may be, this undoubtedly will add to the complexity of these systems. In particular, the RF circuitry and antennas must be designed to be able to operate at multiple frequency bands. Recent advancements in antenna technology, the availability of efficient computer aided design (CAD) tools, and the availability of fast and powerful computers have resulted in a variety of different techniques for designing low-profile, cost effective, and highly efficient multiple-frequency antennas [21, 44, 45, 46, 49, 50, 51, 52, 66]. Many of the techniques used for designing dual-band antennas make use of certain approaches to manipulate the current distribution of one of the higher order resonant modes of the structure to change its resonant frequency as well as current distribution. For example in [44], a rectangular patch antenna is modified by a slot insertion at a particular location in order to alter one resonant mode more than the other and achieve a dual-band operation. However, the range of achievable frequency ratios (f_R=f_2/f_1, the ratio of the frequency of operation of the second band, f_2, to that of the first one, f_1) for this technique is limited to $1.6 \leq f_R \leq 2$. This idea was later applied to circular and triangular patch antennas where frequency ratios of $1.3 \leq f_R \leq 1.4$ and $1.35 \leq f_R \leq 1.5$ were respectively achieved [45, 46]. Variations of these techniques with differently shaped slots and patches have also been investigated and discussed in detail in Chapter 4 of [21].

Slot antennas belong to another category of low-profile printed antennas that show higher efficiency and can provide multi-band operation. At the same time, the configuration and radiation characteristics of slot antennas appear to be more amenable to miniaturization and reconfigurability [97, 98, 100]. In particular, the uniplanar nature of these antennas allows for simple integration of active or passive lumped components into the topology of the antenna without the need for having via holes. Examples of different techniques that are used to design dual-band slot antennas are presented in [49, 50, 51, 52, 66]. In [49], a single-element dual-band CPW-fed slot antenna with similar radiation patterns at both bands is studied. In [50], a compact dual-band CPW-fed slot antenna, with a size reduction of about 60% compared to a conventional slot antenna, is studied. Other topologies have also been used to achieve dual- or multi-band operations. Examples of these include structures that make use of parasitic elements [51], multiple radiating elements [52], or create fictitious resonant modes [66]. These approaches, however, can only be used to design antennas that have fixed dual- or multi-band characteristics.

Electronic reconfigurability is usually achieved by incorporating switches, variable capacitors, phase shifters, or ferrite materials in the topology of the antenna [100, 101, 102, 103]. Most frequently, lumped components such as PIN diodes, varactor diodes, or MEMS switches or varactors are used in the design of reconfigurable antennas. These components may be used to electronically change the frequency response (e.g.,

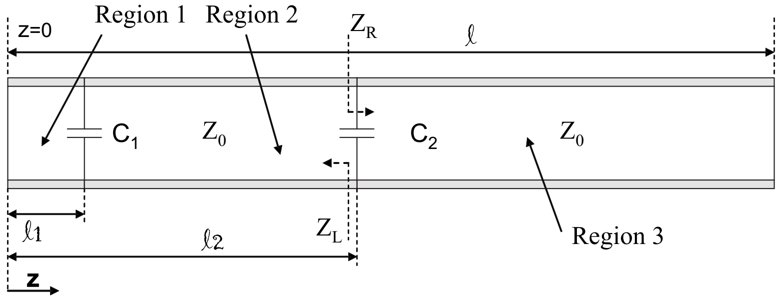

Figure 5.1: Transmission line model of a slot antenna loaded with two lumped capacitors.

see [100], [101], [102], and [103]), radiation patterns (e.g., see [104]), gain, or a combination of different radiation parameters of such antennas. In Chapter 4, a dual-band slot antenna was proposed that uses a single varactor to achieve tunability in only its second band of operation and has a fixed first band. The frequency ratio of this antenna can electronically be tuned from 1.2 to 1.65 (or equivalently 30% tunability). In this chapter, we use a similar approach to design a far more versatile dual-band antenna with a greatly enhanced tunability range. It is shown that by strategically placing two varactor diodes along a bent slot antenna, an agile dual-band tunable antenna can be achieved. In this design, the frequency of one of the bands (either f_1 or f_2) can be fixed at will and the frequency of the other band can continuously be tuned over a wide frequency range. Furthermore, if desired, the frequencies of both bands can simultaneously be tuned over a wide frequency range by changing the bias voltages of the varactors. Measurement results indicate that frequency ratios in the range of $1.3 \leq f_R \leq 2.67$ (more than one octave tunability) can be achieved. The antenna uses a simple feed structure and matching network to achieve excellent simultaneous impedance match at both frequencies of operation and over its entire tuning range. Furthermore, the antenna shows similar radiation patterns and polarization at both bands with low levels of cross-polarized radiation. Most importantly the radiation patterns of the antenna remain practically unchanged as its frequency response is tuned over the wide tunable frequency range of operation.

5.1 Loaded Slot Antennas For Dual-Band Operation

5.1.1 Resonant Frequencies of a Loaded Slot

A narrow slot antenna, at its first resonance, may be considered as a $\lambda/2$ transmission line short circuited at both ends [91]. Loading such a structure with two capacitors, as shown in Figure 5.1, increases the line capacitance at two points, and therefore, reduces the frequencies of its first and all higher order resonances. This reduction, however, is not uniform and depends on the locations of the capacitors, their values, and the slot line impedance. The transmission line equivalent circuit model shown in Figure 5.1 can be used to determine the resonant frequencies of this loaded slot antenna. Transverse resonant condition [105] requires that:

$$Z_R + Z_L = 0 \tag{5.1}$$

where Z_R and Z_L are the input impedances to the right and left of the reference point, as shown in Figure 5.1. In this case, Z_R and Z_L can simply be obtained from the following equations:

$$Z_R = \frac{\jmath Z_0 \tan(\theta - \theta_2)}{1 - \omega C_2 Z_0 \tan(\theta - \theta_2)} \tag{5.2}$$

$$Z_L = \jmath Z_0 \frac{\tan(\theta_1) + \tan(\theta_2 - \theta_1)[1 - \omega C_1 Z_0 \tan(\theta_1)]}{1 - \omega C_1 Z_0 \tan(\theta_1) - \tan(\theta_1)\tan(\theta_2 - \theta_1)} \tag{5.3}$$

$$\theta = \beta(\omega)\ell, \quad \theta_1 = \beta(\omega)\ell_1, \quad \theta_2 = \beta(\omega)\ell_2 \tag{5.4}$$

where $\beta(\omega)$ is the frequency-dependent propagation constant of the slot line. In addition to being a function of frequency, β is a function of the slot line width,

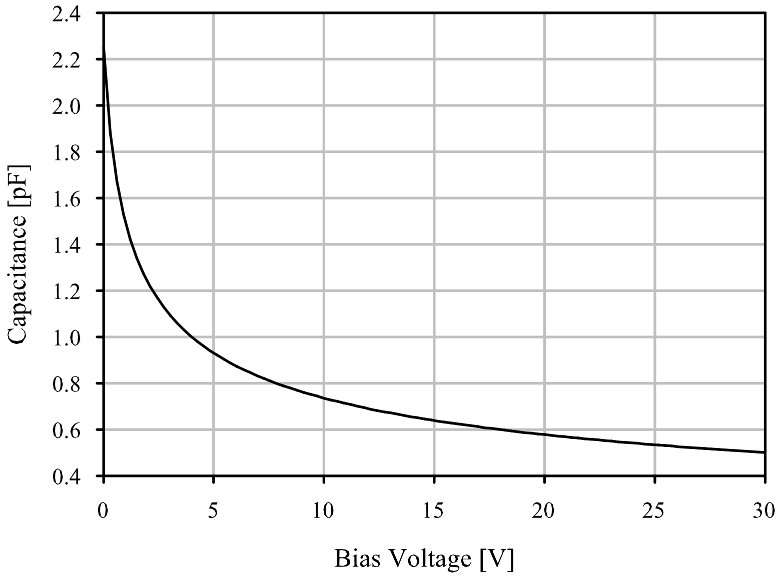

Figure 5.2: Typical capacitance of a SMTD3001 varactor (from Metelics Corp.) as a function of its bias voltage.

relative dielectric constant (ϵ_r), and thickness (h) of the substrate that the slot line is printed on, if any. $\beta(\omega)$ can easily be calculated from the expressions given in [83] and [106]. Using (5.2) and (5.3) in (5.1) an expression for the resonant condition of the loaded transmission line of Figure 5.1 can be achieved:

$$\begin{aligned} &\{\tan(\theta_1) + \tan(\theta_2)[1 - \omega C_1 Z_0 \tan(\theta_1)]\}(1 - \omega C_2 Z_0 \tan(\theta - \theta_2)) + \\ &\qquad \{1 - \omega C_1 Z_0 \tan(\theta_1) - \tan(\theta_2)\tan(\theta_1)\}\tan(\theta - \theta_2) = 0 \end{aligned} \tag{5.5}$$

The roots of this expression are the resonant frequencies of the loaded slot antenna shown in Figure 5.1. As is observed from (5.5), these resonant frequencies have explicit dependence to the variables ℓ_1, ℓ_2, C_1, and C_2. Therefore, by fixing one or more of these variables and changing the rest, the resonant frequencies of the slot antenna can be changed. In particular, if ℓ_1 and ℓ_2 are fixed, C_1 and C_2 can be tuned electronically (by using varactor diodes) to achieve a dual-band reconfigurable antenna. Here C_1 and C_2 are replaced by two identical SMTD3001 varactors from Metelics Corp. The varactors' capacitances vary from 2.25 pF to 0.5 pF as the bias voltage is increased

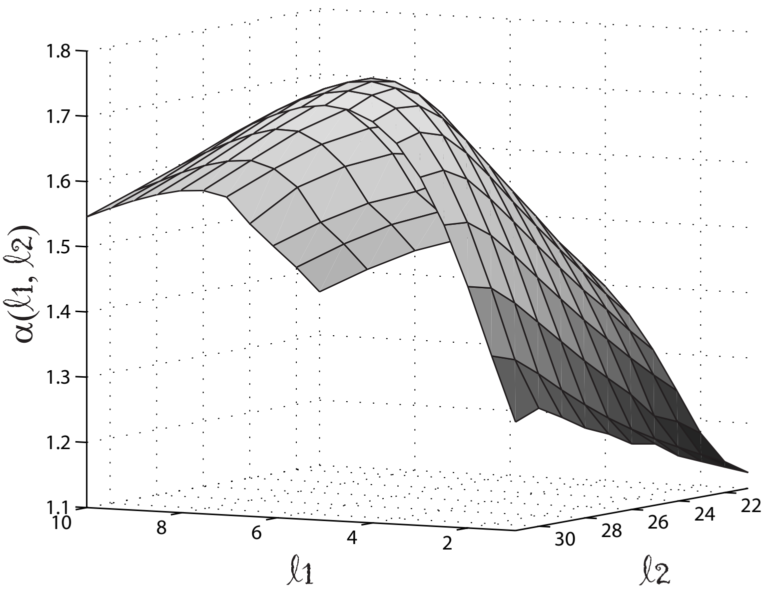

Figure 5.3: Calculated values of $\alpha = \max\{f_R(C_1, C_2)\}/\min\{f_R(C_1, C_2)\}$ for rectangular slot antenna with $\ell = 62$ mm and $w = 2$ mm loaded with two identical varactors with tuning range of 0.5 pF$\leq C_1, C_2 \leq 2.25$ pF. Here $f_R = f_2/f_1$ for a dual-band slot antenna loaded with two varactors located at a distance of ℓ_1 and ℓ_2 from one end.

from 0 V to 30 V (see Figure 5.2).

In this chapter, our goal is to maximize the tunability range of the antenna's frequency ratio (i.e. to maximize the tunability range of $f_R = f_2/f_1$) for a given set of varactors. In order to do that, (5.5) is solved for fixed values of ℓ_1 and ℓ_2 and different capacitor values in the range of 0.5 pF$\leq C_1, C_2 \leq 2.25$ pF to obtain $f_1(C_1, C_2)$ and $f_2(C_1, C_2)$. Once these values are obtained, $f_R(C_1, C_2) = f_2(C_1, C_2)/f_1(C_1, C_2)$ is calculated. In order to quantify the tunability range of f_R, for fixed varactor locations, the parameter $\alpha(\ell_1, \ell_2)$ is defined as follows:

$$\alpha(\ell_1, \ell_2) = \frac{\max\{f_R(C_1, C_2)\}}{\min\{f_R(C_1, C_2)\}}, \text{ for fixed } \ell_1 \text{ and } \ell_2. \tag{5.6}$$

This procedure is then repeated for different values of ℓ_1 and ℓ_2 to obtain $\alpha(\ell_1, \ell_2)$ for a range of ℓ_1 and ℓ_2 values. Once this function is obtained, the varactor locations along the slot, ℓ_1 and ℓ_2, are chosen to maximize α and consequently maximize the

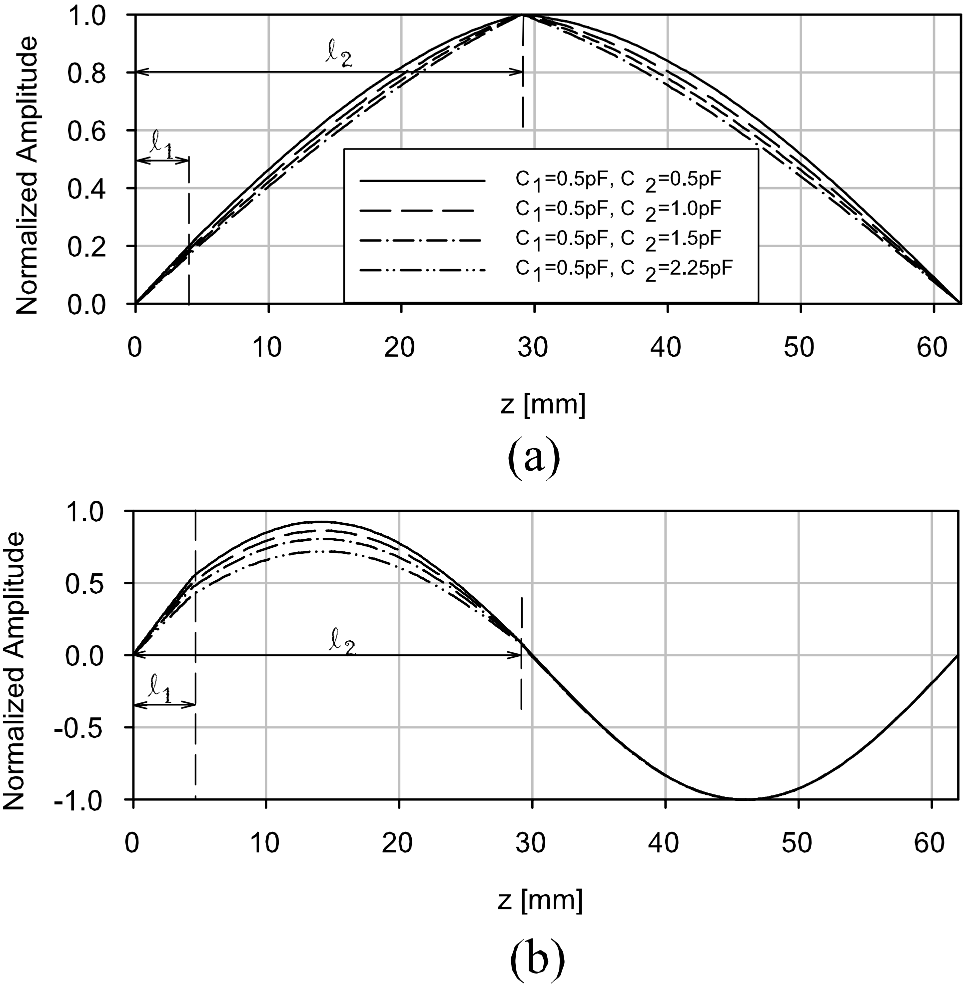

Figure 5.4: Voltage distribution across the slot line shown in Figure 5.1 for a fixed value of $C_1 = 0.5$ pF and different C_2 values. (a) First resonance and (b) Second resonance.

tunability range of f_R. This procedure is performed for a straight slot antenna with a length of $\ell = 62$ mm and width of $w = 1$ mm printed on a 0.5 mm thick substrate with dielectric constant of $\epsilon_R = 3.4$. The slot line characteristics impedance and frequency-dependent propagation constant ($\beta(\omega)$ and Z_0 in (5.4) and(5.5)) are calculated from the formulae given in [83] and [106]. Using the procedure mentioned in the preceding paragraph, $\alpha(\ell_1, \ell_2)$ is calculated for this particular slot antenna and is presented in Figure 5.3. It is observed that α clearly has a maximum that occurs for $\ell_1 = 4.5$ mm and $\ell_2 = 29$ mm.

It should be noted that solutions of (5.5) are only approximations of the real resonant frequencies of the actual antenna, since the effects of radiation from the slot antenna and more importantly the effects of the feed network parameters on the resonant frequency of the antenna are ignored. A more accurate method of predicting the actual resonant frequencies of the structure is to use full wave simulations. In this case, the effects of finite ground planes and dielectric substrates, radiation, and feed network parameters on the antenna's resonant frequencies can be taken into account. This is performed in Chapter 4 where both methods are used to predict the resonant frequencies of a similar slot antenna and the results are presented and compared. It is shown that despite the simplicity of the analytical method, the maximum error between its predicted resonant frequencies and those obtained from full-wave simulations remains below 8%.

5.1.2 Field Distribution Along the Loaded Slot Antenna

In addition to having a large tuning range for f_R, having consistent radiation patterns at both bands and over the entire tuning range is also of significant importance. The radiation patterns of a slot antenna are mainly determined by the electric field, i.e. voltage, distribution over the aperture. For an unloaded slot antenna, the electric field (magnetic current) distribution at the first and second resonance modes resemble that of a half sine wave and a full sine wave respectively. The symmetric field distribution at the first band results in a radiation pattern with maximum directivity at broadside whereas the anti-symmetric field distribution of the second band generates a pattern with a null at broadside. To mitigate this undesired characteristic, it is necessary to study the electric field distribution of the loaded slot antenna. The simple transmission line model of Figure 5.1 is sufficient to qualitatively study the field distribution. The voltages and currents in Regions 1, 2, and 3 can be expressed

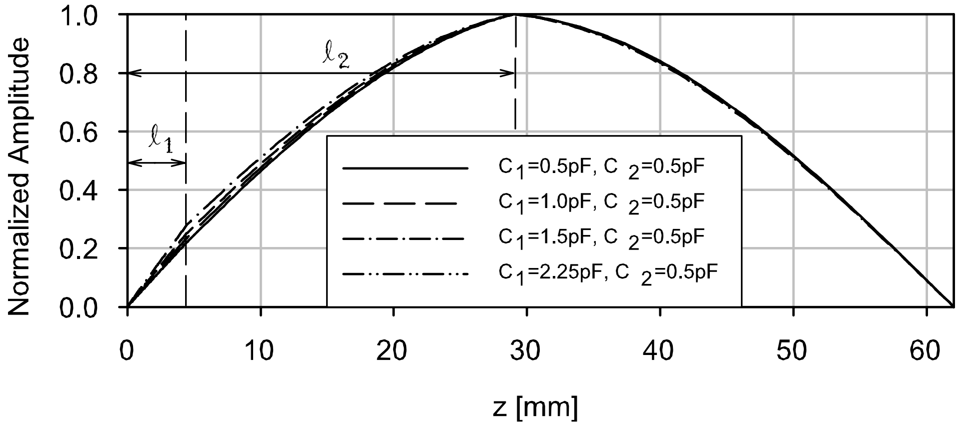

(a)

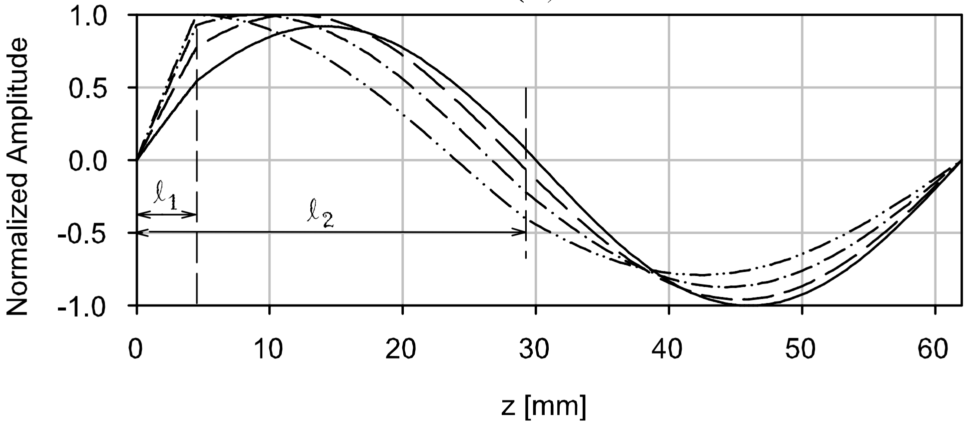

(b)

Figure 5.5: Voltage distribution across the slot line shown in Figure 5.1 for a fixed $C_2 = 0.5$ pF and different C_1 values. (a) First resonance and (b) Second resonance.

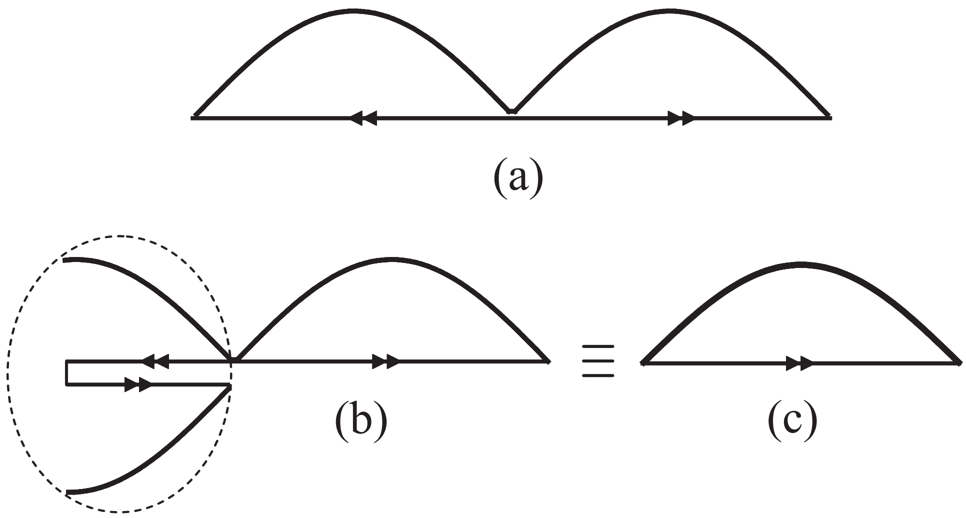

Figure 5.6: (a) Simple representation of the magnetic current distribution of a straight slot antenna at its second resonant mode. (b) Magnetic current distribution of the same slot at second resonant mode when it is bent $\lambda_2/4$ away from its edge will roughly be equivalent to (c) that of the first mode of a slot antenna that has half its length.

as [105]:

$$V_n(z) = V_n^+ \, e^{-\jmath\beta z} + V_n^- \, e^{\jmath\beta z} \tag{5.7}$$

$$I_n(z) = \frac{V_n^+}{Z_0} e^{-\jmath\beta z} - \frac{V_n^-}{Z_0} e^{\jmath\beta z} \tag{5.8}$$

where the subscript n refers to region 1, 2, or 3. The boundary conditions at $z = 0, \ell_1, \ell_2$, and ℓ require that:

$$V_1(0) = 0, V_1(\ell_1) = V_2(\ell_1) \tag{9-a}$$

$$V_2(\ell_2) = V_3(\ell_2), V_3(\ell) = 0 \tag{9-b}$$

$$I_1(\ell_1) = I_2(\ell_1) + \jmath\omega C_1 V_1(\ell_1) \tag{9-c}$$

$$I_2(\ell_2) = I_3(\ell_2) + \jmath\omega C_2 V_3(\ell_2) \tag{9-d}$$

Simultaneous solution of (5.7) and (5.8) subject to the boundary conditions of (9-a)-(9-d), yields the voltage distribution at the first and second resonances of the loaded

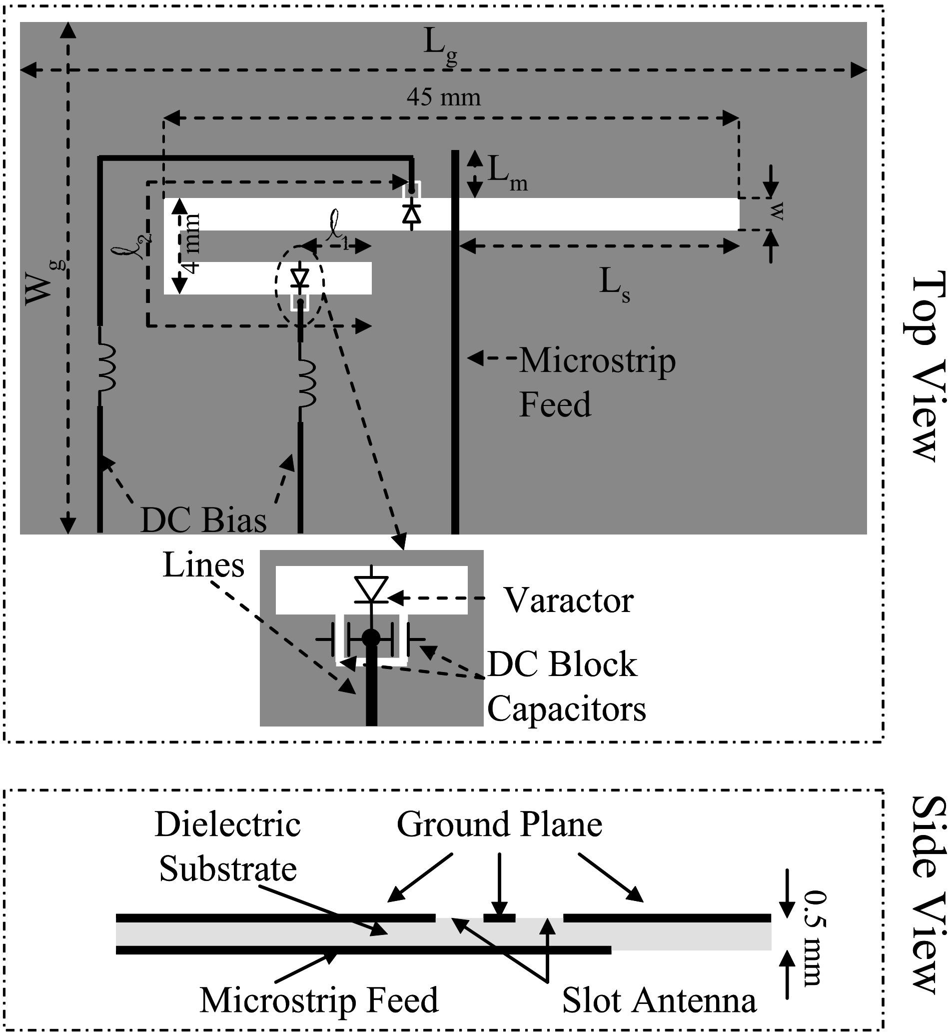

Figure 5.7: Schematic of the proposed dual-band bent slot antenna with two varactors.

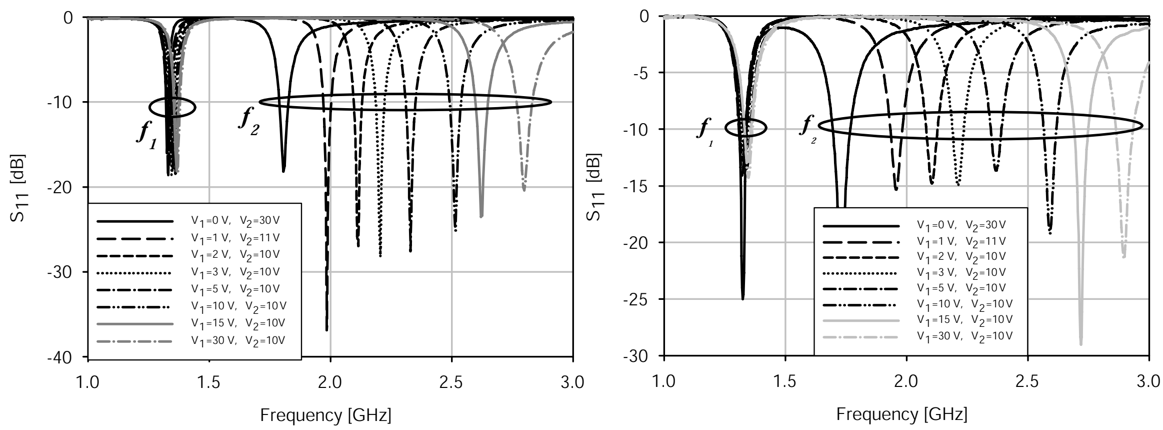

(a) (b)

Figure 5.8: (a) Simulated and (b) measured input reflection coefficients of the dual-band tunable antenna of Figure 5.7. In this example, the frequency of the first band is kept fixed while that of the second band is varied.

line. Figure 5.4 shows the slot antenna's voltage distribution at its first and second resonances for an antenna with $\ell = 62$ mm, $w = 1$ mm, $\ell_1 = 4.5$ mm, and $\ell_2 = 29$ mm printed on a 0.5 mm thick substrate with $\epsilon_r = 3.4$. In this figure, C_1 is fixed at 0.5 pF and C_2 is varied. Figure 5.5 shows the voltage distribution of the two bands for a fixed $C_2 = 0.5$ pF and different values of C_1. It is observed that the field distribution and the resonant frequency of the first mode is mainly affected by changes in C_2 whereas the field distribution and resonant frequency of the second mode is mainly affected by changes in C_1. Examining Figures 5.4(a) and 5.5(a) reveals that changing the values of the capacitors does not significantly affect the field distribution of the first mode and hence has minimal effect on its radiation pattern. However, this is not the case for the second band. In particular, Figures 5.4(b) and 5.5(b) show that the field distribution at the second resonance, and hence its radiation pattern, change as capacitor values are changed. More importantly, because of its semi anti-symmetric field distribution, this mode will still have a null or a minima at the antenna broadside.

Figure 5.6(a) shows the magnitude and direction of the magnetic current of an unloaded slot antenna at its second resonant mode. The antenna has a length of λ_2, where λ_2 is the slot wavelength at the second resonance. If the antenna is folded at a

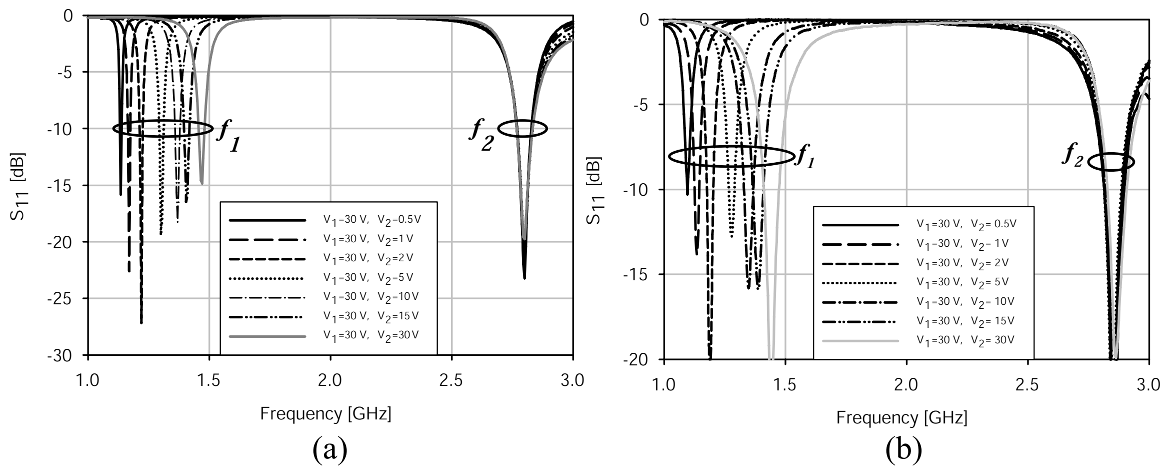

Figure 5.9: (a) Simulated and (b) measured input reflection coefficients of the dual-band tunable antenna of Figure 5.7. In this example, the frequency of the second band is kept fixed while that of the first band is varied.

distance of $\lambda_2/4$ from one end, the magnetic current distribution will assume a form shown in Figure 5.6(b). In this arrangement the oppositely directed magnetic currents inside the dashed contour have similar magnitude but opposite direction. Therefore, that part of the antenna does not effectively contribute to the far-field radiated fields and the folded antenna becomes equivalent to the one shown in Figure 5.6(c). This way, the radiation pattern of the second mode will be similar to that of the first mode. In addition to solving the radiation pattern problems, this approach reduces the overall length of the antenna by about 25%. However, as a result of the slight antenna miniaturization, the antenna gain and efficiency will slightly be reduced (see [1]). This can be viewed as a tradeoff between having similar radiation patterns at both bands and a smaller antenna with the slight reduction in antenna efficiency. In the next section experimental results of such a dual-band reconfigurable antenna are presented and discussed.

5.2 Experimental Results

The schematic of the proposed dual-band slot antenna is shown in Figure 5.7. The antenna uses the folded topology described in the previous section with the smaller and larger sections of 15 mm and 45 mm long, respectively. The overall average length of the antenna is $\ell = 62$ mm with $\ell_1 = 4.5$ mm and $\ell_2 = 29$ mm. The antenna is designed on a 0.5 mm thick RO4003 substrate with dielectric constant of $\epsilon_r = 3.4$, loss tangent of $\tan(\delta) = 0.002$, and an overall ground plane size of 15 cm $\times$ 11 cm. The antenna is fed with an off-centered, open-circuited microstrip line with an impedance of 50 Ω. Matching is performed by appropriately choosing the location of the microstrip feed and the length of the open circuited line (L_S and L_m in Figure 5.7) as described in [91] and [93]. Optimum locations of the feed and lengths of the open circuited stubs are determined by performing optimization using a method of moment (MoM) based full-wave simulation software (IE3D) [82]. The antenna is simulated in IE3D and fabricated on the same RO4003 substrate mentioned above. The input reflection coefficient (S_{11}) of the antenna, for different varactor bias voltages, is measured using a calibrated vector network analyzer (VNA) and the results are presented in Figures 5.8 and 5.9 along with the simulated results. Figure 5.8(a) and 5.8(b) show the simulated and measured dual-band responses of the antenna. It is observed that by applying the appropriate combination of bias voltages (V_1 and V_2), the frequency of the first band is kept fixed and that of the second band is tuned. Similarly, as shown in Figure 5.9(a) and 5.9(b), it is possible to keep the frequency of the second band stationary and sweep the frequency of the first band. As is observed from these figures, a relatively good agreement between the simulated and measured results are observed. The discrepancies between these results can mostly be attributed to the finiteness of the ground plane and the dielectric substrate (which are considered infinite in the simulations), tolerances in the exact value of the dielectric constant of the material ($\pm 3\%$ error specified by manufacturer),

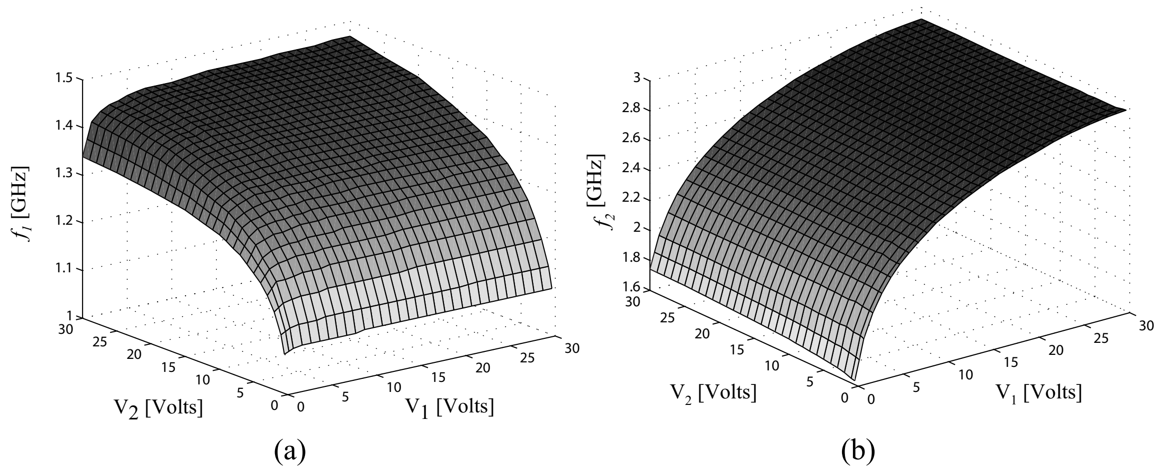

Figure 5.10: Measured frequencies of (a) first band and (b) second band of the tunable dual-band slot antenna shown in Figure 5.7 as a function of the varactors' bias voltages. It is observed that f_1 is less sensitive to V_1 and f_2 is less sensitive to V_2.

Parameter	$L_g \times W_g$	L_s	L_m
Value	15×11 cm^2	27.5 mm	3.2 mm
Parameter	ℓ	ℓ_1	ℓ_2
Value	62.0 mm	4.5 mm	29.0 mm

Table 5.1: Physical parameters of the dual-band reconfigurable slot antenna.

alignment errors during the fabrication process, and numerical errors in the software.

The S_{11} of the antenna is measured for over 300 different combinations of varactor bias voltages (V_1, V_2) and the operation frequencies of the first and second bands are extracted from these measurements results. These results are presented in Figures 5.10(a) and 5.10(b) respectively. It is observed that the frequency of the first band is mainly affected by the bias voltage (capacitance) of the second varactor, whereas the frequency of the second band is mostly affected by the capacitance of the first varactor. This is consistent with the slot antenna's electric field distributions shown in Figures 5.4 and 5.5. The reason for this behavior can become clear by considering the electric field distribution of the unloaded slot antenna in the first and second resonant modes. At first resonance, the voltage at the center of the slot is at its maximum whereas it is zero at the second resonance. Therefore, a capacitor

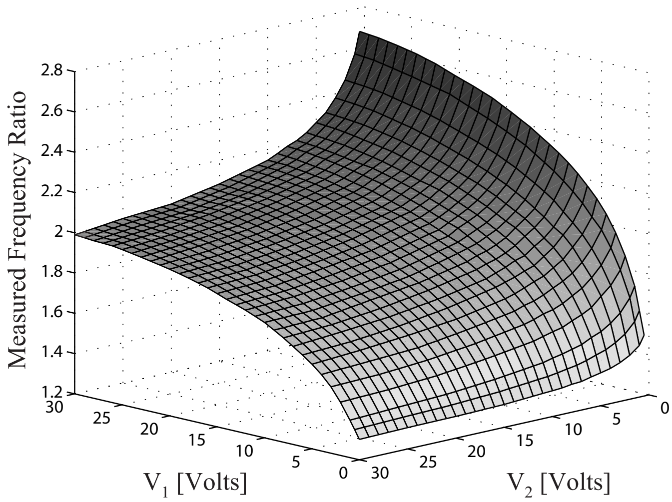

Figure 5.11: Measured frequency ratio, $f_R = f_2/f_1$, of the tunable dual-band slot antenna shown in Figure 5.7 as a function of the varactors' applied bias voltages.

that is placed at the center of the slot antenna observes a short circuit at the second resonance and does not significantly affect this mode. On the other hand, if a capacitor is placed close to the edge of the slot, it observes a much lower impedance at the first resonance than that of the second one and therefore, it mostly affects the second mode. The frequency ratios of the antenna (f_R), as a function of V_1 and V_2, are calculated from the measured S_{11} responses and presented in Figure 5.11. It is observed that a large range of frequency ratios can be obtained by just changing the varactors' bias voltages. In this case $f_R(V_1, V_2)$ attains the maximum value of 2.67 and the minimum value of 1.30 as seen from Table 5.2.

One of the parameters that affect the resonant frequencies and frequency ratios of this antenna is the dimension of its ground plane. These effects are comprehensively studied in Chapter 4, where it is shown that for a fixed DC bias voltage value, decreasing L_g and W_g reduces the frequency of operation of the first and second bands (f_1 and f_2) and the frequency ratio of the dual-band antenna. Furthermore, the ground plane size of a slot antenna also affects its gain and radiation patterns as described in Chapter 4 and the references therein. The ground plane dimensions,

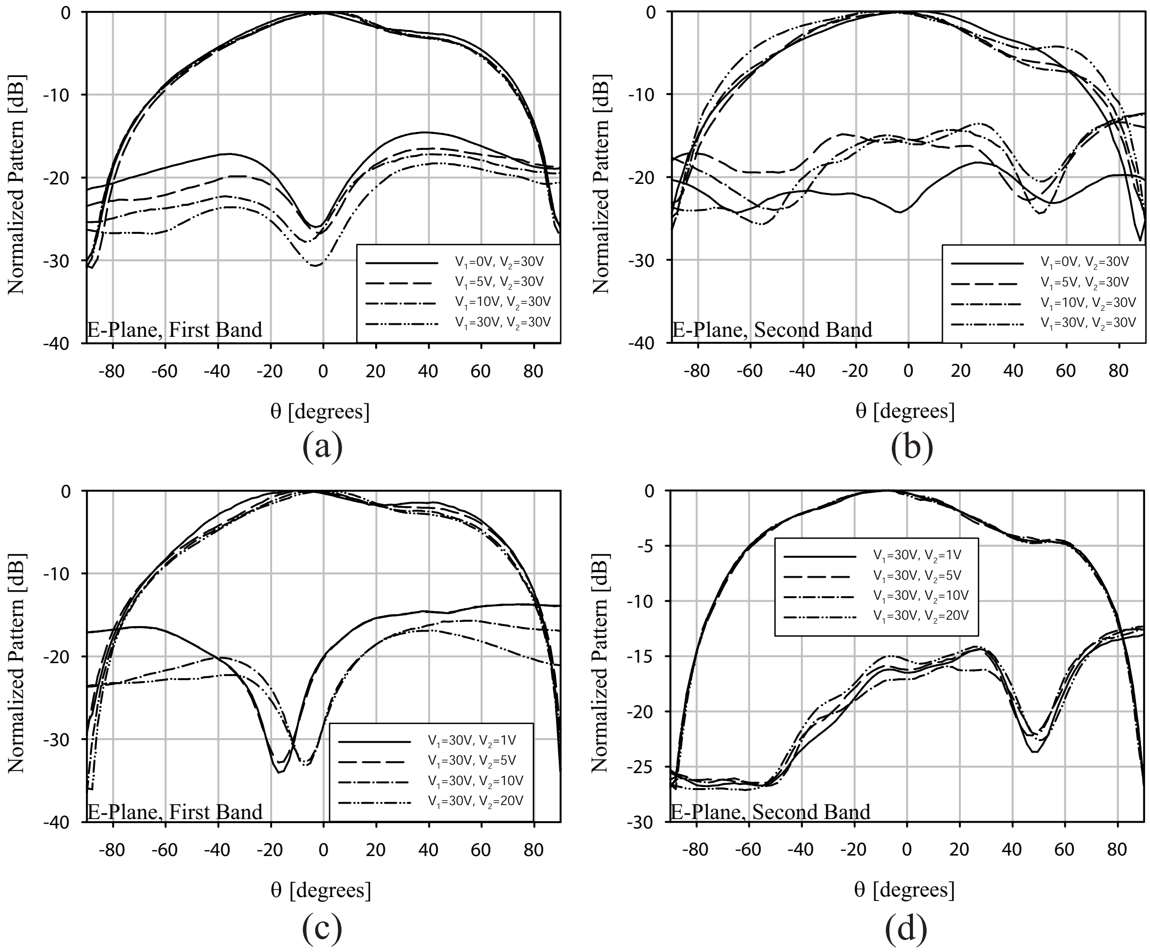

Figure 5.12: Measured E-Plane radiation patterns of the tunable dual-band slot antenna of Figure 5.7 at its first and second bands of operation.

however, are usually determined by the type of application and the constraints on the dimensions of the final product in which the antenna is used. Therefore, the effects of the finite substrate and ground plane size on the performance of the antenna must be taken into account during the design process in order to achieve the desired frequency response and performance.

The co- and cross-polarized radiation patterns of the antenna at the first and second bands are measured for different combinations of bias voltages and are presented in Figures 5.12(a)-(d) and Figures 5.13(a)-(d). Figure 5.12(a) and 5.12(b) show the co- and cross-polarized radiation patterns of the antenna respectively in its first and second bands of operation for a fixed value of V_2 and variable V_1 values. It is seen that

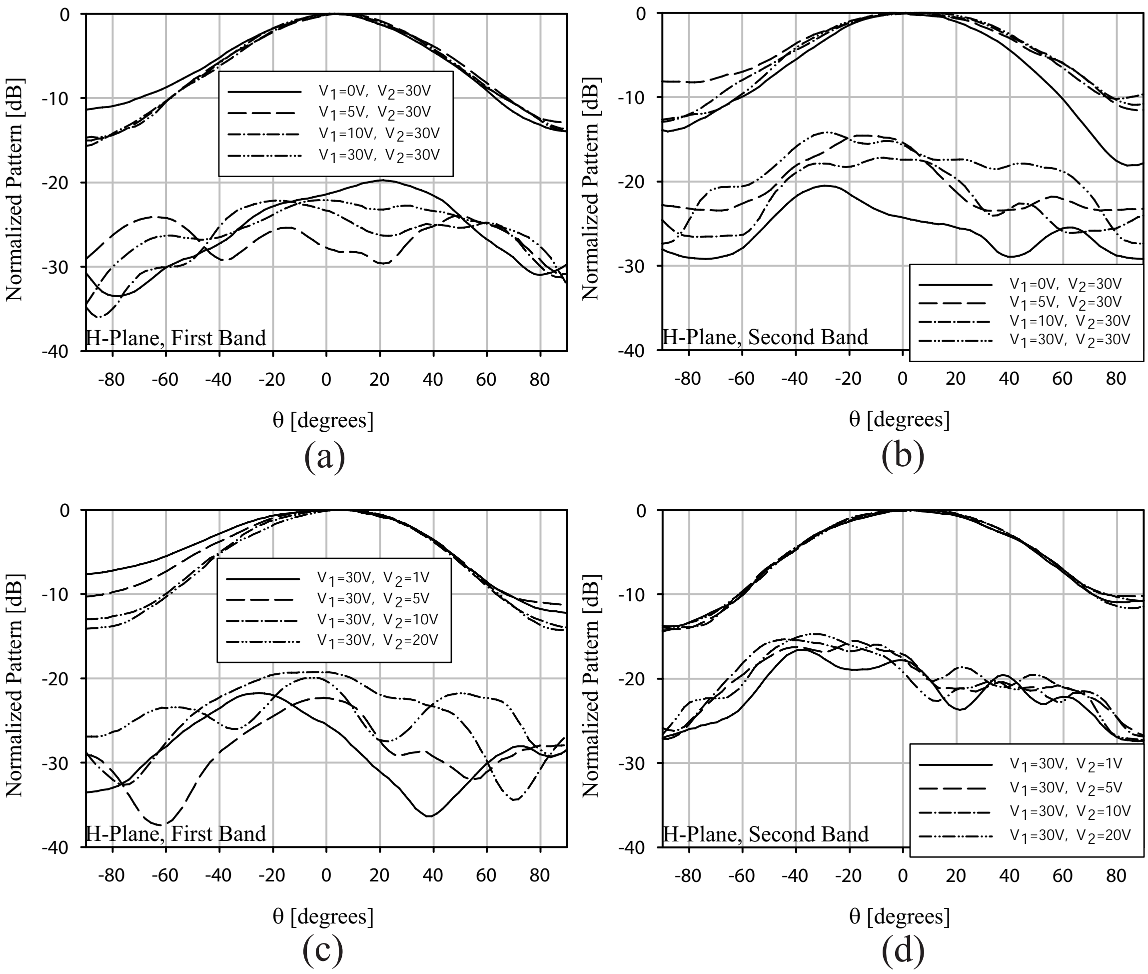

Figure 5.13: Measured H-Plane radiation patterns of the tunable dual-band slot antenna seen in Figure 5.7 at its first and second bands of operation.

(V_1, V_2) [Volts]	(C_1, C_2) [pF]	f_1 [GHz]	f_2 [GHz]	f_R
(30.0, 0.5)	(0.5, 1.75)	1.1	2.94	2.67
(0.0, 30.0)	(2.25, 0.5)	1.34	1.74	1.3

Table 5.2: Electrical parameters of the antenna corresponding to lowest and highest measured f_R values.

the radiation patterns at both bands are similar to each other and the antenna has low levels of cross polarized radiation. Furthermore, as expected, changing V_1 slightly affects the radiation pattern of the second band and has little effect on the patterns of the first band. Nevertheless, for all practical purposes, the radiation patterns remain consistent. Figures 5.12(c) and 5.12(d) show the same patterns for constant values of V_1 and variable V_2 values. In this case, the antenna patterns at the second band remain unaffected whereas the radiation patterns at the first band are slightly affected. In spite of the small changes in the radiation patterns, the antenna has similar radiation patterns at both bands and across its entire frequency of operation. Figures 5.13(a)-(d) show the H-Plane co- and cross-polarized radiation patterns of the antenna for the same varactor bias voltages. Similar to the E-Plane patterns, the H-plane patterns of the first and second bands of operation have small levels of cross-polarized radiation and their co-pol components remain unchanged over the entire band of operation. The gain of the antenna, at broadside, is measured using a double-ridged horn antenna as a reference. The measurement results are presented in Table 5.3. It is observed that as the capacitances of the varactors increase (the bias voltages decrease), the antenna gain drops. Increase in capacitance reduces the resonant frequencies of both bands of the antenna, and therefore, for a fixed physical length, decreases the electrical length of the antenna. This reduction in electrical length (miniaturization) reduces the antenna gain as described in [1]. The antenna efficiency values are calculated from the measured gain and calculated directivity values at bore-sight. For example, for $V_1 = 0$ V and $V_2 = 1$ V the directivity of the antenna at the first and second bands are respectively 1.76 dBi and 1.96 dBi, which corresponds to an efficiency of 58% and 59% for the first and second bands respectively. As the bias voltages increase, so do these efficiency values. For example, when $V_1 = V_2 = 30$ V, the directivity of the antenna at the first and second bands are 1.82 dBi and 2.16 dBi respectively. This corresponds to efficiency values of 87% and 92%

$V_1(\downarrow),\ V_2(\rightarrow)$	1 V	5 V	10 V	20 V	30 V
0 V	-0.6 (-0.4)	0.2 (0.1)	0.3 (0.2)	0.3 (0.2)	0.3 (0.2)
5 V	0.0 (1.5)	0.7 (1.6)	0.8 (1.7)	0.9 (1.8)	0.9 (1.8)
10 V	0.2 (1.7)	0.8 (1.8)	0.9 (1.8)	1.1 (1.8)	1.1 (1.8)
20 V	0.2 (1.7)	1.0 (1.8)	1.1 (1.8)	1.2 (1.8)	1.2 (1.8)
30 V	0.2 (1.7)	1.0 (1.8)	1.1 (1.8)	1.2 (1.8)	1.2 (1.8)

Table 5.3: Measured gain of the dual-band tunable antenna at first (second) bands of operation as a function of varactor bias voltages. All values are in dBi.

at the first and second bands respectively.

5.3 Conclusions

A new technique for designing dual-band reconfigurable slot antennas is proposed. The technique is successfully applied to design a dual-band slot antenna with consistent radiation patterns at both bands and over the entire frequency range of the antenna. Measurement results of the antenna indicate that its frequency ratio can assume any value in the range of $1.3 \leq f_R \leq 2.67$ by changing the DC bias voltages of its two varactors in the range of 0.5 V$\leq V_1, V_2 \leq$ 30 V. Furthermore, good simultaneous impedance match is observed at both bands of operation for the entire range of bias voltages, low levels of cross-polarized radiation is observed, and the radiation patterns of each band remain practically unchanged as the DC bias voltage is changed.

CHAPTER 6

Improved Wire and Loop Slot Antennas

Loop and dipole antennas are perhaps the most used and well known radiating elements whose characteristics have been extensively studied for many decades [56, 107]. Numerous analytical studies on loop antennas of different shapes have been performed by various researchers. Radiated fields of thin circular and elliptical wire loops are derived in [108] and closed form expressions for the fields of a rectangular wire loop are given in [109]. Furthermore, the radiation characteristics of a wire loop antenna printed on a dielectric substrate is theoretically studied in [110]. The complementary structure of a wire loop antenna is a slot loop antenna, which has also been comprehensively studied by various researchers. For example, an annular slot antenna printed on a dielectric half-space is studied in [111] and the performance of a cavity backed annular slot antenna is reported in [112]. All these studies confirm that the annular strip or slot antennas, in their basic form, behave similar to a narrow-band resonant antenna. In order to enhance the bandwidth of loop antennas, different structural variations of the standard loop have been proposed in the past. Wideband and multi-band characteristics of a multi-turn printed loop antenna above a ground plane are presented in [113] and a wideband printed elliptical loop antenna is proposed in [114]. New feeding mechanisms for annular slot antennas are also used in [115, 116, 117] to enhance the bandwidth or to achieve multi-frequency behavior. However, the success of these methods in bandwidth improvements is somewhat limited. That is, in most cases, the maximum percentage bandwidth reported is about 20% [113, 114, 115, 116].

In this chapter, we propose a different technique for substantially enhancing the bandwidth of loop antennas without increasing the dimensions of the antenna. This technique can be equally applied to design wideband annular strip and annular slot antennas using a single topology. Furthermore, for this new loop antenna topology, two very simple feeding and matching mechanisms are also presented. These feeding mechanisms allow for simple integration of the antenna with the rest of the RF front end, which is highly desirable in commercial wireless applications. The modified topology is obtained by creating additional paths for the electric or magnetic current (depending on wire or slot configuration) within the loop structure. The additional path, naturally, allows for creation of resonances at higher frequencies and balances the stored electric and magnetic energy over a wider bandwidth as is discussed in more detail later. In what follows, the design of the bi-semicircular slot and strip antennas are presented in Sections 6.1 and 6.2, respectively. In each section, first a parametric study is performed to obtain the optimum geometrical parameters, that result in the maximum possible bandwidth, for each antenna. Then, prototypes of the strip and slot bi-semicircular antennas are fabricated and detailed measurement results are presented and discussed.

6.1 The Bi-Semicircular Slot Antenna

The first resonance of a wire ring antenna occurs when the loop circumference (C) is about one wavelength. The bandwidth of a loop antenna is a function of the wire diameter and slightly increases as this diameter increases. Similarly for ring slots, the first resonance occurs for $C \approx \lambda$ and the antenna bandwidth increases with

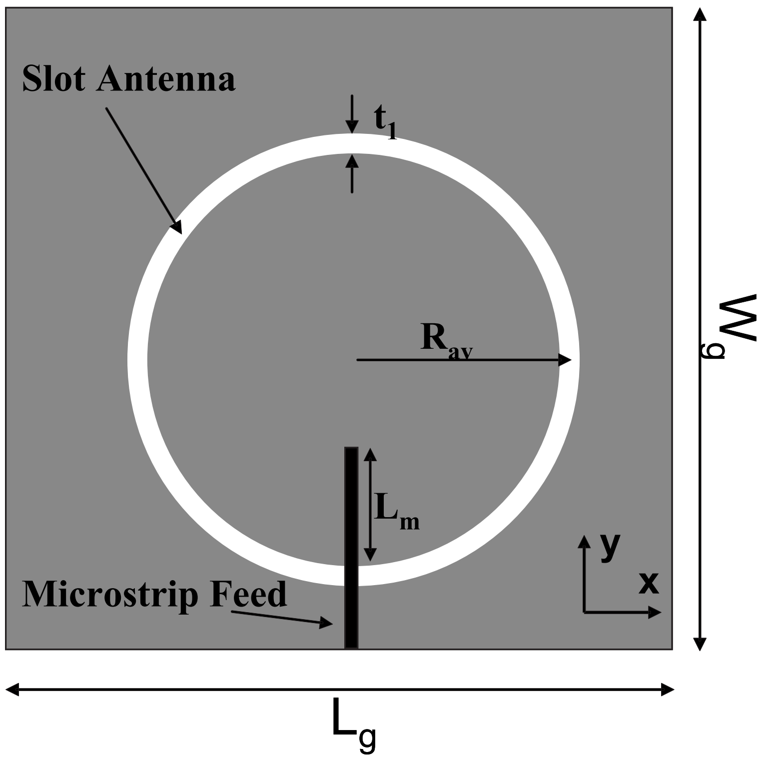

Figure 6.1: Geometry of a microstrip-fed annular slot antenna.

increase in the slot width. The geometry of such an antenna fed by an open-ended microstrip line is shown in Figure 6.1. The length of the open circuited line, L_m, can be adjusted to compensate for the input reactance of the antenna and obtain a good match to the line impedance (in this case 50 Ω). A ring slot with an average radius of R_{av} = 12.5 mm and slot width of t_1 = 1 mm is fabricated on a 0.5 mm thick substrate with a dielectric constant of 3.4 (RO4350B from Rogers Corp.). The measured and simulated S_{11} of this antenna are shown in Figure 6.2. It is shown that the standard slot loop antenna provides a −10 dB bandwidth of about 6%. A number of full-wave simulations are performed to study the effect of the slot width, t_1, on the bandwidth of this antenna using a commercially available EM simulation software [82]. Figure 6.2 shows that as t_1 is increased, the antenna bandwidth also increases. However, because of the circular topology of the antenna, t_1 cannot assume very large values. Furthermore, increasing the slot width creates larger levels of cross

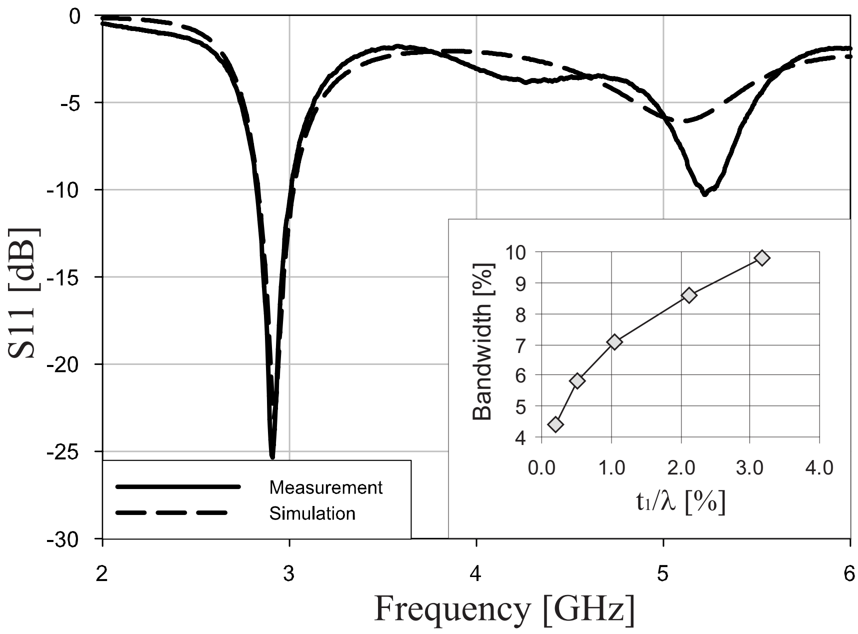

Figure 6.2: Simulated and measured S_{11} of the narrow-band annular slot antenna shown in Figure 6.1 for $R_{av} = 12.5$ mm, $t_1 = 1$ mm, and $L_m = 6$ mm.

polarized radiation. Thus, to improve the antenna bandwidth, a different approach is sought without the need for significantly increasing the slot width or the overall area occupied by the antenna.

Bandwidth enhancement can be accomplished by modifying the topology of the ring slot antenna as shown in Figure 6.3. The basic premise behind the proposed topology is that creating an additional path for the magnetic current allows for creation of other resonant paths within the loop structure. The new antenna is composed of two semi-circular loops and is fed by an open-ended microstrip line. Similar to the previous case, the length of the open stub, L_m, can be adjusted to match the antenna to 50 Ω. This antenna is shown to have a much larger bandwidth than that of the traditional annular ring slot. The bandwidth of this antenna is not only a function of t_1 but also a function of the width of the chord slot, t_2. In order to find the optimum values of the geometrical parameters for this antenna, it is necessary to perform a parametric study to determine the combination of geometrical parameters (t_1, t_2) that result in the maximum bandwidth for a given antenna. This

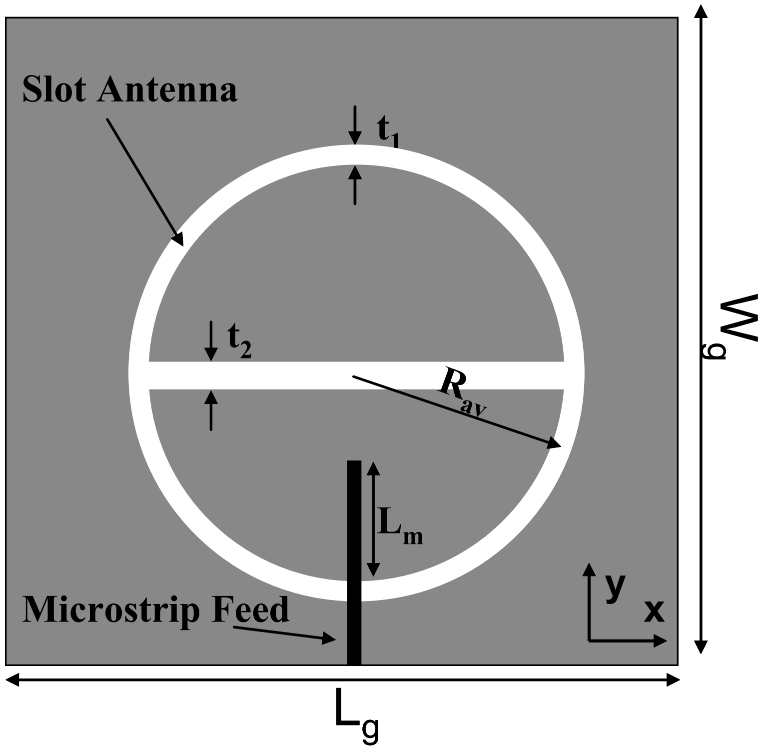

Figure 6.3: Geometry of the bi-semicircular slot antenna.

is done for a slot ring antenna with an average radius of R_{av} = 12.5 mm, printed on a 0.5 mm thick substrate having $\epsilon_r = 3.4$ and loss tangent of $\tan\delta = 0.003$. A number of antennas with fixed average radii and different slot width values (t_1 and t_2) are simulated and each antenna is matched to a 50 Ω line by tuning L_m. The impedance bandwidths (VSWR < 2) of these antennas are calculated from full-wave simulations and presented in Figure 6.4. Observe that the bandwidth of the antenna is significantly increased even for relatively narrow t_1 and t_2 values. The maximum bandwidth for this structure is achieved for $t_1 = t_2 = 2$ mm. As a proof of principle, a bi-semicircular ring with R_{av} = 12.5 mm, t_1 = 1 mm, and t_2 = 1.4 mm is designed and fabricated on the same RO4350B substrate with a ground plane size of $L_g \times W_g$ = 12 cm × 10 cm. Figure 6.5 shows the simulated and measured S_{11} for this antenna. The simulations are performed for two different cases. In the first case, the microstrip feed is perfectly symmetric with respect to the antenna's axis of symmetry (y axis) and in the second case the feed is offset by 1 mm from the axis of symmetry. The response of the antenna appears to be sensitive to the feed location and, as the measurement results show, the actual antenna response is very similar to the simulation results of the off-centered feed. This is the result of alignment errors that are caused during the fabrication process. Nevertheless, the antenna shows a VSWR smaller than 2 over a bandwidth from 3.35 GHz to 5.35 GHz or equivalently 46% fractional bandwidth. This result is in excellent agreement with the data presented in Figure 6.4. The achieved bandwidth is 7.6 times larger than the 6% bandwidth of the original annular ring slot having the same occupied area. The discrepancies that are observed between the measurement and simulation results can be attributed to the finite size of the antenna's ground plane, which is considered to be infinitely large in the simulations. This way, the equivalence principle can be invoked to model the slot antenna with its equivalent magnetic current distribution over the aperture as opposed to modeling the electric current that flows in the ground plane of the slot in obtaining the MoM solution to the problem. This will significantly reduce the memory requirements and will speed up the simulation and full-wave optimization of the structure at the expense of accuracy.

The radiation patterns of the bi-semicircular slot antenna are measured at four different frequencies across its band of operation and are presented in Figures 6.6 and 6.7. Since the antenna radiates almost symmetrically in the upper and lower half spaces, the patterns are only displayed for a single half-space ($z > 0$) and the patterns at lower half-space are similar to those at the upper half-space. Figure 6.6 shows the co- and cross-polarized E-Plane (y-z plane, assuming the antenna is in the x-y plane) radiation pattern of the antenna. It is shown that the radiation patterns as well as the direction of maximum radiation remain consistent as frequency increases. Furthermore, low levels of cross-polarized radiation are observed in this plane. Figure 6.7 shows the measured H-Plane (x-z plane) radiation patterns. Similar to the previous

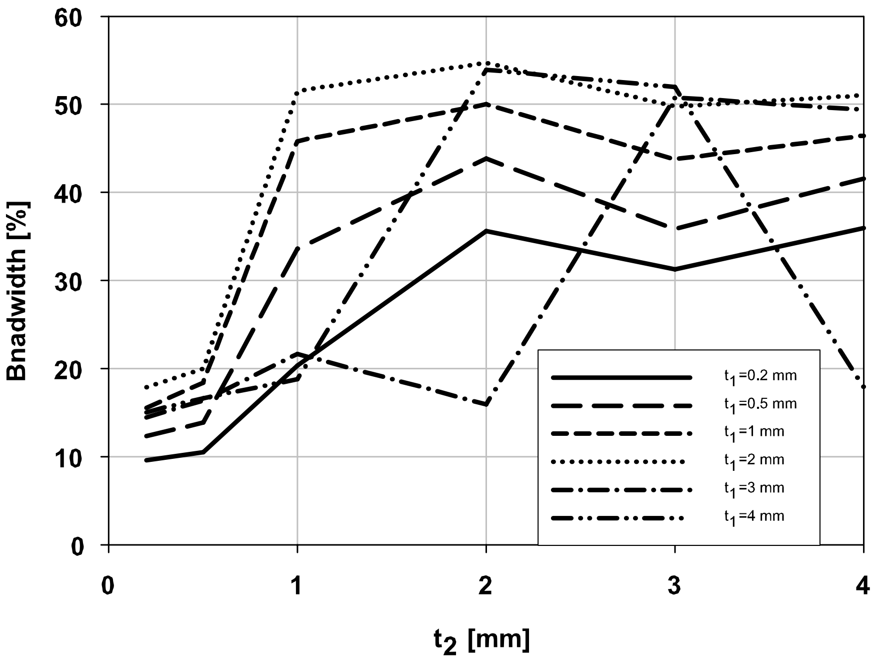

Figure 6.4: The simulated bandwidth values of the bi-semicircular slot antenna as a function of the antenna's geometrical parameters, t_1 and t_2, for an antenna with $R_{av} = 12.5$ mm printed on a 0.5 mm thick substrate with $\epsilon_r = 3.4$ and $\tan\delta = 0.003$.

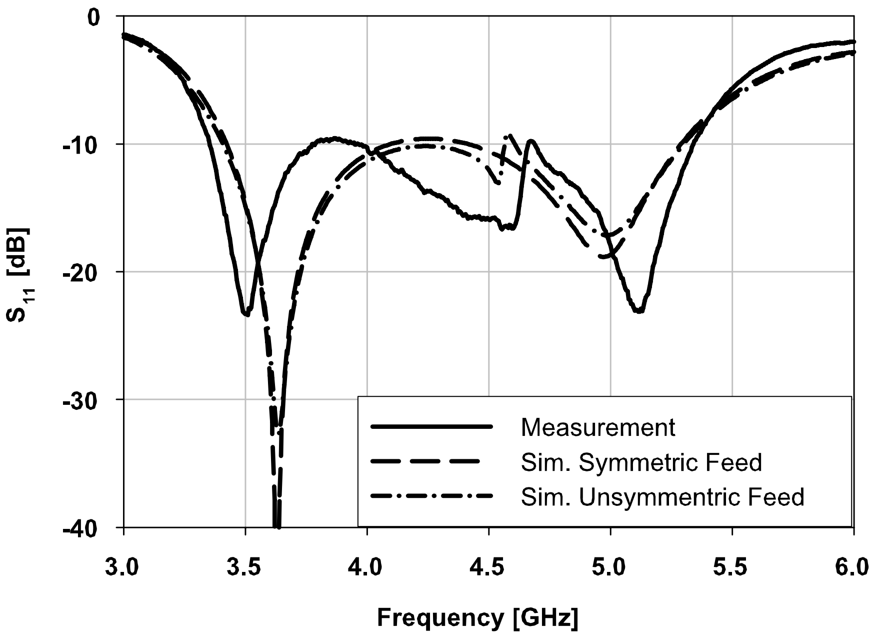

Figure 6.5: Measured and simulated S_{11} of the bi-semicircular slot antenna shown in Figure 6.3 with $R_{av} = 12.5$ mm, $t_1 = 2$ mm, $t_2 = 1.4$ mm, and $L_m = 6$ mm.

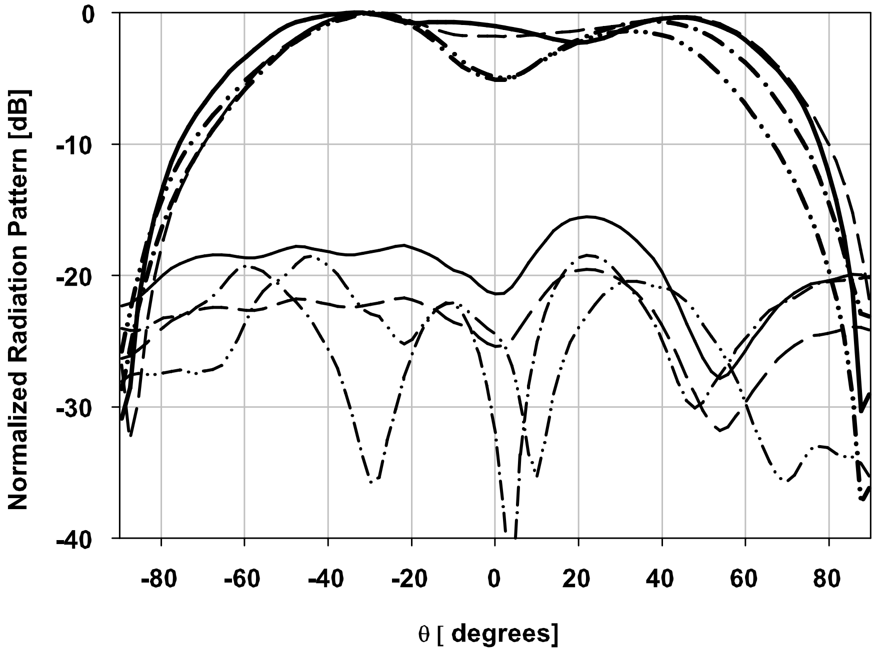

Figure 6.6: Measured E-Plane co- and cross-polarized radiation patterns of the bi-semicircular slot antenna shown in Figure 6.3. 'solid': 3.5 GHz, 'dashed': 4 GHz, 'dash dot': 4.5 GHz, and 'dash dot-dot': 5 GHz.

case, the H-plane patterns also remain consistent across the entire band of the antenna. The gain of the antenna is measured using a double-ridged horn as a reference and is given in Figure 6.8 along with the calculated directivity. The efficiency of the antenna is calculated using the measured gain and calculated directivity values and is also presented in Figure 6.8.

6.2 The Bi-Semicircular Strip Antenna

In this section, we investigate the possibility of using the bi-semicircular loop topology in enhancing the bandwidth of printed-wire loop antennas and study the performance and radiation characteristics of such bi-semicircular strip antennas. Provided that no dielectric substrate is present, the bi-semicircular strip and slot antennas are complementary structures of one another. Therefore, it is expected that the bi-semicircular strip antenna would present a similar wideband operation. The optimum

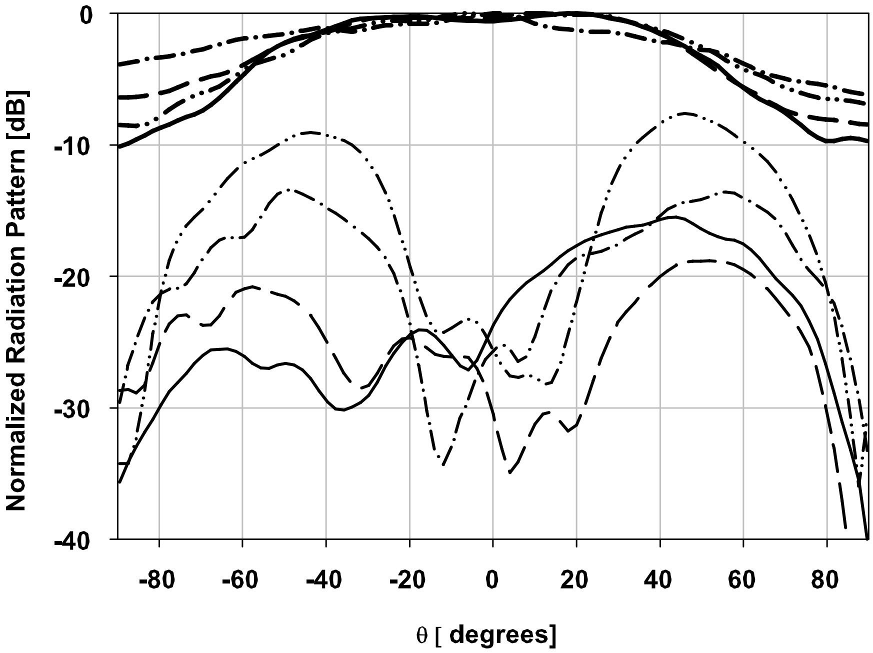

Figure 6.7: Measured H-Plane co- and cross-polarized radiation patterns of the bi-semicircular slot antenna shown in Figure6.3. 'solid': 3.5 GHz, 'dashed': 4 GHz, 'dash dot': 4.5 GHz, and 'dash dot-dot': 5 GHz.

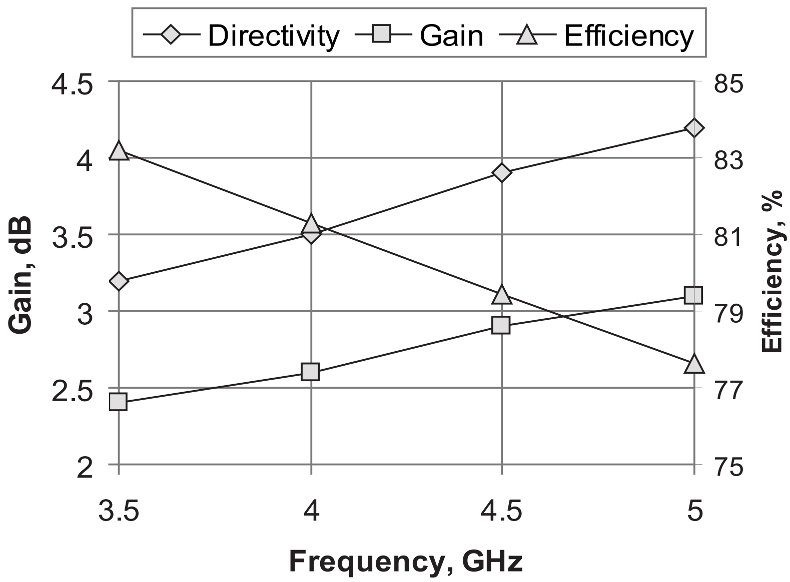

Figure 6.8: Measured gain and calculated directivity of the bi-semicircular slot antenna.

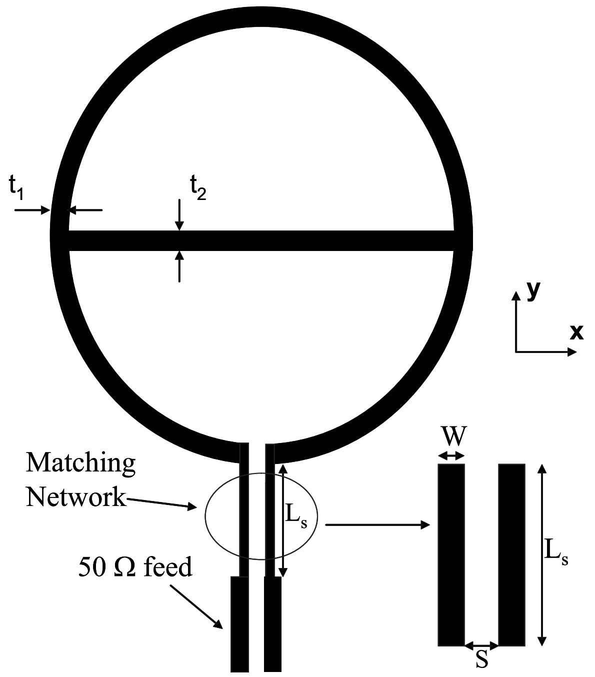

Figure 6.9: Geometry of the bi-semicircular printed wire (strip) antenna.

geometrical parameters of this antenna, however, will not be the same as those of its slot counterpart. This is a consequence of Babinet's principle, which mandates that $Z_s Z_w = Z_0^2/4$, where Z_s and Z_w are respectively the impedances of the complementary slot and wire structures and $Z_0 = 377\ \Omega$, and the fact that the antennas are matched to a 50 Ω line. Thus, it is necessary to perform another sensitivity analysis to determine the optimum geometrical parameters of the antenna that maximize its bandwidth. The topology of the bi-semicircular strip antenna is shown in Figure 6.9, where the antenna is fed with a balanced coplanar strip line with length L_s and impedance of Z_s that is connected to a 50 Ω coplanar strip line. Similar to tuning L_m in Section 6.1, L_s can be tuned to match the input impedance of the antenna to 50 Ω.

The bandwidth of the antenna is a function of its geometrical parameters t_1 and t_2, as shown in Figure 6.9. A number of full-wave simulations are performed using IE3D on an antenna with an average radius of $R_{av} = 12.5$ mm printed on a 0.5 mm thick RO4350B substrate. A matching network composed of a transmission line with

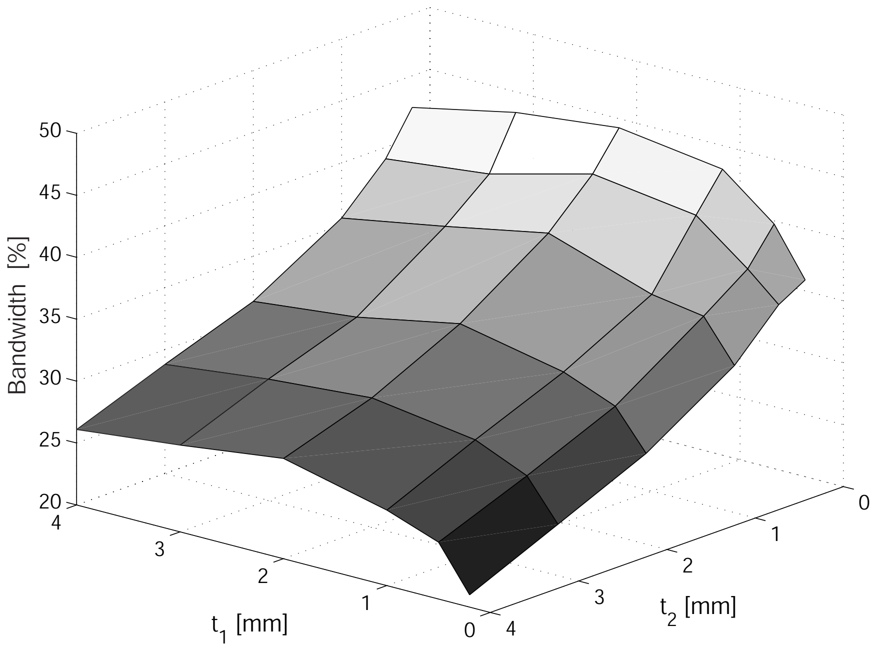

Figure 6.10: Simulated bandwidth of the bi-semicircular wire (strip) antenna as a function of its geometrical parameters, t_1 and t_2 ($R_{av} = 12.5$ mm).

a fixed characteristics impedance of $Z_s = 177\ \Omega$ and variable length of L_s is used to match the input impedance of the antenna to the line impedance. In each case the antenna is matched to a 50 Ω line only by changing L_s. Then the fractional bandwidth of the antenna, over which the VSWR is smaller than 2, is calculated and presented in Figure 6.10. It is seen that a maximum bandwidth of 45% is achieved for $t_1 = 2$ mm and $t_2 = 0.2$ mm. The antenna of Figure 6.9 requires a balanced feed and cannot simply be fed with a coaxial line without using a BALUN. In order to avoid using a BALUN, we can use half of the structure above a ground plane and feed the antenna using a probe. This is shown in Figure 6.11 where instead of using a 50 Ω coplanar strip line after the matching section, a probe is used to feed the antenna. This both reduces the overall dimensions of the antenna and eliminates the need for using a BALUN. As a proof of concept, a bi-semicircular strip antenna with $t_1 = 2$ mm and $t_2 = 0.4$ mm is designed and fabricated on a 3.5 cm $\times$ 1.5 cm, 0.5 mm thick RO4350B substrate with $\epsilon_r = 3.4$. The antenna is matched to 50 Ω by using a

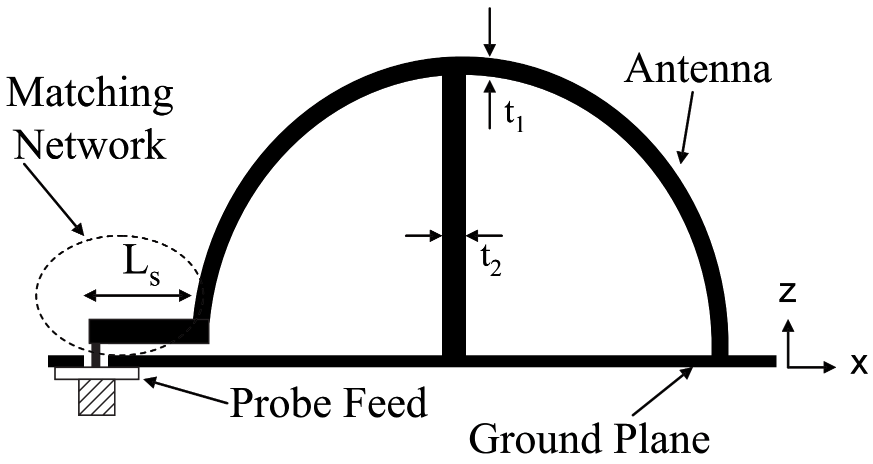

Figure 6.11: Topology of the bi-semicircular strip antenna over a ground plane, which is fed by a coaxial line.

coplanar strip transmission line with $Z_s = 177\ \Omega$ and $L_s = 6$ mm and is mounted on a 30 cm $\times$ 30 cm ground plane.

The input reflection coefficient (S_{11}) of the antenna is measured using a calibrated vector network analyzer and is presented in Figure 6.12. The simulated S_{11} of the coplanar-strip fed version of this antenna, which is printed on an infinite RO4350B substrate, is also presented in Figure 6.12. Comparison of the two curves shows a relatively good general agreement. The discrepancies between the two curves can mostly be attributed to the fact that the simulation result is the response of the antenna shown in Figure 6.9, where a balanced coplanar strip line is used to feed the antenna. On the other hand, the measurement result is the response of the antenna shown in Figure 6.11, where the structure has a finite size ground plane and is fed using a coaxial probe. More accurate simulation results can be obtained by using FDTD- or FEM-based simulation tools to accurately model the effects of the finite ground plane and probe feed at the expense of increase in computational complexity and simulation time. However, given the fact that the ground plane size of this antenna is electrically large, modeling the actual antenna structure with a finite size ground plane (shown in Figure 6.11) is computationally intensive. Moreover, optimizing the

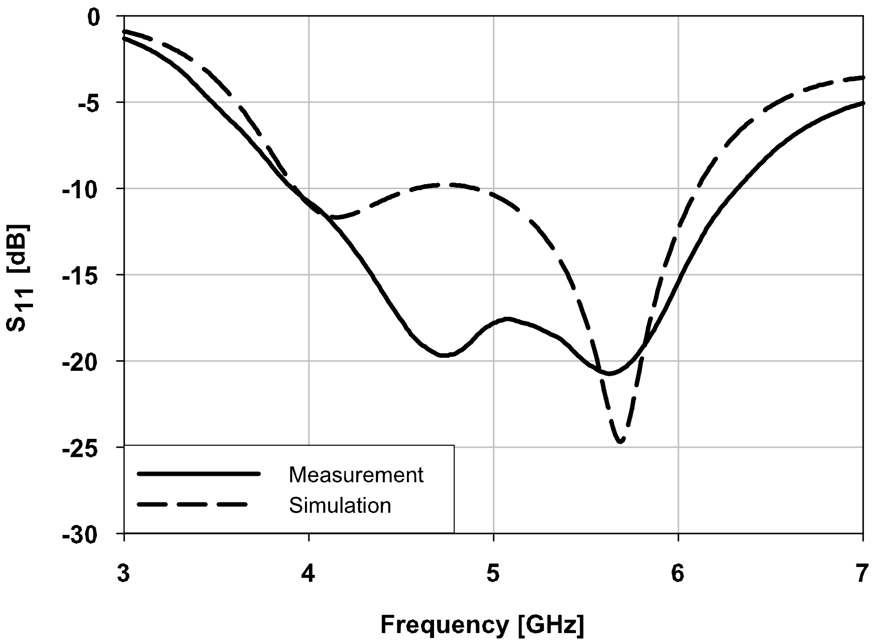

Figure 6.12: Simulated and measured input reflection coefficients of bi-semicircular strip antenna shown in Figure 6.11 with $R_{av} = 12.5$ mm, $t_1 = 2$ mm, $t_2 = 0.4$ mm, and $L_s = 6$ mm.

geometrical parameters of such an antenna using full-wave simulations becomes even more computationally intensive and is not as efficient as modeling the simpler but equivalent structure shown in Figure 6.9. The radiation patterns of the antenna are measured in the anechoic chamber of the University of Michigan at three different planes of radiation and three discrete frequencies and are presented in Figures 6.13, 6.14, and 6.15. Figure 6.13 shows the measured co- and cross-polarized patterns of the antenna in the azimuth plane at 4 GHz, 5 GHz, and 6 GHz. The radiation patterns in two elevation planes are also measured. Figure 6.14 shows the measured patterns in the x-z plane, which contains the antenna. In this figure, no symmetry in the patterns is observed. This is not unexpected, since the structure is fed from one end and hence, it is not symmetric in this plane. Figure 6.15 shows the measured radiation patterns in the y-z plane. From these figures, it is observed that the radiation patterns remain consistent as frequency is varied. The maximum gain of the antenna at each principal plane of radiation (x-y, x-z, and y-z planes) is measured using a double-ridged horn

	X-Y Plane		X-Z Plane		Y-Z Plane		
Frequency	G [dBi]	D [dBi]	G [dBi]	D [dBi]	G [dBi]	D [dBi]	η_{av}
4 GHz	-1.6	-1.2	2.1	2.6	2.3	2.5	92%
5 GHz	0.8	1.0	2.3	2.5	4.6	5.0	86%
6 GHz	0.8	1.0	1.9	2.0	6.0	6.4	84%

Table 6.1: Measured gain and simulated directivity values of the bi-semicircular strip antenna of Section 6.2 at three principal planes of radiation and three different frequencies.

as a reference and is presented in Table 6.1. Further, the directivity of the antenna, at the direction of maximum radiation in each principal plane, is calculated and presented in Table 6.1. The measured gain and calculated directivity values are used to calculate the average antenna efficiency at each frequency and the results are also presented in Table 6.1.

6.3 Conclusions

A technique for systematically improving the bandwidth of annular loop antennas is presented. The technique can equally be applied to design both wideband annular strip and slot antennas. In each case, a simple feeding network and matching technique is used, which facilitates the integration of the antenna to the rest of the RF front end. Measured results of the fabricated prototypes of the wideband bi-semicircular strip and slot antennas demonstrate a very large bandwidth over which the antennas have consistent radiation patterns, low cross polarized radiation, and high efficiency values.

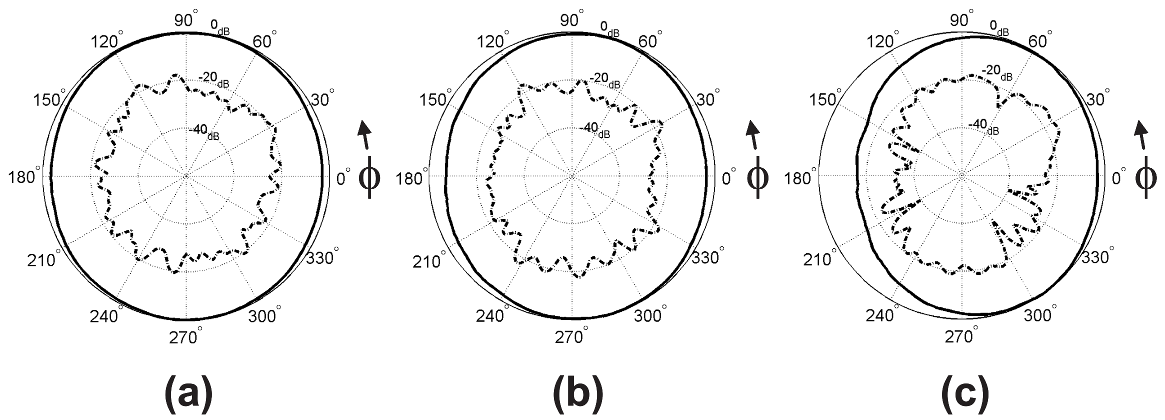

Figure 6.13: Measured radiation patterns of the bi-semicircular strip antenna in the azimuth plane (x-y plane) at a) 4 GHz, b) 5 GHz, and c) 6 GHz. 'solid line': Co-Pol, 'dash-dotted line': Cross-Pol.

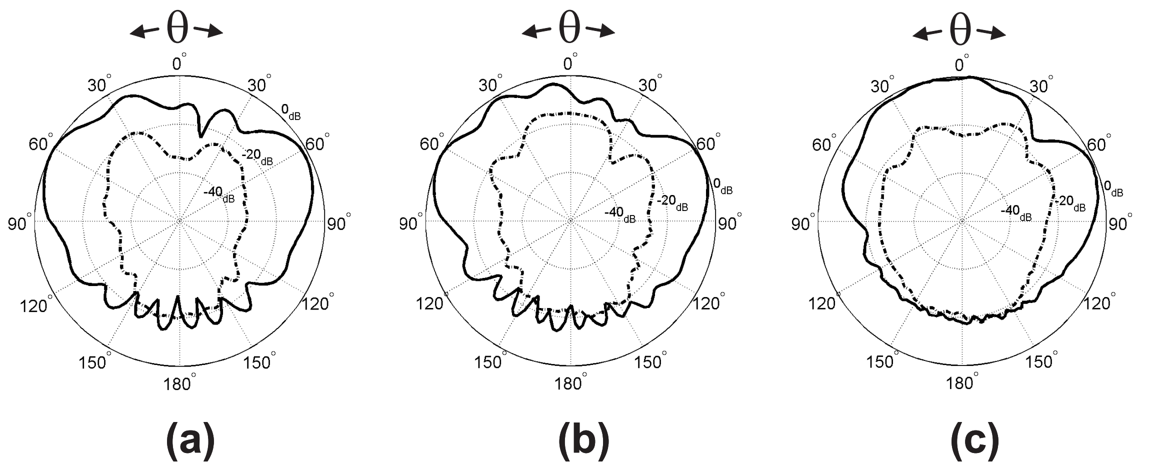

Figure 6.14: Measured radiation patterns of the bi-semicircular strip antenna of in the elevation plane (x-z plane) at a) 4 GHz, b) 5 GHz, and c) 6 GHz. 'solid line': Co-Pol, 'dash-dotted line': Cross-Pol.

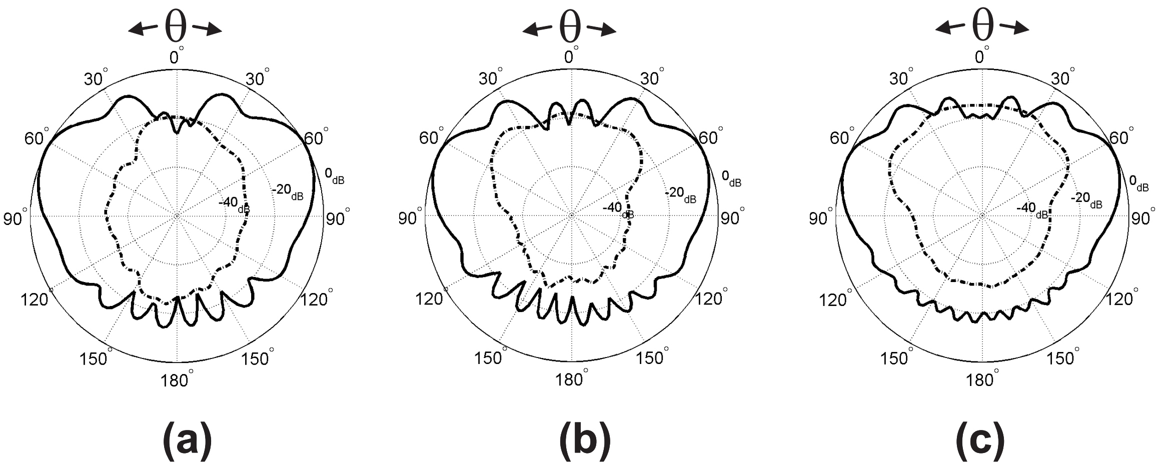

Figure 6.15: Measured radiation patterns of the bi-semicircular strip antenna of in the elevation plane (y-z plane) at a) 4 GHz, b) 5 GHz, and c) 6 GHz. 'solid line': Co-Pol, 'dash-dotted line': Cross-Pol.

CHAPTER 7

A Compact Ultra Wideband Antenna

A few decades after the early investigations on ultra-wideband (UWB) wireless systems, they have found a wide range of applications including ground penetrating radars, high data rate short range wireless local area networks, communication systems for military, and UWB short pulse radars for automotive and robotics applications to name a few. Such systems require antennas that are able to operate across a very large bandwidth with consistent polarization and radiation patterns parameters over the entire band. A number of techniques have been developed in the past to design antennas with wideband impedance matched characteristics. Traveling wave antennas and antennas with topologies that are invariant by rotation are inherently wideband and have been extensively used [56, 57, 62]. Self complementary concept [65] is another method that can provide a constant input impedance irrespective of frequency, provided that the size of the ground plane for the slot segment of the antenna is large and an appropriate self-complementary feed can also be designed. Theoretically, the input impedance of self-complementary antennas is 186 Ω and cannot be directly matched to standard transmission lines. Another drawback of self-complementary structures is that they cannot be printed on a dielectric substrate, since the dielectric constant of the substrate perturbs the self-complementary condition. Another technique for designing wideband antennas is to use multi-resonant radiating structures. Log-periodic antennas, microstrip patches with parasitic elements, and slotted microstrip antennas for broadband and dual-band applications are examples of this category [21, 28, 56, 66, 118].

The electric dipole and monopole above a ground plane are perhaps the most basic types of antennas available. Variations of these antennas have recently been introduced for obtaining considerably larger bandwidths than the traditional designs [72, 73, 74]. Impedance bandwidth characteristics of circular and elliptical monopole plate antennas are examined in [72]. Wideband characteristics of rectangular and square monopole antennas are studied in [74] and a dielectric loaded wideband monopole is investigated in [73]. A drawback of these types of antennas is that the antenna polarization as a function of frequency changes. In this chapter, a new type of single-element wideband antenna is proposed that can provide wider bandwidth and consistent polarization over the frequency range that the antenna is impedance matched. The antenna is composed of two parallel coupled sectorial loop antennas (CSLA) that are connected along an axis of symmetry. The geometrical parameters of this antenna are experimentally optimized and it is shown that the antenna can easily provide a wideband impedance match over an 8.5:1 frequency range. The gain and radiation patterns across the frequency range of operation remain almost constant particularly over the first two octaves of its return loss bandwidth. The antenna geometry is then modified in order to reduce its size and weight without compromising its bandwidth. This helps fabrication and installation of the antenna when used for lower frequency applications such as ground penetrating radars or broadcast television, where the physical size of the antenna is large.

In what follows, first the principle of operation of the CSLA is introduced, then the design and experimental optimization of the geometrical parameters of the CSLA is presented. Finally, the geometry of this optimized CSLA is modified to reduce the height, weight, and overall metallic surface of the antenna and two modified CSLAs

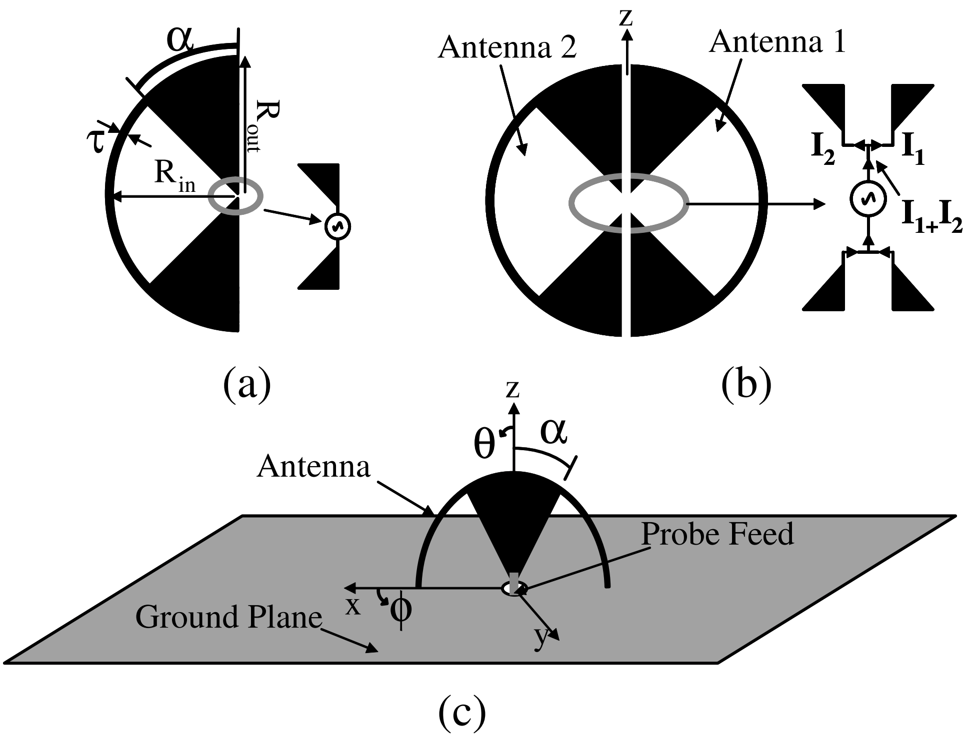

Figure 7.1: Topology of a sectorial loop antenna (a) and a coupled sectorial antenna (b) and (c).

are introduced and the radiation parameters of the optimized antennas across their entire bands of operation are presented and discussed.

7.1 Coupled Sectorial Antenna

7.1.1 Principle of Operation

The topology of a Sectorial Loop Antenna (SLA) composed of an arch and two sectors is shown in Figure 7.1(a). The input impedance of this relatively narrow band antenna, Z_s, is a function of three geometrical parameters, R_{in}, R_{out}, and α. Such loop antennas, similar to a circular loop, present a strong anti-resonance (also called parallel-resonance) when the antenna circumference is about $C \approx 0.5\lambda$. In other words, the equivalent circuit of the antenna is a high-Q parallel RLC and hence, Z_s is inductive immediately below and capacitive immediately above this anti-resonance. For $C > 0.5\lambda$, other anti-resonances are not very sharp (equivalent circuits are low Q parallel RLC) and the variations of the input reactance are not very large. If these variations are minimized, the antenna bandwidth can be increased significantly. One way of controlling the input impedance is by connecting two identical antennas in parallel and controlling the mutual coupling between them. Here, this is accomplished by connecting two identical SLAs in parallel as shown in Figure 7.1(b). In this case, because of the symmetry, the input currents I_1 and I_2 are equal but the direction of magnetic field of loop # 1 (Antenna #1) is opposite to that of loop #2 (Antenna #2) and therefore, the magnetic flux of the two loops link strongly, giving rise to a strong mutual coupling. The geometrical parameters can be varied to control the mutual coupling as a function of frequency. For the two-port system of antennas shown in Figure 7.1(b), the following equations can be written:

$$\begin{cases} V_1 = Z_{11}I_1 + Z_{12}I_2 \\ V_2 = Z_{21}I_1 + Z_{22}I_2 \end{cases}$$

where, V_1, I_1, V_2, and I_2 are the voltages and currents at the input ports of Antenna #1 and Antenna #2 respectively (see Figure 7.1(b)). Z_{11} (Z_{22}) is the input impedance of Antenna #1 (Antenna #2) in the presence of Antenna #2 (Antenna #1) and when it is open circuited. Z_{21} and Z_{12} represent the mutual coupling between the two antennas. In this case, reciprocity mandates that $Z_{12} = Z_{21}$ and symmetry requires that $Z_{11} = Z_{22}$. When the two antennas are connected in parallel and fed with a single source, as is shown in Figure 7.1(c), we will have $V_1 = V_2$ and as a consequence of symmetry $I_1 = I_2 = I$. The input impedance of the antenna can then be obtained from:

$$Z_{in} = \frac{1}{2}(Z_{11} + Z_{12}) \tag{1}$$

In order to achieve a wideband operation, spectral variations of Z_{11} and Z_{12} must counteract each other. That is, when the real (imaginary) part of Z_{11} increases with frequency, the real (imaginary) part of Z_{12} should decrease so that their average remains constant. This can be accomplished by optimizing the geometrical parameters of the antenna. Here, Z_{11} and Z_{12} are obtained by calculating the input and mutual impedances of two adjacent SLA (as shown in Figure 7.1(c)) using full-wave FDTD simulations. Figure 7.2 shows the real and imaginary parts of Z_{11} and Z_{12} for two adjacent SLAs, e.g. Antenna #1 in Figure 7.1(b), with $R_{in} = 13$ mm and $R_{out} = 14$ mm for different values of α when they are placed at a distance of $d = 0.01\lambda_{max}$ apart (λ_{max} is the wavelength at lowest frequency of operation). It is seen that as α increases, the variations in the imaginary parts of Z_{11} and Z_{12} counteract each other and a relatively constant input impedance is achieved. This suggests that the bandwidth of the antenna may be enhanced by choosing an α value in the range of $40° \leq \alpha \leq 80°$. In the next sub-section, an experimental approach is followed to find the optimum value for α that provides the largest bandwidth.

7.1.2 Sensitivity Analysis

An experimental sensitivity analysis is carried out to determine the optimum geometrical parameters of the proposed CSLA. The antenna is composed of two sectorial loops connected in parallel along the axis of symmetry (z-axis) as shown in Figure 7.1(a). The three parameters that affect the antenna response are the inner and outer radii of the loop, R_{in} and R_{out}, and the angle α as shown in Figure 7.1. The lowest frequency of operation is determined by the overall effective circumference of each sectorial loop as expressed by the following approximate formula:

$$f_l = \frac{2c}{(\pi - \alpha + 2)\sqrt{\epsilon_{eff}}(R_{in} + R_{out})} \tag{2}$$

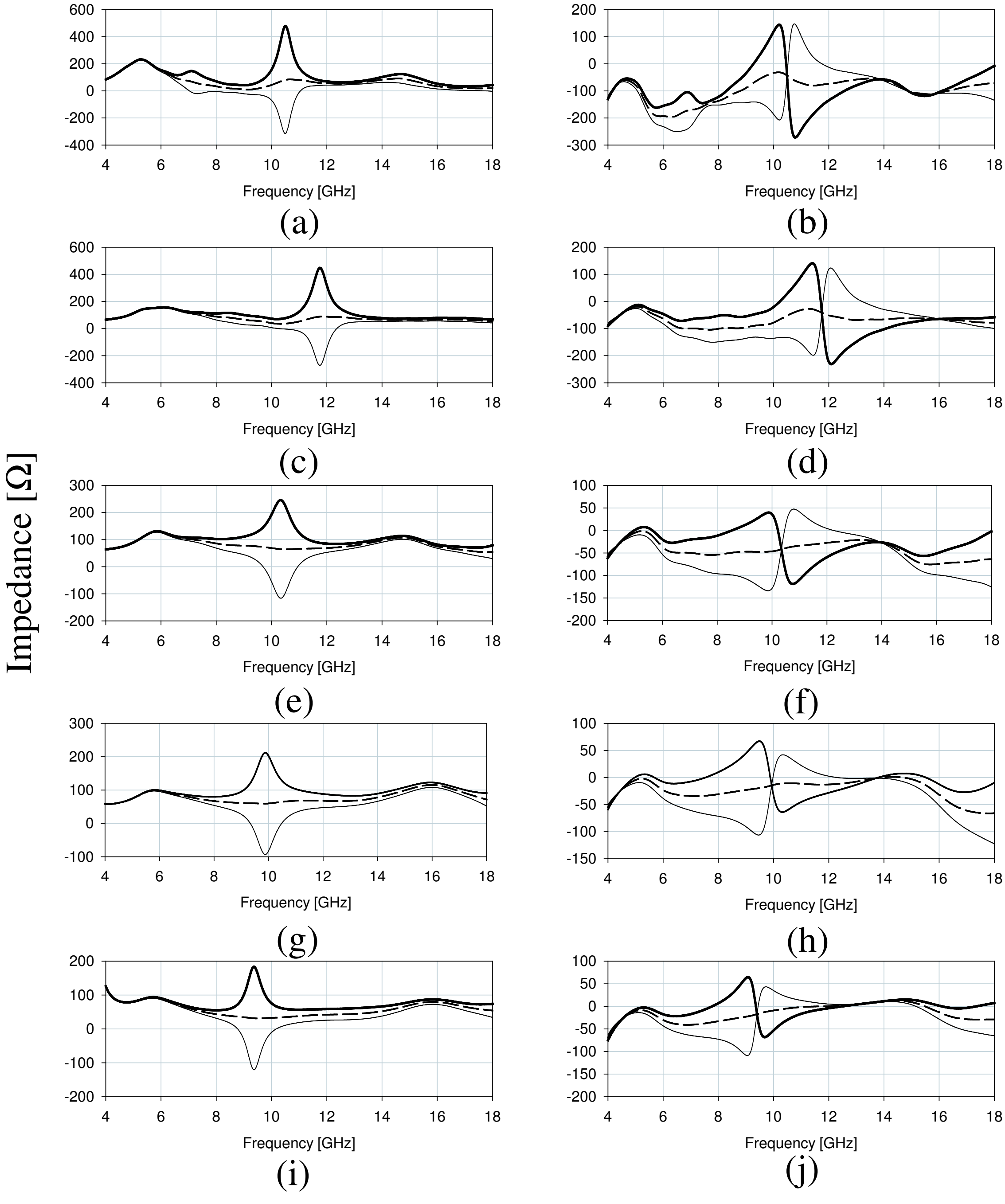

Figure 7.2: Self and mutual impedances of two SLAs that are d=$0.01\lambda_0$ apart. Thick solid line: Self impedance, Thin solid line: Mutual Impedance Dashed line: Input impedance as defined by (4). (a, c, e, g, i) Real part for $\alpha = 5°, 20°, 40°, 60°, 80°$ respectively and (b, d, f, h, k) Imaginary part for $\alpha = 5°, 20°, 40°, 60°, 80°$ respectively.

where ϵ_{eff} is the effective dielectric constant of the antenna's surrounding medium, c is the speed of light, and R_{in}, R_{out}, and α are the geometrical parameters of the antenna. Choosing the lowest frequency of operation, the average radius of the loop, $R_{av} = (R_{in} + R_{out})/2$, can be determined from (2). Therefore the parameters that remain to be optimized are α and $\tau = (R_{out} - R_{in})$. In order to obtain the optimum value of α, nine different antennas with α values ranging from $5°$ up to $80°$ with $R_{in} = 13$ mm and $R_{out} = 14$ mm were fabricated and their S_{11} as a function of frequency were measured. Since the antenna topology shown in Figure 7.1 needs a balanced feed, half of the antenna along the plane of zero potential (z=0) over a ground plane fed by a coaxial cable is used. In order to circumvent the fabrication process, the antennas are fabricated using printed circuit technology and printed on a 3 cm $\times$ 1.5 cm thin dielectric substrate with a dielectric constant of $\epsilon_r = 3.4$ and thickness of 500 μm and are mounted on a 10 cm $\times$ 10 cm ground plane. For brevity, only measured S_{11} values for $\alpha = 5°, 20°, 40°, 60°, 80°$ are presented in Figure 7.3(a). It is shown that as α increases from $5°$ to $90°$, the impedance bandwidth increases and reaches its maximum at $\alpha = 60°$, at which an impedance bandwidth ranging from 3.7 GHz to 10 GHz is achieved. The next step in the experimental optimization of the geometrical parameters of CSLA is to find the optimum value of the arch thickness, τ. This is done by fabricating antennas with $\alpha = 60°$, $R_{av} = 13.5$ mm, and three different arch thicknesses of $\tau = 0.4$, 1.0, and 1.6 mm. The measured S_{11} of these antennas are shown in Figure 7.3(b). It is observed that thinner arch thicknesses provide a wider bandwidth. For the thinnest value of $\tau = 0.4$ mm, an antenna with an operating band from 3.7 GHz to 11.6 GHz is obtained.

7.1.3 Radiation Parameters

In the previous section, the optimum geometrical parameters of the antenna were experimentally obtained. Based on this process, a CSLA with $R_{in} = 27.8$ mm,

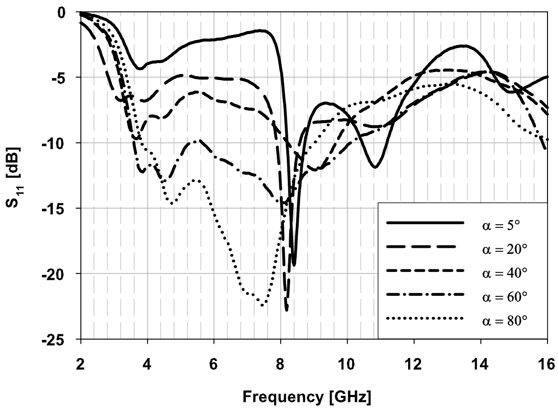

(a)

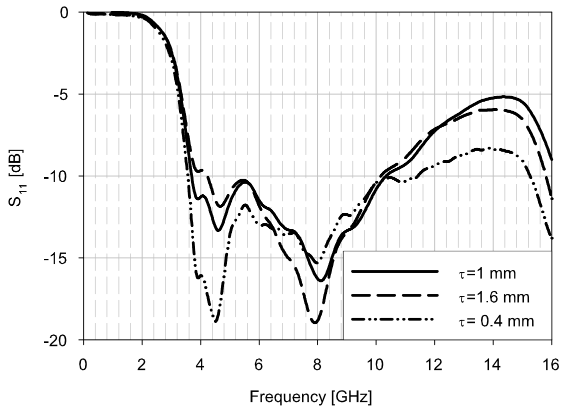

(b)

Figure 7.3: Measured S_{11} values of a number of CSLAs used in the experimental optimization process. (a) R_{in} = 13 mm , R_{out} = 14 mm, and different α values. (b) R_{av} = 13.5 mm, $\alpha = 60^o$, and different τ values ($\tau = R_{out} - R_{in}$).

$R_{out} = 28$ mm, and $\alpha = 60°$ is fabricated, on a 6 cm $\times$ 3 cm substrate with $\epsilon_r = 3.4$ and a thickness of 0.5 mm, and mounted on a 20 cm $\times$ 20 cm ground plane. The dimensions are increased to lower the lowest and highest frequencies of operation and simplify the radiation pattern measurements. The antenna has a VSWR of lower than 2.2 from 1.78 GHz to 14.5 GHz (see Figure 7.9), which is equivalent to an 8.5:1 impedance bandwidth. The radiation patterns of the antenna are measured across the entire frequency band and are presented in Figures 7.4, 7.5, and 7.6. Figure 7.4 shows the far-field co- and cross polarized (E_θ, E_ϕ) radiation patterns in the azimuth plane (x-y plane) for $\phi = 0°$ to 360°. It is shown that the radiation patterns remain similar up to about f = 8 GHz. As the frequency increases beyond 8 GHz, however, the radiation patterns start to change and show higher directivities in other directions.

The radiation patterns in the elevation planes are also measured for two principal planes at ($\phi = 0°, 180°, 0° \leq \theta \leq 180°$) and ($\phi = 90°, 270°, 0° \leq \theta \leq 180°$), and are presented in Figures 7.5 and 7.6 respectively. As frequency increases, the electrical dimensions of the antenna increase and as a result, the number of lobes increases. Also, the number of minor side lobes in the back of the ground plane ($90° \leq \theta \leq 180°$)

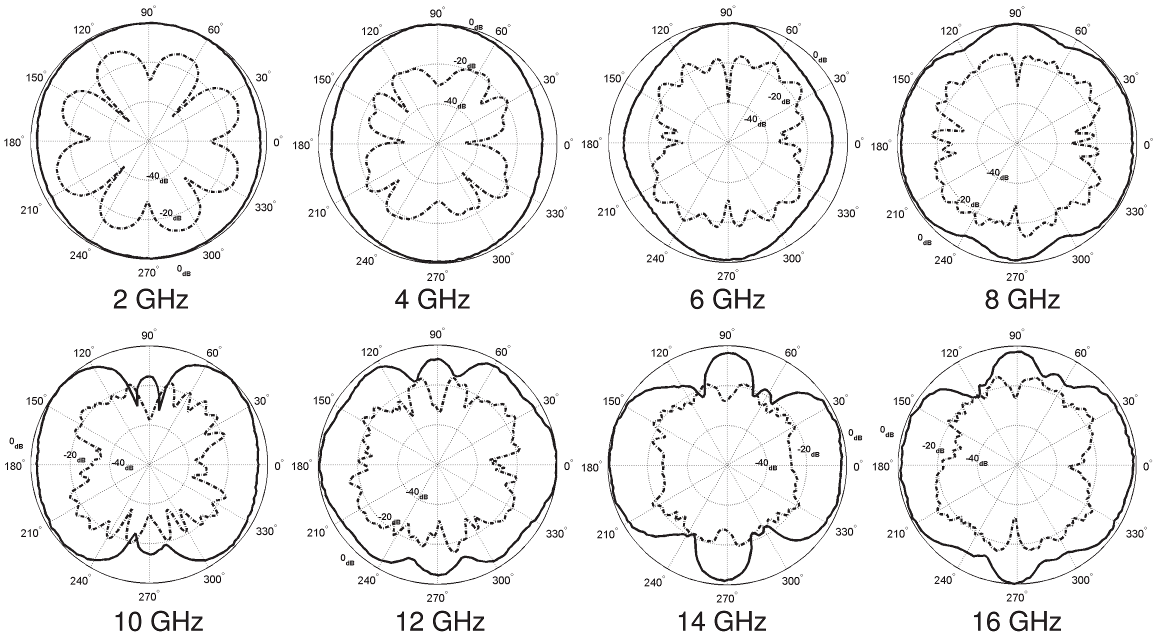

Figure 7.4: Measured radiation patterns of the CSLA in Section 7.1 in the azimuth plane. The solid line is co-pol (E_θ) and the dash-dotted line is the cross-pol (E_ϕ) components.

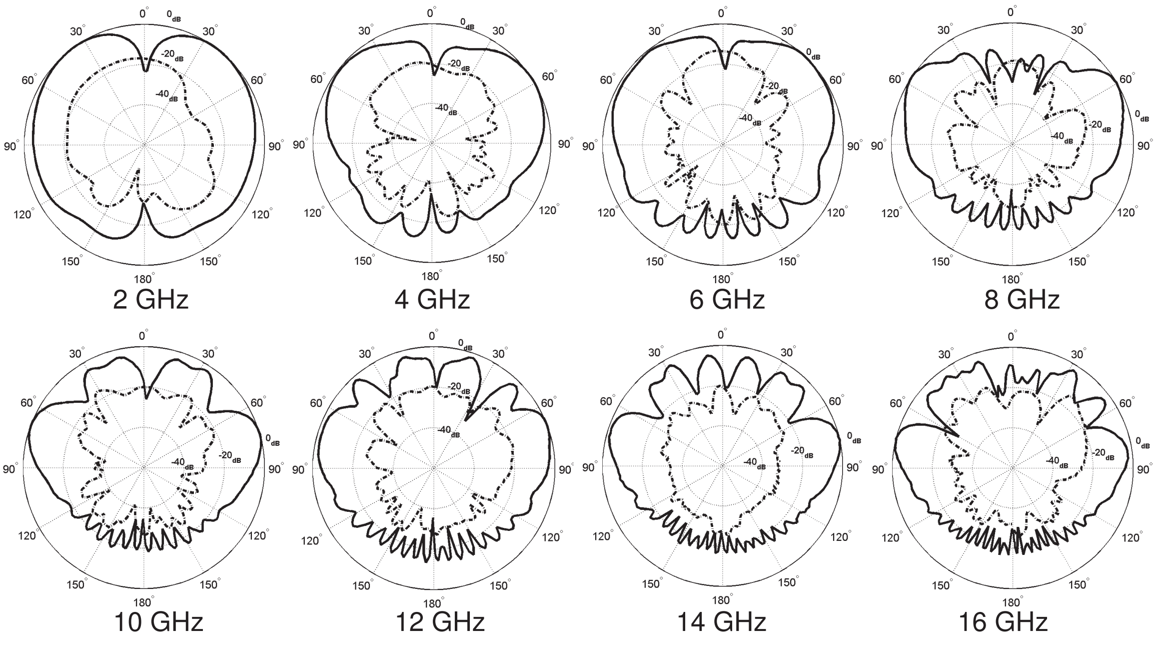

Figure 7.5: Measured radiation patterns of the CSLA of Section 7.1 in the elevation plane ($\phi = 0°, 180°, 0° \leq \theta \leq 180°$). The solid line is co-pol (E_θ) and the dash-dotted line is the cross-pol (E_ϕ) components.

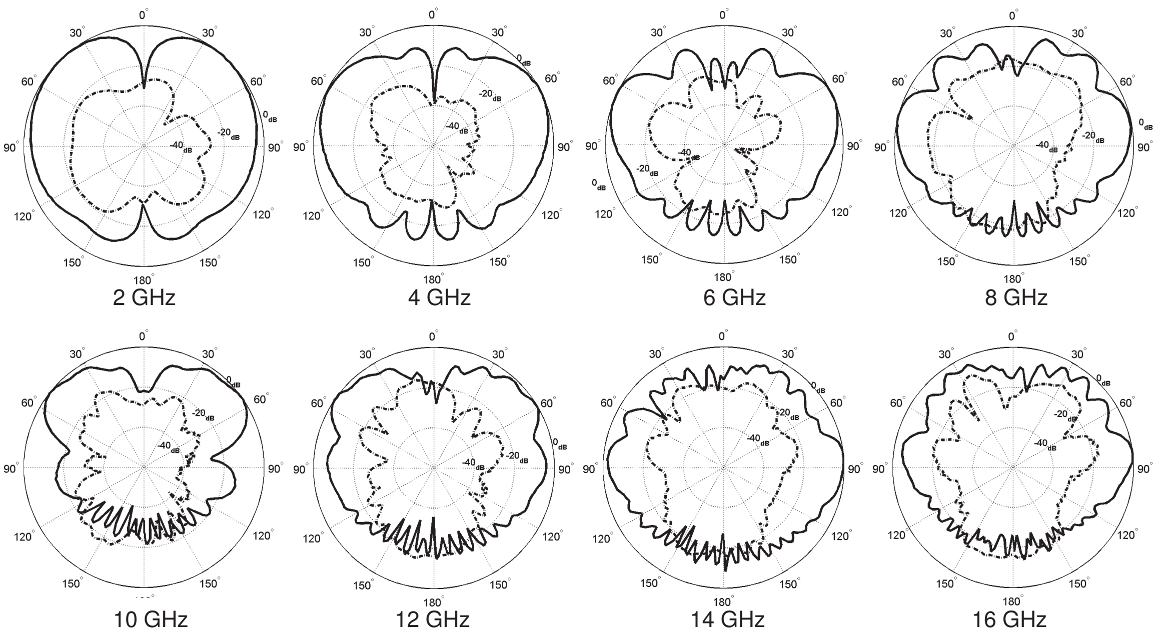

Figure 7.6: Measured radiation patterns of the CSLA of Section 7.1 in the elevation plane ($\phi = 90°, 270°$, $0° \leq \theta \leq 180°$). The solid line is co-pol (E_θ) and the dash-dotted line is the cross-pol (E_ϕ) components.

increases significantly. This is caused by diffractions from the edge of the ground plane, which has very large electrical dimensions at higher frequencies. At lower frequencies, the radiation patterns are symmetric; however, as frequency increases, the symmetry is not observed very well. This is caused by the presence of the coaxial cable that feeds the antenna and disturbs the symmetry of the measurement setup. Since the cable is electrically large at higher frequencies, a more pronounced asymmetry on the radiation patterns are observed at higher frequencies. In all the measured radiation patterns, the cross polarization level (E_ϕ) is shown to be negligible. This is an indication of good polarization purity across the entire frequency band.

7.2 Modified CSLAs

In this section, we examine the possibilities of further reducing the size and weight of the CSLA by modifying its geometry. The Coupled Sectorial Loop Antenna demon-

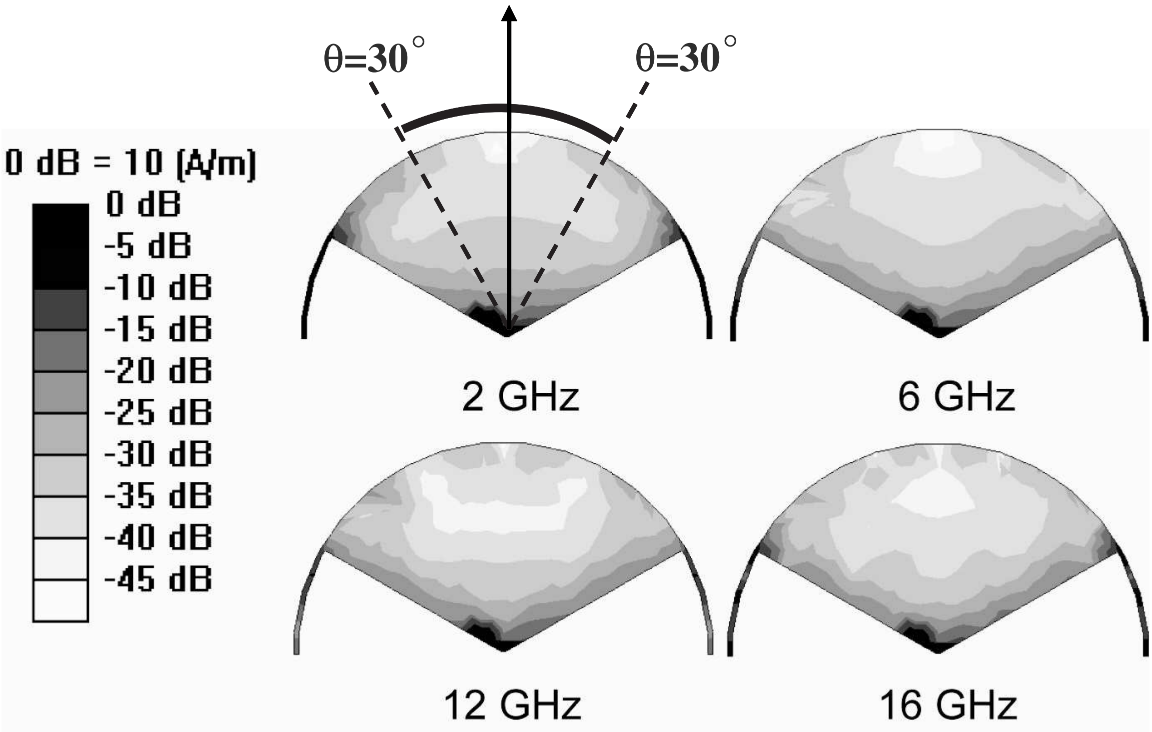

Figure 7.7: Electric current distribution across the surface of the CSLA of Section 7.1 at four different frequencies.

strated in the previous section was optimized to achieve the highest bandwidth allowing variation of only two independent parameters. Size reduction is very important for applications where the wavelength is large such as ground penetrating radars or VHF broadcast antennas. To examine ways to reduce the weight and size of the antenna, the current distribution over the metallic surfaces of the antenna is studied. The electric currents on the antenna surface is computed using a full-wave simulation tool based on the Method of Moments (MoM). The magnitude of the electric current on the surface of the antenna is shown in Figure 7.7 at four different frequencies. It is noticed that the current magnitude is very small over a sector in the range of $0° \leq \theta \leq 30°$. This suggests that this sector of the antenna can be removed without significantly disturbing the CSLA's current distribution. This modification results in a design shown in Figure 7.8(a) and, because of its similarity to the letter "M", this antenna will be referred to as M1-CSLA. Applying the same approach to M1-CSLA

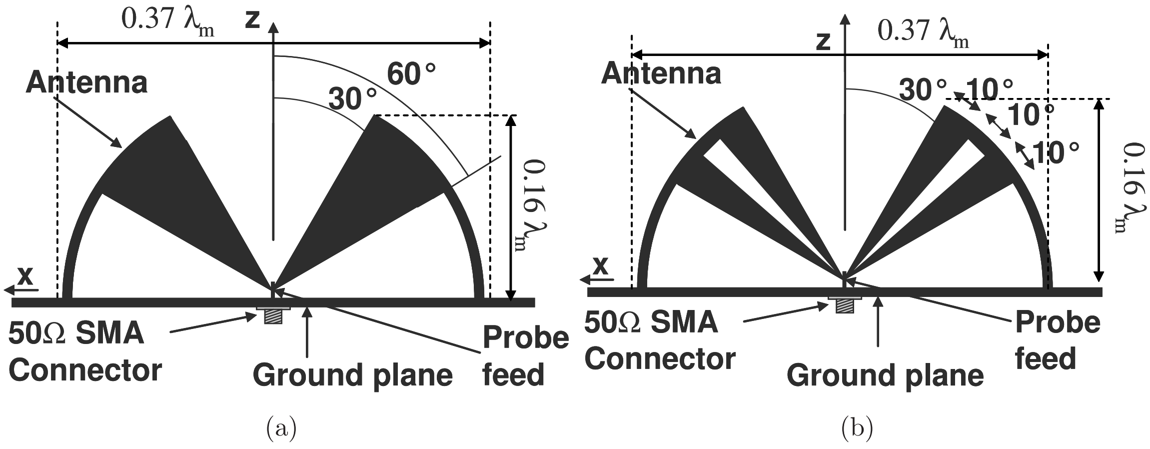

Figure 7.8: Topology of the modified CSLAs of Section 7.2. (a) M1 CSLA. (b) M2-CSLA.

Antenna Type	Frequency Range	BW	Highest VSWR
Original CSLA	1.7 GHz - 14.5 GHz	8.50:1	2.2
M1-CSLA	2.0 GHz -14.7 GHz	7.35:1	2.2
M2-CSLA	2.05 GHz - 15.3 GHz	7.46:1	2.2

Table 7.1: Bandwidths of original, M1-, and M2-CSLAs.

and examining the current distribution reveals that the electric current density is larger around the edges at $\theta = 30°, 60°$ and has lower values in the area between $(30° < \theta < 60°,\ \phi = 0°, 180°)$. Therefore, two other pie-slice sections of the antenna, which are confined in the ranges $40° < \theta < 50°$ for $\phi = 0°$ and $180°$, can be removed to obtain the antenna shown in Figure 7.8(b). For obvious reasons, this antenna is called M2-CSLA. Prototypes of M1- and M2-CSLA with $\alpha = 60°$, $R_{in} = 27.8$ mm and $R_{out} = 28$ mm are fabricated on a thin substrate with thickness of 0.5 mm and dielectric constant of 3.4 and are mounted on a 20 cm $\times$ 20 cm square ground plane. The measured input reflection coefficients of these two antennas are given in Figure 7.9 along with the S_{11} of the original CSLA with the same dimensions. It is seen that all of the antennas have VSWRs lower than 2.2 in a very large frequency band as shown in Table 7.1. The best input match is, however, observed for M2-CSLA with a VSWR lower than 2 across its entire band of operation.

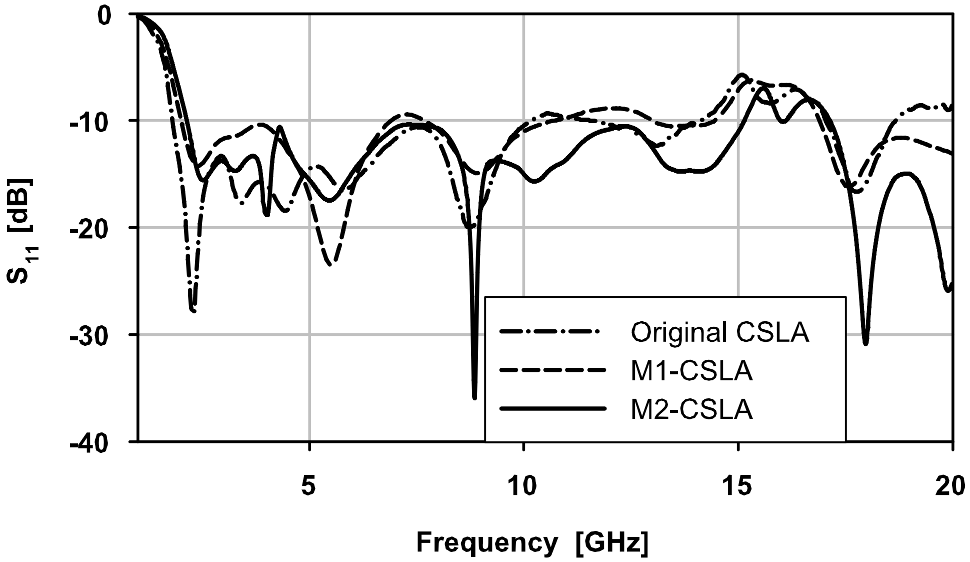

Figure 7.9: Measured S_{11} values of the original CSLA of Section 7.1 and M1- and M2-CSLAs of Section 7.2.

The radiation patterns of M2-CSLA are measured at three different planes at eight discrete frequency points and are presented in Figures 7.10, 7.11, and 7.12. The co-polarized, E_θ, and cross-polarized, E_ϕ, far-field radiation patterns in the azimuth plane are shown in Figure 7.10 and are observed to be similar to those of the original CSLA. The elevation patterns at two different planes ($\phi = 0°, 180°, 0° \leq \theta \leq 180°$) and ($\phi = 90°, 270°, 0° \leq \theta \leq 180°$) are measured and reported in Figures 7.11 and 7.12. It is observed that, similar to the original CSLA, the minor side lobe levels increase with frequency.

The gains of the three CSLAs are measured in the anechoic chamber of the University of Michigan in the frequency range of $f = 2$ GHz-16 GHz using a double-ridge standard horn reference antenna and are presented in Figure 7.13. The gain of the antennas are measured at $\phi = 90°, \theta = 90°$. As frequency increases, the electrical dimensions of the antenna increase and therefore, the antenna gain should increase. However, as is observed from Figure 7.13, the antenna gain decreases as frequency increases from 6 GHz up to 10 GHz. This is a consequence of the change in the direction of maximum radiation in the azimuth plane as is observed from Figures 7.4

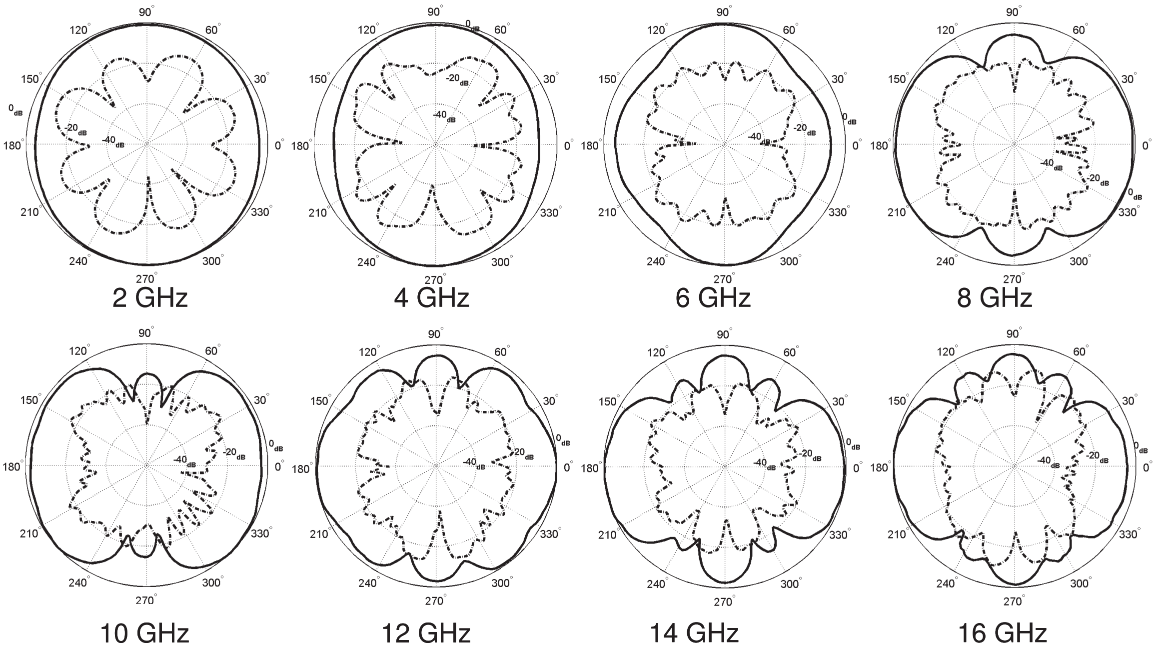

Figure 7.10: Measured radiation patterns of M2-CSLA in Section 7.2 in the azimuth plane. The solid line is co-pol (E_θ) and the dash-dotted line is the cross-pol (E_ϕ) components.

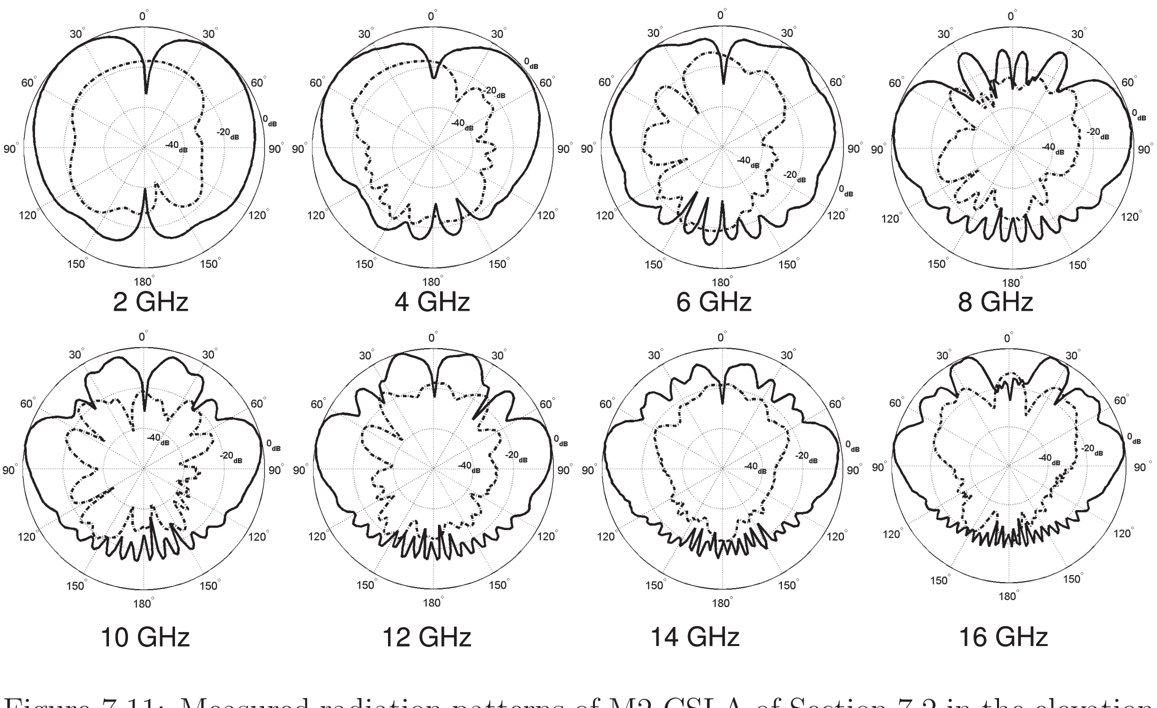

Figure 7.11: Measured radiation patterns of M2-CSLA of Section 7.2 in the elevation plane ($\phi = 0°, 180°,\ 0° \leq \theta \leq 180°$). The solid line is co-pol (E_θ) and the dash-dotted line is the cross-pol (E_ϕ) components.

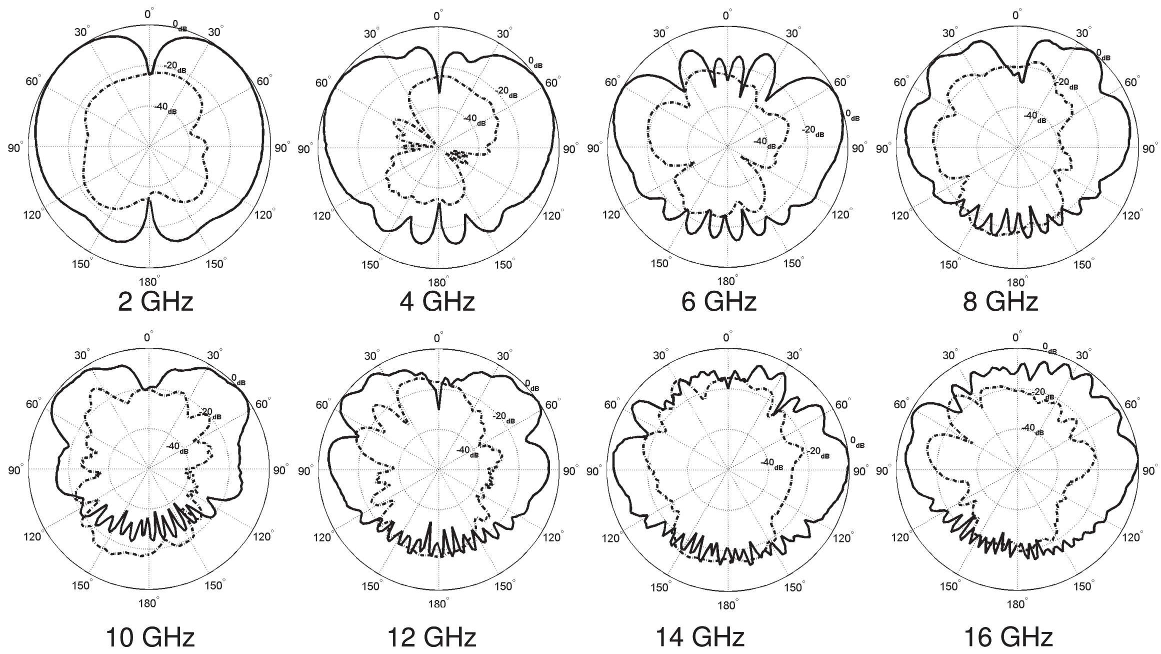

Figure 7.12: Measured radiation patterns of M2-CSLA of Section 7.2 in the elevation plane ($\phi = 90°, 270°$, $0° \leq \theta \leq 180°$). The solid line is co-pol (E_θ) and the dash-dotted line is the cross-pol (E_ϕ) components.

and 7.10.

7.3 Time Domain Measurements

As shown in the previous section, the proposed antennas, and particularly M2-CSLA, present a very wide bandwidth. However, having a wideband frequency-domain response does not necessarily ensure that the antenna behaves well in the time domain as well; that is, a narrow time-domain pulse is not widened by the antenna. Some multi-resonant wideband antennas, such as log-periodic antennas, due to multiple reflections within the antenna structure, widen a narrow pulse in time domain. Therefore, in order to ensure the usefulness of the proposed antenna for time-domain applications, the time-domain responses of the antennas must also be examined. The time-domain reflection coefficients of the CSLAs are measured using the time-domain capabilities of an HP8720B network analyzer. The network

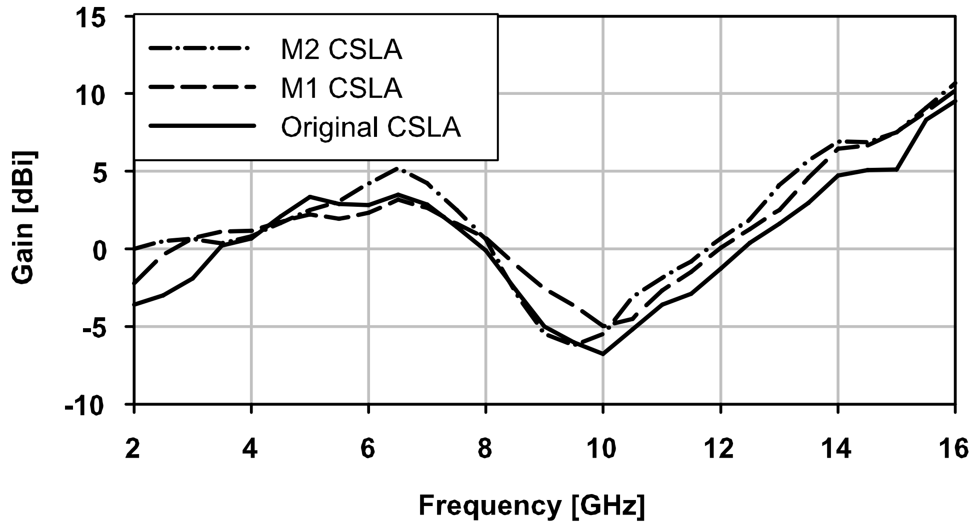

Figure 7.13: Measured gain of the original CSLA of Section 7.1 and M1- and M2-CSLAs of Section 7.2. The gains are measured in the azimuth plane at ($\phi = 90°$, $\theta = 90°$).

analyzer calculates the time-domain response by measuring the wideband frequency-domain response (in this case in the 2-12 GHz band) and calculating its inverse Fourier transform to obtain an approximation of the impulse response of the network. Figure 7.14 shows the time-domain variations of the reflection coefficients, $|\Gamma|$, of these three antennas in logarithmic scale. It is observed that all of the antennas have a reflection at $t = 0$ ns, which corresponds to the discontinuity at the plane of calibration (input of the SMA connector). The peak reflection at $t = 80$ ps corresponds to the probe-antenna transition. M2-CSLA shows stronger small reflections, which is a consequence of the larger number of discontinuities in its structure.

In addition to the input reflection coefficient, the time-domain impulse responses of a system that contains two identical CSLAs (Original CSLA, M1-CSLA, or M2-CSLA) are also measured. The measurement setup is shown in Figure 7.15. The antennas are placed 30 cm apart and parallel to each other inside an anechoic chamber. The normalized time-domain impulse response of this system is measured and presented in Figure 7.16 along with the time-domain impulse response of a coaxial cable with the same electrical length as a reference. It can be seen that the multiple small peaks

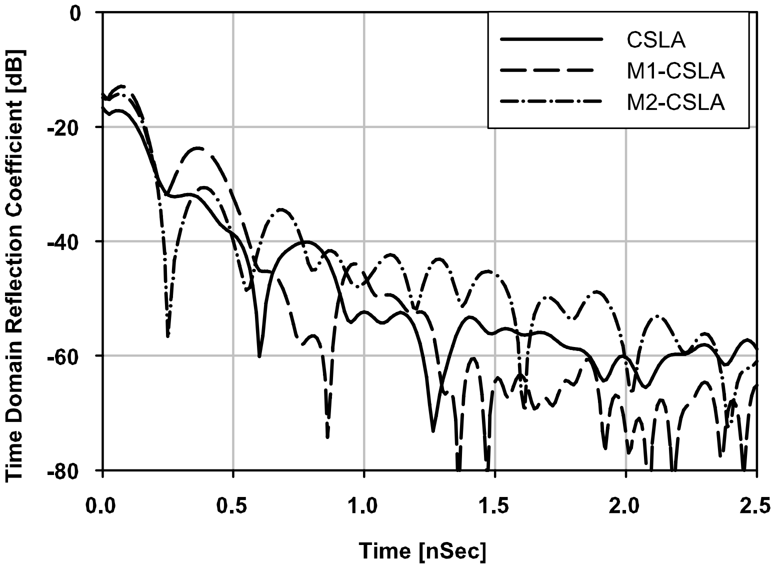

Figure 7.14: Time-domain reflection coefficients, $|\Gamma|$, of the original CSLA of Section 7.1 and M1- and M2-CSLAs of Section 7.2.

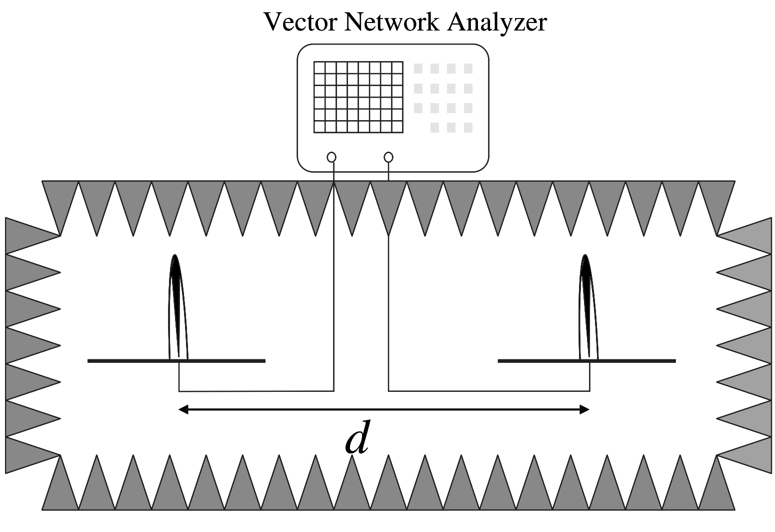

Figure 7.15: The setup used for measuring the time-domain impulse responses of three different CSLAs.

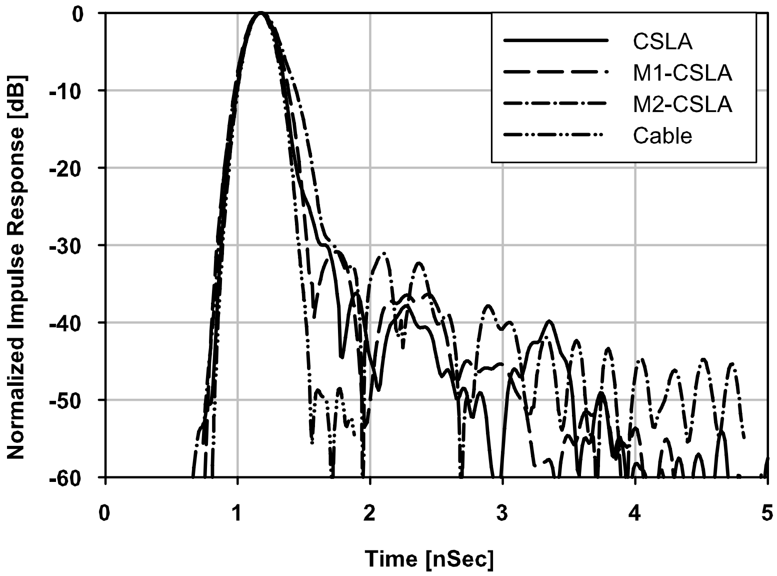

Figure 7.16: Time-domain impulse response of the system consisting two identical CSLAs as shown in Figure 7.15.

that come after the main peak are at least 30 dB lower in magnitude than the main peak. It is also observed that the original CSLA and M1-CSLA have a response that is closer to that of the coaxial cable (which ideally should be a delta function) than is the impulse response of M2-CSLA. The time-domain impulse response of M2-CSLA is more distorted and has stronger multiple reflections, which are caused by the larger number of discontinuities in its structure.

7.4 Conclusions

A novel ultra-wideband coupled sectorial loop antenna is designed and is shown to have a 8.5:1 impedance bandwidth. The antenna has consistent radiation parameters over a 4.5:1 frequency range with excellent polarization purity over the entire 8.5:1 frequency range. Modified versions of this antenna, with reduced metallic surfaces and similar radiation parameters, were also designed, fabricated, and measured. Furthermore, the time-domain impulse-response measurement results show that the antenna does not significantly distort the temporal response of a signal whose spectral content does not fall outside the operating band of the antenna.

CHAPTER 8

Conclusions and Future Work

8.1 Conclusions

The main subject of this thesis was to develop techniques for designing miniaturized antennas and address the adverse affects of miniaturization. Arguably, the most important adverse affect of miniaturization is the reduction in the antenna bandwidth that occurs. Therefore, most of this thesis was devoted to introducing novel techniques that can be used to enhance the bandwidth of (miniaturized) antennas. Some of the techniques that were used in this dissertation are well known techniques that are used in a new context and in novel designs. These include parasitic coupling for bandwidth enhancement of miniaturized antennas and electronically changing the frequency response of the antenna as a means of bandwidth enhancement. Is was shown that invoking these well-known concepts in novel designs and architectures can result in antennas with significantly enhanced performance over current state-of-the-art designs reported in literature. Other techniques and topologies used in this dissertation are, to the best of my knowledge, reported for the first time in this thesis. These include, creating a fictitious resonance in microstrip-fed slot antennas, distributed inductive loading for antenna miniaturization, bi-semicircular topology for enhancing the bandwidth of slot and strip loop antennas, and the coupled sectorial loop antennas for UWB applications.

Although the main goal of this dissertation was to develop techniques to address the adverse effect of antenna miniaturization, the techniques that are developed are self-sufficient and can be used individually, or in conjunction with one another, in a number of other applications. Multi-band cellular phones, multi-standard PCS devices, implantable biomedical devices, UWB radios, etc. are examples of some applications in the Telecommunications, Biomedical Therapies, and Computer Industry that can benefit from the contributions of this Ph.D. dissertation.

8.2 Future Work

8.2.1 Miniaturized Antennas for Wireless Integrated Micro-Systems

The goal of the center for Wireless Integrated MicroSystems (WIMS) at The University of Michigan is to develop functional microsystems that could be either in the form of an implantable neural prostheses or in the form of an integrated environmental monitoring sensor network. In the environmental test-bed, the goal is to design miniaturized microsystems that include some kind of an environmental sensor (e.g., a temperature or μgas sensor), the appropriate analog and digital circuitry that are required to post process the data, and a wireless interface that uses an integrated antenna to transmit and receive RF signals. The overall dimensions of the system is expected to be smaller than 1 cm $\times$ 1 cm $\times$ 1 cm and the wireless interface uses the Zigbee standard for communicating at the ISM band at 2.4 GHz. Therefore, the maximum linear dimensions of the antenna used in this system must be smaller than about 1 cm $\times$ 1 cm. As mentioned in this dissertation, such antennas have very small bandwidth and efficiency. An example of a 2.4 GHz miniaturized antenna occupying an area of about 3.5 mm $\times$ 3.5 mm is shown in Figure 8.1. The

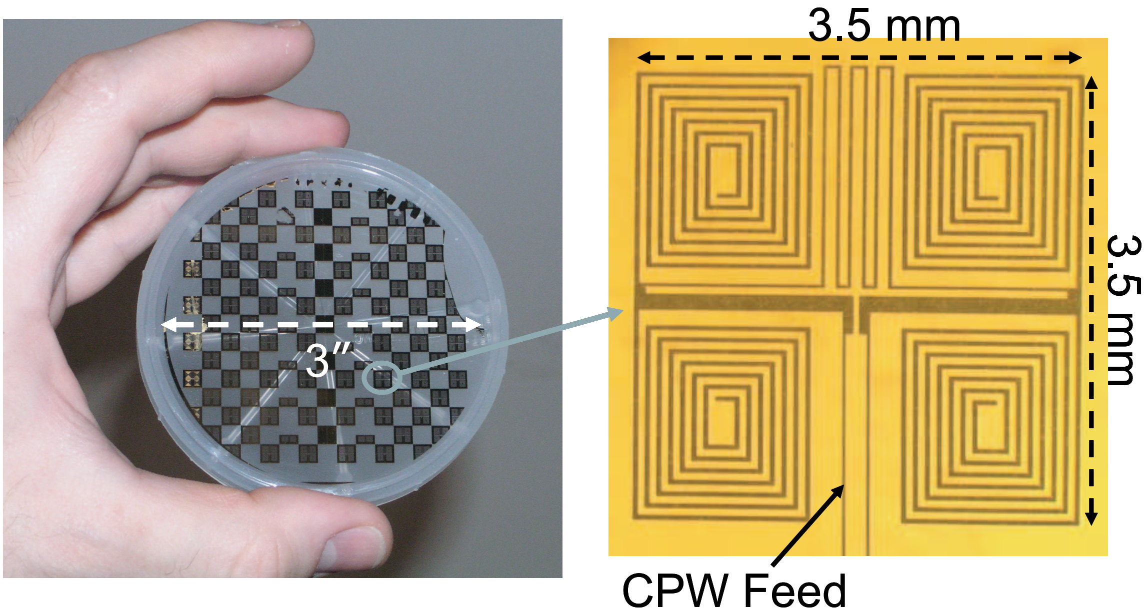

Figure 8.1: Photograph of a miniaturized antenna fabricated on a high-resistivity wafer. The antenna operates at 2.4 GHz and occupies an area of about 3.5 mm $\times$ 3.5 mm.

electrical dimensions of this antenna are about $0.027\lambda_0 \times 0.027\lambda_0$. This antenna is about 20 times smaller than traditional slot or patch antennas with the same resonant frequency. The dimensions of this antenna are small enough for the WIMS application. However, this antenna has a very narrow bandwidth (0.5% fractional impedance bandwidth). Therefore, it is of utmost importance to enhance the bandwidth of this antenna, in order to satisfy the requirements of the WIMS project. This can be done using techniques presented in Chapters 4 and 5 of dissertation.

The next natural step in continuation of the research presented in this dissertation is to use the topology presented in Figure 8.1 with the bandwidth enhancement techniques discussed in this dissertation. This can result in miniaturized slot antennas with enhanced bandwidth. These antennas can become viable candidates for miniaturized wireless communication devices such as the WIMS integrated sensor project.

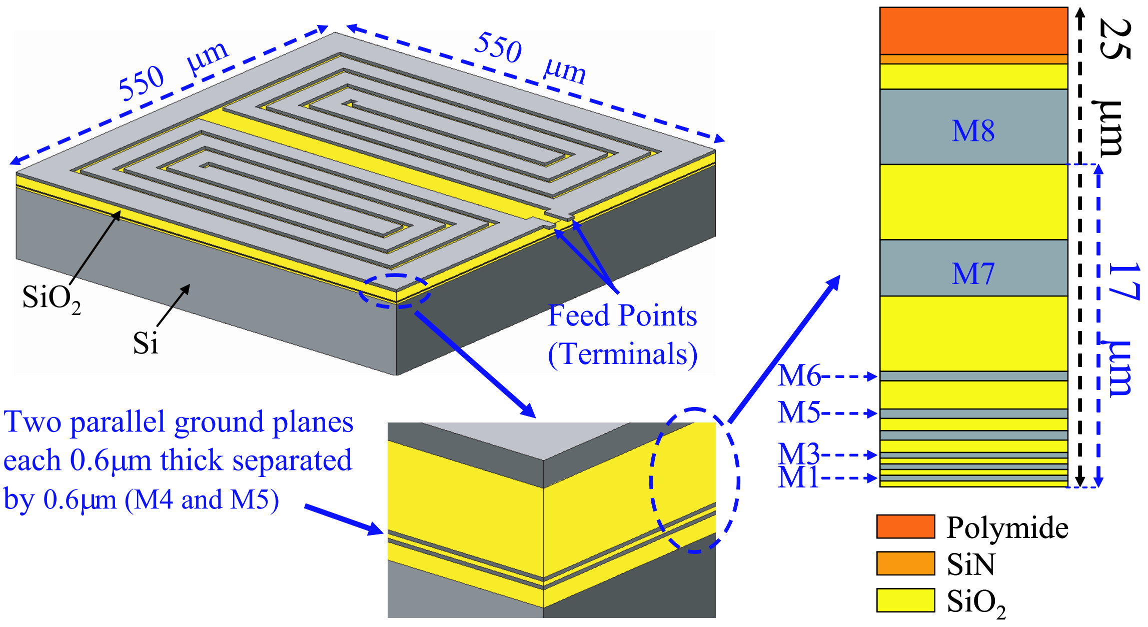

Figure 8.2: Topology of a 10 GHz on-chip miniaturized slot antenna. The antenna is designed using IBM 0.13 μm RF CMOS process.

8.2.2 On-Chip Miniaturized Slot Antennas

The ultimate goal of today's wireless system designers is to integrated every component of a wireless system on a chip or in a small package. Since antennas are the largest components of wireless systems, antenna miniaturization is of particular importance. Many of the miniaturization techniques that have been developed so far, including the techniques discusses in this dissertation, can be used to design the first generation of on-chip antennas. However, in on-chip applications, occupying an small area on a chip is of utmost importance. This necessitates reducing the antenna dimension as much as possible. Figure 8.1 shows a photograph of the 2.4 GHz Zigbee slot antenna that occupies an area of about 3.5 mm $\times$ 3.5 mm. Even though this antenna is , electrically, very small, its physical dimensions are still very large for placing it on a chip. However, if the frequency of operation is increased, it would be possible to use a similar topology in order to implement a miniaturized on-chip antenna.

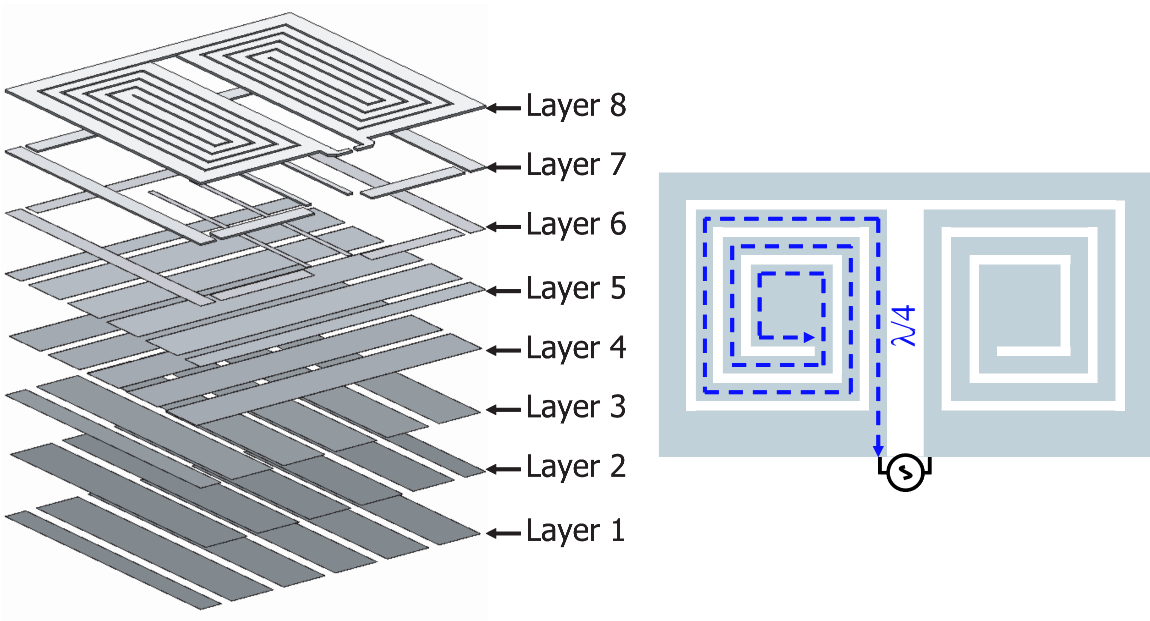

Figure 8.3: Schematic of different layers of the on-chip miniaturized antenna shown in Figure 8.2.

Figure 8.2 shows the topology of a miniaturized, on-chip antenna that operates at 10 GHz; the antenna is a $\lambda/4$ notch slot and occupies an area of about 550 μm $\times$ 550 μm. This antenna is designed to operate on a low-resistivity silicon chip using the IBM 0.13 μm CMOS RF process. In this process, the silicon substrate is about 300 μm thick and has bulk conductivity of $\sigma = 50 - 100$ S/m. On top of this silicon substrate, a 17 μm thick Silicon Dioxide (SiO_2) layer exists that host 8 different metallic layers, as shown in Figure 8.2 and Figure 8.3. In order to separate the radiating parts of the antenna from the lossy silicon substrate, two floating ground metallic layers are used as shielding planes as shown in Figure 8.3. Other metallic layers on this structure must be filled with dummy structures in order to satisfy the design rules. This antenna is followed by a 10 GHz LNA that is matched to the input impedance of the antenna. The combination of the miniaturized slot antenna and the LNA forms the first generation of integrated on-chip RF front-ends using this type of miniaturized slot antenna. One drawback of this type of antenna is its small radiation efficiency caused by the presence of the low-resistivity silicon substrate. Enhancing the efficiency of the antenna in the presence of the lossy silicon substrate is perhaps the major task that still needs to be accomplished. This allows for using such antennas in truly integrated on-chip transceivers.

8.2.3 Metamaterials and Antenna Miniaturization

The techniques used to reduce the size of antennas can be categorized into two different categories. Antenna miniaturization using magneto-dielectric materials and antenna miniaturization using optimum antenna topology. It is possible to reduce the dimensions of an antenna by virtue of loading it with a material that has a very large permittivity (ϵ_r) or permeability (μ_r) value. The latter case is mostly used for low frequency applications, where magnetic materials, such as ferrites, have significantly large μ_r values. In recent years, researchers have developed artificial electro-magnetic materials at microwave frequencies. These materials include artificial magnetic conductors, reactive impedance surfaces (also known as high-impedance surfaces), and magneto-dielectric materials. These materials have been used as substrates for planar antenna to reduce their overall physical dimensions; Figure 8.4 shows several examples of such miniaturized antennas developed at The University of Michigan.

The miniaturization techniques presented in this dissertation are examples of techniques that use optimal antenna topology in order to achieve antenna miniaturization. Combining the two miniaturization techniques mentioned here is an interesting direction for future research. Using metamaterials as substrates for planar miniaturized antennas creates the possibility of further reducing the dimensions of the antenna and enhancing its bandwidth and radiation efficiency.

8.2.4 RF-MEMS Bases Reconfigurable RF Front Ends

Micro-Electro-Mechanical-Systems (MEMS) are micro-scaled devices that provide a link between mechanical and electrical phenomena and are fabricated using micro-

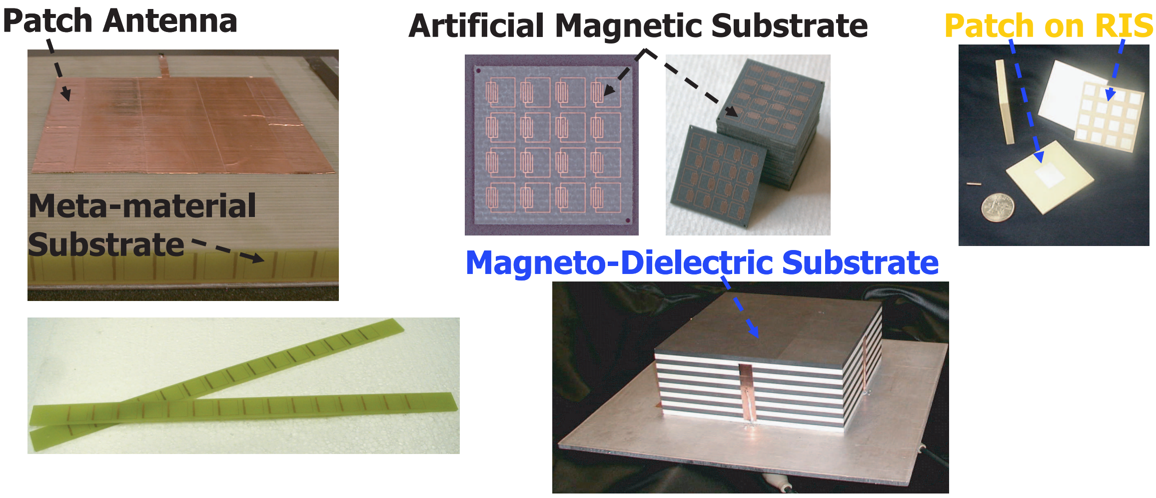

Figure 8.4: Photograph of a number of compact antennas fabricated on metamaterial substrates (photo courtesy of Prof. Kamal Sarabandi).

fabrication techniques used in the Integrated Circuit (IC) industry. MEMS were initiated in 1970s and have been developed for accelerometers, gyroscopes, pressure sensors, temperature sensors, bio-sensors, etc. One sub-area of the field of MEMS, which deals with devices that work at microwave frequencies, is called RF (Radio Frequency) MEMS. Due to its outstanding performance, RF MEMS has immense potential for commercial and defense applications. One of the most important components in the RF/Microwave applications is RF MEMS switch. It is essentially a miniature device, which uses mechanical movement to achieve an open or short circuit in a transmission line. One example of such switches is the capacitive switch shown in Figure 8.5. In this case, the switch has two different states. The up state, in which the device has a very low capacitance (e.g., 35 fF), and the down state, in which the device has a considerably larger capacitance value (e.g., 1.2 pF). These MEMS switches can be used in the design of reconfigurable antennas and RF circuits. Figure 8.5 shows a switchable slot antenna that uses two parallel capacitive RF MEMS switches. This antenna operates in the Ka Band. The antenna is simulated using IE3D and the simulations results are presented in Figure 8.6. It is observed that the antenna can operate in the frequency range of 27 GHz to 40 GHz by using four

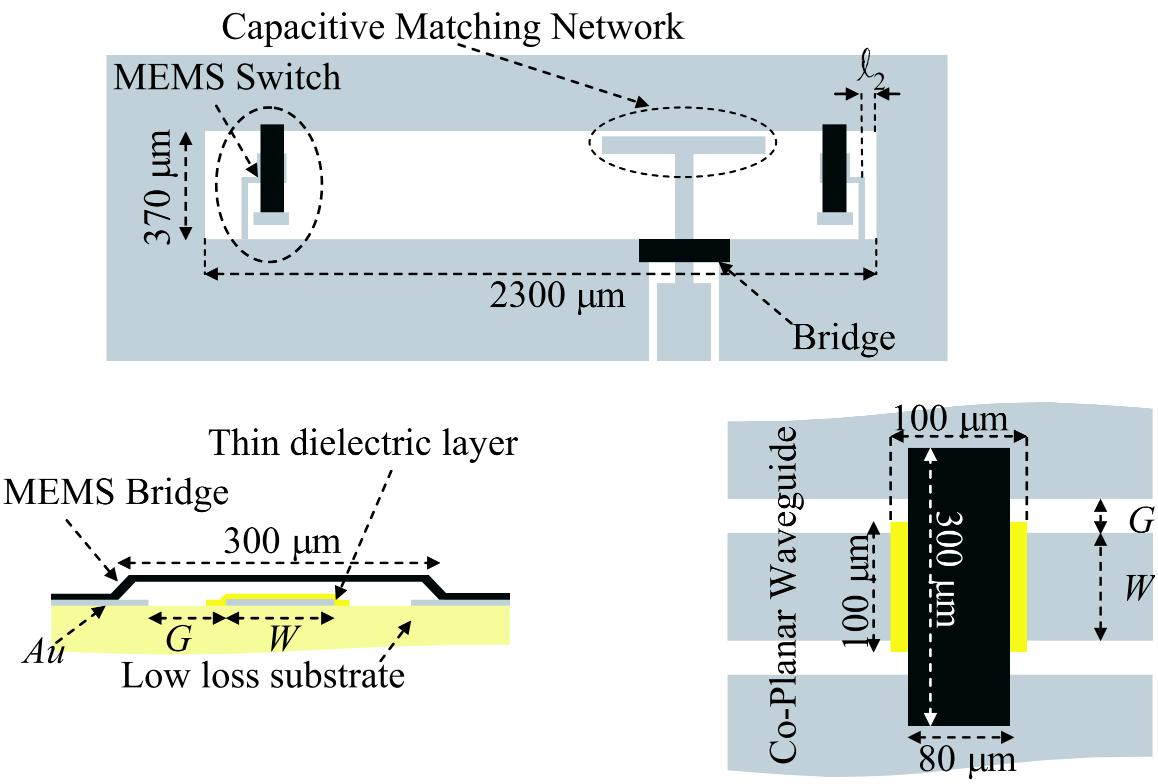

Figure 8.5: Topology of a 2-bit reconfigurable slot antenna. The antenna uses 2 capacitive RF MEMS switches to achieve reconfigurability.

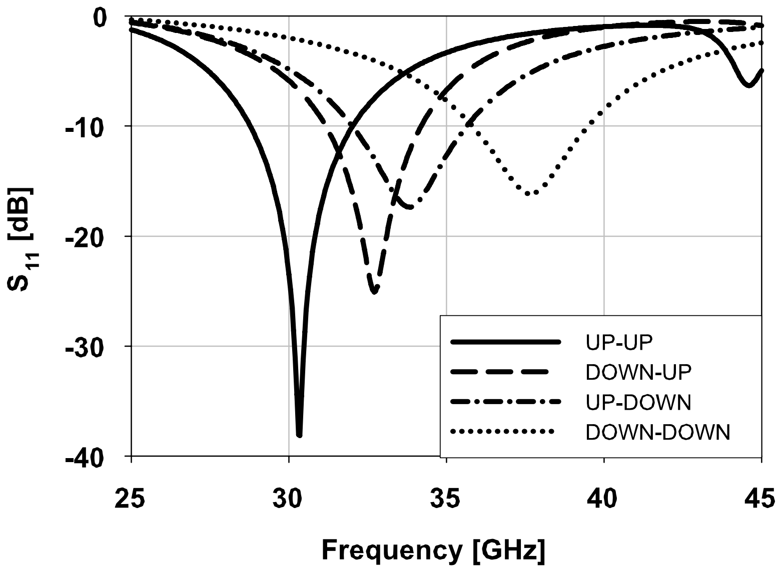

Figure 8.6: Simulated S_{11} results of the 2-bit RF MEMS switchable antenna shown in Figure 8.5.

different switch combinations (see Figure 8.6). An interesting direction of future work is to use these antennas in designing totally reconfigurable, integrated transceivers at millimeter wave frequencies.

8.2.5 Miniaturized Radomes for Small Antennas

Frequency selective surfaces (FSS) have been the subject of intensive investigation for their widespread applications as spatial microwave and optical filters for more than four decades. Frequency selective surfaces are usually constructed from periodically arranged metallic patches of arbitrary geometries or their complimentary geometry having aperture elements similar to patches within a metallic screen. These surfaces exhibit total reflection or transmission, for the patches and apertures respectively, in the neighborhood of the element resonances. The most important step in the design process of a desired FSS is the proper choice of constituting elements for the array. The element type and geometry, the substrate parameters, the presence or absence of superstrates, and inter-element spacing generally determine the overall frequency response of the structure, such as its bandwidth, transfer function, and its dependence

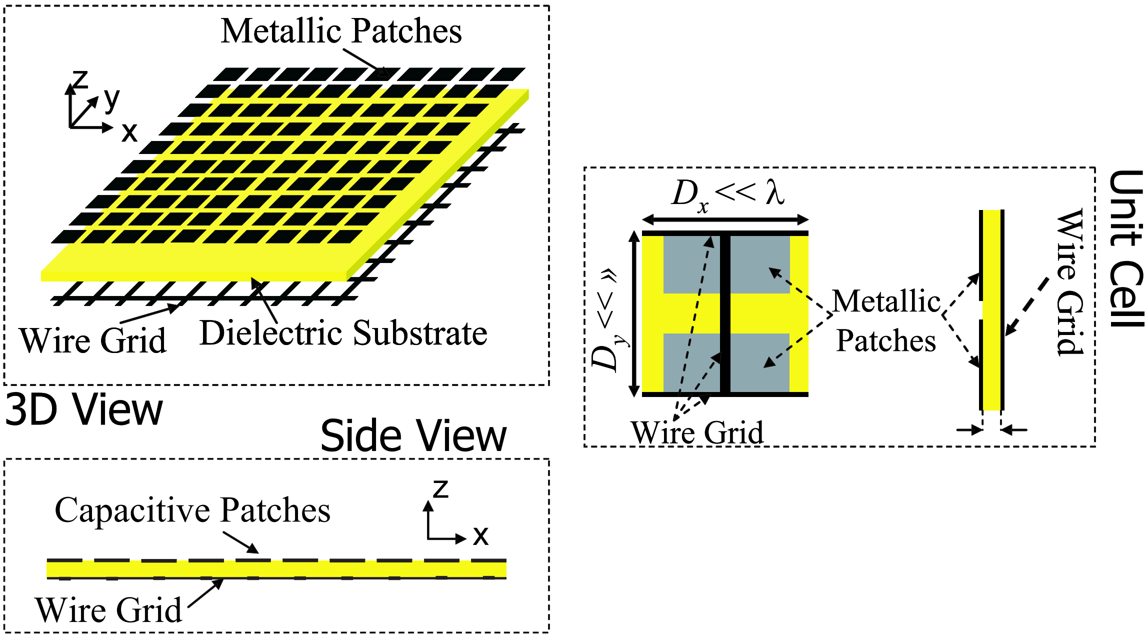

Figure 8.7: Topology of a band-pass FSS designed based on the concept of metamaterials and equivalent media.

on the incidence angle and polarization. The shapes and configurations that can be chosen for the FSS elements are limited only by the imagination of the designer.

One common feature of the FSSs is that the size of the resonant elements and their spacing are comparable to half a wavelength at the desired frequency of operation. In practice frequency selective surfaces have finite dimensions. In order to observe the desired frequency response, the finite surface must include a large number of the constituting elements (usually more than 400 that typically corresponds to an area of $10\lambda \times 10\lambda$) and be illuminated by a planar phase front. For some applications, such as antenna radomes at lower frequencies, frequency selective surfaces of relatively small electrical dimensions that are less sensitive to incidence angle and can operate for non-planar phase fronts are highly desirable. Radomes for miniaturized low-frequency antennas and antenna arrays is an example of this category.

In recent years, the concept of artificially engineered materials have been used for a variety of different wireless applications. These materials exhibit properties, such as negative real permittivity or permeability, that are not usually observed in

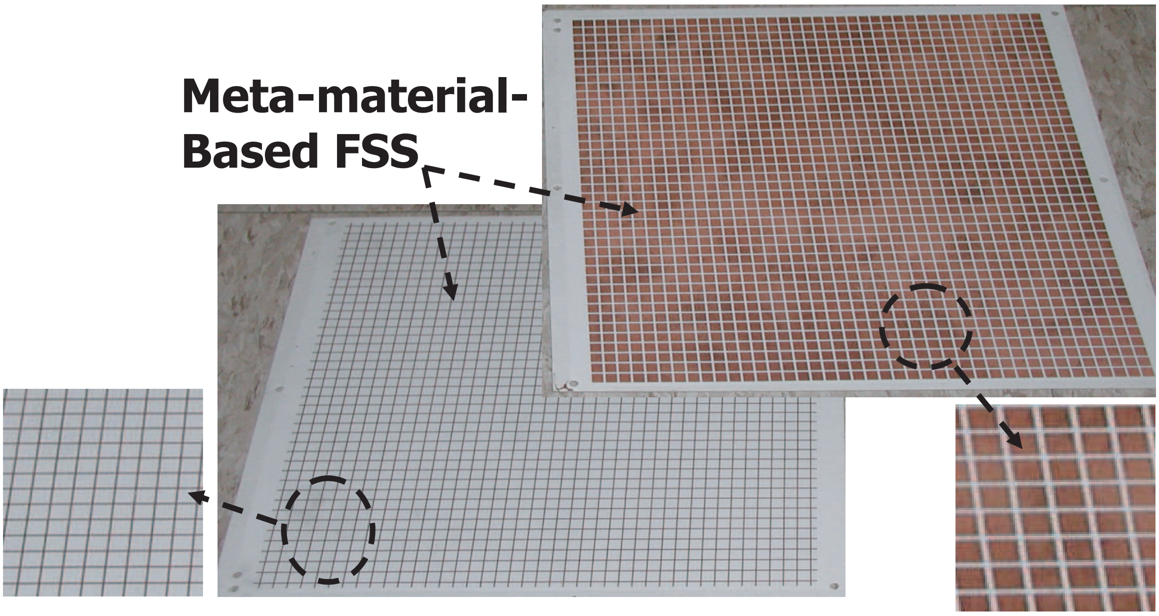

Figure 8.8: Photograph of a band-pass FSS.

nature. A popular method to engineer such structures is to use periodic structures of resonant unit-cells with periods and unit cell dimensions that are much smaller than the operating wavelength. This way, a relatively small effective medium with the desired properties (e.g. negative real permittivity) can be obtained. Figure 8.7 and Figure 8.8, show a new type of engineered material that can act as a first order band-pass frequency selective surface. The structure consists of a periodic array of small metallic patches printed on one side of a dielectric substrate and a wire grid structure printed on the other side, both having the same period. The periodicity of the printed patterns is much smaller than the wavelength of operating frequency. A unit cell of this structure consists of two halves of two adjacent patches backed by a piece of wire on the other side of the substrate. The wire acts as an inductor and the two patches separated by a small gap act as two plates of a printed capacitor. The combination therefore acts as a parallel LC circuit having a band-pass characteristic. The substrate is formed by periodically repeating this unit cell in two dimensions. In the future, studying possibilities of designing FSSs of any order using the filter theory and cascading a number of such layers such that the spacing between the elements act as impedance inverters, can be carried out. By choosing the number of layers, controlling the coupling coefficient between layers, and choosing an appropriate resonant frequency of each layer, multi-band and wideband FSS operation can easily be implemented.

APPENDIX

APPENDIX A

A Measurement System for Ultra Wideband Communication Channel Characterization

In order to assess the performance of any communication system it is necessary to characterize the communication channel. Channel characterization can be done in two ways: 1) experimentally and 2) by computer simulation. Some of the more commonly used attenuation models are heuristic, based on measured data [119, 120]. In some cases overly simplified electromagnetic formulations [121], with little correlation to the physics of the problem, have also been used. Thus, while simple to implement, these models lack the desired accuracy and generality.

In recent years significant efforts have been devoted towards the development of physics-based electromagnetic (EM) models, which apply analytic and numeric techniques for channel modeling [122, 123, 124, 125, 126, 127, 128, 129, 130, 131]. These models allow for characterization of the communications channel to a high degree of fidelity. Furthermore, they can be used to simulate different propagation environments, including the polarimetric aspects of the channel.

Despite significant progress in this area, experimental characterization of a communications channel is still necessary for gaining insight into the mechanisms of wave propagation as well as for the validation of computer models. Past experimental work on channel characterization has been carried out often over limited bandwidths [132, 133, 134, 135, 136, 137], and at times for specific systems such as AMPS and PCS wireless communication systems [138]. In these experimental efforts, limited channel characteristics such as path loss and fading statistics have been determined. Although channel characterization over a narrow bandwidth is straightforward, coherent measurements over a wider bandwidth is significantly more complex. Basically, the problem stems from the fact that coherent receivers with a wide bandwidth allow significant noise power to enter the receiver, which limits the system's dynamic range. Measurement systems employing a single vector network analyzer have been proposed for indoor channel characterization efforts [139, 140, 141, 142]. With this approach, coherent, wideband propagation measurements can be performed over relatively short distances. To maintain coherence, the signal generated by the network analyzer is relayed to the distant transmitter via long RF cables or optical links [142]. While this approach performs well in an indoor setting, it is impractical for an outdoor setting where multiple sites, often behind significant foliage, need to be accessed. To circumvent this problem a novel approach, based on a stepped frequency technique is developed. The system uses two vector network analyzers (VNAs), one as a transmitter and one as a receiver and is synchronized in frequency step by using two rubidium atomic clocks. The sensitivity of the receiver is determined by the intermediate frequency (IF) filter internal to the VNA, which can be set as low as 3 Hz. The combination of the narrowband IF filter and the synchronized frequency sweep allows for highly sensitive measurements to be performed over a very wide bandwidth. This bandwidth is in principle limited by the antennas and the specific VNAs used. In Section A.1, the design and operating principles of the system are discussed and in Section A.2 results from a measurement campaign, conducted at the Lakehurst Naval Air Station, in Lakehurst, New Jersey, are presented and analyzed. Also in Section A.2 the techniques used for post processing the data, extracting the

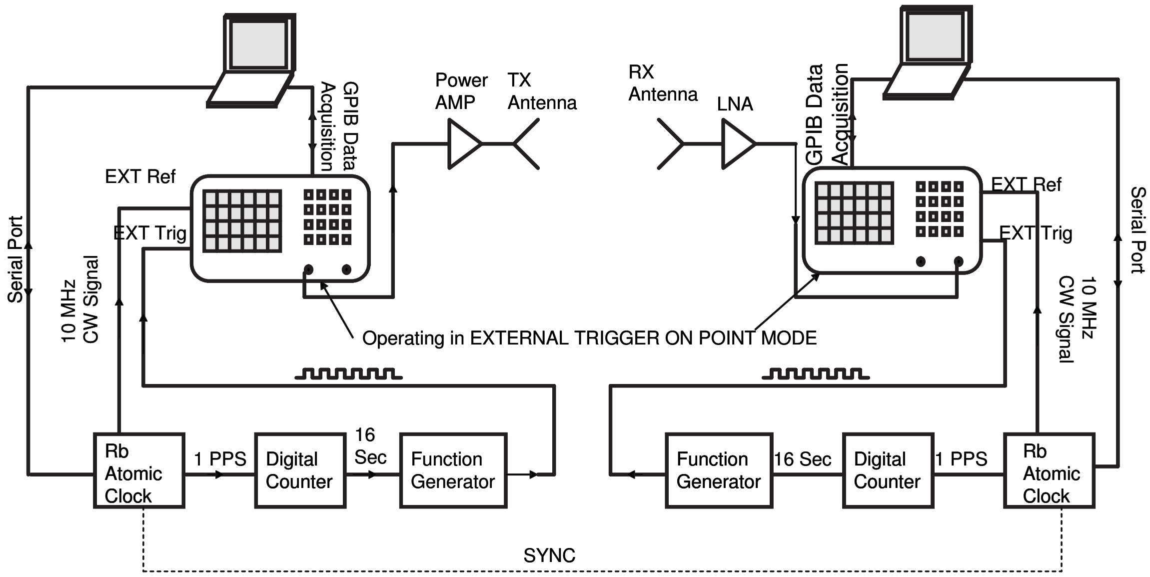

Figure A.1: Block diagram of the propagation measurement system.

attenuation characteristics of the channel, and its frequency decorrelation are studied.

A.1 Wideband Measurement System

A VNA is a microwave measurement instrument capable of measuring both the amplitude and phase of the reflection and/or transmission coefficients of the device under test (DUT). In addition to different processing and calibration units, any VNA has a microwave signal generator, which can be either in the form of an analog sweeper or a synthesized source, and a number of built in, high performance vector receivers capable of measuring both the amplitude and phase of the input signal. The microwave sweeper allows for rapid acquisition of the signal in broadband measurements. It also provides a constant output power over the entire frequency band. For accurate phase measurements, the receiver uses a phase lock loop (PLL) and either an internal or an external source as a reference signal for the PLL. Most VNAs such as the HP8753D or HP8720D have the option to use an external continuous wave (CW) reference (usually a 10 MHz sinusoidal wave). This allows the user to select a

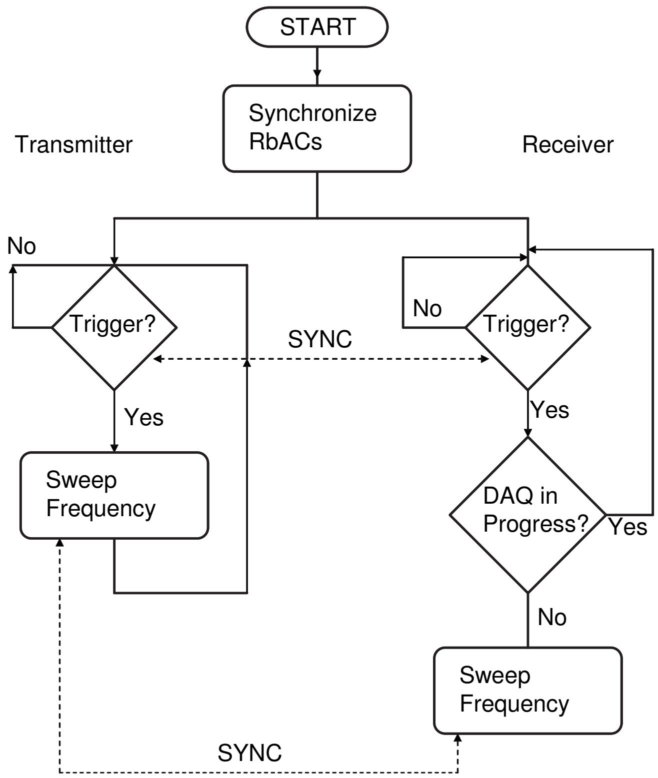

Figure A.2: Flow chart of the system operation.

highly-stable CW signal as a frequency reference, in order to achieve high accuracy.

A communication channel can be viewed as a two port passive device with input and output ports located at the transmitter and receiver respectively. The advantages of using a VNA as the transceiver are its stepped frequency mode of operation and its inherent ability to sweep over a wide frequency band (50 MHz - 20 GHz for an HP8720D) while maintaining a high receiver sensitivity. To maximize receiver sensitivity the receiver bandwidth (IF filter) can be set as low as 3 Hz while sweeping through a wide frequency band. This allows for coherent measurements (magnitude and phase) of very weak signals over a wide dynamic range. Unlike most two port devices, however, the ports of this system are distant from each other and in order to perform transmission (S_{21}) measurements, it is necessary to employ two VNAs, one as a transmitter (Tx) and one as a receiver (Rx). In addition, amplifiers, antennas, filters, and data acquisition systems are also needed. The difficulty of this type of

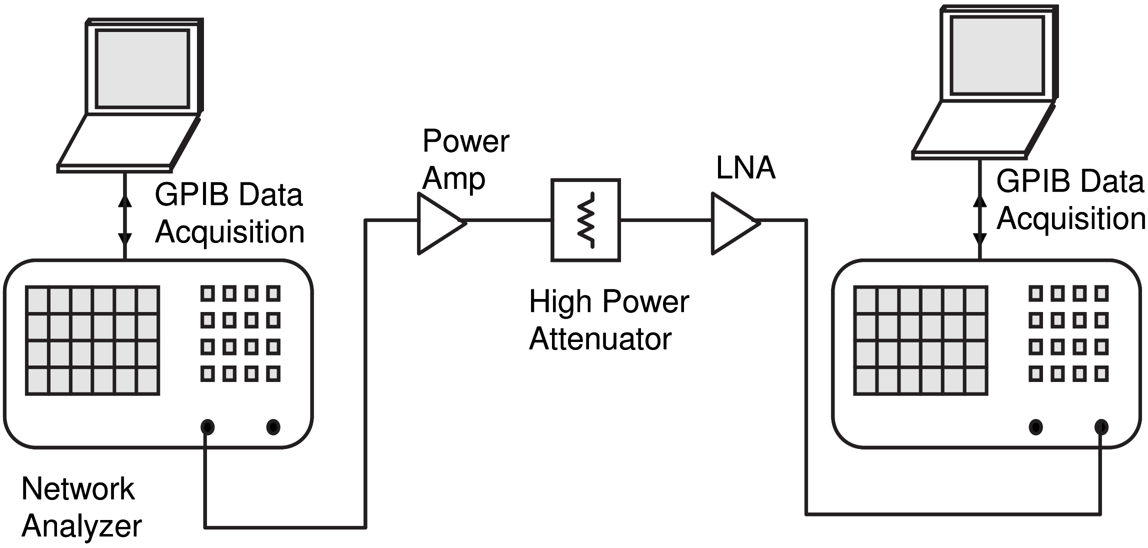

Figure A.3: Block diagram of the calibration set-up of the system.

disconnected system is in providing a common, stable reference to the PLLs of both VNAs, and also in synchronizing their respective frequency sweeps. Both of these difficulties are solved by using two identical, highly-stable synchronized Rubidium Atomic Clocks (RbAC) [143]. Synchronization of the time references of these atomic clocks is accomplished by simply connecting the time reference output of one to the time reference input of another. Once synchronized, each atomic clock provides what is essentially a common highly-stable 1 Pulse Per Second (PPS) system clock (which synchronizes the respective frequency sweeps). In addition, the RbACs also provide an ultra-low-noise highly accurate and stable frequency standard operating at 10 MHz. This 10 MHz CW reference is used as the reference for the VNA PLLs. The short term and long term stability of these atomic clocks are, respectively, $1 \times 10^{-12}/10$ sec and $5 \times 10^{-10}/\text{year}$.

In order to measure the channel response correctly, both the transmitter and the receiver must synchronously sweep through the frequency band. The allowed timing error must lie within the ± 3 dB bandwidth of the receiver IF filter, around the frequency being measured. For large propagation delays, which cause a timing error outside this allowed range, a delay can be introduced in the timing of the receiver

RbAC to account for the propagation delay. This delay is controlled by the serial port line to the data acquisition computer, shown in the system block diagram in Figure A.1. In results shown later, however, propagation loss over distances of up to 1.1 km were measured without a need for any timing adjustments to the receiver clock. The atomic clocks could be used to trigger each sweep through the frequency band and the VNAs allowed to then independently sweep through the band. There is, however, sufficient difference in the nominal sweep times of each independent VNA, even when set to be identical, to cause the system to loose synchronization. Therefore, the atomic clocks are used to trigger a function generator that sends a burst of TTL compatible pulses to the VNA and with each pulse moves the VNA, step by step, through each discrete frequency point to be measured in the band. This is accomplished by operating the VNAs in the "External Trigger On Point" mode. In this mode an external trigger is required, at the "EXT TRIG" input of the VNAs, to step the network analyzers to through each discrete frequency point in the measurement band. This can be seen in Figure A.1, which shows a block diagram of the measurement system. Figure A.1 shows the implementation of this, for both the Tx and Rx VNAs. The 1 PPS output of the rubidium atomic clock is used as a system clock that is then fed to a digital counter that creates a time reference (in this case, by dividing it by 16). This time reference is used to set the period of the frequency sweep (16 s). The 1 PPS time reference from RbAC in turn signals a function generator to send a burst of N trigger pulses to the "EXT TRIG" port of the VNA at the rate of ν pulse per second, where N is the total number of frequency points. Thus, a frequency sweep is performed in $t = N/\nu$ seconds. The sweep can be performed over a continuous frequency band or the VNAs can be programmed to operate at discrete sub-bands, with non-uniform frequency sampling. This is particularly useful for conducting measurements in places where transmission over certain frequency bands or at certain frequencies within the measurement band

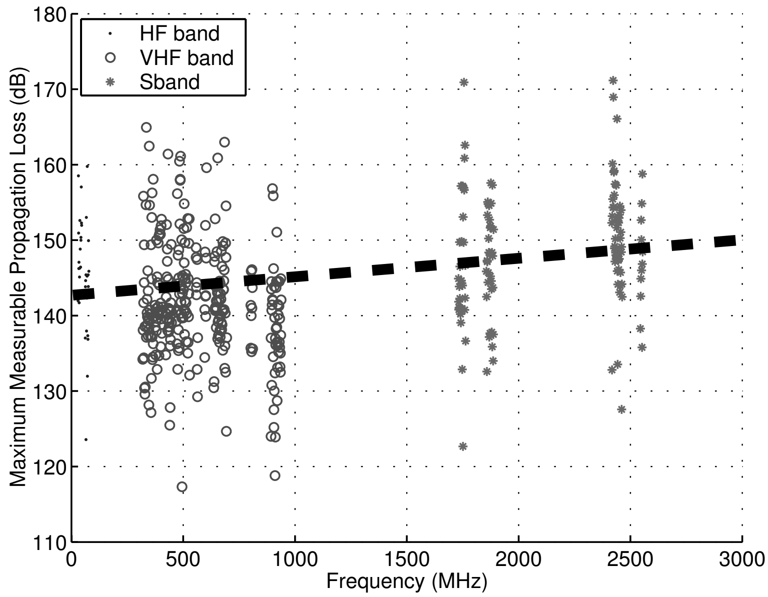

Figure A.4: Measurable propagation loss of the system.

is not allowed, for example near or in airports, military bases, etc.

Figure A.2 shows the flowchart of the system operation. To summarize the system set-up and operation, the first step is to synchronize the 1 PPS outputs of the transmitter and receivers of the RbACs so that the Tx/Rx time references are the same. This can be done simply by feeding the 1 PPS output of one of the clocks to the synchronization input of the other one [143]. Every 16 second, the function generator receives a trigger signal from the digital counter and sends a burst of N pulses (TTL compatible) to the VNA at the rate of ν PPS. This is the trigger signal denoted "trigger" in Figure A.2, which causes the transmitter VNA to start stepping through the desired frequency band. The same thing happens simultaneously at the receiver end, except that the receiver VNA begins to receive the signal that has been transmitted by the Tx VNA. After each frequency sweep, the Tx/Rx computers acquire the measured data for post processing. In order to ensure that a new sweep does not begin while this data acquisition (DAQ in Figure A.2) is in progress, both VNAs are operated in the single sweep, as opposed to the continuous sweep, mode. This mode requires that each VNA is armed by the DAQ computer, before it accepts any trigger signal for a frequency sweep. This allows the DAQ computer to hold the measurement cycle, while DAQ is in progress.

A.1.1 Calibration, and Operation

The received signal power can be obtained using the modified Friis transmission formula:

$$P_R = \frac{P_T G_T G_R}{L_{FS} L_A} \tag{1}$$

where P_T, G_T, and G_R, are the transmitted power and the antenna gains of the transmitter and receiver, respectively, L_{FS} is the free space loss, and L_A is the additional path loss in the channel. The noise power at the input of the receiver VNA is calculated using:

$$N_R = KTB_{IF} \tag{2}$$

where K is the Boltzman's constant and B_{IF} is the IF bandwidth of the VNA that can be set by the user. For the case of HP8753D this bandwidth can vary from 3 Hz to 3.7 kHz. In (2) T is the equivalent noise temperature of the system including the antenna noise temperature. A desired received signal-to-noise ratio, defined as $SNR_R = P_R/N_R$, determines system compatibility in the path loss measurements. For most practical purposes a SNR_R of 15 dB is sufficient for accurately determining the statistical behavior of the channel. Referring to (2), noise power is effected by both the system bandwidth, set by the IF bandwidth of the receiver, and by the equivalent noise temperature, T, which is usually determined by the noise figure (NF) of the first receiver amplifier or pre-amplifier. Therefore, the system SNR_R can be significantly reduced by reducing the IF bandwidth of the receiver VNA. This, however, increases the sweep time and the overall time that takes to complete the measurement. Therefore, depending on the output power, distance, expected path loss, etc., there is tradeoff between the IF bandwidth and sweep time, which determines the measurement speed and the desired SNR_R. Taking this into account, the IF bandwidth for the system was set to 3 kHz. This, in combination with a low-noise pre-amplifier (LNA) with a NF of 1.5 dB and a gain of 27 dB, resulted in a noise floor of -90 dBm for the receiver. In addition, due to the long distances over which this measurement system is used, high power radio frequency (RF) amplifiers were used to amplify the transmitted signal.

To perform measurements over a wide frequency band, it is necessary to use either a very wideband antenna, or to use different antennas for measuring different sub-bands. The gain and radiation characteristics of the antennas used in the system as well as the frequency responses of the power amplifier, LNA, and cables should be measured over the entire frequency band so that their effect can be calibrated out. Two different methods for calibration of the system are used. In the first method, the gains and losses of all of the system components (cables, amplifiers, etc) are characterized individually using the VNA and then effects are accounted for in the calibration process. In the second method, which is illustrated in Figure A.3, the output of the power amplifier is connected to the input of the LNA via a high power calibrated attenuator and the overall transmission coefficient (S_{21}), without the interlaying propagation medium, is determined. In this approach all components except the antennas, are characterized and the method has the advantage of calibrating out the effects of connector losses and mismatches. The antennas used in this system are calibrated standard gain antennas with linear polarization and relatively low gains (wide beam). As is true for most wideband antennas, the location of the phase center of the antenna changes with frequency but the change is less than the extent of the antenna structure. This dispersive behavior of the antenna can cause spectral decorrelation to some extent. However, this decorrelation is much lower than that caused by the channel and therefore, it can be ignored.

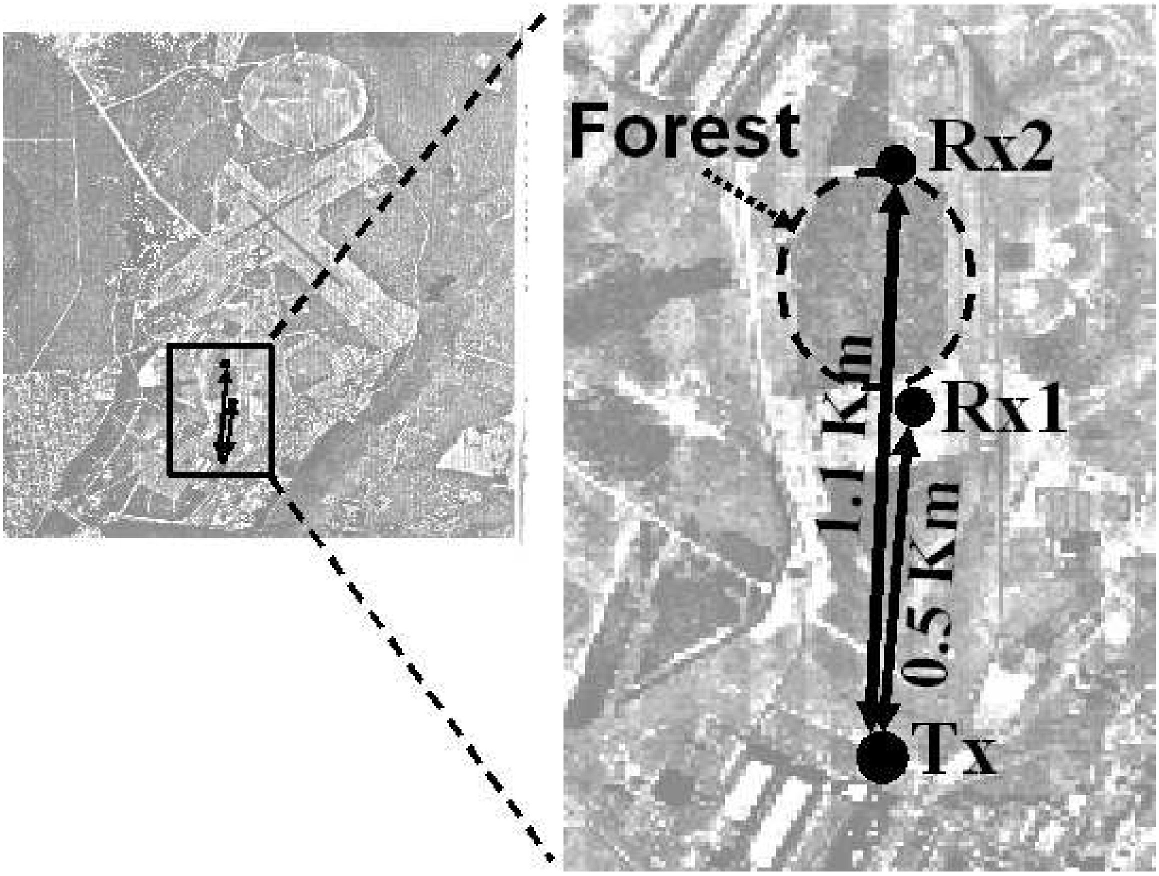

Figure A.5: Lakehurst measurement site.

A.2 Measurement Campaign at Lakehurst

In this section a measurements campaign, using the coherent propagation measurement system conducted at the Lakehurst Navel Air Station, Lakehurst, New Jersey, is described. Results are shown, including system performance specifications, mean path loss (PL) in terms of power, and frequency coherence analysis.

A.2.1 Measurement Parameters

The measurements at Lakehurst were performed in the 30 MHz to 3 GHz range in three sub-bands. These include 30 MHz to 200 MHz (defined as Band 1), 200 MHz to 1 GHz (defined as Band 2), and 1 to 3 GHz (defined as Band 3). These restrictions were placed by the authorities at the Lakehurst base and show the system's capability to operate in arbitrary sub-bands within the system bandwidth. A 10 W power amplifier, Amplifier Research (AR) model 10W1000, was used for the transmission of frequencies at and below 1 GHz, and a 30 W amplifier, AR model 30S1G3, was used for transmission in the 1 to 3 GHz band. For efficient transmission, different antennas were used in each sub-band. EMCO bowtie antennas, models 3109 (rated at 2 kW continuous wave power) and 93110B (from HP) were used for the transmit and receive antennas in Band 1, respectively. EMCO models 3148 and 93146 log-periodic antennas were used for Band 2, and two EMCO model 3115 horn antennas were used for Band 3. Due to transmission restrictions at Lakehurst, the transmission frequencies were limited to specific frequencies and bandwidths within each sub-band. Table A.1 lists the allowed transmission frequencies in terms of center frequency, f_0, and bandwidth, BW, for each allowed transmission band. Note that within the ranges specified in Table A.1 transmission frequencies were at discrete 1 MHz intervals.

Band 1: 30 MHz to 200 MHz		Band 2: 200 MHz to 1 GHz		Band 3: 1 GHz to 3 GHz	
f_0 (MHz)	BW (MHz)	f_0 (MHz)	BW (MHz)	f_0 (MHz)	BW (MHz)
38	16	325	10	1747	32
70	16	350	32	1872	32
–	–	390	32	2440	46
–	–	435	25	2550	10
–	–	493	46	–	–
–	–	524	8	–	–
–	–	561	8	–	–
–	–	600	8	–	–
–	–	641	8	–	–
–	–	670	48	–	–
–	–	806	8	–	–
–	–	915	46	–	–

Table A.1: Allowed transmission frequencies at the Lakehurst base in terms of center frequency f_0, and bandwidth, BW. Frequencies are transmitted at discrete 1 MHz intervals across each range specified.

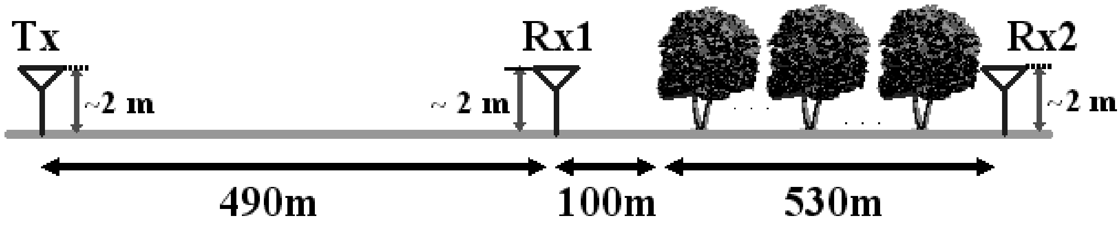

(a)

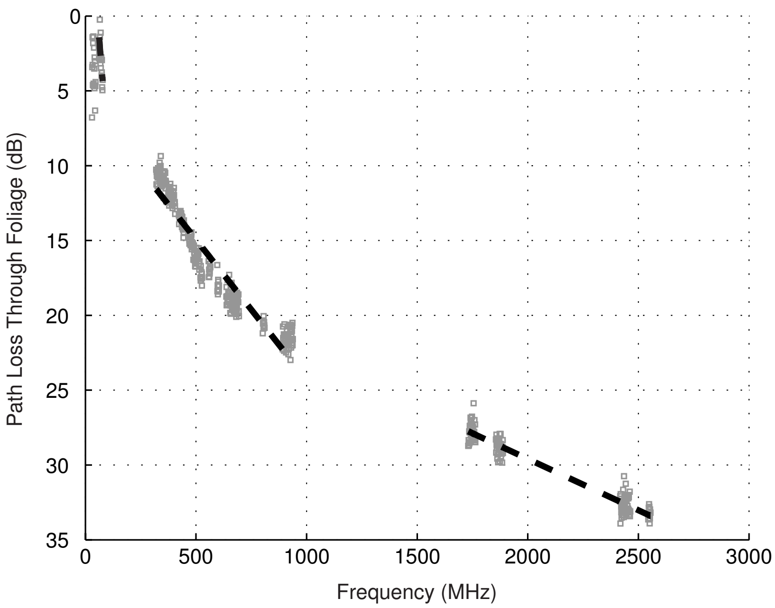

(b)

Figure A.6: Path-loss through forest: (a) measurement scenario; (b) Path Loss above free space, Rx2 referenced to Rx1.

A.2.2 Measurement Results

Before beginning an analysis of the measured data taken at the Lakehurst site, it is important to note the capabilities of the coherent measurement system. Figure A.4 shows an example of the dynamic range of the measurable propagation loss between the transmitter and receiver for the system, through the entire range that measurements were taken. This is essentially a measure of system sensitivity and can be improved by further narrowing the IF bandwidth of the receiver. To determine this maximum measurable propagation loss, the receiver signal is sampled, with no transmitter signal present, and normalized to the transmitter power. In other words, Figure A.4 shows the receiver noise power (including the LNA pre-amplifier), referenced to the transmitter power when the IF bandwidth of the receiver VNA is set at 3 kHz. Figure A.4 is normalized, assuming a transmitter power of 10 W. In Figure A.4, data was taken at each frequency point in the measurement band. The change in power levels observed across the band are typical of noise power fluctuations in a measurement system. The dashed line in the figure is a best fit curve, which is provided as a reference. As can be seen in this figure, the dynamic range of the measurable propagation loss across the measurement band is in excess of 115 dB, for the IF band setting of 3 kHz.

For all measured results shown, the transmitter was at a fixed location, with data from two receive sites provided here. At each receiver location, approximately 100 spatial samples were taken on a line perpendicular to the line between the transmitter and the receiver. In order to capture the effects of slow fading for each sub-band, the spatial samples were taken over a range of 50 λ at the lowest frequency in the sub-band. To capture the effects of fast fading, the sampling increments began at 1/2 λ increments at the highest frequency of the sub-band, gradually increasing to 1/2 λ at the lowest frequency of the sub-band.

The forested areas at the Lakehurst site consisted mainly of pitch pine, with some short vegetation in between. The pine trees had an average tree density of 0.113 Trees/m^2, average height of 9 m, average crown depth of 5 m, and an average trunk diameter of 16 cm.

The left side of Figure A.5, shows an aerial view of the Lakehurst site. On the right side of Figure A.5, the transmitter location, along with the two receive sites, is pictured. The transmitter site is located at the bottom of the photo and is marked as Tx. The receive sites, denoted with Rx1 and Rx2 in Figure A.5, are located vertically from the Tx site at distances of approximately 490, and 1120 m, respectively. Note that the area between the Tx and Rx1 is clear of forest, while the area between Rx1 and Rx2 consists of approximately 100 m of clear area, and 530 m of forest. Rx1 is located at approximately 100 m from the forest and Rx2 is located on the back side of the forest within 2 m of the forest. The transmitter and receiver heights are set at 2 m, at all locations and for all bands measured. Unmarked areas are clear of forest and may include some short vegetation.

In order to isolate the effects of the forest on PL, the measured data taken at Rx2 is normalized to that taken at Rx1. Ideally, if one wants to obtain the path loss of the forested area accurately, estimations of the path loss between the Tx and Rx2 without the forest and with the forest are required. This way, the path loss obtained when there is no forest present can be used for obtaining the forest path loss. This approach, however, is impractical. Another source of error in the approach taken here is the separation between Rx1 and the patch of forest that is not filled with the forest. Figure A.6(a) shows the measurement scenario and Figure A.6(b) shows the PL at Rx2, referenced to that measured at Rx1. The received power P_r, referenced to the transmitter power P_t, is given by:

$$\frac{P_r}{P_t} = \frac{(G_t G_r)^2}{(4R^2)} \frac{1}{R^m} PL, \tag{3}$$

where G_t and G_r are the transmit and receive antenna gains, respectively, R is the distance between transmitter and receiver, PL is the path loss of the forest, and m is an attenuation factor caused by the ground effect. Note that the first factor in (3) corresponds to the free space PL, as previously given. This ground effect can vary from 0f for a very rough ground, to 2, for the case of transmit and receive antennas very close to a perfectly flat earth. If R_1 and R_2 are the distances to Rx1 and Rx2 respectively, the power received at Rx2 referenced to that received at Rx1 is given by:

$$\frac{P_{r2}}{P_{r1}} = \left(\frac{R_1}{R_2}\right)^{m+2} PL_{forest} = \left(\frac{490}{1120}\right)^{m+2} PL_{forest}, \tag{4}$$

where PL_{forest} is the effects of the foliage on PL.

Referring to (4), Figure A.6(b) shows the PL of Rx2, referenced to that of Rx1, or the path loss above free space, for the area in between, which consists mostly of the forested area. As can be seen in Figure A.6(b), as frequency is increased, the attenuation rate of the PL lessens. This bending effect is due to the contribution of higher order scattering on the mean power. At low frequencies, the dominate contributor to the mean power is from single scattering (forward scattering represented by Foldy's theory [144]). As frequency is increased, multiple scattering among leaves and branches, which decays at a lower rate than single scattering, begins to dominate the mean power, thus the bending observed in Figure A.6(b).

A.2.3 Frequency Correlation Analysis

In the wideband measurement system described in the previous sections, the frequencies of the phased lock loops of the two network analyzers are locked together but their phases are not. This means that, at the start of each frequency sweep, the absolute phases of the two locked local oscillators are unknown. As shown later in this sub-section, the difference in the absolute phase between the Tx and Rx VNAs is in the form of a linear phase shift, for each spatial sample, across the measured frequency band. This is similar to the phase shift that is caused by the propagation of the signal through free space. The 10 MHz reference signal from the RbAC signal generator can be expressed as $\cos(\omega_{10}t + \phi_r)$. Where, $\omega_{10} = 2\pi \times 10^7$ and ϕ_r is the random phase of the oscillator. The VNA's synthesizer uses this reference to generate the desired frequencies in the sweep operation. The instantaneous frequency can be expressed as:

$$\omega_{ins} = \alpha(t)\omega_{10} + \alpha'(t)\phi_r \tag{5}$$

where the instantaneous phase is $\alpha(t)\phi_r$. Since a linear frequency sweep as a function of time is being performed, $\alpha(t)$ is a linear function of time. Therefore, (5) represents a linear relation between time and frequency. This means that ϕ_{PLL} is a linear function of both time and frequency. Knowing the behavior of this phase response allows us to take out its effect. In order to remove these delays, a frequency correlation is first performed on each spatial sample and then, an inverse discrete Fourier transform (IDFT) is applied to transform the data in the time domain. These phase delays are mapped into the time domain as time shifts. Recognizing that the free space time shift is constant for all spatial samples, the time domain impulses are now simply shifted to a common reference. The time-domain spatial samples are then averaged. Taking the discrete Fourier transform (DFT) of this function results in the corrected frequency correlation function.

In order to demonstrate this time shift, multi-path effects are ignored and the received signal for each spatial sample, is represented by:

$$S_r(f) = S'(f)\ e^{j(2\pi f \tau_{fs} + \phi_{ch}(f) + \phi_{PLL}(f))}, \tag{6}$$

where $S'(f)$ is a complex amplitude function, τ_{fs} represents the free space propagation delay, $\phi_{ch}(f)$ represents the frequency dependent phase characteristics of the

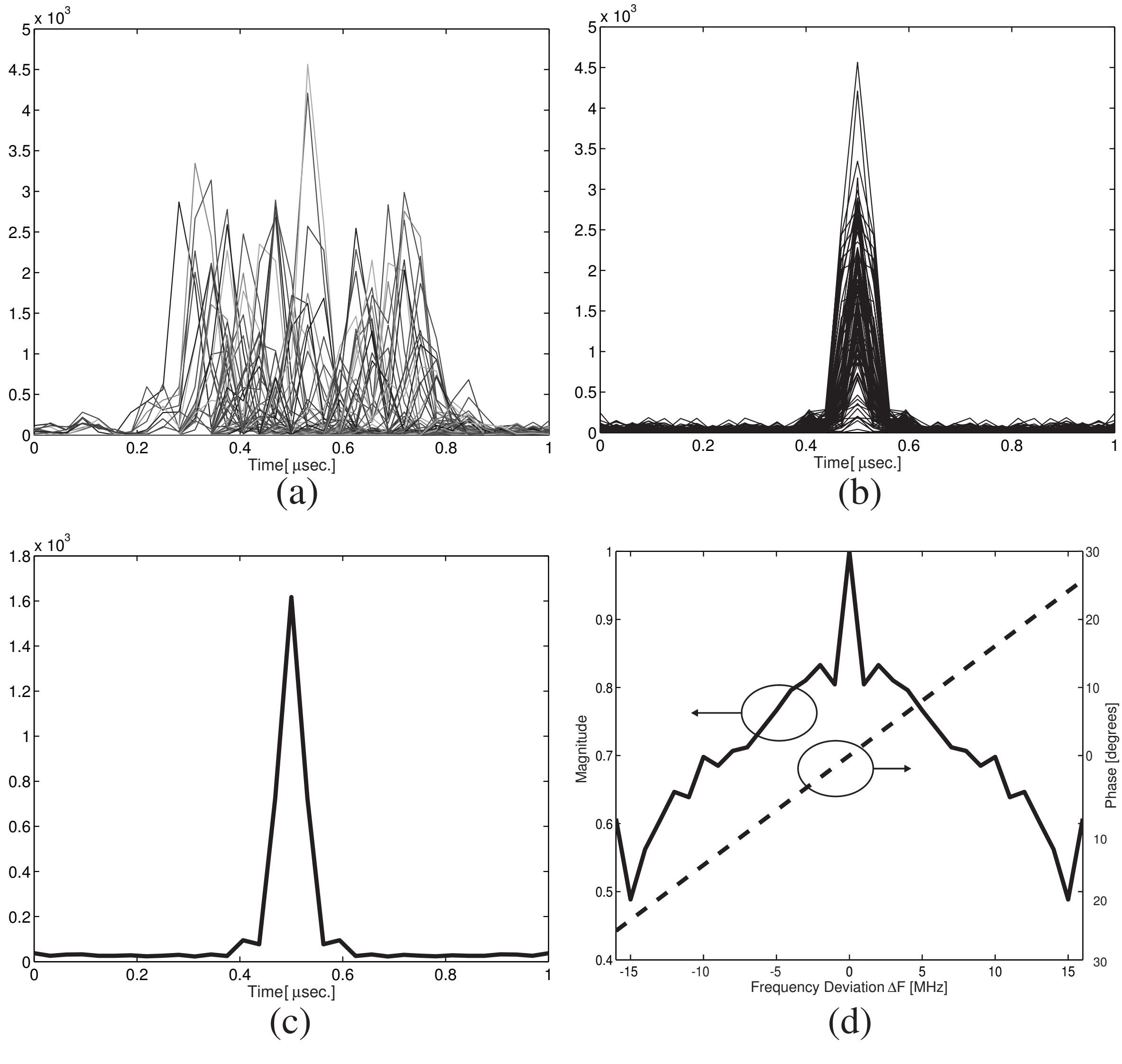

Figure A.7: Frequency correlation analysis in the HF (70± 8 MHz) band. (a) Time domain response of the HF band for 100 spatial samples before correction for PLL phase shift. (b) Time domain response of the HF band for 100 spatial samples after correction for PLL phase shift. (c) Averaged (corrected) time domain response of the HF band. (d) Frequency correlation function of the HF band.

channel (as well as phase noise caused by the PLLs, which will be discussed later in this section), and $\phi_{PLL}(f)$ represents the phase shift caused by the relative phase differences between the PLLs of the VNAs. Calculating the frequency correlation function of (6) results in the following equation:

$$c_s(\Delta f) = \int_{-\infty}^{\infty} S_r(f) S_r^*(f + \Delta f)\ df \tag{7}$$

which, upon inserting (6) in (7), becomes:

$$\begin{aligned} c_s(\Delta f) &= \int_{-\infty}^{\infty} S'(f) S'^*(f + \Delta f) e^{j(\phi_{ch}(f) - \phi_{ch}(f+\Delta f))}\ e^{-j2\pi\Delta f(\tau_{fs} + \tau_{PLL})}\ df \\ &= e^{-j2\pi\Delta f(\tau_{fs}+\tau_{PLL})} c(\Delta f) \end{aligned} \tag{8}$$

Taking the Fourier transform of (A.2.3) results in:

$$\tilde{C}_s(T) = FT\{e^{-j2\pi\Delta f(\tau_{fs}+\tau_{PLL})} c(\Delta f)\} = \tilde{C}(T - \tau_{fs} - \tau_{PLL}) \tag{9}$$

where $c(\Delta f)$ and $\tilde{C}(T)$ represent a Fourier transform pair. The variable time delays (caused by τ_{PLL}) can be observed in the time domain plots in Figure A.7(a), for the upper HF-band measured (70± 8 MHz). In this figure, for measurements taken at site Rx2, approximately 1.1 km from the transmitter (see Figure A.5), the raw frequency domain data was adjusted to remove the free space phase delay of 1.1 km, a frequency correlation performed, and an IDFT applied to the resulting correlation function. The free space phase delay is removed to prevent aliasing in the time domain. For these measurements, the data is sampled in frequency increments of 1 MHz, thus the alias free range of the time domain data is 300 m. By normalizing the frequency data to the free space phase delay, the alias free range is localized around the receiver. If the delay spread (in distance) between the direct and multi-path signal components is less than 300 m (a valid assumption over the distances involved), the transformed

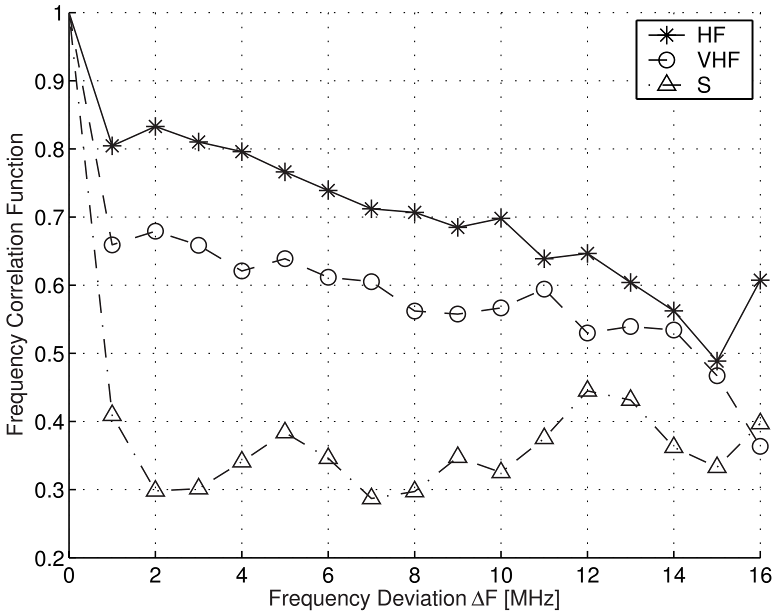

Figure A.8: A comparison of the frequency correlation functions for HF, VHF, and S-bands

data can be assumed to be alias free.

The shift in the observed peaks of the traces in Figure A.7(a) correspond to the phase shift caused by the unknown relative phases of the PLLs. It is now a simple matter to shift each peak to a common reference, as shown for all spatial samples in Figure A.7(b), and average the spatial samples in the time domain, as shown in Figure A.7(c). Thus the effect of random phase shift, observed in each spatial sample, is mitigated. An FFT is then performed to obtain the desired corrected frequency correlation function and the results is presented in Figure A.7(d).

In order to generate an accurate frequency correlation function, another factor must also be considered. This is the inherent system decorrelation that is caused by phase noise in the error signal (output) of the PLLs. Ideally, if one were to connect the transmit and receive sections of the measurement system together, gather a data set, and perform a frequency correlation, one would see a perfectly correlated channel. In practice, due to this phase noise in the PLLs, the system transfer function would not show perfect frequency correlation. To account for decorrelation caused by this system phase noise, it is recognized that the channel and system frequency correlation functions are statistically independent from one another, and therefore the correlation function of the measured signal is simply the multiplication of the correlation function of the system and that of the channel, or,

$$R_r(\Delta F) = R_{sys}(\Delta F)\ R_{ch}(\Delta F). \tag{10}$$

To correct for the system decorrelation then, a calibration data set is taken by connecting the transmit and receive sections together. Equation (10) is then applied and the measured data set is simply normalized by this calibration data set. Note that this calibration for the system decorrelation has been applied to data shown Figure A.7 as well as all results which follow.

Three sets of data, each selected from HF (70± 8 MHz), VHF (493± 23 MHz), and S-band (1872± 16 MHz), respectively, are used for the frequency correlation analysis. All data in this section is collected from site Rx2. Figure A.8 shows the frequency correlation functions for the three bands, overlapped for comparison. As can be observed in this plot there is a narrowing of the frequency correlation bandwidth for increased frequency. This is expected; as the dimensions of scatterers in the propagation environment (tree trunks, branches, twigs, leaves, short vegetation) become electrically larger, the random scattered field dominates and decorrelates the received signal.

A.3 Conclusions

In this chapter, a novel, ultra wideband measurement system, for communications channel characterization was presented. The system is based on the application of two VNAs, one as a transmitter and one as a receiver, whose frequency sweeps are synchronized by two Rb atomic clocks. These clocks also provide an extremely stable frequency reference for the VNAs. The use of the VNAs and their ability to perform swept frequency measurements, with a narrow-band, IF filter allows for long distance, high-sensitivity propagation measurements. For an IF bandwidth and transmit power of respectively 3 kHz and 10 W, the maximum measurable loss of the system, from 30 MHz to 3 GHz, was shown to exceed 115 dB.

This coherent system allows for measuring the attenuation and phase characteristics of the medium and studying temporal and frequency decorrelations. In order to demonstrate some of these capabilities, data was presented and analyzed from a measurements campaign at the Lakehurst Naval Air Station, in Lakehurst, New Jersey. It was shown that the slope of the attenuation of the mean power, caused by a forested area, tended to decrease with increased frequency, as multiple scattering effects within the forest medium began to dominate the path loss. Also frequency correlation analysis of the measured data was given. To perform this analysis, it was shown that a phase shift, caused by the phase difference in the independent PLLs in the system, must be accounted for, and a method was presented to correct for this shift. Also, after correcting for the inherent system decorrelation, caused by phase noise in the PLL error signal, frequency correlation data for three different sub-bands was presented, for a forested area at the Lakehurst base. It was shown that for higher frequency bands, the signal decorrelated at a faster rate, in frequency, as expected, due to the increased effect of multipath on the received signal, as the forest components become electrically larger.

BIBLIOGRAPHY

BIBLIOGRAPHY

[1] L. J. Chu, "Physical limitations on omni-directional antennas," *J. Appl. Phys.*, vol. 19, pp. 1163–1175, Dec. 1948.

[2] H. A. Wheeler, "Fundamental limitations of small antennas," *Proc. IRE*, vol. 35, pp. 1479–1484, Dec. 1947.

[3] R. C. Hansen, "Fundamental limitations in antennas," *Proc. IEEE*, vol. 69, pp. 170–182, Feb. 1981.

[4] J. S. McLean, "A re-examination of the fundamental limits on the radiation Q of electrically small antennas," *IEEE Trans. Antennas Propag.*, vol. 44, pp. 672–676, May 1996.

[5] R. E. Collin and S. Rothschild, "Evaluation of antenna Q," *IEEE Trans. Antennas Propag.*, vol. 12, pp. 23–27, Jan. 1964.

[6] W. Geyi, P. Jarmuszewski, and Y. Qi, "The foster reactance theorem for antennas and radiation Q," *IEEE Trans. Antennas Propag.*, vol. 48, pp. 401–408, Mar. 2000.

[7] A. Shlivinski and E. Heyman, "Time-domain near-field analysis of short-pulse antennaspart II: reactive energy and the antenna Q," *IEEE Trans. Antennas Propag.*, vol. 47, pp. 280–286, Feb. 1999.

[8] W. Geyi, "A method for the evaluation of small antenna Q," *IEEE Trans. Antennas Propag.*, vol. 51, pp. 2124–2129, Aug. 2003.

[9] J. C. E. Sten, A. Hujanen, and P. K. Koivisto, "Quality factor of an electrically small antenna radiating close to a conducting plane," *IEEE Trans. Antennas Propag.*, vol. 49, pp. 829–837, May 2001.

[10] W. Geyi, "Physical limitations of antenna," *IEEE Trans. Antennas Propag.*, vol. 51, pp. 2116–2123, Aug. 2003.

[11] G. A. Thiele, P. L. Detweiler, R. Penno, "On the lower bound of the radiation Q of electrically small antennas," *IEEE Trans. Antennas Propag.*, vol. 51, pp. 1263–1269, June 2003.

[12] S. R. Best, "A discussion on the quality factor of impedance matched electrically small wire antennas," *IEEE Trans. Antennas Propag.*, vol. 53, pp. 502–508, Jan. 2005.

[13] A. D. Yaghjian and S. R. Best, "Impedance, bandwidth, and Q of antennas," *IEEE Trans. Antennas Propag.*, vol. 53, pp. 1298–1324, Apr. 2005.

[14] H. A. Wheeler, "Small antennas," *IEEE Trans. Antennas Propag.*, vol. 23, pp. 462–469, July 1975.

[15] A. K. Skrivervik, J. F. Zurcher, O. Staub, and J. R. Mosig, "PCS antenna design: the challenge of miniaturization," *IEEE Antennas Propag. Mag.*, vol. 43, pp. 12–276, Aug. 2001.

[16] P. Hallbjorner, "Electrically small unbalanced four-arm wire antenna," *IEEE Trans. Antennas Propag.*, vol. 52, pp. 1424–1428, June 2003.

[17] S. R. Best, "The radiation properties of electrically small folded spherical helix antennas," *IEEE Trans. Antennas Propag.*, vol. 52, pp. 953–960, Apr. 2004.

[18] E. E. Altshuler, "Electrically small self-resonant wire antennas optimized using a genetic algorithm," *IEEE Trans. Antennas Propag.*, vol. 50, pp. 297–300, Mar. 2002.

[19] J. P. Gianvittorio and Y. Rahmat-Samii, " Fractal antennas: a novel antenna miniaturization technique, and applications," *IEEE Antennas Propag. Mag.*, vol. 44, pp. 20–36, Feb. 2002.

[20] S. R. Best, "On the performance properties of the Koch fractal and other bent wire monopoles," *IEEE Trans. Antennas Propag.*, vol. 51, pp. 1292–1300, June 2003.

[21] Wong, K. L., *Compact and Broadband Microstrip Antennas*, Wiley, New York, NY, 2002.

[22] P. C. T. Song, P. S. Hall, and H. Ghafouri-Shiraz, "Novel RF front end antenna package," *Proc. Inst. Elect. Eng. Antennas, Microw. and Propap.*, vol. 150, pp. 290–294, Aug. 2003.

[23] A. Buerkle, K. Sarabandi, and H. Mosallaei, "Compact slot and dielectric resonator antenna with dual-resonance, broadband characteristics," *IEEE Trans. Antennas Propag.*, vol. 53, pp. 1020–1027, Mar. 2005.

[24] A. Buerkle and K. Sarabandi, "A wide-band, circularly polarized, magnetodielectric resonator antenna," *IEEE Trans. Antennas Propag.*, vol. 53, pp. 3446–3442, Nov 2005.

[25] K. Buell, H. Mosallaei, and K. Sarabandi, "A wide-band, circularly polarized, magnetodielectric resonator antenna," *IEEE Trans. Microw. Theory Tech.*, vol. 54, pp. 135–146, Jan. 2006.

[26] H. Mosallaei and K. Sarabandi, "Antenna miniaturization and bandwidth enhancement using a reactive impedance substrate," *IEEE Trans. Antennas Propag.*, vol. 52, pp. 2403–2414, Sep. 2004.

[27] A. Erentok, P. L. Luljak, and R. W. Ziolkowski, "Characterization of a volumetric metamaterial realization of an artificial magnetic conductor for antenna applications," *IEEE Trans. Antennas Propag.*, vol. 53, pp. 160–172, Jan. 2005.

[28] G. Kumar and K. P. Ray, *Broadband Microstrip Antennas*, Artech House, Norwood, MA, 2003.

[29] K. F. Lee, R. Q. Lee, and T. Talty, "Microstrip subarray with coplanar and stacked parasitic elements," *Electron. Lett.*, vol. 26, pp. 668–669, May 1., 1990.

[30] T. M. Au and K. M. Luk, "Effect of parasitic element on the characteristics of microstrip antenna," *IEEE Trans. Antennas Propag.*, vol. 39, pp. 1247–1251, Aug. 1991.

[31] J. Huang and A. C. Densmore, "Microstrip Yagi array antenna for mobile satellite vehicle application," *IEEE Trans. Antennas Propag.*, vol. 39, pp. 1024–1030, July 1991.

[32] S. Egashira and E. Nishiyama, "Stacked microstrip antenna with wide bandwidth and high gain," *IEEE Trans. Antennas Propag.*, vol. 44, pp. 1533–1534, Nov. 1996.

[33] N. Herscovici, "A wide-band single-layer patch antenna," *IEEE Trans. Antennas Propag.*, vol. 46, pp. 471–474, Apr. 1998.

[34] J. Anguera, G. Font, C. Puente, C. Borja, and J. Soler, "Multifrequency microstrip patch antenna using multiple stacked elements," *IEEE Microw. Wireless Compon. Lett.*, vol. 13, pp. 123–124, Mar. 2003.

[35] E. Nishiyama, M. Aikawa, and S. Egashira, "Stacked microstrip antenna for wideband and high gain," *Proc. Inst. Elect. Eng. Antennas, Microw. and Propap.*, vol. 151, pp. 143–148, Apr. 2004.

[36] A. K. Shackelford, L. Kai-Fong, and K. M. Luk, "Design of small-size wide-bandwidth microstrip-patch antennas," *IEEE Antennas Propag. Mag.*, vol. 45, pp. 75–83, Feb. 2003.

[37] F. Yang, Z. Xue-Xia, Y. Xiaoning, and Y. Rahmat-Samii, "Wide-band E-shaped patch antennas for wireless communications," *IEEE Trans. Antennas Propag.*, vol. 49, pp. 1094–1100, July 2001.

[38] C. Chi Yuk, S. Kam Man, C. Chi Hou, and L. Kwai Man, "Bandwidth enhancement technique for quarter-wave patch antennas," *IEEE Antennas Wireless Propag. Lett.*, vol. 2, pp. 130–132, 2003.

[39] P. Bhartia, et al, *Microstrip Antenna Design Handbook*, Artech House, Norwood, MA, 2000.

[40] Y. L. Kuo and K. L. Wong, "Printed double-T monopole antenna for 2.4/5.2 GHz dual-band WLAN operations," *IEEE Trans. Antennas Propag.*, vol. 51, pp. 2187–2192, Sep. 2003.

[41] W. Richards, S. Davidson, and S. Long, "Dual-band reactively loaded microstrip antenna," *IEEE Trans. Antennas Propag.*, vol. 33, pp. 556–561, May 1985.

[42] K. P. Ray and G. Kumar, "Tuneable and dual-band circular microstrip antenna with stubs," *IEEE Trans. Antennas Propag.*, vol. 48, pp. 1036–1039, July 2000.

[43] A. Jaume, E. Martinez, C. Puente, C. Borja, and J. Soler, "Broad-band dual-frequency microstrip patch antenna with modified Sierpinski fractal geometry," *IEEE Trans. Antennas Propag.*, vol. 52, pp. 66–73, Jan. 2004.

[44] S. Maci, B. Bifi Gentili, P. Piazzesi, and C. Salvador, "Dual band slot-loaded patch antenna," *Proc. Inst. Elect. Eng. Antennas, Microw. and Propap.*, vol. 142, pp. 225–232, June 1995.

[45] G. B. Hsieh and K. Wong, "Inset microstrip-line-fed dual-frequency circular microstrip antenna and its application to a two-element dual-frequency microstrip array," *Proc. Inst. Elect. Eng. Antennas, Microw. and Propap.*, vol. 146, pp. 359–361, Oct. 1999.

[46] S. T. Fang and K. L. Wong, "A dual frequency equilateral triangular microstrip antenna with a pair of two narrow slots," *Microw. Opt. Technol. Lett.*, vol. 23, pp. 82–84, Oct. 20, 1999.

[47] C. Zhi Ning, "Suspended plate antennas with shorting strips and slots," *IEEE Trans. Antennas Propag.*, vol. 52, pp. 2525–2531, Oct. 2004.

[48] D. Peroulis, K. Sarabandi, and L. P. B. Katehi, "A planar VHF reconfigurable slot antenna," in *Proc. IEEE AP-S Symp.*, Boston, MA, July 8-13, 2001, vol. 1, pp. 154–157.

[49] D. Llorens, P. Otero, and C. Camacho-Penalosa, "Dual-band single CPW port planar-slot antenna," *IEEE Trans. Antennas Propag.*, vol. 51, pp. 137–139, Jan. 2003.

[50] C. Wang, J. Lee, and R. Huang, "Experimental studies of a miniaturized CPW-fed slot antenna with the dual-frequency operation," *IEEE Antennas Wireless Propag. Lett.*, vol. 2, pp. 151–154, 2003.

[51] T. Morioka, S. Araki, and K. Hirasawa, "Slot antenna with parasitic element for dual band operation," *Electron. Lett.*, vol. 33, pp. 2093–2094, Dec. 4, 1997.

[52] J. S. Chen., "Triple-frequency annular-ring slot antennas fed by CPW and microstrip line," in *Proc. IEEE AP-S Symp.*, Columbus, OH, June 22-27, 2003, vol. 2, pp. 557–560.

[53] G. F. Ross, *The transient analysis of multiple beam feed networks for array systems*, Ph.D. thesis, Polytechnic Institute of Brooklyn, Brooklyn, NY, 1963.

[54] Y. Liuqing and G. B. Giannakis, "Ultra-wideband communications: an idea whose time has come," *IEEE Signal Process. Mag.*, vol. 21, pp. 26–54, Nov. 2004.

[55] E. Baccarelli, M. Biagi, C. Pelizzoni, and P. Bellotti, "A novel multi-antenna impulse radio UWB transceiver for broadband high-throughput 4G WLANs," *IEEE Comm. Lett.*, vol. 8, pp. 419–421, July 2004.

[56] C. A. Balanis, *Antenna Theory: Analysis and Design*, Wiley, New York, NY, 1996.

[57] C. H. Walter, *Traveling Wave Antennas*, Peninsula Pub, 1990.

[58] D. Schaubert, E. Kollberg, T. Korzeniowski, T. Thungren, J. Johansson, and K. Yngvesson, "Endfire tapered slot antennas on dielectric substrates," *IEEE Trans. Antennas Propag.*, vol. 33, pp. 1392–1400, Dec. 1985.

[59] A. K. Y. Lai, A. L. Sinopoli, and W. D. Burnside, "A novel antenna for ultra-wide-band applications," *IEEE Trans. Antennas Propag.*, vol. 40, pp. 755–760, July 1992.

[60] R. Janaswamy and D. Schaubert, "Analysis of the tapered slot antenna," *IEEE Trans. Antennas Propag.*, vol. 35, pp. 1058–1065, Sep. 1987.

[61] S. Joon Shin and D. H. Schaubert, "A parameter study of stripline-fed Vivaldi notch-antenna arrays," *IEEE Trans. Antennas Propag.*, vol. 47, pp. 879–886, May 1999.

[62] R. G. Corzine and J. A. Mosko, *Four Armed Spiral Antennas*, Artech House, Norwood, MA, 1990.

[63] M. N. Afsar, Yong Wang, and R. Cheung, "Analysis and measurement of a broadband spiral antenna," *IEEE Antennas Propag. Mag.*, vol. 46, pp. 59–64, Feb. 2004.

[64] T. W. Hertel and G. S. Smith, "On the dispersive properties of the conical spiral antenna and its use for pulsed radiation," *IEEE Trans. Antennas Propag.*, vol. 51, pp. 1426–1433, July 2003.

[65] Y. Mushiake, *Self-Complementary Antennas: Principle of Self-Complementarity for Constant Impedance*, Springer Verlag, Berlin, Germany, 1996.

[66] N. Behdad and K. Sarabandi, "A wideband slot antenna design employing a fictitious short circuit concept," *IEEE Trans. Antennas Propag.*, vol. 53, pp. 475–482, Jan. 2005.

[67] M. Lapierre, Y. M. M. Antar, A. Ittipiboon, and A. Petosa, "Ultra wideband monopole/dielectric resonator antenna," *IEEE Microw. Wireless Compon. Lett.*, vol. 15, pp. 7–9, Jan. 2005.

[68] K. Kwan-Ho, C. Sung-Bae, P. Young-Jin, and P. Han-Gyu, "Novel planar ultra wideband stepped-fat dipole antenna," in *Proc. IEEE Conf. Ultra Wideband Sys. Technol.*, Reston, VA, Nov. 16-18, 2003, pp. 508–512.

[69] H. G. Schantz, "Introduction to ultra-wideband antennas," in *Proc. IEEE Conf. Ultra Wideband Sys. Technol.*, Reston, VA, Nov. 16-19, 2003, pp. 1–9.

[70] H. G. Schantz, "A brief history of UWB antennas," *IEEE Aerospace Electron. Sys. Mag.*, vol. 19, pp. 22–26, Apr. 2004.

[71] K. Y. Yazdandoost and R. Kohno, "Ultra wideband antenna," *IEEE Communications Magazine*, vol. 42, pp. 29–32, June 2004.

[72] N. P. Agrawal, G. Kumar, and K. P. Ray, "New wideband monopole antennas," in *Proc. IEEE AP-S Symp.*, Montreal, Canada, July 13-18, 1997, vol. 1, pp. 248–251.

[73] M. Lapierre, Y. M. M. Antar, A. Ittipiboon, and A. Petosa, "A wideband monopole antenna using dielectric resonator loading," in *Proc. IEEE AP-S Symp.*, Columbus, OH, June 22-27, 2003, vol. 3, pp. 16–19.

[74] M. J. Ammann and Z. J. Chen, "Wideband monopole antennas for multi-band wireless systems," *IEEE Antennas Propag. Mag.*, vol. 45, pp. 146–150, Apr. 2003.

[75] R. Azadegan, *Highly miniaturized antennas and filters for wireless applications*, Ph.D. thesis, University of Michigann, Ann Arbor, MI, 2004.

[76] K. Sarabandi and R. Azadegan, "Design of an efficient miniaturized UHF planar antenna," *IEEE Trans. Antennas Propag.*, vol. 51, pp. 1270–1276, June 2003.

[77] A. U. Bhobe, C. L. Holloway, M. Piket-May, and R. Hall, "Wide-band slot antennas with CPW feed lines: hybrid and log-periodic designs," *IEEE Trans. Antennas Propag.*, vol. 52, pp. 2545–2554, Oct. 2004.

[78] H. K. Kan and R. B. Waterhouse, "Small square dual spiral printed antennas," *Electron. Lett.*, vol. 37, pp. 478–479, Apr. 12, 2003.

[79] R. Azadegan and K. Sarabandi, "Miniaturized folded-slot: an approach to increase the bandwidth and efficiency of miniaturized slot antennas," in *Proc. IEEE AP-S Symp.*, San Antonio, TX, June 16-21, 2002, vol. 4, pp. 14–17.

[80] K. Sarabandi and H. Mosallaei, "Antenna miniaturization with enhanced bandwidth and radiation characteristics: a novel design utilizing periodic magneto-dielectric," in *Proc. IEEE AP-S Symp.*, San Antonio, TX, June 16-21, 2002, vol. 3, pp. 756–759.

[81] T. Ozdemir, P. Frantzis, K. Sabet, L. Katehi, K. Sarabandi, and J. Harvey, "Compact wireless antennas using a superstrate dielectric lens," in *Proc. IEEE AP-S Symp.*, Salt Lake City, UT, July 16-21, 2000, vol. 3, pp. 1678–1681.

[82] Zeland Software Inc, "IE3D, Electromagnetic Simulation and Optimization Software," .

[83] J. J. Lee, "Slotline impedance," *IEEE Trans. Microw. Theory Tech.*, vol. 39, pp. 666–672, Apr. 1991.

[84] M. Kahrizi, T. Sarkar, and Z. Maricevic, "Analysis of a wide radiating slot in the ground plane of a microstrip line," *IEEE Trans. Microw. Theory Tech.*, vol. 41, pp. 29–37, Jan. 1993.

[85] J. Sze and K. Wong, "Bandwidth enhancement of a microstrip-line-fed printed wide-slot antenna," *IEEE Trans. Antennas Propag.*, vol. 49, pp. 1020–1024, July 2001.

[86] H. L. Lee, H. J. Lee, J. G. Yook, and H. K. Park, "Broadband planar antenna having round corner rectangular wide slot," in *Proc. IEEE AP-S Symp.*, San Antonio, TX, June 16-21, 2002, vol. 2, pp. 460–463.

[87] P. H. Rao, V. Fusco, and R. Cahill, "A broadband antenna for PCN/UMTS applications," in *High Frequency Postgraduate Student Colloquium*, University College Dublin, Ireland, Sep. 7-8, 2000, pp. 2–5.

[88] X. Liang and C. Y. W. Michael, "A microstrip-fed wideband slot array with finite ground," in *Proc. IEEE AP-S Symp.*, Salt Lake City, UT, July 16-21, 2000, vol. 2, pp. 510–513.

[89] N. Behdad and K. Sarabandi, "Dual resonant slot antennas for wireless applications," in *Proc. IEEE AP-S Symp.*, Monterey, CA, June 20-25, 2004, vol. 2, pp. 1931–1934.

[90] Agilent Technologies, "Advance Design Systems," .

[91] Garg et. al., *Microstrip Antenna Design Handbook*, Artech House, Norwood, MA, 2001.

[92] B. Das and K. Joshi, "Impedance of a radiating slot in the ground plane of a microstripline," *IEEE Trans. Antennas Propag.*, vol. 30, pp. 922–926, Sep. 1982.

[93] J. P. Kim and W. S. Park, "Network modeling of an inclined and offcenter microstrip-fed slot antenna," *IEEE Trans. Antennas Propag.*, vol. 46, pp. 1182–1188, Aug. 1998.

[94] B. Stockbroeckx, I. Huynen, and A. V. Vorst, "Effect of surface wave diffraction on radiation pattern of slot antenna etched in finite ground plane," *Electron. Lett.*, vol. 36, pp. 1444–1446, Aug. 17, 2000.

[95] R. M. DeFelice Souza, F. DaCosta Silva, and A. J. Giarola, "Effect of a finite ground plane thickness on the radiation pattern of an aperture antenna," in *Proc. IEEE AP-S Symp.*, Syracuse, NY, June 6-10, 1988, vol. 1, pp. 34–37.

[96] V. Natarajan, E. Chettiar, and D. Chatterjee, "Effect of ground plane size on the performance of a class of microstrip antennas on microwave substrates," in *Proc. IEEE AP-S Symp.*, Monterey, CA, June 20-25, 2004, vol. 4, pp. 4491–4494.

[97] R. Azadegan and K. Sarabandi, "A novel approach for miniaturization of slot antennas," *IEEE Trans. Antennas Propag.*, vol. 51, pp. 421–429, Mar. 2003.

[98] N. Behdad and K. Sarabandi, "Bandwidth enhancement and further size reduction of a class of miniaturized slot antennas," *IEEE Trans. Antennas Propag.*, vol. 52, pp. 1928–1935, Aug. 2004.

[99] B. Zheng and Z. Shen, "Effect of a finite ground plane on microstrip-fed cavity-backed slot antennas," *IEEE Trans. Antennas Propag.*, vol. 53, pp. 862–865, Feb. 2005.

[100] D. Peroulis, K. Sarabandi, and L. P. B. Katehi, "Design of reconfigurable slot antennas," *IEEE Trans. Antennas Propag.*, vol. 53, pp. 645–654, Feb. 2005.

[101] J. T. Aberle, O. Sung-Hoon, D. T. Auckland, and S. D. Rogers, "Reconfigurable antennas for wireless devices," *IEEE Antennas Propag. Mag.*, vol. 45, pp. 148–154, Dec. 2003.

[102] B. A. Cetiner, H. Jafarkhani, Q. Jiang-Yuan, Y. H. Jae, A. Grau, and F. De Flaviis, "Multifunctional reconfigurable MEMS integrated antennas for adaptive MIMO systems," *IEEE Communications Magazine*, vol. 42, pp. 62–70, Dec. 2004.

[103] P. J. Rainville and F. J. Harackieewicz, "Magnetic tuning of a microstrip patch antenna fabricated on a ferrite film," *IEEE Communications Magazine*, vol. 2, pp. 483–485, Dec. 1992.

[104] S. Zhang, G. H. Huff, J. Feng, and J. T. Bernhard, "A pattern reconfigurable microstrip parasitic array," *IEEE Trans. Antennas Propag.*, vol. 52, pp. 2773–2776, Oct. 2004.

[105] D. M. Pozar, *Microwave Engineering*, Wiley, New York, NY, 2004.

[106] R. Janaswamy and D. H. Schaubert, "Characteristic impedance of a wide slotline on low-permittivity substrates," *IEEE Trans. Microw. Theory Tech.*, vol. 34, pp. 900–902, Aug. 1986.

[107] K. Chang, *Microwave Ring Circuits and Antennas*, Wiley, New York, NY, 1996.

[108] C. Zuffada and F. C. Yang, "Currents and fields of thin circular and elliptical loops," *IEEE Trans. Electromagn. Compat.*, vol. 33, pp. 97–104, May 1991.

[109] B. Levin, "Field of a rectangular loop," *IEEE Trans. Antennas Propag.*, vol. 52, pp. 948–952, Apr. 2004.

[110] H. A. N. Hejase, "Analysis of a printed wire loop antenna," *IEEE Trans. Microw. Theory Tech.*, vol. 42, pp. 227–233, Feb. 1994.

[111] C. E. Tong and R. Blundell, "An annular slot antenna on a dielectric half-space," *IEEE Trans. Microw. Theory Tech.*, vol. 42, pp. 967–974, July 1994.

[112] N. Nikolic, J. S. Kot, and T. S. Bird, "Theoretical and experimental study of a cavity-backed annular-slot antenna," *Proc. Inst. Elect. Eng. Antennas, Microw. and Propap.*, vol. 144, pp. 337–340, Oct. 1997.

[113] H. Nakano, M. Fukasawa, and J. Yamauchi, "Multi-frequency and wide-band VSWR characteristics of loop antennas," in *Proc. IEEE AP-S Symp.*, Salt Lake City, UT, July 16-21, 2000, vol. 3, pp. 1524–1527.

[114] F. A. Alhargan and S. R. Judah, "Wide band confocal annular elliptic microstrip antenna," in *Proc. IEEE AP-S Symp.*, Newport Beach, CA, June 18-23, 1995, vol. 2, pp. 1006–1009.

[115] P. Minard and A. Louzir, "A new wide frequency band feeding technique of annular slot antenna," in *Proc. IEEE AP-S Symp.*, San Antonio, TX, June 16-21, 2002, vol. 1, pp. 406–409.

[116] H. Tehrani and K. Chang, "A multi-frequency microstrip-fed annular slot antenna," in *Proc. IEEE AP-S Symp.*, Salt Lake City, UT, July 16-21, 2000, vol. 2, pp. 632–635.

[117] N. Behdad and K. Sarabandi, "Wideband double-element ring slot antenna," *Electron. Lett.*, vol. 40, pp. 408–409, Apr. 1, 2004.

[118] N. Behdad and K. Sarabandi, "A multiresonant single-element wideband slot antenna," *IEEE Antennas Wireless Propag. Lett.*, vol. 3, pp. 5–8, 2004.

[119] Y. Okumura, E. Ohmori, T. Kawano, and K. Fukuda, "Field strength and its variability in VHF and UHF land mobile service," *Rev. Elec. Comm. Lab*, vol. 16, pp. 825, Sept.-Oct 1968.

[120] N. C. Rogers, A. Seville, J. Richter, D. Ndzi, N. Savage, R.F.S. Caldeirinha, A. K. Shukla, M. O. Al-Nuaimi, K. Craig, E. Vilar, and J. Austin, "A generic model of 1-60 GHz radio propagation through vegetation-final report," Tech. Rep., Document produced by QinetiQ for the UK Radiocommunications Agency, May, 2002.

[121] A. G. Longley and P. L. Rice, "Prediction of tropospheric radio transmission loss over irregular terrain, a computer method - 1968," Tech. Rep. ERL79-ITS67, ESSA Research Laboratories, Washington, D.C., 1968, US Government Printing Office.

[122] K. Sarabandi and I. Koh, "An overview of physics-based wave propagation in forested environment," in *International Workshop on Wave Propagation, Scattering and Emission (WPSE03): Theory, Experiments, Numerical Simulation and Inversion*, Shanhai, China, June 1-4, 2003, pp. 632–635.

[123] F. Wang, I. Koh, and K. Sarabandi, "Theory and measurements of millimeter-wave propagation through foliage," in *Proc. USNC/URSI Symp.*, Columbus, OH, June 22-27, 2003.

[124] F. Aryanfar, I. Koh, and K. Sarabandi, "Physics based ray-tracing propagation model for sub-urban areas," in *Proc. IEEE AP-S Symp.*, Columbus, OH, June 22-27, 2003, vol. 4, pp. 903–906.

[125] L. Pierce and K. Sarabandi, "Parallelized physics-based foliage wave propagation model," in *Proc. EMCC Annual Meeting*, Hampton, VA, May 20-22, 2003.

[126] I. Koh and K. Sarabandi, "Polarimetric channel characterization of foliage for performance assessment of GPS receivers under tree canopies," *IEEE Trans. Antennas Propag.*, vol. 50, pp. 713–726, May 2002.

[127] K. Sarabandi and I. Koh, "Effect of canopy-air interface roughness on HF-VHF propagation in forest," *IEEE Trans. Antennas Propag.*, vol. 50, pp. 111–122, Feb. 2002.

[128] K. Sarabandi and I. Koh, "A complete physics-based channel parameter simulation for wave propagation in a forest environment," *IEEE Trans. Antennas Propag.*, vol. 49, no. 2, pp. 260–271, Feb. 2001.

[129] I. Koh, F. Wang, and K. Sarabandi, "Estimation of coherent field attenuation through dense foliage including multiple scattering," *IEEE Trans. on Geosci. Remote Sens.*, vol. 41, pp. 1132–1135, May 2003.

[130] M. D. Casciato, S. Oveisgharan, and K. Sarabandi, "Radio wave propagation in the presence of a coastline," *Radio Sci.*, vol. 38, no. 5, pp. 1085, 2003.

[131] M. D. Casciato and K. Sarabandi, "High frequency radio wave diffraction from singly curved surfaces- a heuristic approach," *Proc. Inst. Elect. Eng. Part H - Microw., Antennas, Propag.*, vol. 151, no. 1, pp. 43–53, Feb. 2004.

[132] N. C. Currie, F. B. Dyer, and E. E. Martin, "Millimeter foliage penetration measurements," in *Proc. IEEE AP-S Symp.*, Amherst, MA, Oct. 1976, vol. 14, pp. 93–96.

[133] F. K. Schwering, E. J. Violette, and R. H. Espeland, "Millimeter-wave propagation in vegetation: experiments and theory," *IEEE Trans. Geosci. Remote Sens.*, vol. 26, no. 3, pp. 355–367, May 1988.

[134] A. Y. Nashashibi, K. Sarabandi, S. Oveisgharan, M. C. Dobson, W. Walker, and E. Burke, "Millimeter-wave measurements of foliage attenuation and ground reflectivity of tree stands at nadir incidence," *IEEE Trans. Antennas Propag.*, vol. 52, no. 5, pp. 1211–1222, May 2004.

[135] R. J. C. Bultitude, P. Melancon, H. Zaghloul, G. Morrison, and M. Prokki, "A comparison of indoor radio propagation characteristics at 910 MHz and 1.75 GHz," *IEEE J. Sel. Areas Comm.*, vol. 7, no. 1, pp. 20–30, Jan. 1989.

[136] J. G. O. Moss, M. P. Fitton, A. M. Street, K. M. Brown, C. C. Constantinou, and D. J. Edwards, "Spatio-temporal variability analysis of the wideband microcellular environment," in *Proc.IEEE Vehicular Technol. Conf.*, May 1998, pp. 293–297.

[137] J. Liu, C. P. Wei, D. Chang, C. Chang, and C. Cheng, "Estimating the RF attenuation rate via roadside trees with extraction techniques," *Microw. Opt. Technol. Lett.*, vol. 30, no. 4, pp. 242–246, Aug. 2001.

[138] C. L. Rino and J. Owen, "Wideband propagation measurements in forested media," Tech. Rep. under contract DAAD-07-85-C-K569, SRI International (project 8899), submitted to U.S. Army Communications-Electronics Command (CECOM), Fort Monmouth, NJ, Aug. 1988.

[139] S. J. Howard and K. Pahlavan, "Measurement and analysis of the indoor radio channel in the frequency domain," *IEEE Trans. Inst. Meas.*, vol. 39, no. 5, pp. 751–755, Oct. 1990.

[140] H. Zaghloul, G. Morrison, and M. Fattouche, "Frequency response and path loss measurements of indoor channel," *Electron. Lett.*, vol. 27, no. 12, pp. 1021–1022, Oct. 1991.

[141] A. M. Street, J. G. O. Moss, and D. J. Edwards, "Outdoor-indoor wideband channel study for third generation communication systems," *Inst. Elect. Eng. Conf. Antennas Propag.*, pp. 128–131, Mar. 31-Apr. 1, 1999.

[142] A. M. Street, L. Lukama, and D. J. Edwards, "Use of VNAs for wideband propagation measurements," *Proc. Inst. Elect. Eng. Comm.*, vol. 148, no. 6, pp. 411–415, Dec. 2001.

[143] PRS10, "PRS10 Rubidium Frequency Standard," Tech. Rep., Stanford Reasearch Systems.

[144] L. L. Foldy, "The multiple scattering of waves," *Phys. Rev.*, vol. 67, pp. 107–119, 1945.